

Searches for supersymmetry in final states containing b-tagged jets with the ATLAS detector



Calum Macdonald

Supervisor: Davide Costanzo

Department of Physics and Astronomy
University of Sheffield

This dissertation is submitted for the degree of
Doctor of Philosophy

August 2017

Dedicated to the memory of Kathleen Mary Macdonald

Abstract

Supersymmetry is one of the most theoretically studied subjects in modern particle physics; so far no direct experimental proof of its existence has been observed. The Large Hadron Collider (LHC) is a machine designed to create high energy particle collisions, which are analysed by multiple experiments, probing the substructure and fundamental properties of matter. The experiment ATLAS is used in this thesis in searches for the signatures supersymmetric particles as they decay. A detailed overview of two signature searches for third generation supersymmetry in events with b -tagged jets is the main focus of this thesis. A data-driven technique for estimating the Multi-jet background in zero lepton final state signatures is additionally presented.

The first search used a dataset with an integrated luminosity of 3.2 fb^{-1} collected in 2015 during Run-II of the LHC at a centre-of-mass energy of $\sqrt{s} = 13 \text{ TeV}$. The analysis was optimised for a simplified signal model in which only the supersymmetric partners of the bottom quark are pair-produced in LHC collisions. No significant excess above the Standard Model background was observed, setting 95% CL limits on the masses of the scalar bottom quark and lightest neutralino. Many sophisticated techniques for estimating the Standard Model backgrounds were employed using Monte-Carlo simulation and data-driven techniques, which are applicable to many hadron collider analyses. The prospects of future discovery of scalar bottom quarks were studied, resolving a 5σ discovery potential above 1 TeV at the High Luminosity LHC for low mass neutralinos.

The second search was performed at the end of Run-I of the LHC using a dataset corresponding to an integrated luminosity of 20.3 fb^{-1} at $\sqrt{s} = 8 \text{ TeV}$. The analysis focused on a unique search for the pair-production of scalar top and bottom quarks decaying asymmetrically to neutralinos and charginos in a more complex and arguably more realistic model scenario. The models targeted were inspired by a natural pMSSM scenario with low mass supersymmetry partner of the third generation quarks. Again, no significant deviation from the Standard Model background was observed setting 95% CL limits on the masses of the third generation supersymmetric quarks. The results of the analysis were interpreted in the context of a full pMSSM scan together with many other ATLAS analyses to provide the theoretical

community with a more meaningful summary of the exclusion limit on supersymmetric particles set by ATLAS.

Acknowledgements

Firstly I would like to thank my family for all the loving support over the last 3 to 4 years, without them this thesis would not have been possible. Special thanks goes for my brother Chris for the grammar and spell checking. My biggest thanks goes to Robyn for putting up with all my stress, late nights at work and travelling to Switzerland multiple times to see me.

To all the people at the University of Sheffield Physics and Astronomy department, many of whom I have known since the start of my undergraduate degree, a big thank you for all the great times and fantastic education. In no particular order, thanks goes to Dave, Jamie, Tom, Amy, Johnny, Andy and Karl for many years of great times in the department. I have also had the pleasure of sharing the office with many great people: Matt, Anthony, Kerry, Vangelis, Guillermo, Harry, Steve, Gary. Thanks to Mike and Manu for keeping me sane with many memorable laughs.

I would like to thank Professor Neil Spooner, Dr Vitaly Kudryavtsev and Dr Susan Cartwright for starting my career in particle physics with the DM-Ice experiment as an undergraduate. If I never had the experience with working such great physicists on a friendly experiment at an young age I would not be where I am today.

I owe a fantastic experience as a PhD student to my supervisor Davide Costanzo, a great particle physicist and programmer whose support, guidance and approach has made me the enthusiastic physicist I am today. My second supervisor Dan Tovey has been a great inspiration for me too.

I have had the pleasure of working with several great post-docs in my time based in Sheffield and based at CERN. Most notably: Dr Kerim Suruliz and Dr Martin Tripiana Gorgojo who got me through my first year and who I have bugged many times on skype. Both have been great inspirations.

To the other students on the sbottom and tbMET analysis teams: John, Giuseppe and Silvia; your friendliness and great work is the reason why I have enjoyed my PhD so much. I would like to also thank Dr. Monica D'Onofrio and Dr. Iacopo Vivarelli for many hours of discussions and long email threads who have both truly been an inspiration to me.

For all the memories and good times at CERN, many thanks to all my friends while I was on LTA, particularly John, Jamie and Kārlis.

The Sheffield ATLAS group have been a pleasure to work with, thanks especially to: Ian, Mark, Paul M, Trevor, Per and all those who have come and gone during my time.

Table of contents

List of figures	xii
List of tables	xxiii
Nomenclature	xxviii
1 Introduction	1
2 Theoretical Motivation	4
2.1 The Standard Model of Particle Physics	4
2.1.1 Particle Classification	5
2.1.2 The Standard Model Lagrangian Density	6
2.1.3 Quantum Electrodynamics (QED)	7
2.1.4 Quantum Chromodynamics (QCD)	8
2.1.5 Electroweak Theory (EWT)	11
2.1.6 Spontaneous Symmetry Breaking (SSB)	12
2.2 Beyond the Standard Model	16
2.3 The Hierarchy Problem	17
2.4 Supersymmetry	18
2.4.1 Weiss-Zumino Model	18
2.4.2 The Minimal Supersymmetric Standard Model (MSSM)	20
2.4.3 Unification	22
2.4.4 R-parity	22
2.4.5 The Phenomenological MSSM (pMSSM)	23
2.4.6 Naturalness	24
2.4.7 Summary of Supersymmetry	26
3 Collider Physics	28
3.1 Colliders	28

3.1.1	Collision Rate	29
3.1.2	The Parton Distribution Function	29
3.2	Particle Production at Colliders	30
3.2.1	Initial and Final State Radiation	32
3.2.2	Pileup	33
3.2.3	Structure of an Event	33
3.2.4	Final State Observation	34
3.3	Supersymmetry at Hadron Colliders	35
3.3.1	Production Mechanisms	36
3.3.2	Supersymmetry in Final States	36
3.3.3	Simplified Models	38
3.3.4	Searches for Supersymmetry at the LHC	39
4	The LHC and The ATLAS Detector	44
4.1	The Large Hadron Collider (LHC)	44
4.2	The ATLAS Detector	45
4.2.1	Overview of ATLAS	46
4.2.2	ATLAS Coordinate System	47
4.3	Magnet System	47
4.4	Inner Detector	49
4.4.1	Insertable B-Layer	50
4.4.2	The Pixel Detector	51
4.4.3	SCT	52
4.4.4	TRT	52
4.5	Calorimeters	53
4.5.1	Electromagnetic Calorimeter	54
4.5.2	Hadronic Calorimeter	55
4.6	Muon Spectrometer	56
4.7	Triggers	57
4.8	Datasets and Simulation	59
4.8.1	Datasets	59
4.8.2	Simulating ATLAS	60
5	Analysis Tools	64
5.1	Physics Objects	65
5.1.1	Tracks	65
5.1.2	Jets	66

5.1.3	B-tagged jets	70
5.1.4	Electromagnetic Objects	72
5.1.5	Muons	73
5.1.6	Missing Transverse Energy	73
5.1.7	Signal Objects	74
5.1.8	Truth Level Objects	74
5.2	Removing Overlapping Objects	75
5.3	Event Cleaning	76
5.4	Matching Simulation to Data	77
5.4.1	b-tagging SF	77
5.4.2	Lepton SFs	78
5.4.3	Other SFs	78
5.4.4	Pileup weight	78
5.5	Systematic Uncertainties	78
5.5.1	Jet Energy Scale (JES)	79
5.5.2	Jet Energy Resolution (JER)	79
5.5.3	B-tagging and Mis-tagging	80
5.5.4	Missing Transverse Energy	80
5.5.5	Lepton Energy Scale and Resolution	80
5.5.6	Pileup	80
5.5.7	Theoretical Modelling Uncertainties	81
5.6	Discriminant Variables	81
5.6.1	Object Based Variables	81
5.6.2	Variables Sensitive to SM Backgrounds	82
5.6.3	Variables sensitive to BSM signals	84
5.7	Statistical Tools	86
5.8	Significance	87
5.9	HistFitter	88
5.9.1	Likelihood Fit	88
5.9.2	Profile Likelihood Ratio	89
5.9.3	Background-only Fit	90
5.9.4	Model-dependent Fit	91
5.9.5	Model-independent Fit	91
6	Jet Smearing	93
6.1	JetSmearing Technique	94
6.2	Constructing the Jet Response	98

6.3	Performing JetSmearing	99
6.3.1	Selecting Seed Events	99
6.3.2	Smearing Seed Events	101
6.4	Correcting the Jet Response	102
6.4.1	Di-jet Balance Corrections	102
6.4.2	Photon-b-jet Balance Corrections	104
6.4.3	Z-boson-b-jet Balance Corrections	107
6.4.4	Balance Corrections Summary	107
6.4.5	Di-jet $\Delta\phi$ Corrections	109
6.4.6	Effect of ϕ corrections on the Final Estimate	110
6.5	Systematic Uncertainties	111
6.6	Method Validation	113
6.7	Conclusion	115
7	Searches for SUSY in Two b-jets + E_T^{miss} Final States	117
7.1	A search for scalar bottoms with 3.2 fb^{-1} of data at $\sqrt{s} = 13 \text{ TeV}$	119
7.2	MC samples	122
7.3	Nominal Background Estimation	125
7.4	Multi-jet Background Estimate	126
7.5	Z+jets Background Estimate	128
7.5.1	Data-Driven Z+jets from γ +jets	130
7.5.2	Data-Driven Z+jets Extrapolating Over b-jet Multiplicity	138
7.5.3	Data-Driven Z + jets Summary	142
7.6	Systematic Uncertainties	144
7.7	Results	146
7.7.1	Model-dependent Limits	150
7.7.2	Model-independent Limits	151
7.8	Conclusions	153
7.9	Future Prospects for Scalar Bottom Pair Production at the HL-LHC	154
7.9.1	Signal Regions	155
7.9.2	Results and Limits	156
8	A Search for SUSY in a Realistic pMSSM Scenario	158
8.1	Single Top + E_T^{miss} Final States	159
8.2	Searches for SUSY in Single Top + E_T^{miss} Final States in 2012 data at $\sqrt{s} = 8 \text{ TeV}$	159
8.2.1	Simplified Signal Models	160

8.2.2	pMSSM Inspired Model	160
8.2.3	Analysis Strategy	163
8.2.4	MC samples	164
8.2.5	Signal Region Definitions	164
8.2.6	Background Estimation	165
8.2.7	Systematic Uncertainties	168
8.2.8	Results	168
8.3	Interpretation in the ATLAS pMSSM scan	171
8.3.1	Overview of the Signal Models Considered	172
8.3.2	Categorisation	173
8.3.3	Truth Level Implementation	173
8.3.4	Results and Interpretation	175
8.4	Conclusions	176
 9 Conclusions		 179
 References		 182
 Appendix A SCT Service Work		 200
 Appendix B Auxillary material for the 2015 data direct $bb+E_T^{\text{miss}}$ analysis		 203
B.1	Systematic Uncertainties	203
B.2	Data-Driven Z + jets from an Extrapolation in b-jet Multiplicity	208
B.3	Data-Driven Z + jets from γ + jets	210
B.4	Limits	211
 Appendix C Auxillary material for the 2012 single top + E_T^{miss} analysis		 215
C.1	Background Estimation	215
C.1.1	Control Region Definitions	215
C.1.2	Validation Region Definitions	218
C.1.3	Results	220
C.1.4	Limits	222

List of figures

2.1	(a) Electron screening: the bare electron charge is masked by virtual electron-positron pairs. (b) The “running” of the QED and QCD coupling constants. Taken from [1].	10
2.2	Graphical representation of the Higgs potential for a singular complex scalar field.	13
2.3	Left and right handedness of SM fermions depicting vectors for the particle spin and direction of motion.	15
2.4	Pictorial representation showing the light cone for a W boson decay in which an electron and anti-neutrino are produced. The higgs field changes a left-handed electron into a right-handed fermion, this is what causes the observed electron to have a mass.	16
2.5	Evolution of the inverse gauge couplings $\alpha_a^{-1}(Q)$ in the Standard Model (dashed lines) and the MSSM (solid lines). In the MSSM case, the sparticle masses are treated as a common threshold varied between 500 GeV and 1.5 TeV, and $\alpha(m_Z)$ is varied between 0.117 and 0.121, as seen in the blue and red lines. Taken from [2].	23
2.6	(Left) The Higgs mass for large $\tan\beta = 20$ in the $X_t/m_s, m_s$ plane. Contours show the corresponding observed values for m_h . (Right) The white region is the range in which \tilde{t}_1 and \tilde{t}_2 are allowed. Taken from [3].	26
2.7	A representation of the SUSY phase space. As with the pMSSM, the CMSSM (Constrained MSSM), is further contained within the phase-space of the MSSM. Taken from [4]	27
3.1	MSTW (Martin-Stirling-Thorne-Watt) 2008 NLO parton distribution functions at 10 GeV^2 (left) and 10^4 GeV^2 (right). Plots taken from [5].	30
3.2	Theoretical cross sections for many processes, plotted as a function of centre-of-mass energy for electron-positon colliders (left) and proton-proton (anti-proton) colliders (right) [6].	31

3.3	Examples of Feynman diagrams for pair production of $t\bar{t}$ (top-row) and top quark decay (bottoms row).	32
3.4	Examples of Feynman diagrams for pair production of $t\bar{t}$ showing (a) ISR and (b) FSR.	33
3.5	Structure of a $t\bar{t}H$ (top-quark pair production in association with a Higgs boson) event at generator level, produced by Sherpa 1.1[7], taken from [8]. .	34
3.6	Gluino (left) and scalar top (right) production cross sections in pp collisions at $\sqrt{s} = 13, 14, 33$ and 100 TeV [9]	35
3.7	QCD Feynman diagrams for pair production of gluinos and squarks	37
3.8	Production diagrams showing two possible decay chains after sparticles have been pair produced. The left diagram shows pair production of gluinos decaying to scalar b-quarks (\tilde{b}_1) and b-quarks which subsequently decay to neutralinos ($\tilde{\chi}_1^0$) and b-quarks ($pp \rightarrow \tilde{g}\tilde{g} \rightarrow bb\tilde{b}_1\tilde{b}_1 \rightarrow bbbb\tilde{\chi}_1^0\tilde{\chi}_1^0$). The right diagram shows pair production of scalar top quarks decaying to neutralinos and top quarks, which subsequently decay to W bosons either hadronically or leptonically.	38
3.9	Left: gluino pair production and its subsequent decay to scalar quarks and neutralinos; the experimental signature of multiple jets and E_T^{miss} is also shown. Right: the same signature is mimicked by the production of a Z boson in association with jets[10].	39
3.10	Pictorial representations of different SUSY models showing the masses of the sparticles and their decays. The arrows indicate the decay paths of the sparticles with the thickness of the arrow dependent on the branching ratio of the decay.	40
3.11	A summary of all direct ATLAS searches for SUSY as of March 2016 [11].	41
3.12	Summary of CMS searches for SUSY as of the ICHEP 2014 conference [12].	42
3.13	A summary of the limits set on all sparticle masses in the context of the pMSSM, set by analyses contributing towards the Run-I pMSSM summary paper [11].	43
4.1	Schematic diagram of the LHC site at CERN, Geneva [13].	45
4.2	Diagram of the ATLAS detector taken from [14].	46

4.3	Example of an ATLAS event display for a singular typical di-jet data event recorded in 2010. The ID is shown in light grey, the electromagnetic calorimeter is shown in green, the hadronic calorimeter is shown in red and the muon spectrometer is shown in blue. The left panel and top-right panel show a view of the detector in the $x - y$ plane and $z - y$ plane respectively. These displays show various tracks (in the ID) and various energy deposits in the calorimeters. The bottom-right panel shows the transverse energy (E_T) energy deposits as a function of η and ϕ , coloured lines show circles of radii 0.4 in the $\eta - \phi$ plane, demonstrating the reconstruction of energetic showers either as electromagnetic objects or jets, see Sections 5.1.4, 5.1.2.	48
4.4	ATLAS magnetic system: the inner detector is surrounded by a solenoid magnet; a toroid magnet system encompasses the muon spectrometer [15].	49
4.5	Radiation lengths (X_0) in the Inner Detector (ID) (including the services) as a function of $ \eta $ and averaged over ϕ . The breakdown indicates the contributions of external services and of individual sub-detectors. Taken from [16].	50
4.6	Impact parameter distributions of reconstructed tracks with and without IBL for simulated $t\bar{t}$ events; (right) transverse impact parameter distribution d_0 and (left) longitudinal impact parameter distribution $z_0 \times \sin \theta$ with respect to the true values. Taken from [17]	51
4.7	Schematic diagram of the SCT quadrants. Two types of sensors are indicated in the diagram: Contact Image Sensors (CiS) and Hamamatsu. Taken from [18].	52
4.8	Diagram of drift circles in an array of straw tubes of the TRT. The straw tubes are coloured yellow with the anode in the centre shown in red. An electric field is applied across the tube between the cathode shell and the inner anode. When an ionising particle travels through the noble gas a so-called <i>drift circle</i> can be inferred (grey-blue circles) from the drift time. When multiple drift circles are combined, taking into account the magnetic field, the particle track can be reconstructed (dashed-green line).	53
4.9	ATLAS calorimeters: EM and hadronic section showing both barrel and endcap regions of the detector.	54
4.10	Schematic diagram(s) of a EMcal barrel module located in the electromagnetic calorimeter.	55
4.11	Interaction lengths (I_0) in the calorimeter systems as a function of $ \eta $ and averaged over ϕ . Taken from [16].	56

4.12	Longitudinal diagram of the muon spectrometer (MS), side A of ATLAS. The x-axis indicates the distance from the IP along the beam pipe, the y-axis indicates the distance in height from the beam pipe.	57
4.13	Schematic diagram showing the overview of the ATLAS trigger system in Run-I and Run-II. Taken from [19].	58
4.14	Summary of different ATLAS sub-detectors and their purpose in terms of physics objects identification.	60
4.15	Summary of the 2012 Run-I and 2015 Run-II data sets used in analyses. . .	61
4.16	Example of double-counting when matching ME+PS in MC simulation of multiple partons.	62
5.1	An overview of the ATLAS data flow showing both data and simulation [20].	65
5.2	a) The emission of a single gluon from the production of a $q\bar{q}$. (b) shows multiple emissions of gluons from a $q\bar{q}$, (c) then shows the hadronisation of these gluons forming bound states such as pions and kaons, (d) shows the event display from the OPAL detector at LEP for the production of $e^+e^- \rightarrow Z \rightarrow q\bar{q} \rightarrow \text{hadrons}$. Taken from [10].	66
5.3	Illustration of the infra-red sensitivity of a cursory designed jet algorithm (top). Illustration of the product of a collinear unsafe jet algorithm. A collinear splitting changes the number of jets (bottom). Taken from [21]. . .	68
5.4	Monte-Carlo level on jet clustering with the anti- k_T algorithm using $R_C = 1.0$ in the $y - \phi$ plane. Taken from [22].	69
5.5	Decay of a u-quark and a b-quark	70
5.6	MVx algorithms in simulated $t\bar{t}$ samples: MV1 was used for the Run-I analyses and MV2c20 was used for the Run-II analyses.	71
5.7	MVc20 algorithm truth level acceptance and rejection efficiencies for a simulated $t\bar{t}$ MC sample. The various percentages corresponds to Working Points (WPs).	72
5.8	Schematic diagram illustrating the interplay between the production at generator level and the measurement in the ATLAS detector of a scalar top event. Taken from [23].	75
5.9	Simulated distributions of the m_{CT} discriminant for $t\bar{t}$ and a supersymmetric signal model with a scalar bottom mass of 1000 GeV and a neutralino mass of 1 GeV.	85
5.10	A typical analysis strategy flow with HistFitter with N CRs, N VRs and N SRs. Taken from [24].	89

6.1	Jet response, R_{MC} , for Truth jets with $500 < p_T < 1000$ GeV for b-veto jets on the left and b-tagged jets on the right. Two distinct regions of the jet response are shown: the main body of the response, known as the Gaussian core; and the non-Gaussian low-side tail.	95
6.2	A pictorial overview of the JetSmearing method in the transverse plane (p_x, p_y) . Jets are indicated by the black arrows, b-jets by green arrows and E_T^{miss} (MET) indicated by red arrows. The size of the arrows indicates the magnitude of the transverse energy (momentum). Well measured events are first selected in data. Each jet in the event is then smeared n times to create n pseudo-events. This is performed via a smearing response map derived in MC and corrected for in data.	97
6.3	Jet responses measured in di-jet Pythia MC (R_{MC}) as a function of truth jet p_T	99
6.4	Key distributions in the choice of the JetSmearing <i>seed selection</i>	100
6.5	Figure showing the building up of <i>pseudo-events</i> from the smearing of <i>seed events</i> . A value of $n_{smears} = 5000$ with 2015 data	101
6.6	Gaussian width of data (black) and pseudo-data (red) as a function of average di-jet p_T . Data points are fitted to the functional form given in Equation 6.8.	104
6.7	(Top) two plots of the key variables for particular p_T ranges. (Bottom) width of photon-b-jet balance variables used to probe the Gaussian core of the b-tagged jet response as a function of photon p_T	106
6.8	Probing the b-jet jet response with variables R_b and R_{MPF} for b-jets balanced against a well measured Z-boson of low, medium and high p_T	108
6.9	$\sigma(\Delta\phi(j_1, j_2))$ as a function of average di-jet p_T for data (black), pseudo-data (red) and corrected pseudo-data (pink)	110
6.10	$\min[\Delta\phi(\text{jet}_{1-4}, E_T^{miss})]$ distribution with different selections, the QCD background is estimated by the JetSmearing method.	112
6.11	Key distributions with the Multi-0L pre-selection.	113
6.12	Key distributions with the Exclu-0L pre-selection.	114
6.13	Seed events for the pseudo-data passing the Exclu-0L selections. Seed events have prescales applied and are normalised to unit area.	115
7.1	The 95% CL limit obtained with the Run-1 pp collision data for direct sbottom pair production decaying with (a) 100% BR to neutralinos ($\tilde{\chi}_1^0$) in the $(m_{\tilde{b}}, m_{\tilde{\chi}_1^0})$ mass plane, (b) 100% BR to the 2 nd heaviest neutralino ($\tilde{\chi}_2^0$), in the $m_{\tilde{b}} - m_{\tilde{\chi}_2^0}$ mass plane and (c) 100% BR to lightest chargino in the $m_{\tilde{b}} - m_{\tilde{\chi}_1^\pm}$ mass plane [25].	118

7.2	Scalar bottom pair production cross section in pp collisions at $\sqrt{s} = 8$ TeV and $\sqrt{s} = 13$ TeV [26].	119
7.3	Direct pair production of scalar bottom quarks, decaying exclusively to neutralinos.	120
7.4	Observed and expected exclusion limits on the lightest scalar bottom and neutralino masses set by Run-I searches for direct scalar bottom pair-production [27]. The areas on the $m_{\tilde{b}} - m_{\tilde{\chi}_1^0}$ mass plane targetted by the Run-II analysis are superimposed on top.	121
7.5	SM backgrounds as a percentage of the total background in SRAx and SRB. The Z+jets background is the most dominant background in the SRAx regions and the $t\bar{t}$ background the most dominant in the SRB regions. . . .	122
7.6	Overview of the SRAx strategy. The four main backgrounds (solid boxes) are normalised in orthogonal control regions with a high purity of the SM background they attempt to normalise. The dashed boxes indicate the the various regions, indicating the selections which make them orthogonal. The other backgrounds in the VRs/SRs are not normalised in any control region.	123
7.7	Overview of the SRB strategy. The two main backgrounds (solid boxes) are normalised in orthogonal control regions with a high purity of the SM background they attempt to normalise. The dashed boxes indicate the the various regions, indicating the selections which make them orthogonal. In the B region case, the Single-Top, W+jets and other backgrounds are not normalised in any control regions.	124
7.8	SRAx control regions showing data and the total SM background before performing a likelihood fit. Four control regions, defined to have high purity of the Z (a), $t\bar{t}$ (b), Single Top (c) and W+jets (d) backgrounds are shown. The yellow uncertainty band only shows statistical errors.	127
7.9	SRB control regions showing data and the total SM background before performing a likelihood fit. (a) shows the Z+jets pure control region and (b) shows the top pure control region. The yellow uncertainty band only shows statistical errors.	128
7.10	Key distributions in the QCD (multi-jet) sbottom CR and VR.	129
7.11	Feynman diagrams showing the production of Z+jets. (a) The gluon splitting gives two quarks which can potentially result in a pair of b-tagged jets of typically low invariant mass. (b) two-additional parton diagram in which may lead to a final state with two b-tagged jets.	130
7.12	Truth boson p_T in the four signal regions as simulated using Sherpa MC.	131

7.13	γ +jets events are used for estimating the $Z \rightarrow \nu\bar{\nu}$ +jets background. Data containing a single photon and the same jet kinematics as the SRs are selected. These events are re-weighted to account for cross-sectional differences as a function of the boson p_T . The E_T^{miss} from the neutrino decays is mimicked by adding the photon p_T , finally the full SR selections are applied to estimate the $Z \rightarrow \nu\bar{\nu}$ background.	132
7.14	m_{CT} distribution for data and MC background events in the two γ + jets control regions. Only statistical uncertainties are shown.	133
7.15	Comparisons of $Z \rightarrow \nu\nu + b$ -jets and $\gamma + b$ -jets Monte-Carlo events after applying the SRA selections to the $Z \rightarrow \nu\nu + b$ -jet and the ER γ A selections to the $\gamma + b$ -jets. The left column shows the comparison before p_T re-weighting and the right column shows after p_T re-weighting, as described in 3. By construction the p_T re-weighting procedure matches up the reconstructed photon p_T in ER γ A to the truth vector boson p_T in SRA (Figure 7.15b) Only statistical uncertainties are shown.	135
7.16	Various VR/SR plots with the Z + jets background estimated using the data-driven technique described in this section. All other SM backgrounds show only MC statistical uncertainties.	137
7.17	$Z \rightarrow \ell\bar{\ell}$ +light-jets events are used for estimating the $Z \rightarrow \nu\bar{\nu}$ + b -jets background. Data with two leptons consistent with a Z boson and no b -tagged jets are used as a template. The lepton pair is used as fake- E_T^{miss} and the same jet kinematic selections as the SRs are applied. These events are normalised to events with two b -tagged jets in data. Corrections derived from MC accounting for the lepton reconstruction efficiency and the ratio of $\text{BR}(Z \rightarrow \ell\bar{\ell}) / \text{BR}(Z \rightarrow \nu\bar{\nu})$ are applied. A final estimate of the $Z \rightarrow \nu\bar{\nu}$ + b -jets in the SRs can hence be obtained.	138
7.18	(a) Comparison of the m_{CT} shape for $Z \rightarrow \nu\nu$ events with no and two b -jets. (b) Comparison of the m_{CT} shape for events with two b -jets and either no or two leptons.	140
7.19	m_{CT} distributions for (a) ERzA-0b2l raw (b) ERzA-0b2l with non- Z MC background subtraction. In the case of two b -tagged jets, m_{CT} is shown in ERzA-2b2l (c) before apply a selection on the original E_T^{miss} and (d) after applying a selection of original $E_T^{\text{miss}} < 100$ GeV and a Z mass window selection of $106 \text{ GeV} > m_{\ell\ell} > 76 \text{ GeV}$. The shaded bands show the Monte Carlo statistical uncertainties.	141

7.20	Key distributions after applying the full data driven from Z+light-jets method in SRA.	143
7.21	Comparison between data and SM predictions for the m_{CT} variable in the SRAx regions. Non Z+jets backgrounds are estimated from MC and normalised in the CRs and only show MC statistical uncertainties. The left plot (a) shows the Z+jets background estimated using the data-driven method derived from γ +jets and the right plot (b) shows the data-driven prediction derived using Z+light jets processes.	144
7.22	CR plots for the 2015 $bb+E_T^{\text{miss}}$ analysis published in [28]	146
7.23	SR plots for the 2015 $bb+E_T^{\text{miss}}$ analysis published in [28] . The errors represent statistical and systematic uncertainties on the SM background. Signal samples for varying scalar bottom and neutralino masses are shown. No significant deviation from the SM background can be seen.	150
7.24	Combined expected and observed exclusion limits at 95% CL in the $(m_{\tilde{b}}, m_{\tilde{\chi}_1^0})$ plane (a). For each signal point, the signal region which leads to the best expected limit is chosen, indicated in (b). The dashed black and solid bold red lines show the 95% CL expected and observed limits respectively, including all uncertainties except the theoretical signal cross-section uncertainty. The shaded (yellow) bands around the expected limits show the impact of the experimental uncertainties while the dotted red lines show the impact on the observed limit of the variation of the nominal signal cross-section by 1σ theoretical uncertainty [28].	152
7.25	Distributions of the leading two jet p_{TS} , E_T^{miss} and m_{CT} for 300 fb^{-1} before any selection on the variable. Three signal points and the SM backgrounds are shown.	157
7.26	Expected reach of the HL-LHC for 95% level exclusion (dashed lines) and 5σ discovery potential for 300 and 300 fb^{-1} of data.	157
8.1	Feynman diagrams of the single top + E_T^{miss} final state signature produced by asymmetric decays of the stop or sbottom into the neutralinos and charginos.	159
8.2	The dependence of the masses of the third generation squarks (left), the lightest chargino and the lightest neutralino (right) on the pMSSM parameters μ and $m_{\tilde{q}_{L,3}}$ in the Natural pMSSM grid. A small mass difference between the $\tilde{\chi}_1^0$ and $\tilde{\chi}_1^\pm$ can be seen in the right plot.	161
8.3	Branching ratios of the dominant decays of scalar top (left) and scalar bottom (right) quarks in the Naturally inspired pMSSM signal scenarios as a function of the left-handed third generation common mass parameter ($m_{\tilde{q}_{L,3}}$).	163

8.4	Plots showing the best SRs and significances over the Natural pMSSM μ $m_{\tilde{q}_{L,3}}$ grid. The left plot shows the best SR, three inclusive SRs (labelled: 1, 2, 3) and one exclusive SR (labelled: 4), at each grid point. The plot on the right shows the corresponding combined best significance values from the best SRs. The significance in these plots has been calculated using the Z_N -function of Equation 5.14. The solid black line shows the expected exclusion limit contour ($Z_N = 1.64$).	166
8.5	Best signal regions obtained in the asymmetric grid $\Delta m(\tilde{\chi}_1^\pm, \tilde{\chi}_1^0) = 5\text{GeV}$ and $\Delta m(\tilde{\chi}_1^\pm, \tilde{\chi}_1^0) = 20\text{GeV}$ for a branching ratio of $k = 0.5$ (50%).	166
8.6	Distributions the two of the main discriminating variables that were used in the SRinA, before the final selection of the variable is applied. The left plot shows the kinematic variable am_{T2} , the right plot shows the m_T distribution.	167
8.7	Post-fit key kinematic distributions of am_{T2} for SRinA (top-left), SRinB (top-right), SRinC (bottom-left) and SReXA (bottom-right). Both statistical and systematic uncertainties are shown.	170
8.8	Single Top + E_T^{miss} analysis limits on the Natural pMSSM and simplified model grids	171
8.9	Efficiency vs truth acceptance plots for all four tb+MET SRs	174
8.10	Exclusion power of the Single Top + E_T^{miss} analysis interpreted in the context of the pMSSM.	177
8.11	Number of pMSSM models where the best expected exclusion was the Single Top + E_T^{miss} analysis. The axes represent the two decay modes of the scalar top and scalar bottom quarks to the highest neutralino and chargino states, the third axis show the remaining fraction of decays to higher neutralino and chargino mass states denoted as X	178
8.12	Number of pMSSM models where the best expected exclusion was the Single Top + E_T^{miss} analysis. The bottom axis shows the combined branching ratio of scalar tops (sbottoms) to the highest neutralino and chargino states, the right axis shows the combined branching ratio of scalar tops (sbottoms) to the second lightest neutralino and chargino states and the left axis show the remaining fraction of decays to higher neutralino and chargino mass states denoted as X	178
A.1	Layout of one type of SCT module used in the 4 barrel layers.	200

B.1 Expected and observed exclusion limits at 95% CL in the $(m_{\tilde{b}}, m_{\tilde{\chi}_1^0})$ plane for the four signal regions defined in this analysis. The dashed black and solid bold red lines show the 95% CL expected and observed limits respectively, including all uncertainties except the theoretical signal cross-section uncertainty. The shaded (yellow) bands around the expected limits show the impact of the experimental uncertainties while the dotted red lines show the impact on the observed limit of the variation of the nominal signal cross-section by 1σ theoretical uncertainty. Also shown for reference are the observed limits from the previous analysis [29]. 212

B.2 Expected and observed exclusion limits at 95% CL in the $(m_{\tilde{b}}, m_{\tilde{\chi}_1^0})$ plane for the four signal regions defined in this analysis. The dashed black and solid bold red lines show the 95% CL expected and observed limits respectively, including all uncertainties except the theoretical signal cross-section uncertainty. The shaded (yellow) bands around the expected limits show the impact of the experimental uncertainties while the dotted red lines show the impact on the observed limit of the variation of the nominal signal cross-section by 1σ theoretical uncertainty. Numbers show the observed CLs values. 213

B.3 Combined expected and observed exclusion limits at 95% CL in the $(m_{\tilde{b}}, m_{\tilde{\chi}_1^0})$ plane (a). For each signal point, the signal region which leads to the best expected limit is chosen, indicated in (b). The dashed black and solid bold red lines show the 95% CL expected and observed limits respectively, including all uncertainties except the theoretical signal cross-section uncertainty. The shaded (yellow) bands around the expected limits show the impact of the experimental uncertainties while the dotted red lines show the impact on the observed limit of the variation of the nominal signal cross-section by 1σ theoretical uncertainty. Also shown for reference are the observed limits from the previous analysis [?]. The expected and observed CLs values are shown in (c) and (d), respectively. The 95% CL exluded model cross sections are shown in (e). 214

C.1 Pre-fit kinematic distribution plots for the inclusive CRs. The plots on the left show variables after cuts in the CRWs, the right shows variables after cuts in the CRTs. The rows correspond (in descending order) to the CRs associated with: SRinA, SRinB and SRinC. 217

C.2 Pre-fit Kinematic distributions in the exclusive CRs. The plots in the left column show variables after cuts in the CRWs, the right column shows variables after cuts in the CRTs. In the CRs associated with SRExA are shown. 219

C.3 Single Top + E_T^{miss} analysis limits on simplified model grids with alternative branching ratios of the scalar top decays. 224

List of tables

2.1	The fundamental boson of the SM of particle physics showing their associated particles states. The quantum spin and mass of these quanta are shown [30].	5
2.2	The fundamental matter particles of the SM of particle physics and their key properties. These particles are subdivided into quarks and leptons, they all have spin $\frac{1}{2}$ [30, 31].	6
2.3	The components of the SM Lagrangian density decomposed to the terms associated with different matter and force particles sectors.	7
2.4	The spinor states of Electro-weak theory broken-down into the three generations showing left- and right-handed chiral states [1, 31].	11
2.5	The chiral supermultiplets in the Minimal Supersymmetric SM (MSSM) showing their formularisation as doublets or singlets. The quantum numbers associated with the various SM groups are shown [2].	21
2.6	The gauge supermultiplets in the Minimal Supersymmetric SM (MSSM). [2]	21
2.7	The 19 parameters of the pMSSM with a description of each.	25
4.1	Rejection of simulated light jets in $t\bar{t}$ events for a b -tagging efficiency of 60%, data obtained from [17]. For more details on the IP3D and IP3D+ SV1 algorithms see Section 5.1.3.	51
4.2	ATLAS performance goals of the calorimeters. Taken from [16].	56
4.3	Summary of the most relevant ATLAS High Level Triggers. The naming convention and corresponding physics object are ‘ given, XX refers to an online threshold associated to the p_T of the triggered object.	59
5.1	Types of fits performed by HistFitter.	90
6.1	JetSmearing seed selections	100
6.2	Analyses used to correct the R_{MC} map used in the JetSmearing procedure.	102
6.3	Summary of analysis selection in the di-jet balance analyses.	104
6.4	Summary of analysis selection in the boson-b-jet balance analyses.	105

6.5	Selections used at pre-selection level in the case of two different analyses using JetSmearing.	111
7.1	Preselection criteria, common to all signal and control region of the analysis.	121
7.2	Summary of the $bb+E_T^{\text{miss}}$ SR targets and their corresponding VRs and CRs	121
7.3	Definition of the control regions associated to SRAx. Four signal regions designed with high purity of Z+jets, $t\bar{t}$, Single-Top and W+jets backgrounds respectively. All regions are orthogonal to each other by the application of kinematic and object based selections.	123
7.4	Control and validation regions associated to SRB.	124
7.5	MC samples used by the $bb+E_T^{\text{miss}}$ analysis in Run-II of the LHC.	125
7.6	Definition of the multi-jet control (CRQCD) and validation (VRQCD) region for the jet smearing method.	127
7.7	Definition of the emulation regions used as templates in the γ + jets data-driven method.	133
7.8	Definition of the loose control regions used in estimation of the κ factor in the γ + jets data-driven method.	136
7.9	Definition of the various 2-lepton emulation (ERzA) and normalisation (CRzA) regions.	142
7.10	Calculation of $\frac{\Gamma_{Z\ell\ell;2b}^{\text{data}}}{\Gamma_{Z\ell\ell;0b}^{\text{data}}}$ from CRzA-0b2l and CRzA-2b2l. The superscript, Γ^{data} , refers to the Data with non-Z Monte-Carlo subtracted.	142
7.11	Expected Z + jets background in VRAmct, SRA250, SRA350 and SRA450 for two different data-driven Z + jets estimation methods.	143
7.12	Theoretical uncertainty as a percentage relative to the total uncertainty for the Z + jets, W + jets, $t\bar{t}$ and Single Top backgrounds in all SRs. The individual uncertainties can be correlated and do not necessarily add in quadrature to the total background uncertainty.	145
7.13	Fit results in the control and validation regions associated to the SRA selection for an integrated luminosity of 3.2 fb^{-1} . The results are obtained from the control regions using the background-only fit (see text for details). The errors shown are the statistical plus systematic uncertainties.	147
7.14	Normalization factors obtained from the background-only fit with 3.2 fb^{-1} , for each of the main backgrounds in SRA. The uncertainties include both statistical and systematic sources.	147

7.15	Fit results in the control and validation regions associated to the SRB selection for an integrated luminosity of 3.2 fb^{-1} . The results are obtained from the control regions using the background-only fit (see text for details). The errors shown are the statistical plus systematic uncertainties.	148
7.16	Normalization factors obtained from the background-only fit with 3.2 fb^{-1} , for each of the main backgrounds in SRB. The uncertainties include both statistical and systematic sources.	148
7.17	Observed data and post-fit results in SRAx and SRB signal regions for an integrated luminosity of 3.2 fb^{-1} . The results are obtained from the A and B region CRs using the background-only fit (see text for details). The errors shown are the statistical plus systematic uncertainties, they are not necessarily added in quadrature due to the correlation between certain uncertainties. Additionally two background-only fits were performed, without fitting the Z + jets backgrounds, these are referred to as non-Z fits. The results using the two data-driven estimates of the Z + jets background are therefore also shown. The original MC yields before the background-only fit was performed are shown as pre-fit MC yields.. . . .	149
7.18	Left to right: 95% CL upper limits on the visible cross section ($\langle \epsilon \sigma \rangle_{\text{obs}}^{95}$) and on the number of signal events (S_{obs}^{95}). The third column (S_{exp}^{95}) shows the 95% CL upper limit on the number of signal events, given the expected number (and $\pm 1\sigma$ excursions on the expectation) of background events. The last two columns indicate the CL_B value, i.e. the confidence level observed for the background-only hypothesis, and the discovery p -value ($p(s = 0)$).	153
7.19	Summary of selection requirements for the bottom squark pair production signal regions. The value of x notes the selection of the variable m_{CT}	155
7.20	Expected numbers of events for SM background and three bottom squark pair signal points, for different m_{CT} thresholds and an integrated luminosity of 300 fb^{-1} . The uncertainties shown are statistical only.	156
8.1	A list of various supersymmetric particles; their masses, decay widths and decays with branching ratios in the Natural pMSSM model with $\mu=110$, $m_{\tilde{q}_{L,3}} = 400$	162
8.2	Summary of all MC simulation used in the Single Top + $E_{\text{T}}^{\text{miss}}$ analysis. The programs used in the ME+PS associated with the SM background process are indicated as well as the type of simulation used.	165
8.3	Summary of the selections used to design the SRs.	165

8.4	Background scale factors for the $t\bar{t}$ and W samples, as obtained by the background fit.	168
8.5	Summary of the background-only-fit results for the Single top + E_T^{miss} analysis. 169	
8.6	Breakdown of upper limits calculated by the asymptotic calculation method. Left to right: 95% CL upper limits on the visible cross section ($\langle\epsilon\sigma\rangle_{\text{obs}}^{95}$) and on the number of signal events (S_{obs}^{95}). The third column (S_{exp}^{95}) shows the 95% CL upper limit on the number of signal events, given the expected number (and $\pm 1\sigma$ excursions on the expectation) of background events. The last two columns indicate the CL_B value, i.e. the confidence level observed for the background-only hypothesis, and the discovery p -value ($p(s=0)$). 170	
8.7	Range of the free pMSSM parameters considered in the ATLAS pMSSM summary scan[32].	172
8.8	Fraction of models excluded by the individual analyses, the total does not equal the sum of all analyses since multiple analyses may exclude the same model. All ATLAS analyses included in the pMSSM interpretation are cited. Table has been taken from [32].	176
B.1	Breakdown of uncertainty on background estimates	204
B.2	Breakdown of uncertainty on background estimates	205
B.3	Breakdown of uncertainty on background estimates	206
B.4	Breakdown of uncertainty on background estimates	207
B.5	Correction factors for the Z + jets derived in m_{CT} bins in SRA and ERzA-2b2l with Sherpa MC samples.	208
B.6	Correction factors for the Z + jets background derived in m_{CT} bins in SRA and CRzA-2b2l with MadGraph+Pythia8 MC samples.	209
B.7	Single bin correction factor for the Z + jets background derived in m_{CT} bins in SRA and CRzA-2b2l with Sherpa and MadGraph+Pythia8 MC samples. 209	
B.8	Yields of the SM background processes predicted in (a) CRzA-0b2l and (b) CRzA-2b2l.	210
B.9	Yields of the SM background processes and Data observed at 3.2 fb^{-1} in the template (emulation) regions ER γ A(s) and ER γ B. The Multi-jet background is estimated from MC and not the JetSmearing method. Only statistical uncertainties are shown.	210
B.10	Yields of the SM background processes and Data observed at 3.2 fb^{-1} in CR γ L and CRzL.	211
C.1	Summary of selections used in the Top Control Regions.	215

C.2	Summary of selections used in the inclusive W +jets Control Regions.	216
C.3	Summary of cuts used in all of the inclusive Validation Regions.	218
C.4	Summary of selections used in exclusive Top and W +jets Validation Regions	219
C.5	Background fit results for the inclusive A regions. Only systematic uncertainties are shown.	220
C.6	Background fit results for the inclusive B regions. Only systematic uncertainties are shown.	221
C.7	Background fit results for the inclusive C regions. Only systematic uncertainties are shown.	221
C.8	Background fit results for the exclusive A regions. Only systematic uncertainties are shown.	222
C.9	List of fitted systematic uncertainties for the background prediction in SRinA. Since the different contributions are correlated, the total uncertainty is not obtained by simply adding them in quadrature.	223
C.10	List of fitted systematic uncertainties for the background prediction in SRinB. Since the different contributions are correlated, the total uncertainty is not obtained by simply adding them in quadrature.	225
C.11	List of fitted systematic uncertainties for the background prediction in SRinC. Since the different contributions are correlated, the total uncertainty is not obtained by simply adding them in quadrature.	226
C.12	List of fitted systematic uncertainties for the background prediction in SRexA. Since the different contributions are correlated, the total uncertainty is not obtained by simply adding them in quadrature.	227

Nomenclature

Roman Symbols

\hbar	h-bar - Planck's constant divide by 2π
E_T^{miss}	Missing Transverse Energy
\mathcal{L}	Langragian Density
\mathcal{R}	Rate
p_T	Transverse momentum
R_{MC}	Jet energy response used by the JetSmearing method
\sqrt{s}	Centre of mass energy
\tilde{f}_L, \tilde{f}_R	Left and right handed fermions
A_μ	vector field
A_i^{SR}	Signal region acceptance for a given process
b	Background or Bottom quark
c	Charmed quark
d	Down quark
E	Energy
e	Charge of an electron, also symbolises an electron
E_T	Transverse Energy
$F_{\mu\nu}$	Electro-magnetic tensor field

g	Gluon, g factor of the electron, or coupling strength of the SU(2) part of the EW force
G, G^a	Gluon fields
g'	Coupling strength of the U(1) part of the EW force
g_s	Coupling strength of the strong nuclear force
H	Higgs field
h	Planck's constant
H_T	Scalar sum of object transverse momenta
K, K^0, \bar{K}^0	Kaons
L	Integrated Luminosity
L_ℓ	Left-handed leptons
m	Mass, generally given in units of GeV
pp	proton-proton
Q	Energy/momentum transfer
R_C	Cone radius in η - ϕ space
R_p	R -parity
R_p	R-parity
R_{MPF}	Jet response variable measured by Momentum Projection Fraction
$R_{Z/\gamma}$	Jet response variables measured by the balance of a Z boson with a photon
s	Signal or Strange quark
t	Top quark
u	Up quark
W	W boson

X_t	Stop mixing angle
Y	Weak hyper-charge
y	Rapidity
Z	Z boson

Greek Symbols

α_i	Coupling constant associated with a force
β	Synchrotron radiation function or SUSY vacuum expectation ratio
\tilde{b}_1	Lightest scalar bottom quark
ΔR	Separation distance in η - ϕ space
ΔR_{ij}	Separation distance in y - ϕ space
ℓ	Leptons
η	Pseudo-Rapidity
λ	De broglie wavelength or Lagrangian parameter associated with higher order couplings of fields
μ	Muon.
μ_X	Normalisation factor for background (or signal) X
$\tilde{\chi}_1^0$	Lightest neutralino
Ω	Density parameter from General Relativity
ϕ	Angular separation
$\sigma(A), \sigma(E)$	Gaussian width of a function
$\sigma(pp)$	Cross section
σ_b	Error on the background
τ	Tau lepton
τ_p	Life time of a proton

$\tilde{\chi}_{1,2,3,4}^0$ Chargino states

ε Efficiency

Acronyms / Abbreviations

4D 4-Dimensional

AF-II ATLAS Fast II Simulation

ALICE A Large Ion Collider Experiment

ATLAS A Toroidal LHC ApparatuS

BDT Boosted Decision Tree

BR Branching Ratio

BSM Beyond the Standard Model

CB ComBined muon

CERN Conseil Européen pour la Recherche Nucléaire

CL Confidence Level

CMS Compact Muon Solenoid

CMSSM Constrained Minimal Supersymmetric Standard Model

CP Charge Parity

CPU Central Processing Unit

CR Control Region

CSC Cathode Strip Chambers

CT Calorimeter Tagged muon

DE Dirac Equation

DESY Deutsches Elektronen-SYnchrotron

DF Different Flavour

DM Dark Matter

EF	Event Filter
EM	Electro-Magnetic
EMcal/EMcalo	ElectroMagnetic Calorimeter
ER	Emulation Region
EW	ElectroWeak
EWT	ElectroWeak Theory
FCal	Forward Calorimeter
FSR	Final State Radiation
GRL	Good Run List
GUT	Grand Unified Theory
Hcal	Hadronic Calorimeter
HEC	Hadronic Electromagnetic Calorimeter
HL-LHC	High Luminosity Large Hadron Collider
HLT	High Level Trigger
IBL	Insertable B-Layer
ICHEP	International Conference on High Energy Physics
ID	Inner Detector
ISR	Initial State Radiation
JER	Jet Energy Resolution
JES	Jet Energy Scale
JVT	Jet Vertex Tagger
KGE	Klein-Gordon Equation
L2	Level 2 triggers system
LAr	Liquid Argon

LCW	Local Cluster Weighting
LEP	The Large Electron–Positron Collider
LHC	Large Hadron Collider
LHCb	Large Hadron Collider beauty
LINAC	LINear ACcelerator
LLR	Log Likelihood Ratio
LO	Leading Order
MC	Monte Carlo
MDT	Muon Drift Tubes
ME	Matrix Element
MET	Missing Transverse Energy, usually denoted by E_T^{miss}
MS	Muon Spectrometer
MSSM	Minimal Supersymmetric Standard Model
MSTW	Martin-Stirling-Thorne-Watt
MV	Multi-Variate
NLO	Next-to-Leading Order
NMSSM	Next-to-Minimal Supersymmetric Standard Model
OP	Operation Point
OPAL	Omni-Purpose Apparatus at LEP
OS	Opposite Sign
PDF	Parton Distribution Function or Probability Distribution Function
PETRA	Positron-Elektron-Tandem-Ring-Anlage
pMSSM	Phenomenological Minimal Supersymmetric Standard Model
PS	Parton Shower

PSB	Proton Synchrotron Booster
PU	PileUp
PV	Primary Vertex
QCD	Quantum ChromoDynamics
QED	Quantum Electro Dynamics
QFD	Quantum Flavour Dynamics
QFT	Quantum Field Theory
RECO	Reconstructed level value
ROI	Regions Of Interest
RPC	Resistive Plate Chambers
RPV	R-parity violation
SA	Stand-Alone muon
SCT	SemiConductor Tracker
SF	Same Flavour
SLAC	Stanford Linear Accelerator Center
SM	Standard Model
SPEAR	Stanford Positron Electron Asymmetric Rings
SPS	Super Proton Synchrotron
SR	Signal Region
SS	Same Sign
SSB	Spontaneous Symmetry Breaking
ST	Segmented Track muon
SU(2)	Special Unitary Group of 2 degrees
SUSY	SUperSYmmetry

TF	Transfer Factor
TGC	Thin Gap Chambers
TOE	Theory Of Everything
TRT	Transition Radiation Tracker
TRUTH	Generator level true value
U(1)	Unitary Group on 1 degree
UA1 and UA2	Underground Area 1(2) experiments
UE	Underlying Event
UV	Ultra Violet
VR	Validation Region
WIMPs	Weakly Interacting Massive Particles
WP	Working Point
WZM	Wess-Zumino Model

Author's Contribution

The ATLAS experiment is currently one of the largest collaboration of scientists in the world. The majority of the content within this thesis builds upon work performed by a large number of people since the formation of the group in 1992. The work performed by the author is summarised in this section.

$bb + E_T^{\text{miss}}$ Analysis (Chapter 7): The main content of this thesis will focus on the $bb + E_T^{\text{miss}}$ analysis, also referred to as the sbottom analysis. The author was one of the main analysers of this Run-II search for scalar bottom quarks. The author made significant contributions to the analysis; focusing on data-driven techniques to estimate the $Z + \text{jets}$ and multi-jet backgrounds. The data-driven estimation technique of $Z + \text{jets}$ from the extrapolation over b -jet multiplicity was unique to the analysis, whereas a second technique exploiting similarities between $\gamma + \text{jets}$ and $Z + \text{jets}$ is a well used technique. In addition to this the author designed a single-top control region, which was the first use of such a control region by any SUSY analyses, this idea has since been used by multiple analyses. The results of the first $\sqrt{s} = 13 \text{ TeV}$, 3.2fb^{-1} analysis were first published as a conference note [33]. A follow up paper was also published in EPJC [28]. The author was also involved in analysis projection studies for the High-Luminosity LHC (HL-LHC) with $30\text{-}300\text{fb}^{-1}$ of data at $\sqrt{s} = 14 \text{ TeV}$, the details of the studies were documented as a part of a public paper [34].

$t\bar{b} + E_T^{\text{miss}}$ Analysis (Chapter 8): The author was one of the main analysers for this Run-I of the LHC analysis, which was published as part of the end of Run-I Third Generation SUSY summary paper [25]. The author was responsible for the optimisation of the inclusive signal regions and defining control and validation regions. The final statistical interpretation of the results was performed by the author.

Additionally, the author interpreted the analysis results in the context of the pMSSM (phenomenological Minimum Supersymmetric Standard Model) [32]. This involved the implementation of a TRUTH level analysis and running the full reconstruction analysis on $\mathcal{O}(1000)$ signal models.

JetSmearing (Chapter 6): The estimation of the Multi-jet (QCD) background is of key importance to searches for SUSY in all hadronic final states. The mis-measurement of multi-jet events may lead to large amounts of missing transverse momentum which mimic beyond the Standard Model signals. The author played a key role in developing the Run-I JetSmearing method from [35] to be used for multiple Run-II analyses.

Other Analyses: The author contributed towards a search for the pair produced supersymmetric partner of the gluino in multiple b-jet final states, estimating the multi-jet background and signal region design. This analysis was published in [36]. Due to the similarities between this search and Chapter 7, the analysis is not discussed in this thesis.

Another similar analysis to the analysis of Chapter 7 is a search for Dark Matter + heavy-flavour jets. The author additionally contributed toward this analysis, published in [37]. Despite this analysis being a search for Dark Matter rather than specifically supersymmetry, the final state is similar to that of Chapter 7. Therefore, this analysis is also not discussed in detail in this thesis.

Service work: Appendix A details the ATLAS detector, details of the SCT are also given in detail. The author contributed towards the running of the SCT by providing an online tool for monitoring live data from the DAQ.

Additional Contributions: As well as taking control room shifts, monitoring the Inner Detector, the author performed work on the Data-Quality of the SCT. The author was responsible for checking the Data-Quality of the SCT for the first ever recorded collision data at $\sqrt{s} = 13$ TeV.

Calum Macdonald
August 2017

Chapter 1

Introduction

What happens if we keep cutting up an apple into smaller and smaller pieces? At what point can we no longer cut it? Ancient Greek philosophers were the first documented to consider the smallest discrete pieces of matter, coining the term *atomos*, from the Greek word for “indivisible”. Through thousands of years of science, probing matter, we now know our world is built from ninety two naturally occurring chemical elements. Their atomic nuclei consist of varying numbers of *protons* and *neutrons*. We have found that these subatomic particles are made up of point-like particles - *up* and *down quarks* bound together by the *strong nuclear force*. We also know that the nuclei of atoms are surrounded by clouds of point-like particles - *electrons*, attracted to the nuclei by the *electro-magnetic force*. The field of Chemistry incorporates the physics behind how matter changes state. An isotope of Nitrogen-13 can decay to a Carbon-13 isotope emitting β radiation¹, which we know occurs due to the existence of the *weak nuclear force*.

Quantum Field Theory (QFT) tells us that other point-like particles arise from quantum excitations of the forces of nature. These particles are *force carriers* with significantly different properties to matter particles. These particles differ by their intrinsic quantum spin - the minimum possible value of their angular momentum. Matter particles are fermions, they have spin- $\frac{1}{2}$ and obey Fermi-statistics, which is to say that no two particles with the same spin can occupy the same quantum state, without this, atoms can not form. Force carriers, in contrast, are bosons of spin-1 and obey Bose-Einstein-statistics; they can occupy the same state. The *photon* is the quantum of light, it is said to carry the *electromagnetic force*. The less well known fundamental particles are: the *gluons*, which carry the strong nuclear force, and the *vector bosons* which carry the weak nuclear force².

¹ β radiation is the high-energy emission of an electron or positron (the anti-particle of the electron with opposite charge)

²There are two *W* bosons, a positively charged (W^+), negatively charged (W^-) and a neutral (*Z*) boson

We have excellent direct and indirect experimental evidence that all these particles exist from almost a century of particle physics experiments. In addition to the particles described, further fundamental particles, which decay quickly to these stable particles, have been discovered. Three generations of matter particles exist³: up and down quarks, electron and an electron-neutrino; strange and charm quarks, muon and a muon-neutrino; and top and bottom quarks, tau and a tau-neutrino. The second and third generations appear identical to the first except they are heavier. But how do we know all these particles are fundamental and point-like? How do we know these particles have no substructure?

Our belief is motivated by the Standard Model of particle physics, a QFT that classifies all particles and forces as point-like quanta and describes their interactions. Firstly, this model has been probed thousands of times experimentally and has yet to yield any evidence of substructure. Secondly, this model explains all known composite particles states that have been observed so far. Thirdly, the theory is valid up to the Planck scale, upon which the notion of point-like particles breaks down due to the effects of General Relativity. To have a theory which can explain so many experimental observations and can be extrapolated to the smallest scale possible without any inconsistencies is theoretically very appealing. The Standard Model also explains how the fundamental particles acquire mass via interactions with the *Higgs boson*, a unique scalar particle⁴.

When the measured interaction strength of the forces is extrapolated to smaller distances (higher energies beyond our current scientific reach), an interesting feature occurs: if particles are point-like then the forces appear to converge toward a point in which they are *unified*. But if the observed particles are not point-like, and have substructure, this does not occur. Convergence of the coupling constants suggests that at some energy level all physics is unified as one Theory Of Everything (TOE).

Despite having said this, in reality, the three fields do not actually converge at the same point, they in fact meet at three separate points at an energy of $\mathcal{O}(10^{12} - 10^{16})$ GeV. This can be resolved to a single unifying point of $\mathcal{O}(10^{16})$ GeV by *supersymmetry*. Providing unification of the forces is a bi-product of *supersymmetric models*. Such models were first proposed to solve the fine-tuning of the Higgs mass and were also found to provide an explanation of the missing mass content of the universe - Dark Matter, unification was a theoretically appealing bi-product.

Supersymmetry (SUSY) is a symmetry between particles of matter and force particles. Supersymmetric models say that for every fermion there exists a boson with spin that differs by $\frac{1}{2}$, and vice-versa for all bosons. These particles are supersymmetric partners of the

³For each matter particle, an anti-particle of opposite charge exists too.

⁴Scalar particles are bosons with spin-0.

Standard Model particles. They must be of very high mass, otherwise we would have observed them. Therefore the symmetry is said to be *broken*.

This thesis initially describes the Standard Model of particle physics in more detail and the mathematical motivations behind its construction. Failings of the Standard Model which lead to the hypothesis of supersymmetric models are discussed as well as a detailed description of supersymmetry. In order to discover new particles beyond the Standard Model we need larger and more powerful machines to analyse subatomic particles. Particle colliders are the most preferable means for doing this. Chapter 3 gives an overview of general collider physics and how supersymmetric particles may be produced and studied. The *Large Hadron Collider* is one machine capable of reaching high enough energies to probe these models. Sophisticated detectors are needed to analyse and measure the products of these collisions.

The *ATLAS* detector is one of two all-purpose detectors situated on the ring of the Large Hadron Collider. The detector was used in this thesis in searches of supersymmetry. Chapter 4 gives an overview of the Large Hadron Collider and *ATLAS*. How the detector accurately measures and reconstructs particles is explained in detail in Chapter 5, in addition to this the procedure of statistical interpretation of the measurements is also given. Chapter 6 details a method for estimating a large Standard Model background caused by the mis-measurement of hadronisation of gluons and quarks. A simple search for the supersymmetric partner of the *bottom* quark is detailed in Chapter 7, future prospects for the discovery of such particles are also detailed. Chapter 8 details an analysis searching for evidence of both supersymmetric partners of top and bottom quarks. This final analysis is interpreted in the context of thousands of supersymmetric models which may be more realistic manifestations of supersymmetry in nature.

In the pursuit of attempting to explain our observable universe, the discovery of supersymmetry would possibly lead us toward a better understanding of the world we live in. This is the ultimate goal of science. The universe does not however owe us an explanation. Supersymmetry may not be discovered in the life-time of anyone⁵ currently living on planet Earth. This would not mean that supersymmetry definitely does not exist but many of the appealing theoretical implications become dampened. Equally, supersymmetry may not exist, we just don't know yet. It is therefore important for the current and future generations to pursue other theories of our universe and to develop experimental tests for them. The techniques aimed at the discovery of new particles in colliders, described in this thesis, can be used to probe many theories for physics beyond the Standard Model.

⁵as of 2016

Chapter 2

Theoretical Motivation

2.1 The Standard Model of Particle Physics

The Standard Model (SM) of particle physics describes the subatomic scale by classifying all the known fundamental particles and forces. The model is extremely elegant and has been probed by many precision experiments since its conception in the mid-1970s [38–40]. It incorporates one of most precise scientific measurements ever made - the measurement of the g -factor¹ of the electron [41]. The particle data group lists the world average of all experiments , and cites the theoretical value for the electron to be [30, 42, 43]:

$$\begin{aligned} \left(\frac{g-2}{2}\right)_e^{\text{exp.}} &= (1, 159, 652, 181.11 \pm 0.075) \times 10^{-12} \\ \left(\frac{g-2}{2}\right)_e^{\text{theory.}} &= (1, 159, 652, 188.4 \pm 4.3) \times 10^{-12} \end{aligned}$$

giving the one of the most striking agreements between theory and experiment. The formalisation of the theory lead to the discovery of multiple particles predicted by the model; famously the vector bosons [44, 45] and the Higgs boson [46, 47].

Despite this, there are good reasons to believe the SM is a lower order approximation of a more general theory of the universe [48–52]. Supersymmetry (SUSY) [53–58] is one such Beyond the SM (BSM) theoretical framework that can provide solutions to many of the shortcomings of the SM. This chapter provides an overview of the SM of particle physics, its shortcomings and supersymmetry.

¹a constant that relates a particle's spin angular momentum to its total magnetic moment.

2.1.1 Particle Classification

The SM classifies all particles into three sub-groups: leptons, quarks and field particles. This classification is based on the quantum mechanical properties of the particles, such as spin and charge. The matter particles (leptons and quarks) are fermions of half integer spin. The field particles are bosons of integer spin.

In the SM there are four types of field particles: gluons, which mediate the strong nuclear force; photons, the mediator of the electromagnetic force; W and Z gauge bosons, carriers of the weak nuclear force; and the Higgs boson, the particle responsible for giving mass to fundamental particles². Table 2.1 provides a summary of these four fields and their quantum excitations, otherwise known as particles.

Table 2.1 The fundamental boson of the SM of particle physics showing their associated particles states. The quantum spin and mass of these quanta are shown [30].

Boson		Field	Number of Particles	Spin	Mass (GeV)
Photon	γ	Electromagnetic	1	1	$\gamma(0)$
Gluon	g	Strong Nuclear	8	1	$g(0)$
Gauge Bosons	W^+, W^-, Z^0	Weak Nuclear	3	1	$W(80.4), Z(91.2)$
Higgs	H	Higgs Field	1	0	$H(125)$

The SM is algebraically based on a product of groups, $\mathcal{G}_{SM} = SU(3)_c \times SU(2)_L \times U(1)_Y$, the generators of said group describe the presence and interactions of the forces of the SM. The special unitary group of 3-dimensions ($SU(3)_c$) forms a foundation for the theory of Quantum ChromoDynamics (QCD) describing the strong nuclear force. The electroweak force, a unification of the electromagnetic and weak nuclear forces, is split into two sectors: the electroweak sector, represented by $SU(2)_L$; and the weak hyper charge sector, represented by $U(1)_Y$. The two sectors of the electroweak force ($SU(2)_L \times U(1)_Y$) are built upon the theories of Quantum ElectroDynamics (QED) and Quantum Flavour Dynamics (QFD), the mixing of the eigenstates of the electroweak force gives rise to the separate forces of electromagnetism and the weak nuclear force. The electroweak force particles therefore have spin 1.

The final field particle, the Higgs boson, is unique as its spin is 0. The field arises from Spontaneous Symmetry Breaking (SSB) of $SU(2)_L \times U(1)_Y$.

Matter particles, unlike bosons which have integer spin, are fermions with spin $\frac{1}{2}$. They are represented mathematically by four-dimensional complex vectors called Dirac spinors (ψ) [59, 31], which can be decomposed into left- and right-handed chiral components.

²It should be noted that the Higgs fields is generally not considered a fundamental force, it is a force in the sense of its interactions with other particles

2.1 The Standard Model of Particle Physics

Fermions interactions can be explained by the presence of the SM generators (\mathcal{G}_{SM}) acting upon the spinor states. In nature at least three generations of fermions exist, each generation contains a positively charged quark ($\frac{2}{3} e$), a negatively charged quark ($-\frac{1}{3} e$), a negatively charged lepton ($-1 e$) and a neutral anti-neutrino ($0 e$). The elementary charge, e , has a measured value of $1.6021766208(98) \times 10^{-19}$ Coulombs [1]. For every fermion there also exists an anti-particle of opposite charge³. The three generations have identical properties except their mass. The particles of generation-II and generation-III are of higher mass and are unstable, they decay via the bosons to the Generation-I particles. A summary of the matter particles of the SM is shown in Table 2.2.

Table 2.2 The fundamental matter particles of the SM of particle physics and their key properties. These particles are subdivided into quarks and leptons, they all have spin $\frac{1}{2}$ [30, 31].

Quarks					Leptons			
	Particle		Charge (e)	Mass	Particle		Charge (e)	Mass
I	Up	u	$+\frac{2}{3}$	2.3 MeV	Electron	e	-1	0.5 MeV
	Down	d	$-\frac{1}{3}$	4.8 MeV	Electron Neutrino	ν_e	0	< 2 eV
II	Charm	c	$+\frac{2}{3}$	1.3 GeV	Muon	μ	-1	106 MeV
	Strange	s	$-\frac{1}{3}$	95 MeV	Muon Neutrino	ν_μ	0	< 2 eV
III	Top	t	$+\frac{2}{3}$	173 GeV	Tau	τ	-1	1.8 GeV
	Bottom	b	$-\frac{1}{3}$	4.2 GeV	Tau Neutrino	ν_τ	0	< 2 eV

2.1.2 The Standard Model Lagrangian Density

The SM can be expressed mathematically with the use of a Lagrangian density, describing a combination of the kinematic and potential energy of all known particles and their interactions. The formula is expressed in Equation 2.1 [62, 1, 63, 64], a description of each term is provided in Table 2.3.

$$\begin{aligned}
 \mathcal{L}_{\text{SM}} = & \mathcal{L}_{\text{B}} + \mathcal{L}_{\text{W}} + \mathcal{L}_{\text{G}} + \mathcal{L}_{\phi} + \mathcal{L}_{\text{other}} \\
 & + \sum_{\ell=e,\mu,\tau} \mathcal{L}(\ell) + \sum_{\ell=e,\mu,\tau} \mathcal{L}_{\text{Y}}(\ell) + \sum_{f=1,2,3} \mathcal{L}(f) + \sum_{f=1,2,3} \mathcal{L}_{\text{Y}}(f) \quad (2.1)
 \end{aligned}$$

³In the case of the neutral neutrino, its anti-neutrino differs by chirality: a neutrino is left-handed and an anti-neutrino is right-handed. It is possible that a neutrino is a Majorana fermion [60, 31] and it is its own anti-particle with a left and right-handed state. If this is true, phenomena such as neutrinoless double beta decay and other lepton violating processes would be allowed - such processes have yet to be observed [61].

2.1 The Standard Model of Particle Physics

The following sections shall explain the origin and relevance of each term.

Table 2.3 The components of the SM Lagrangian density decomposed to the terms associated with different matter and force particles sectors.

Term	Description
\mathcal{L}_B	Gauge term associated with the Abelian group $U(1)_Y$
\mathcal{L}_W	Gauge term associated with the non-Abelian group $SU(2)_L$
\mathcal{L}_G	Gauge term associated with the non-Abelian group $SU(3)_c$
\mathcal{L}_ϕ	Unitary gauge field representing the Higgs $SU(2)_L$ doublet
$\mathcal{L}(\ell)$	Lepton term associated with gauge boson interactions
$\mathcal{L}(f)$	Quark term associated with gauge boson interactions
$\mathcal{L}_Y(\ell)$	Yukawa term for lepton masses obtained via SSB ^a of $SU(2)_L \times U(1)_Y$
$\mathcal{L}_Y(f)$	Yukawa term for quark masses obtained via SSB of $SU(2)_L \times U(1)_Y$
$\mathcal{L}_{\text{other}}$	Gauge-fixing term for field strength tensor ^b and ghost particles ^c

^aSpontaneous Symmetry Breaking

^bWith the use of gauge fixing, inverse propagators can be defined. This is to remove eigenvectors with eigenvalues of 0, which are not invertible.

^cQCD needs to include non-physical ghost particles, they are needed to cancel non-physical polarisation states of gluons.

2.1.3 Quantum Electrodynamics (QED)

The theory of QED is one of the simplest Quantum Field Theories (QFT); it quantum mechanically describes the classical field theory of electromagnetism. For a relativistic massive scalar field described by the Klein-Gordon-Equation (KGE)⁴, it can be shown that the invariance of the equations of motion under a global $U(1)$ rotation of the field, requires the presence of a massless vector field - the electromagnetic field.

The Dirac Lagrangian The Dirac Equation (DE) [59] provides an alternative form and solution for a relativistic version of the Schrödinger equation [66]. The formulation solves the problem of a negative-energy solutions possible with the KGE, it predicts a symmetry between charged fermions leading to the discovery of anti-particles [67]. The associated Lagrangian density of the DE is given by:

$$\mathcal{L}_{\text{Dirac}} = \bar{\psi}(i\gamma^\mu \partial_\mu - m)\psi \quad (2.2)$$

⁴The KGE [65] is a relativistic version of the Schrödinger equation [66]

2.1 The Standard Model of Particle Physics

where ψ is the spinor field (of spin- $\frac{1}{2}$) with two chiral components relating to left and right-handed projections. The gamma matrices, γ^μ , govern translations of ψ in 4D, they are constructed with the 2D Pauli matrices for the purpose of the two chiral components. Anti-particles are represented by bar notation, defined as: $\bar{\psi} \equiv \psi^\dagger \gamma^0$. The Lagrangian can be required to be locally gauge invariant under a U(1) space-time rotation. By choosing a gauge to remove non-physical degrees of freedom, the Lagrangian for QED is obtained in Equation 2.3; it describes the massive spinor field (ψ) and additionally a massless spin-1 vector field (A_μ) representing the electromagnetic force. The middle term shows that coupling strength between the two fields is proportional to e .

$$\mathcal{L}_{\text{QED}} = -\frac{1}{16\pi} F_{\mu\nu} F^{\mu\nu} - e\bar{\psi}\gamma^\mu A_\mu \psi + \bar{\psi}(i\gamma^\mu \partial_\mu - m)\psi \quad (2.3)$$

Where $A_\mu = (\phi, \vec{A})$ is a four-vector representing the massless vector field of electromagnetism, the electric field is $\vec{E} = -\nabla\phi - \frac{\partial\vec{A}}{\partial t}$ and the magnetic field (\vec{B}) is the curl of \vec{A} . $F_{\mu\nu} = \partial_\mu A_\nu - \partial_\nu A_\mu$ is the kinetic term of A_μ and is derived from the Proca Equation [68] - the relativistic wave equation of a vector field. The resulting Lagrangian for QED, \mathcal{L}_{QED} , describes the interactions between fermions, their anti-particles and photons. The DE is essential to representing the fermionic fields of the SM. The subsequent sections will show how this equation is built into QCD 2.1.4 and electro-weak theory 2.1.5 in order to explain the interactions between matter particles and the forces of nature.

2.1.4 Quantum Chromodynamics (QCD)

The theory of QCD is built upon the observation that in nature only three types of particle states are observed: baryons, anti-baryons (three quarks) and mesons (quark-anti-quark pairs). Over several years many new particles in the form of resonances were discovered with different charge, such as Kaon spin-0 mesons [69–71] and the ρ spin-1 mesons [72] leading to the prediction of the *strange* quark. In 1974 simultaneous experiments at SLAC [73] and Brookhaven [74] observed the resonance of the J/ψ particle which lead to the realisation of the existence of the charmed quark (or charm quark). The Upsilon mesons were discovered in 1977 at Fermilab [75] leading to the formulation of the third generation quarks, which was verified with the discovery of the top quark in 1995 [76]. In order to explain these resonances the quark model was proposed. The model features the problem that no isolated quarks have ever been observed, yet baryons with three same-flavour quarks are allowed, for example the $\Delta^{++}(|u\rangle|u\rangle|u\rangle)$ baryon violates the spin statistics theorem - as quarks are fermions. This can be solved with the introduction of the colour quantum number. Subdividing quarks into six orthogonal coloured states: red, green or blue and their anti-colours ($R, G, B, \bar{R}, \bar{G}, \bar{B}$)

2.1 The Standard Model of Particle Physics

allows for the baryonic state $\Delta^{++}(|u_R\rangle|u_G\rangle|u_B\rangle)$ to exist as the three up-quarks are not the same quantum spin- $\frac{1}{2}$ state. There are three coloured states and three anti-colour states, the coloured (anti-coloured) states can be represented by a 3-dimensional column (row) vector of Dirac spinors (adjoint spinors):

$$\vec{\psi} = \begin{pmatrix} \psi_r \\ \psi_g \\ \psi_b \end{pmatrix}$$

$$\vec{\bar{\psi}} = (\bar{\psi}_{\bar{r}} \quad \bar{\psi}_{\bar{g}} \quad \bar{\psi}_{\bar{b}})$$

QCD Lagrangian To describe rotations and translations in this colour-phase-space the generators of the special unitary group SU(3) are used. This gives rise to eight degrees of freedom and eight generators denoted as $T^a = \frac{1}{2}\lambda^a$ where λ^a are the Gell-Mann matrices [1, 31]. Following the same mathematics as with the Dirac Lagrangian for a spinor in U(1), a 3-component spinor in SU(3) is required to be locally gauge invariant under the transformation:

$$\vec{\psi} \rightarrow U \vec{\psi} = e^{iT^a a_a} \vec{\psi} \quad (2.4)$$

where a_a are scalar numbers representing the magnitude of the rotations. With a choice of gauge, the resulting QCD Lagrangian density describes how coloured quantum states interact with one another via massless bosons:

$$\mathcal{L}_{\text{QCD}} = -\frac{1}{4}F_{\mu\nu}^a F^{a\mu\nu} - g_s \bar{\psi}_i \gamma^\mu T_{ij}^a G_\mu^a \psi_j + \bar{\psi}_i (i\gamma^\mu \partial_\mu - m\delta_{ij}) \psi_j \quad (2.5)$$

Where G^a are the eight gluons of the strong nuclear force, g_s is the coupling strength, $F_{\mu\nu}^a = \partial_\nu G_\mu^a - \partial_\mu G_\nu^a + g_s f^{abc} G_\mu^b G_\nu^c$ and ψ_i denotes the index of the vector of spinors. A key difference between the QED Lagrangian (Equation 2.3) and the QCD Lagrangian (Equation 2.5) is that because QED is an Abelian gauge theory (U(1)) and QCD is a non-Abelian gauge theory (SU(3)) where the structure constants, f^{abc} , are non-zero for the latter group. Multiplying out the first term of Equation 2.5, $F_{\mu\nu}^a F^{a\mu\nu}$, gives additional terms which correspond to three and four point self interactions of the associated fields.

From the QCD Lagrangian of Equation 2.5, the gauge term of \mathcal{L}_{SM} associated with the non-Abelian group SU(3)_c, \mathcal{L}_{G} is obtained. The equation also provides part of the $\sum_{f=1,2,3} \mathcal{L}(f)$ term associated with the interaction of fermions and gluons; the $\mathcal{L}_{\text{other}}$ term from ghost-particles and gauge-fixing needed to cancel non-physical polarisation states and to define inverse propagators of gluons are included in the QCD Lagrangian [31].

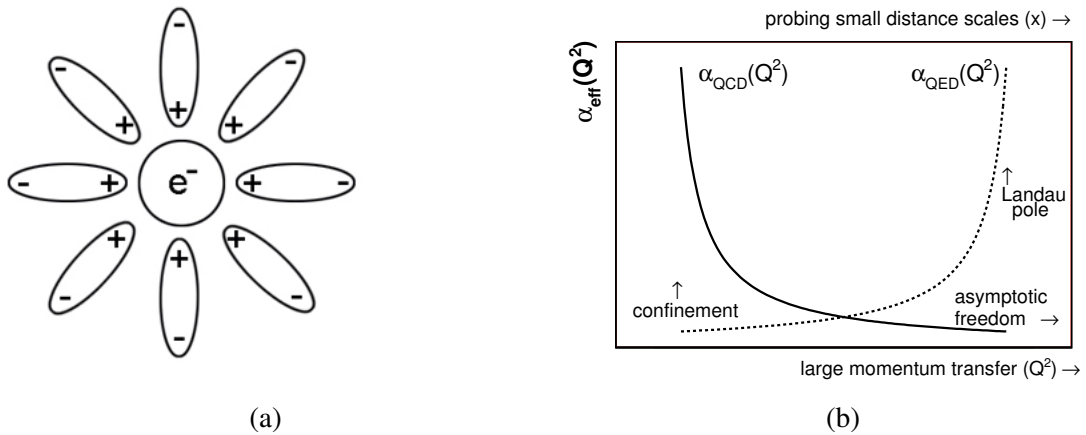


Fig. 2.1 (a) Electron screening: the bare electron charge is masked by virtual electron-positron pairs. (b) The “running” of the QED and QCD coupling constants. Taken from [1].

2.1.4.1 Coupling Strength

The additional direct couplings of the gluons has implications to the strength of the strong nuclear force as a function of distance - an effect known as *charge screening*. In the theory of QED an electron emits *virtual* photons, which in turn annihilate to produce virtual electron-positron pairs. The positively charged virtual positrons are attracted to the electron and the virtual electrons are repelled, as seen in Figure 2.1a, causing the bare charge of the electron to be *screened*. Considering a single test charge moving closer to an electron, with increasing energy needed, the cloud of electron-positron pairs gets penetrated and fewer virtual particles screen the bare charge; this results in the measured charge to increase. Figure 2.1b shows how $\alpha_{\text{QED}}(Q^2)$ increases at smaller distances (larger momentum transfer). The determined value of $\alpha_{\text{QED}}(0) = \frac{e^2}{4\pi\epsilon_0\hbar c} \approx 7.297 \times 10^{-3}$ is given in [30].

The effect of screening is analogous in QCD with coloured quark states and gluons rather than electron-positron pairs and photons. However, the self interactions of the gluons reverses the effect. The gluon coloured states are mixed colour-anti-colour superposition, this results in an anti-screening effect where a coloured quark state is surrounded by other coloured quark states at large distances. Probing the coloured quark with a test charge results in less colour charge measured at smaller distances- the coloured quark becomes less confined. This behaviour is seen in Figure 2.1b, $\alpha_{\text{QCD}}(Q^2)$ ⁵ decreases at smaller distances (larger momentum transfer).

Understanding QCD is critical in understanding of the production of particles at hadron colliders which is described in more detail in Chapter 3.

⁵ $\alpha_{\text{QCD}}(0) = \frac{g_s^2}{4\pi\epsilon_0\hbar c}$

2.1.5 Electroweak Theory (EWT)

The theories of QED and QCD describe the electromagnetic force and strong nuclear force respectively; they explain how an atomic nucleus is held together and how electrons are bound in orbital states. These theories however cannot explain how a neutron can decay into a proton and emit an electron and a electron-anti-neutrino. They do not explain observed decays such as charged pion decays to muons or muon decays to electrons, both of which have observed lifetimes of $\mathcal{O}(10^{-8})$ and $\mathcal{O}(10^{-6})$ seconds respectively [1]. This is because particles decaying via the electromagnetic force typically have lifetimes of $\mathcal{O}(10^{-16})$ seconds. A neutral pion has a decay time of 8.4×10^{-17} to photons or electron-positron pairs, which is mediated by the electromagnetic force [77]. However, the decay times of charged pions and muons are too long to occur via strong or electromagnetic interactions. These interactions are explained by the theory of Quantum Flavour Dynamics (QFD). In the SM, QED and QFD are united by ElectroWeak Theory (EWT). The unification of the electromagnetic and weak nuclear forces was first suggested by Glashow [38] by considering the group $SU(2)_L \times U(1)_Y$. The theory was constructed in such a way due to the experimental observation by Wu [78] that weak interactions maximally violate parity. This this lead to formulating spinor states of fermions as left-handed doublets (χ_L) and right-handed singlets (ξ_R), vice versa for anti-spinor states, shown in Table 2.4.

Table 2.4 The spinor states of Electro-weak theory broken-down into the three generations showing left- and right-handed chiral states [1, 31].

	Generation-I		Generation-II		Generation-III	
ψ_{leptons}	$\begin{pmatrix} \nu_L^e \\ e_L \end{pmatrix}, \begin{pmatrix} \bar{\nu}_R^e \\ \bar{e}_R \end{pmatrix}$	e_R, \bar{e}_L	$\begin{pmatrix} \nu_L^\mu \\ \mu_L \end{pmatrix}, \begin{pmatrix} \bar{\nu}_R^\mu \\ \bar{\mu}_R \end{pmatrix}$	$\mu_R, \bar{\mu}_L$	$\begin{pmatrix} \nu_L^\tau \\ \tau_L \end{pmatrix}, \begin{pmatrix} \bar{\nu}_R^\tau \\ \bar{\tau}_R \end{pmatrix}$	$\tau_R, \bar{\tau}_L$
ψ_{quarks}	$\begin{pmatrix} u_L \\ d_L \end{pmatrix}, \begin{pmatrix} \bar{u}_R \\ \bar{d}_R \end{pmatrix}$	$u_R, d_R, \bar{u}_L, \bar{d}_L$	$\begin{pmatrix} c_L \\ s_L \end{pmatrix}, \begin{pmatrix} \bar{c}_R \\ \bar{s}_R \end{pmatrix}$	$c_R, s_R, \bar{c}_L, \bar{s}_L$	$\begin{pmatrix} t_L \\ b_L \end{pmatrix}, \begin{pmatrix} \bar{t}_R \\ \bar{b}_R \end{pmatrix}$	$t_R, b_R, \bar{t}_L, \bar{b}_L$

Section 2.1.3 described how the theory of QED requires the presence of the electromagnetic field if the Lagrangian of a Dirac spinor is to remain invariant under a global $U(1)$ rotation. Constructing left-handed and right handed fermions as doublets and singlets⁶ requires a $SU(2)_L \times U(1)_Y$ symmetry transformation on the left-handed and right-handed

⁶and constructing left-handed and right-handed anti-fermions as singlets and doublets

chiral components, such as:

$$\chi_L \rightarrow \chi'_L = \exp \left[-i\frac{g}{2}\vec{\alpha}(x) \cdot \vec{T} + i\frac{g'}{2}\beta(x)Y \right] \chi_L \quad (2.6)$$

$$\xi_R \rightarrow \xi'_R = \exp \left[i\frac{g'}{2}\beta(x)Y \right] \xi_R \quad (2.7)$$

where the generators, T^i and Y are defined to satisfy $[Q, T^i] = i\epsilon_{ijk}T^j$, in order to conserve charge, $Q = T^3 + \frac{Y}{2}$. $\vec{\alpha}(x)$ and $\beta(x)$ are the vectors of magnitudes and magnitudes of the transformations. The factors g and g' are coupling strengths associated with these transformations.

For the Lagrangian to remain invariant, four vector fields, $W_\mu^1, W_\mu^2, W_\mu^3$ and B_μ , (W bosons and B boson eigenstates) are introduced. Thus the covariant derivative is modified such that:

$$\partial_\mu \rightarrow \mathcal{D}_\mu = \partial_\mu + i\frac{g'}{2}YB_\mu + ig\vec{T} \cdot \vec{W} \quad (2.8)$$

The resulting total Lagrangian can be decomposed in terms of exchanging a neutral current and a charged current, for which the latter occurs only for the left-handed doublets. By doing so, the four physical vector fields can be written as a mixture of the gauge fields since a charge current exchange is observed experimentally. One neutral current exchange occurs via the generator W_μ^3 to only left-handed doublets and the other exchange via B_μ occurs to both left and right-handed doublets and singlets:

$$W_\mu^\pm = \frac{1}{2}(W_\mu^1 \mp iW_\mu^2) \quad (2.9)$$

$$\begin{pmatrix} Z_\mu \\ A_\mu \end{pmatrix} = \begin{pmatrix} \cos \theta_w & \sin \theta_w \\ -\sin \theta_w & \cos \theta_w \end{pmatrix} \begin{pmatrix} W_\mu^3 \\ B_\mu \end{pmatrix} \quad (2.10)$$

Where the Weinberg angle (θ_w) follows the relation $g \sin \theta_w = g' \cos \theta_w = e$. A_μ is the vector field representing the photon (as in Equation 2.3); and W_μ^\pm and Z_μ are vector fields of the W and Z bosons. EWT in $SU(2)_L \times U(1)_Y$ accounts for the remaining fermion interaction terms with the electroweak bosons and added to the gauge boson term ($\sum_{f=1,2,3} \mathcal{L}(f)$) of the SM Lagrangian. The electroweak bosons also contribute: quark interactions, $\sum_{q=1,2,3} \mathcal{L}(q)$; \mathcal{L}_B and \mathcal{L}_W , the kinetic terms of the W , Z and γ bosons.

2.1.6 Spontaneous Symmetry Breaking (SSB)

The last piece of the SM Lagrangian (\mathcal{L}_{SM}) is the mechanism for how all elementary particles obtain mass. This is achieved via the Higgs mechanism in $SU(2)_L \times U(1)_Y$. No mass terms

2.1 The Standard Model of Particle Physics

are needed for gluons (G_μ^a) as they are massless yet a mechanism is needed for massive fermions and the EW bosons in $SU(2)_L \times U(1)_Y$ space.

Considering a Lagrangian for a complex scalar boson in doublet form, $\mathcal{L}_{\vec{\phi}}$, with a potential term (\mathcal{V}) defined with a negative squared mass term:

$$\mathcal{V}(\vec{\phi}) = \mu^2(\vec{\phi}^\dagger \vec{\phi}) + \lambda(\vec{\phi}^\dagger \vec{\phi})^2 \quad (2.11)$$

Where the $SU(2)_L$ doublet of complex scalar Higgs fields is defined as:

$$\phi^+ = \frac{\phi_1 + i\phi_2}{\sqrt{2}} \quad (2.12)$$

$$\phi^0 = \frac{\phi_3 + i\phi_4}{\sqrt{2}} \quad (2.13)$$

$$\vec{\phi} = \begin{pmatrix} \phi^+ \\ \phi^0 \end{pmatrix} \quad (2.14)$$

A graphical representation of this field ϕ^+ as a function of the potential can be seen in Figure 2.2.

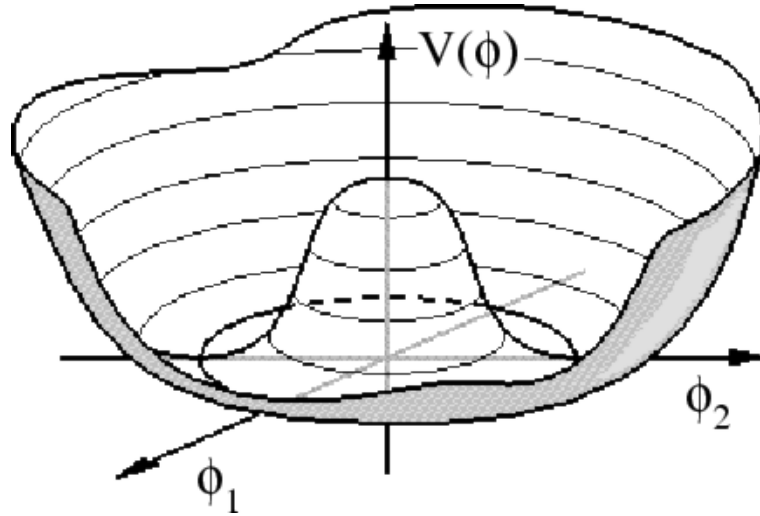


Fig. 2.2 Graphical representation of the Higgs potential for a singular complex scalar field.

Due to this choice in potential, a non-zero minima can be found. The $SU(2)$ symmetry of this minima can be *spontaneously broken* with the choice:

$$\phi_1^2 + \phi_2^2 + \phi_3^2 = 0, \quad \phi_3^2 = \frac{\mu^2}{\lambda} = v^2 \quad (2.15)$$

Resulting in a minima defined as:

$$\vec{\phi}^\dagger \vec{\phi}|_{min} = \frac{\mu^2}{2\lambda} \quad (2.16)$$

In order to remain invariant under the derivative transformation of Equation 2.8 the Higgs doublet must also transform under the same transformation as the fermionic doublet (Equations 2.6, 2.7).

Due to the gauge invariance of \mathcal{L}_ϕ the field ϕ_3 can be redefined to lie at the minima $\phi_3 = H + v$, where H is the scalar Higgs field:

$$\vec{\phi} = \frac{1}{\sqrt{2}} \begin{pmatrix} 0 \\ H + v \end{pmatrix} \quad (2.17)$$

Since the vector boson fields are present in the gauge invariant \mathcal{L}_ϕ term, their masses are determined to be:

$$\begin{aligned} M_W &= \frac{1}{2} g v \\ M_Z &= \frac{1}{2} (g^2 + g'^2)^{1/2} v \\ M_\gamma &= 0 \\ M_H &= \sqrt{-2\mu^2} \end{aligned}$$

The vector bosons have *eaten up* the remaining three fields (ϕ_1, ϕ_2, ϕ_4), which become longitudinal polarisations of the vector bosons⁷.

This choice of minima was verified in 1983, the vector bosons were discovered and observed to be massive by the experiments UA1 and UA2 [79]. The ATLAS and CMS experiments also announced the discovery of a massive scalar boson consistent with the properties of a Higgs boson in 2012 [80, 81]:

Finally, the terms $\sum_{\ell=1,2,3} \mathcal{L}_Y(\ell)$ and $\sum_{f=1,2,3} \mathcal{L}_Y(f)$, which are $SU(2)_L \times U(1)_Y$ gauge invariant, are included in \mathcal{L}_{SM} to generate lepton and quark masses. The Dirac mass terms of fermions, $m_i \bar{\psi}_i \psi_i$, are not gauge invariant under the EWT symmetry, therefore the Higgs

⁷Due to special relativity, a particle with a longitudinal polarisation must travel slower than the speed of light and hence obtain mass. The total polarisations for the mixed photon mass eigenstate (A_μ) cancel out and hence the state is massless.

doublet is also used to give fermions mass by including the following terms:

$$\sum_{\ell=e,\mu,\tau} \mathcal{L}_Y(\ell) = \sum_{\ell=e,\mu,\tau} -G_\ell \left[\bar{L}_\ell \vec{\phi} \ell_R + \bar{\ell}_R \vec{\phi}^\dagger L_\ell \right] \quad (2.18)$$

$$\sum_{f=1,2,3} \mathcal{L}_Y(f) = \sum_{i=1,2,3} \left(-G_d^{ij} \left[\bar{Q}_i \vec{\phi} d_{jR} \right] - G_u^{ij} \left[\bar{Q}_i \vec{\phi}^* u_{jR} \right] \right) \quad (2.19)$$

Here, L_ℓ denotes the left-handed leptons ($\chi_L(\ell)$); Q_i denotes the left-handed quarks ($\chi_L(f)$); ℓ_R , u_{jR} , d_{jR} are the right-handed leptons, $\frac{2}{3}e$ charged quarks and $-\frac{1}{3}e$ charged quarks respectively ($\xi_R(\ell, f)$).

These terms dictate how fermions obtain mass via the Higgs mechanism. A physical fermion is a superposition of its left- and right-handed chirality states:

$$f = f_L + f_R \quad (2.20)$$

Figure 2.3 pictorially describes the difference between a right-handed and a left-handed fermion. A right-handed particles spin vector is aligned with its vector of motion, a left-handed particles spin vector is aligned to the negative vector of its motion.

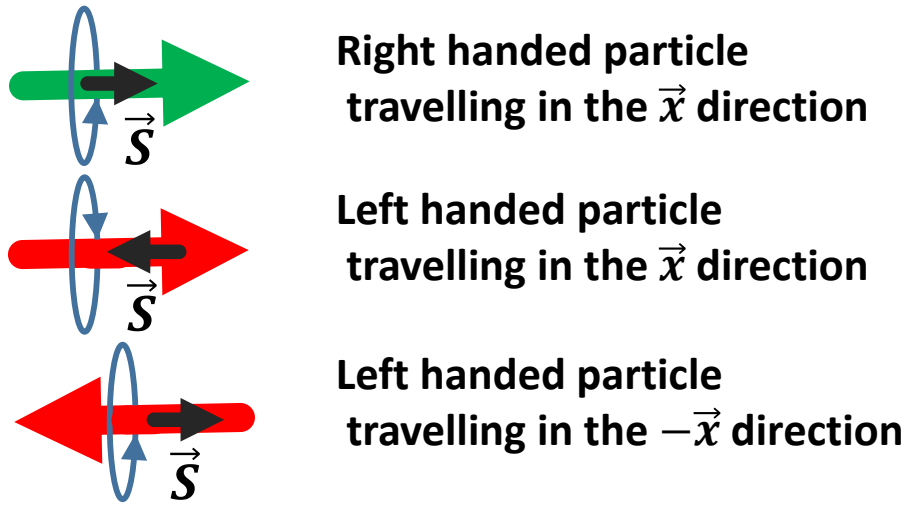


Fig. 2.3 Left and right handedness of SM fermions depicting vectors for the particle spin and direction of motion.

A fermion will change *handedness* as it interacts with the Higgs boson, it switches between left-chiral and right-chiral state as seen in Equations 2.18 and 2.19. Figure 2.4 shows the light cone for a decay of a W boson in which an electron and an anti-neutrino are produced. As is seen in Table 2.4, an anti-neutrino (in the SM) only exists as a massless right-handed chiral component. No left-handed component exists, therefore the Higgs field

does not interact with the anti-neutrino, it travels away at the speed of light. Contrary to this, the electron interacts with the Higgs field. It switches the left-handed state travelling in the positive \vec{x} direction to a right-handed state travelling in the negative \vec{x} direction. As indicated by the light grey line of Figure 2.4, the physical electron is slowed down by the changing between left- and right- chiral fields and hence it acquires mass. How strongly the Higgs field couples to the left and right components therefore determines how massive the fermion is.

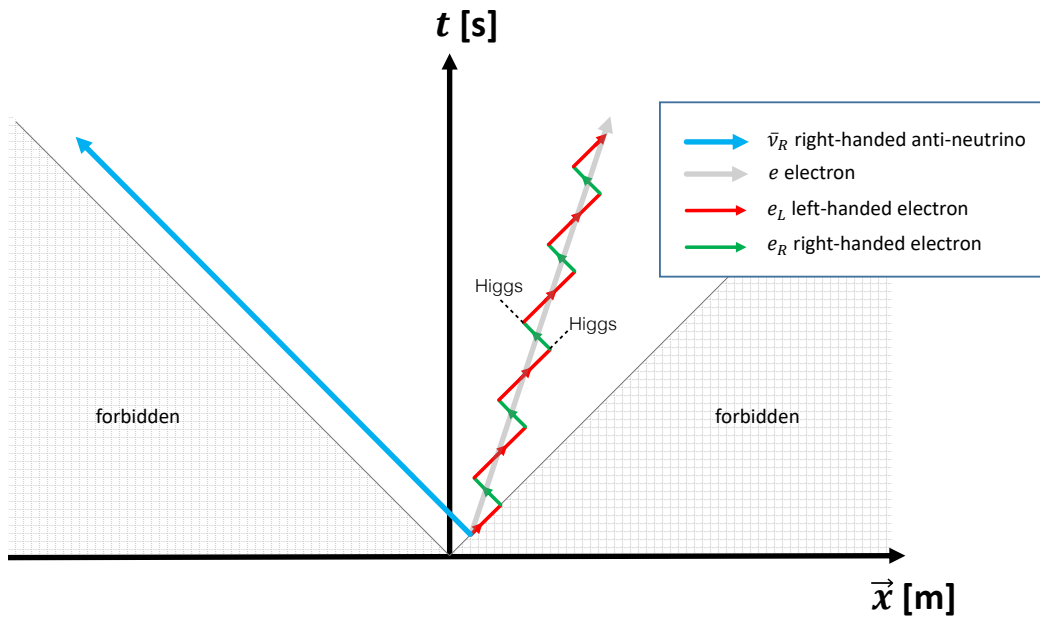


Fig. 2.4 Pictorial representation showing the light cone for a W boson decay in which an electron and anti-neutrino are produced. The higgs field changes a left-handed electron into a right-handed fermion, this is what causes the observed electron to have a mass.

2.2 Beyond the Standard Model

Despite many precision experiments probing the properties of particles and composite particles of Tables 2.1-2.2, the SM lepton neutrinos of all three flavours have been observed to be massive [82, 83], which is not predicted by the left-handed doublet and right-handed singlet formulation of the fermions in the SM. This observed fact is a key shortcoming of the SM indicating that the theory is not complete. Many additional extensions to the SM [84–86] include the graviton, the spin-2 boson associated with the force of gravity but has yet to be experimentally observed.

Several astronomical and cosmological observation indicate there is more matter in the universe than luminous matter. This was first observed in the rotational velocity curves

of stars in galactic bodies by Jan Oort [87], stars far from the galactic centre orbit faster than is expected, this was observed to be flat with distance by Rubin in 1970 [88]. Soon after Oort's observation, Zwicky [89] applied the viral theorem to the *Coma galaxy cluster* and inferred the presence of *unseen* mass within the galaxies of the cluster. Additionally, clusters of galaxies that have collided [90] and the gravitational lensing of galaxies [91] also indicate that more matter than can be seen [92, 93] exists. Attempts to explain these observations with massive astronomical objects composed of baryonic matter that emit little or no radiation, such as white dwarf stars, have not been able to account for the amount of unknown matter [94]. This indicates that the luminous baryonic matter is not the only type of matter in universe and some Beyond the SM physics may yet be discovered. A popular explanation for these phenomena is that galaxies are surrounded by a halo of unknown matter - dark matter. Calculations estimate that $\sim 85\%$ of the mass density of the visible universe is dark matter and $\sim 15\%$ ordinary matter [95–97]. The most popular candidates for dark matter are Weakly Interacting Massive Particles (WIMPs), some unknown massive stable particles yet to be experimentally observed.

2.3 The Hierarchy Problem

The Higgs, given by the term \mathcal{L}_ϕ of the SM Lagrangian, receives higher order loop corrections from the SM fermions. The top quark is the heaviest fermion - meaning its coupling strength, $\lambda_t \sim 0.94$ [76, 98], to the Higgs field is the largest. For a generic fermion, coupling to the Higgs field with the term $-\lambda_f H \bar{f} f$, the first order loop diagram yields a correction:

$$\Delta m_H^2 = -\frac{|\lambda_f|^2}{8\pi^2} \Lambda_{\text{UV}}^2 + \mathcal{O}(m_H^2 \ln \Lambda)^2 + \dots \quad (2.21)$$

Where Λ_{UV}^2 denotes the ultra-violet momentum cut-off: the smallest energy scale at which either new or existing physics causes the theory to break down. For example, the cut-off must be at least at the Planck scale $M_P = \sqrt{\frac{\hbar}{8\pi G}} = 1.22 \times 10^{19}$ GeV, the scale at which point like particles become so massive they would instantaneously create black-holes.

If no new physics exists at energy levels reachable by the LHC, this would suggest that the Higgs boson is un-natural. A natural theory is one in which the theory is not dependent on an energy scale much larger than the scale the theory describes. The Higgs mass can be decomposed to:

$$m_H = m_{\text{bare}} + \Delta m_H \quad (2.22)$$

Taking the case in which no new physics exists up to the Planck scale, would mean the bare mass is $\mathcal{O}(10^{19})$ GeV, hence is un-natural as there is a remarkable cancellation to give a measured value of 125 GeV.

2.4 Supersymmetry

The underlying postulation of supersymmetric theories is that there exists some transformations which can change a boson, ϕ , into a fermion, ψ , and vice versa. This can be represented by a generator Q such that:

$$Q\phi = \psi \quad (2.23)$$

$$Q\psi = \phi \quad (2.24)$$

Therefore in SUSY models each SM particle has an associated ‘‘superpartner’’ which differs by spin $\pm\frac{1}{2}$. Supersymmetric models were first theorised to solve the hierarchy problem of Section 2.3 by adding extra particles to the SM, consequently providing candidates for dark matter WIMPs.

2.4.1 Weiss-Zumino Model

The simplest SUSY model that can be used to demonstrate how to solve the hierarchy problem is the Wess-Zumino Model (WZM) 1974 [99]. The model is built upon 3 fields:

$$\omega \rightarrow \text{A massive Weyl spinor in the Majorana basis} \quad (2.25)$$

$$\phi \rightarrow \text{A complex scalar field} \quad (2.26)$$

$$F \rightarrow \text{A complex auxiliary field} \quad (2.27)$$

For the purpose of simplicity a Majorana fermion [60] is used, calculations of scattering amplitudes and various properties can also be performed with Weyl spinors [100]. The Lagrangian density for the model is given by:

$$\mathcal{L}_{\text{WZM}} = \partial_\mu \phi^* \partial^\mu \phi + i\omega^\dagger \bar{\sigma}^\mu \partial_\mu \omega - \frac{m}{2}(\omega\omega + \bar{\omega}\bar{\omega}) \quad (2.28)$$

$$+ F^*F + m(\phi F + \phi^* F^\dagger) + \frac{g_s}{2} \left(\phi^2 F + (\phi^\dagger)^2 F^\dagger + \phi\omega\omega + \phi^\dagger \bar{\omega}\bar{\omega} \right) \quad (2.29)$$

2.4 Supersymmetry

The trick to keep the Lagrangian invariant under infinitesimal supersymmetric transformations is to require the auxiliary field to transform in a specific way:

$$\delta_\varepsilon \phi = \varepsilon \omega \quad (2.30)$$

$$\delta_\varepsilon \omega_\alpha = -i(\sigma^\mu \varepsilon^\dagger)_\alpha + \varepsilon_\alpha F \quad (2.31)$$

$$\delta_\varepsilon F = -i\varepsilon^\dagger \bar{\sigma}^\mu \partial_\mu \omega \quad (2.32)$$

Since the auxiliary field F is non-propagating, $\frac{\partial \mathcal{L}_{\text{WZM}}}{\partial (\partial_\mu F)} = 0$, the Euler-Lagrange equation of motion for the auxiliary field (F and F^*) can be used to rewrite the Lagrangian as:

$$\mathcal{L}_{\text{WZM}} = \partial_\mu \phi^* \partial^\mu \phi + i\omega^\dagger \bar{\sigma}^\mu \partial_\mu \omega - \frac{m}{2}(\omega\omega + \bar{\omega}\bar{\omega}) - m^2 \phi \phi^\dagger \quad (2.33)$$

$$- \frac{mg_s}{2} (\phi^2 \phi^\dagger + \phi(\phi^\dagger)^2) - \frac{g_s^2}{4} (\phi \phi^\dagger)^2 - \frac{g_s}{2} (\phi \omega \omega + \phi^\dagger \bar{\omega} \bar{\omega}) \quad (2.34)$$

By rewriting the complex field ϕ in terms of real scalar fields:

$$\phi = \frac{1}{\sqrt{2}}(\phi_1 + i\phi_2) \quad (2.35)$$

The free part of the Wess-Zumino Lagrangian ⁸ becomes:

$$\mathcal{L}_{\text{WZM}}^{\text{free}} = \partial_\mu \phi_1 \partial^\mu \phi_1 - \frac{1}{2}m^2 \phi_1^2 + \partial_\mu \phi_2 \partial^\mu \phi_2 - \frac{1}{2}m^2 \phi_2^2 + \frac{1}{2} \bar{\psi}_M (i\gamma^\mu \partial_\mu - m) \psi_M \quad (2.36)$$

The model describes two real massive scalar fields and a massive Majorana fermion. When the Higgs field is introduced to this model the hierarchy problem is solved with $\lambda_\psi = \lambda$ and $\lambda_{\phi_1} = \lambda_{\phi_2} = \lambda_\phi = \lambda^* \lambda$ because now two extra scalar fields which couple to the fermionic field with the same properties also exists. The scalar fields give extra corrections to the Higgs mass which cancels with the one from the fermion field:

$$\Delta m_H^2 = -\frac{|\lambda_\psi|^2}{8\pi^2} \Lambda_{\text{UV}}^2 + \dots \quad (2.37)$$

$$+ 2 \times \frac{\lambda_\phi}{16\pi^2} \Lambda_{\text{UV}}^2 + \dots \quad (2.38)$$

$$\approx 0 \quad (2.39)$$

Thus there is no fine tuning of the bare higgs mass with the loop corrections. In this simplified model however $m = m_{\phi_1} = m_{\phi_2} = m_\psi$ which is not reality as we would have experimentally observed these particles; SUSY must therefore be a broken theory.

⁸Where $\bar{\psi}_M \psi_M = \omega\omega + \bar{\omega}\bar{\omega}$

2.4.2 The Minimal Supersymmetric Standard Model (MSSM)

The MSSM [101, 85, 102, 103] is the lowest order supersymmetric extension to the SM, as with the WZM, it attempts to stabilise the weak scale. The WZM only includes two scalar and one fermionic fields interacting with each other and a Higgs field, whereas the full MSSM attempts to incorporate all aspects and properties of the SM. The model forms *supermultiplets* between SM particles and their supersymmetric partners⁹. For example, the left-handed positron state, $\chi_{\bar{e}}$ is transformed into a supermultiplet containing a scalar positron state, $\tilde{\phi}_{\bar{e}}$ and a auxiliary field $F_{\bar{e}}$:

$$\varepsilon_1 = \tilde{\phi}_{\bar{e}} + \theta \cdot \chi_{\bar{e}} + \frac{1}{2} \theta \cdot \theta F_{\bar{e}} \quad (2.40)$$

θ denotes extra fermionic coordinates needed to correctly transform fermions into bosons and vice versa. All left and right-handed SM fermions are organised into supermultiplets, the superpartners of the fermions are denoted with a tilde and their names are prepended with the word “scalar”, as with the positron and scalar positron. Due to the left-handedness of the SM vector bosons left-handed fermions such as the top, t_L has a left-handed superpartner - the scalar top, \tilde{t}_L , where the label only refers to the superpartner rather than the helicity of the sparticle. The Higgs field in the MSSM is organised into two complex supermultiplets in $SU(2)_L$ doublet form, with eight real scalar degrees of freedom. When electroweak symmetry is broken, three of these fields become massless Nambu-Goldstone bosons - longitudinal modes of Z^0 and W^\pm bosons, as in Chapter 2.1.6. There remains five massive Higgs eigenstates: two CP-even neutral scalars h^0 and H^0 ; one CP-odd neutral scalar, A^0 ; and two charged scalar bosons, H^\pm . The MSSM therefore predicts the existence of an extra four Higgs bosons, where h^0 is by convention the lightest Higgs - generally favoured to be the boson discovered in 2012. The supermultiplet doublets of the Higgs have superpartners called the Higgsinos with spin- $\frac{1}{2}$. A summary of the fermions, Higgs bosons and their superpartners are given in Table 2.5. As with the fermions, the gauge bosons are combined with spin $\frac{1}{2}$ superpartners to form gauge supermultiplets. The superpartner of the three un-mixed states of the W bosons (W_μ) are called Winos, the B boson (B_μ) superpartner is called a Bino and gluinos are the superpartners to gluons; the bosons are summarised in Table 2.6.

Mass eigenstates In the SM the W bosons and B boson mix to give mass eigenstates of the W^\pm , Z^0 and γ bosons. Analogously to this, depending on the free MSSM parameters, mixing of sparticles may occur. The neutral Higgsinos, bino and neutral wino mix to form neutralinos denoted as $\tilde{\chi}_{1,2,3,4}^0$, the index is mass ordered. The charged Higgsinos mix (\tilde{H}_u^+ ,

⁹referred to as sparticles

2.4 Supersymmetry

Table 2.5 The chiral supermultiplets in the Minimal Supersymmetric SM (MSSM) showing their formularisation as doublets or singlets. The quantum numbers associated with the various SM groups are shown [2].

Description	Particle(s) Spin- $\frac{1}{2}$	Sparticle(s) Spin-0	(SU(3) _C , SU(2) _L , U(1) _Y)
Left-handed quarks	$Q_i = \begin{pmatrix} u \\ d \end{pmatrix}, \begin{pmatrix} c \\ s \end{pmatrix}, \begin{pmatrix} t \\ b \end{pmatrix}$	$\tilde{Q}_i = \begin{pmatrix} \tilde{u} \\ \tilde{d} \end{pmatrix}, \begin{pmatrix} \tilde{c} \\ \tilde{s} \end{pmatrix}, \begin{pmatrix} \tilde{t} \\ \tilde{b} \end{pmatrix}$	$(\mathbf{3}, \mathbf{2}, \frac{1}{6})$
Right-handed quarks	$u_i = u, c, t$ $d_i = d, s, b$	$\tilde{u}_i = \tilde{u}, \tilde{c}, \tilde{t}$ $\tilde{d}_i = \tilde{d}, \tilde{s}, \tilde{b}$	$(\mathbf{3}, \mathbf{1}, -\frac{2}{3})$ $(\mathbf{3}, \mathbf{1}, \frac{1}{3})$
Left-handed leptons	$L_i = \begin{pmatrix} \nu_e \\ e \end{pmatrix}, \begin{pmatrix} \nu_\mu \\ \mu \end{pmatrix}, \begin{pmatrix} \nu_\tau \\ \tau \end{pmatrix}$	$\tilde{L}_i = \begin{pmatrix} \tilde{\nu}_e \\ \tilde{e} \end{pmatrix}, \begin{pmatrix} \tilde{\nu}_\mu \\ \tilde{\mu} \end{pmatrix}, \begin{pmatrix} \tilde{\nu}_\tau \\ \tilde{\tau} \end{pmatrix}$	$(\mathbf{1}, \mathbf{2}, -\frac{1}{2})$
Right-handed leptons	$e_i = e, \mu, \tau$	$\tilde{e}_i = \tilde{e}, \tilde{\mu}, \tilde{\tau}$	$(\mathbf{1}, \mathbf{1}, \mathbf{1})$
Up-type Higgs	$(\tilde{H}_u^+ \quad \tilde{H}_u^0)$	$(H_u^+ \quad H_u^0)$	$(\mathbf{1}, \mathbf{2}, \frac{1}{2})$
Down-type Higgs	$(\tilde{H}_d^0 \quad \tilde{H}_d^-)$	$(H_d^0 \quad H_d^-)$	$(\mathbf{1}, \mathbf{2}, -\frac{1}{2})$

Table 2.6 The gauge supermultiplets in the Minimal Supersymmetric SM (MSSM). [2]

Spin- $\frac{1}{2}$	Spin-1	(SU(3) _C , SU(2) _L , U(1) _Y)
\tilde{g} (gluinos)	g (gluons)	$(\mathbf{8}, \mathbf{1}, 0)$
$\tilde{W}^1, \tilde{W}^2, \tilde{W}^3$ (winos)	W^1, W^2, W^3 (W bosons)	$(\mathbf{1}, \mathbf{3}, 0)$
\tilde{B}^0 (bino)	B^0 (B boson)	$(\mathbf{1}, \mathbf{1}, 0)$

\tilde{H}_d^-) with the charged winos (\tilde{W}^+, \tilde{W}^-) to form two chargino states, $\tilde{\chi}_{1,2}^\pm$. The neutralino mixing is governed by:

$$\tilde{\chi}_i^0 = \mathcal{N}_{ij} \psi_j^0 \quad (2.41)$$

where $\psi^0 = (\tilde{B}, \tilde{W}^0, \tilde{H}_d^0, \tilde{H}_u^0)$ and \mathcal{N}_{ij} represents the elements in the neutralino mixing matrix. The neutralinos exhibit a key property which may provide a candidate for dark matter - they are massive and the lightest neutralino is stable too (if R_p is conserved, see Chapter 2.4.4). The scalar fermions have potential to form mixed mass eigenstates. Generally the amount of mixing is only considered non-negligible for 3rd generation scalar fermions. For the first and second generation squarks, the mixing angles of the left- and right-handed squarks are expected to be very small. This is to avoid virtual diagrams which could contribute to flavour changing and CP-violating processes such as Kaon oscillations ($K^0 \leftrightarrow \bar{K}^0$) [104]. The

Yukawa couplings of the third generation fermions are also much larger than the first and second generation quarks, resulting in a large angle for their associated supersymmetric partners.

In the case of the heaviest third generation particle, the top quark, the two scalar top fields corresponding to the left and right-handed chiral states $(\tilde{t}_L, \tilde{t}_R)$ form two scalar top-quarks $(\tilde{t}_1, \tilde{t}_2)$ based on the scalar top mixing angle $(\theta_{\tilde{t}})$ [2]:

$$\begin{pmatrix} \tilde{t}_1 \\ \tilde{t}_2 \end{pmatrix} = \begin{pmatrix} \cos \theta_{\tilde{t}} & -\sin \theta_{\tilde{t}}^* \\ \sin \theta_{\tilde{t}} & \cos \theta_{\tilde{t}}^* \end{pmatrix} \begin{pmatrix} \tilde{t}_L \\ \tilde{t}_R \end{pmatrix} \quad (2.42)$$

2.4.3 Unification

As discussed in previous sections the electromagnetic and weak nuclear forces are known to be two components of the electro-weak force $(SU(2) \times U(1))$. This implies that the strong nuclear force $(SU(3))$ and the force of gravity may also be unified with the electro-weak force, at some energy scale. This unification is known as Grand Unified Theory (GUT). Figure 2.5 depicts the evolution of the running coupling constants of the SM (dashed lines), as can be seen the current particle content of the SM is not enough to unite the strength of the fundamental couplings at one energy level. The following couplings are represented in the figure by:

$$\begin{aligned} U(1) &\rightarrow g' \\ SU(2) &\rightarrow g \\ SU(3) &\rightarrow g_s \end{aligned}$$

where g' and g are the couplings in Equation 2.8 and g_s is the coupling in Equation 2.5. The relation between force strength the coupling constant is given by $\alpha_i = g_i^2/4\pi$.

When new particles predicted by the MSSM are included in the evolution of the running constants (red and blue lines of Figure 2.5), a singular point at $\mathcal{O}(10^{16})$ GeV unites the electromagnetic, weak nuclear and strong nuclear forces. This is a bi-product of the MSSM, which is theoretically attractive giving SUSY theories additional motivation to be pursued experimentally.

2.4.4 R-parity

In the SM the proton is stable, the Super-Kamiokande experiment in Japan [105] sets a limit on the decay of a proton via a kaon, $p \rightarrow K^+ \bar{\nu}$, of $\tau_p > 2.3 \times 10^{33}$ years [106]. This upper

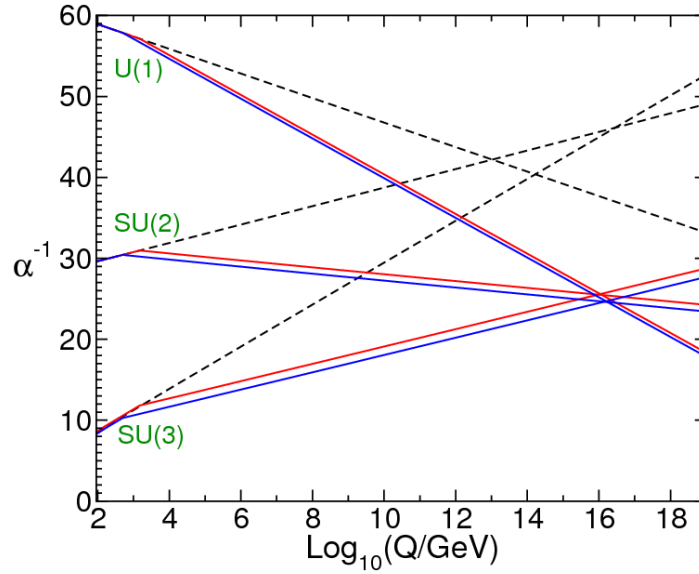


Fig. 2.5 Evolution of the inverse gauge couplings $\alpha_a^{-1}(Q)$ in the Standard Model (dashed lines) and the MSSM (solid lines). In the MSSM case, the sparticle masses are treated as a common threshold varied between 500 GeV and 1.5 TeV, and $\alpha(m_Z)$ is varied between 0.117 and 0.121, as seen in the blue and red lines. Taken from [2].

limits implies that if a process existed in nature allowing for the proton to decay, it must be extremely rare. In the MSSM proton decays are possible, one way to avoid such processes is to impose the conservation of R -parity (R_p). This is a multiplicative quantum number that, if conserved, removes all lepton number violating terms of $\mathcal{L}_{\text{MSSM}}$. It is defined as follows:

$$R_p = (-1)^{2S+3B+L} \quad (2.43)$$

where S is the spin, B is the baryon number and L is the lepton number. All SM particles have $R_p = 1$ and all SUSY particles have $R_p = -1$. If R -parity is conserved, the LHC will produce SUSY particles in pairs since the LHC is a pp collider with an initial state of $R_p = 1$. The neutralino $\tilde{\chi}_1^0$, the Lightest Supersymmetric Particle (LSP) will be stable if R -parity is conserved, providing a very good candidate for dark matter.

2.4.5 The Phenomenological MSSM (pMSSM)

The MSSM has ~ 120 free parameters making the interpretation of all possible models particularly challenging. The number of parameters can be reduced by imposing the following constraints, motivated by experimental observations and theoretical simplification [107]:

Theoretical assumptions:

- R -parity is conserved
- The Lightest Supersymmetric Particle (LSP) is the lightest neutralino ($\tilde{\chi}_1^0$)
- The first and second generation scalar leptons and quarks are mass degenerate. Their Yukawa couplings are negligible and do not affect other observables (as discussed in Chapter 2.4.2).
- The so-called *soft parameters* are real [107], therefore no new sources of CP violation exist.
- At the electroweak scale, Minimal Flavour Violation [108] is imposed.

Experimental constraints:

- Measurements from flavour physics, such as the measured lifetime of the decay of $B_s \rightarrow \mu\mu$ measured by LHCb and CMS [109]. The branching ratio of $b \rightarrow s\gamma$ is considered. Finally, the branching ratio of $B^+ \rightarrow \tau^+ \nu_\tau^-$ is included.
- Precision electro-weak measurement of $(g-2)_\mu$ [110]
- Cosmological measurements of the dark matter density of the universe, $\Omega_{\text{DM}} = 0.227 \pm 0.014$, measured by WMAP [97]. Measurements on the upper limits in LSP mass - spin-independent cross section plane by LUX [111] are applied. An upper limit on the dark matter relic densities in SUSY models is set to the observed value plus 3σ , $\Omega_{\text{SUSY}} h^2 < 0.1238$ [112].
- Collider constraints on measurements of the Higgs mass at the LHC and LEP. Limits set by LEP and the LHC can also be applied to the mass of charginos providing that all scalar neutrinos are heavier than 160 GeV and the charginos have a $\Delta m(\tilde{\chi}_1^\pm, \tilde{\chi}_1^0)$ of at least 2 GeV [32].

The pMSSM therefore contains only 19 free parameters, which are listed in Table 2.7.

2.4.6 Naturalness

In the MSSM the mass of the Higgs boson, at first loop order, is governed by the Equation 2.44[3]:

$$\begin{aligned}
 m_h^2 &= m_Z^2 \cos 2\beta^2 + \Delta_t \\
 &= m_Z^2 \cos 2\beta^2 + \frac{3m_t^4}{4\pi^2 v^2} \left[\log \left(\frac{m_s^2}{m_t^2} \right) + \frac{X_t^2}{m_s^2} \left(1 - \frac{X_t^2}{12m_s^2} \right) \right] + \dots
 \end{aligned} \tag{2.44}$$

Table 2.7 The 19 parameters of the pMSSM with a description of each.

Name	Parameter
Bino mass parameter	$ M_1 $
Wino mass parameter	$ M_2 $
Gluino mass parameter	$ M_3 $
Left-handed 1st and 2nd gen. scalar quark masses	$m_{\tilde{Q}_1} (= m_{\tilde{Q}_2})$
Right-handed 1st and 2nd gen. up-type scalar quark masses	$m_{\tilde{u}_1} (= m_{\tilde{u}_2})$
Right-handed 1st and 2nd gen. down-type scalar quark masses	$m_{\tilde{d}_1} (= m_{\tilde{d}_2})$
Left-handed 3rd gen. scalar quark mass	$m_{\tilde{Q}_3}$
Right-handed scalar top quark mass	$m_{\tilde{u}_3}$
Right-handed scalar bottom quark mass	$m_{\tilde{d}_3}$
Left-handed 1st and 2nd gen. scalar lepton masses	$m_{\tilde{L}_1} (= m_{\tilde{L}_2})$
Right-handed 1st and 2nd gen. scalar lepton masses	$m_{\tilde{e}_1} (= m_{\tilde{e}_2})$
Left-handed 3rd gen. scalar tau mass	$m_{\tilde{L}_3}$
Right-handed 3rd gen. scalar tau mass	$m_{\tilde{e}_3}$
Bilinear Higgs mass parameter	μ
Trilinear top coupling	$ A_t $
Trilinear bottom coupling	$ A_b $
Trilinear τ coupling	$ A_\tau $
Pseudo scalar Higgs boson mass	M_A
Ratio of Higgs vacuum expectation values	$\tan \beta$

Where $\beta = v_u/v_d$ is the ratio of electroweak vacuum expectation values and Δ_t arises from the loop corrections of heavy top and scalar top quarks. m_s denotes the mass scale of SUSY, generally given by the scalar top masses: $m_s = \sqrt{m_{\tilde{t}_1} m_{\tilde{t}_2}}$. $X_t = A_t - \mu \cot \beta$ is the scalar top mixing angle that governs the amount of mixing in Equation 2.42, the trilinear top coupling, A_t , is one of the free parameters in the MSSM (see Table 2.7). The value for the Higgs vacuum expectation value (vev)¹⁰ is $v \approx 174$ GeV. In the regime of large $\tan \beta \gg 1$ the lightest possible combined scalar top mass (m_s) consistent with the Higgs mass occurs at a value of $X_t \approx \sqrt{6}$ with $m_s \approx 500$ GeV, as can be seen in Figure 2.6. The hierarchy problem is solved by SUSY models as long as m_s remains on the 100 GeV - 1 TeV scale, above this value a little hierarchy problem is present.

¹⁰The vev is introduced in Chapter 2.1.6 as the ratio of the constant terms proportional to ϕ^2 and ϕ^4 in the Higgs potential.

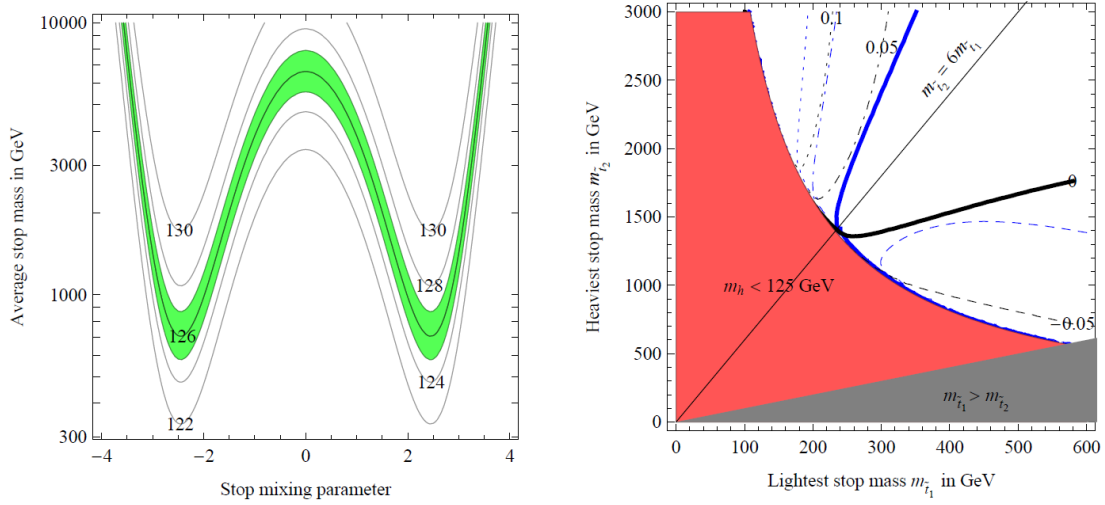


Fig. 2.6 (Left) The Higgs mass for large $\tan\beta = 20$ in the $X_t/m_s, m_s$ plane. Contours show the corresponding observed values for m_h . (Right) The white region is the range in which \tilde{t}_1 and \tilde{t}_2 are allowed. Taken from [3].

2.4.7 Summary of Supersymmetry

If supersymmetry exists in nature, a zoo of new particles may be waiting to be discovered. The MSSM has a gigantic phase-space for new particles to exist in. The core work performed in this thesis was on searches for experimental evidence of these particles by considering simplified models of the MSSM. Models considering sole production of a particular SUSY particle and models imposing the additional constraint of the naturalness argument of Section 2.4.6 on the pMSSM were primarily used. The importance of simplified models or constrained models is to provide scenarios that can be experimentally tested. More details on use of such models for searches for SUSY signals in Hadron Colliders is given in Section 3.3.4.

Even if the MSSM could be completely excluded, it does not cover the entire possible SUSY phase-space as seen in Figure 2.7. The Next-to-Minimal Supersymmetric Standard Model (for which the MSSM is $N=0$) adds N additional super-fields to the MSSM. This adds even more phase-space for SUSY to hide in.

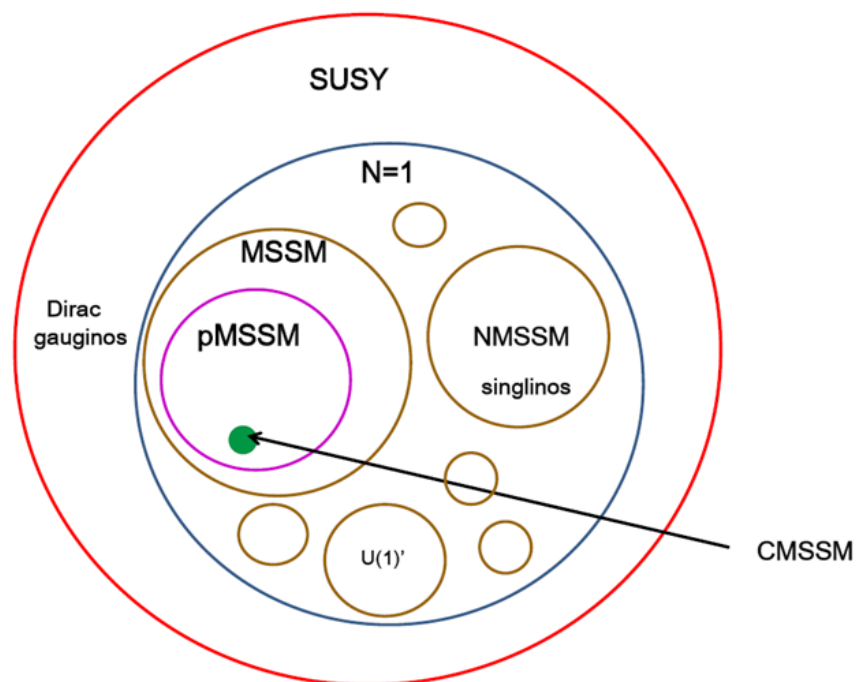


Fig. 2.7 A representation of the SUSY phase space. As with the pMSSM, the CMSSM (Constrained MSSM), is further contained within the phase-space of the MSSM. Taken from [4]

Chapter 3

Collider Physics

In the pursuit of new physics the majority of experimental information in high-energy regimes at the subatomic scale has historically been obtained from charged particle accelerators. They provide insight into the subatomic world via the creation of new bound states or interactions of particles, as well as the production of new particles. The first particle accelerators were constructed in the early 1930s [113], with the energy per particle beam of the order $\mathcal{O}(100)$ keV. The Large Hadron Collider (LHC), the most powerful accelerator on the planet, collides beams of 6.5 TeV and is designed to collide beams of 7 TeV. The LHC is effectively the worlds most powerful microscope probing distances shorter than 10^{-20} m ¹.

3.1 Colliders

Colliding two beams of particles instead of colliding one beam with a fixed target has been the preferred method in experimental particle physics over the last 40 years. The beams of particles are accelerated, focused and *bunched* with the use of super-conducting magnets. By focusing two beams to a point at the centre of a detector, the products of these head-on collisions can be analysed. Particles moving with a circular trajectory lose energy (synchrotron radiation) with each revolution given by [114]:

$$\lim_{v \rightarrow c} \Delta E = \frac{4\pi q^2}{3 R} \left(\frac{E}{mc^2} \right)^4$$

where E is the energy of the beam, m is the mass of the particle being accelerated, R is the radius of the collider. Hence the amount of energy lost by an electron beam in relation to the

¹From the de Broglie equation, $\lambda = h/p$, where h is Plank's constant, p is momentum and λ is the wavelength.

amount of energy lost by a proton beam of the same energy and collider radius is:

$$\frac{\Delta E_{\text{electron}}}{\Delta E_{\text{proton}}} = \left(\frac{m_{\text{proton}}}{m_{\text{electron}}} \right)^4 \approx 10^{13}$$

Proton accelerators provide much more energy per unit cost compared with electron colliders. In addition to this, they collide beams of tightly packed quarks and gluons rather than point-like particles.

3.1.1 Collision Rate

A disadvantage to colliders is that the collision rate is low compared with a fixed target experiment, the relationship between the rate (\mathcal{R}) and cross-section (σ) and other parameters of the beam is given by [115]:

$$\mathcal{R} = \sigma \cdot \mathcal{L} \tag{3.1}$$

$$\mathcal{L} = f_{\text{rev}} \cdot n_b \cdot \frac{N_1 N_2}{A} \tag{3.2}$$

The quantities associated with the luminosity (\mathcal{L}) are: f_{rev} , the frequency of revolution of bunches; n_b , the number of bunches per beam; N_1 and N_2 are the number of particles per bunch in beams 1 and 2; A is the area of the crossing of the beams². For colliders the luminosity is typically $\mathcal{L} \approx 10^{31} - 10^{34} \text{ cm}^{-2}\text{s}^{-1}$, whereas for a fixed target experiment $\mathcal{L} \approx 10^{37} \text{ cm}^{-2}\text{s}^{-1}$.

3.1.2 The Parton Distribution Function

Protons are made up of partons: gluons and quarks. A proton is typically thought to consist of two up quarks, one down quark, bound together by gluons. Quantum fluctuations result in c and s quarks as well as anti-quarks being present in the proton, the momentum fraction carried by a parton (x) depends on the energy scale (Q) - these are known as Parton Distribution Functions (PDF). Figure 3.1 shows two plots of the PDF at energies of $Q^2 = 10 \text{ GeV}^2$ (left) and $Q^2 = 10^4 \text{ GeV}^2$ (right), where the y-axis shows the probability that the labelled parton carries x amount of the proton energy³.

²The area of the beam is given in [115] and is related to the transverse beam emittance, the β function at the collision point and a factor relating to the crossing angle at the interaction point.

³It should be noted that at $Q^2 = 10 \text{ GeV}^2$ no third generation quarks are present in the proton, at $Q^2 = 10^4 \text{ GeV}^2$ a small fraction of b-quarks are present but no top quarks. This has implications for the production of 3rd generation scalar quarks as pair production via quark fusion or scattering is suppressed.

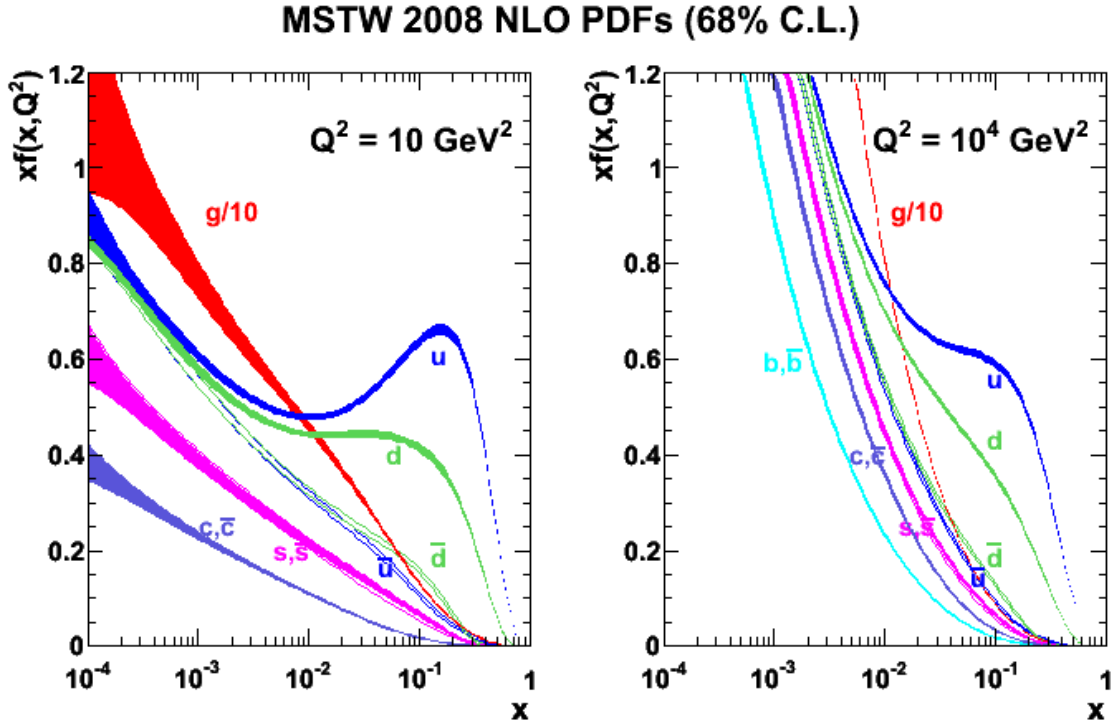


Fig. 3.1 MSTW (Martin-Stirling-Thorne-Watt) 2008 NLO parton distribution functions at 10 GeV^2 (left) and 10^4 GeV^2 (right). Plots taken from [5].

3.2 Particle Production at Colliders

Particles are produced in collisions at a rate dependent on the centre-of-mass energy and on the probability of interactions of the particle constituents. This is determined by the PDF. What is observed by particle physics detectors is either directly the particles produced in collisions or from the decays of produced particles.

The number of interactions produced in collisions is given by particle production cross-sections, denoted by σ in Equation 3.1. This production rate, as well as being determined by the PDF, is dependent on the coupling strength of all the SM particles. Figure 3.2 shows the production cross section for many different SM physics processes for a range of different centre-of-mass energies for electron-positron (left) and proton-proton (or proton-anti-proton) colliders (right).

In the case of $t\bar{t}$ production, the top row of Figure 3.3 shows four Feynman diagrams of production mechanisms possible at a large enough centre-of-mass energy some of which combine to give the total $\sigma_{t\bar{t}}$ depending on the type of collider: Figure 3.3a shows $t\bar{t}$ production from an electron-positron collision via a Z boson; Figure 3.3b shows $t\bar{t}$ production

3.2 Particle Production at Colliders

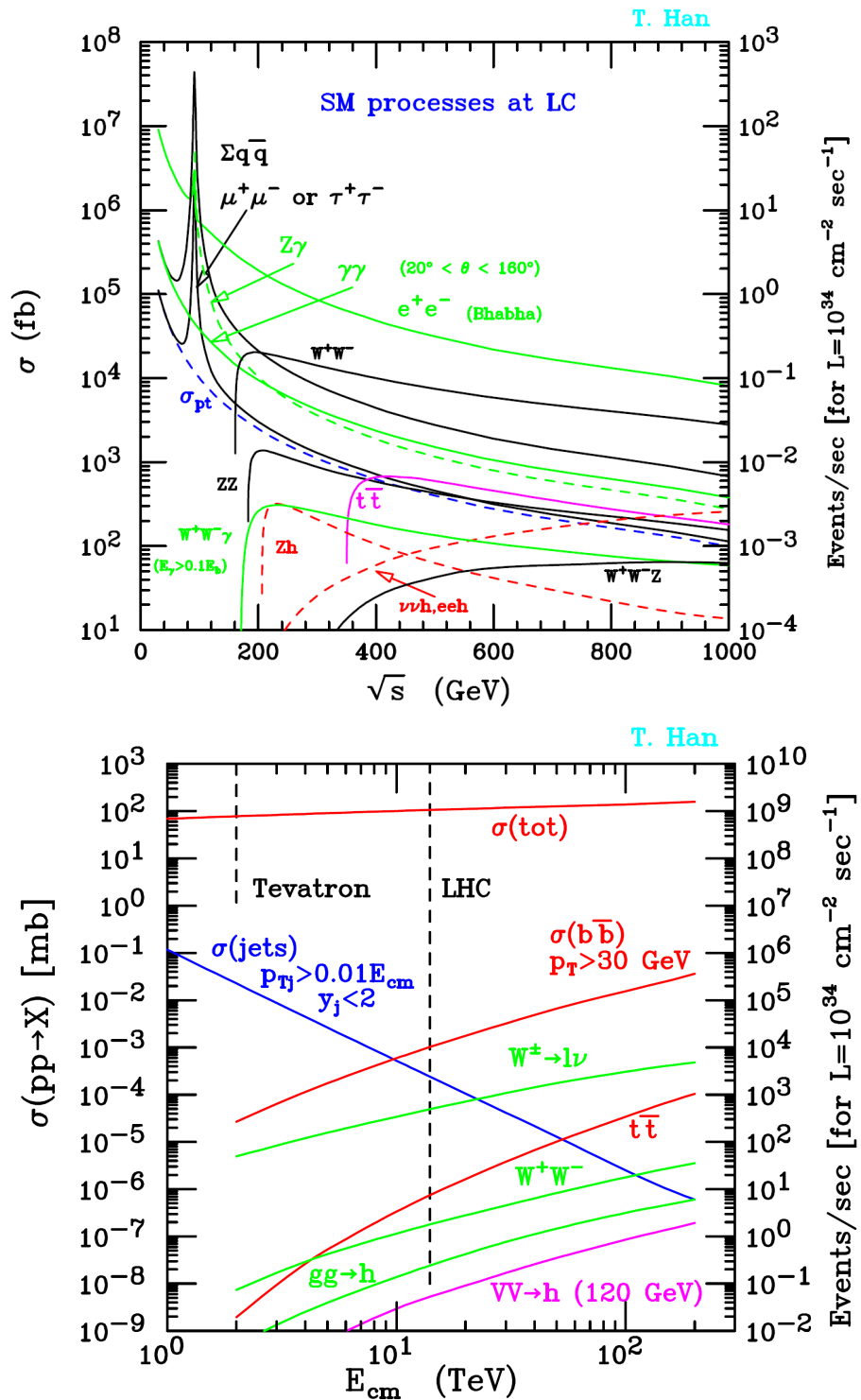


Fig. 3.2 Theoretical cross sections for many processes, plotted as a function of centre-of-mass energy for electron-positron colliders (left) and proton-proton (anti-proton) colliders (right) [6].

from a quark-anti-quark collision from two protons via the strong interaction of a gluon; Figures 3.3c and 3.3d shows two production diagrams from incoming gluons from within two protons via the strong nuclear force. The bottom row of Figure 3.3 shows different decays of top (anti-top) quarks. In the case of top quarks there is a $\approx 100\%$ branching ratio of decays to W bosons and b quarks [116].

There are many different types of particles that can be produced at colliders via the strong and electro-weak interactions, which subsequently decay via the SM forces into various final state particles with various branching ratios. The rate at which these particles are produced and the rate at which the final state particles are observed is dependent on the free-parameters of the SM Lagrangian (Equation 2.1), which for the most part are well understood and measured.

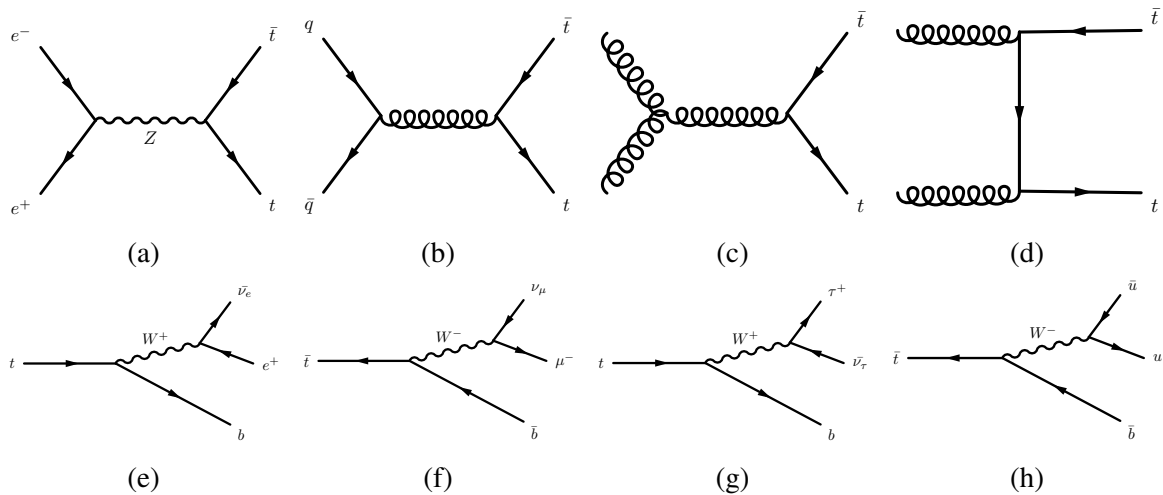


Fig. 3.3 Examples of Feynman diagrams for pair production of $t\bar{t}$ (top-row) and top quark decay (bottoms row).

3.2.1 Initial and Final State Radiation

The concept of Initial State Radiation (ISR) and Final State Radiation (FSR) is particularly important when attempting to simulate known SM and potential BSM processes produced in colliders. ISR occurs when an incoming parton radiates a particle before the main interaction. FSR occurs when an outgoing parton radiates a particle after the main interaction. An example of ISR of a gluon and FSR of a gluon is shown in Figure 3.4a and Figure 3.4b respectively.

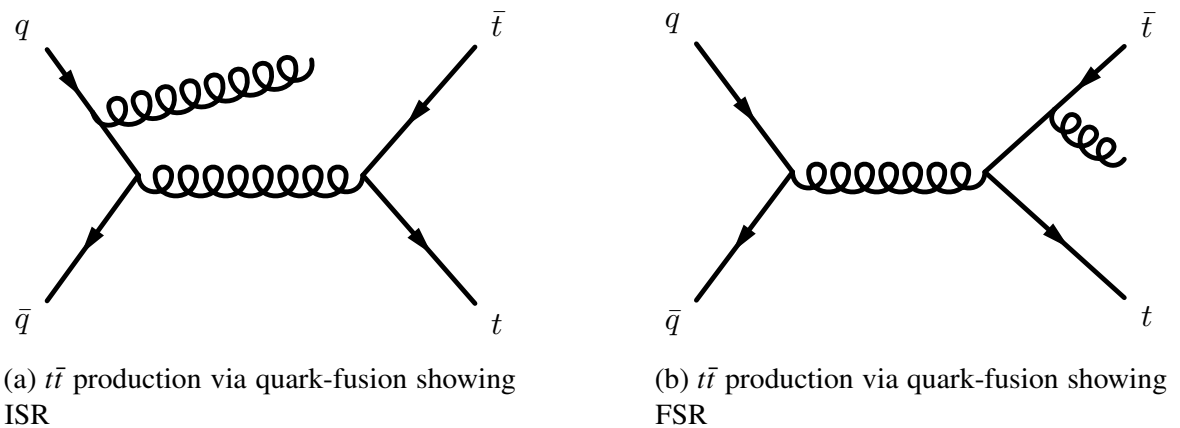


Fig. 3.4 Examples of Feynman diagrams for pair production of $t\bar{t}$ showing (a) ISR and (b) FSR.

3.2.2 Pileup

Pileup is defined as the overlap of multiple events which can be either *in-time pileup* or *out-of-time pileup*. The collision rate of Equation 3.1 is dependent on the number of bunches per beam n_b and the number of protons per beam $N_{1,2}$. Out-of-time pileup is increased when n_b is increased or when the time between the bunches is decreased. A detector has a specific *operation cycle time* which is the time it takes to read-out the collision of two bunches (bunch crossing), if the readout between bunch crossings is not quick enough events can overlap. In-time pileup is when several pp interactions occur per bunch crossing, leading to large amount of mostly soft hadronic activity in an event. Throughout this thesis the term *pileup* refers to in-time pileup and is quantified by $\langle\mu\rangle$ - the averaged number of interactions per bunch crossing.

3.2.3 Structure of an Event

Figure 3.5 shows a pictorial representation of a $t\bar{t}h$ event produced by a Monte-Carlo generator - *Sherpa1.1* [7, 7] (see Chapter 4.8.2 for more detail). A hard interaction of two partons (curly blue) from two colliding protons is indicated by the large dark red dot, the two gluons producing the hard interaction undergo ISR. The hard interaction itself produces two top and a Higgs, FSR also occurs in the hard interaction indicated by the curly red line emitted from the large red dot. The three smaller red dots indicate the decays of the tops and the Higgs producing a shower of particles. The light green ellipses are final-state partons which hadronise, with the darker green dots indicating hadronic decays in the detector. Leptons and photons are represented in yellow. The figure also shows the presence of an *underlying event*

(UE) from the same pp interaction as a purple ellipse, this too produces a softer shower of particles in the detector. The remaining initial partons of the pp collision (beam remnants) are shown in light blue.

What is observed on a detector level is the collection of hadronic fragments (small dark green dots), the leptons (yellow lines) and photons (wave like yellow lines). The goal of a physics analysis is to attempt to observe these hard interactions, based on the final state observation.

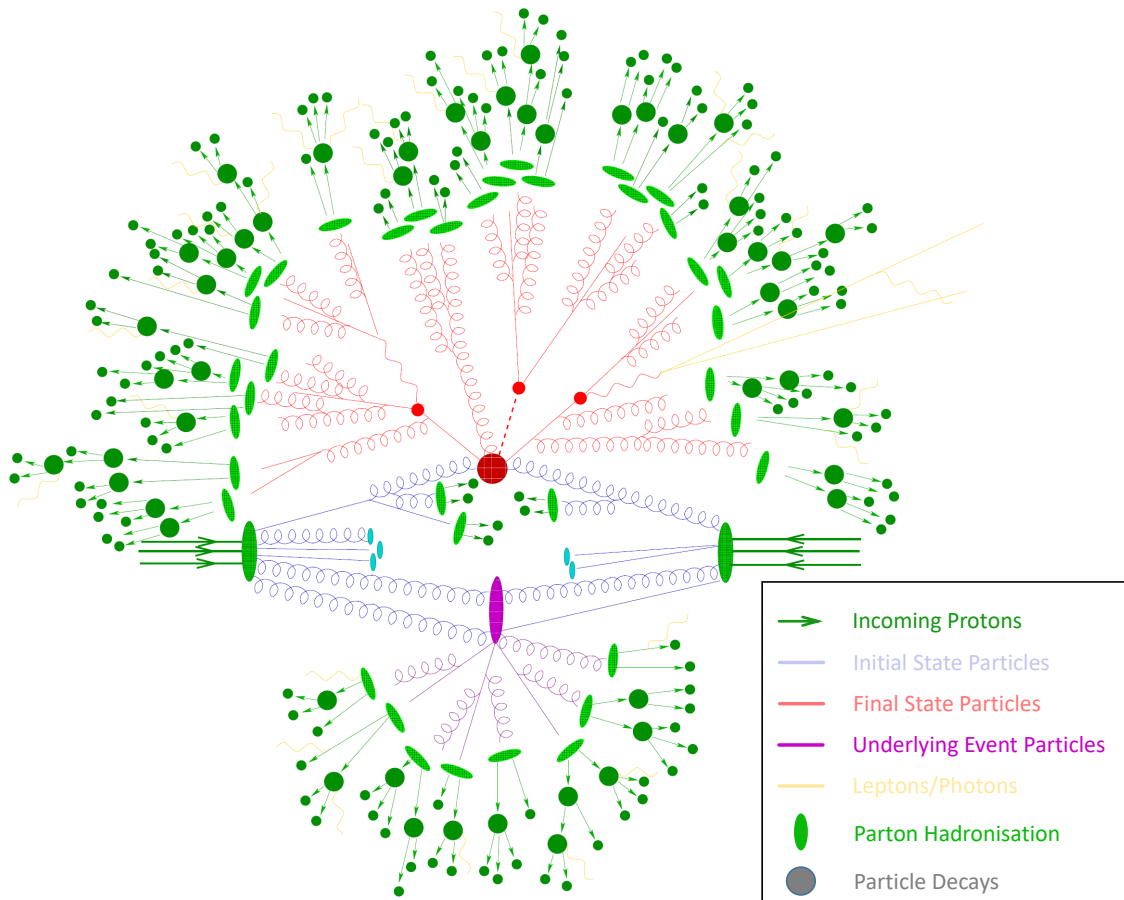


Fig. 3.5 Structure of a $t\bar{t}H$ (top-quark pair production in association with a Higgs boson) event at generator level, produced by Sherpa 1.1[7], taken from [8].

3.2.4 Final State Observation

No free quark has ever been observed, due to the nature of the strong nuclear force at smaller distances, as discussed in Chapter 2.1.4.1. When quarks are produced in collisions at the centre of detectors they shower hadronically, forming hadronic “jets” of particles, as seen

in Figure 3.5. The detectors measure the deposition of energy and the momentum of these particle jets; it is possible to then tag if these jets arise from c , b or t quarks. The detectors (at the LHC) are generally capable of detecting electrons, muons and photons. τ aus decay very quickly⁴ either hadronically as jets or leptonically into electrons or muons and neutrinos. Importantly neutrinos and any other undetectable particles, such as neutralinos, that are produced do not interact with the detectors and the pass through them. The presence of invisible particles can be observed with missing transverse energy:

$$E_T^{miss} = \sum_{\text{invisible}} p_T = - \sum_{\text{visible}} p_T \quad (3.3)$$

Typical hadron collider detectors (ATLAS and CMS at the LHC) are cylindrical in design. There is no incoming momentum in the transverse plane of the detectors, therefore the sum of all momentum in the transverse plane should be equal to zero. If a particle escapes detection this is manifested in the E_T^{miss} . Chapter 5.1 will provide more detail on these observable objects and how they are reconstructed.

3.3 Supersymmetry at Hadron Colliders

SUSY can be experimentally searched for either indirectly or directly. Indirect searches look for processes that are rare or even forbidden in the SM with contributions for sparticle loops, for example: muon decays to electrons via photons $\mu \rightarrow e\gamma$ [117]; R_b - the fraction of hadronic Z decays with $b\bar{b}$ pairs [118]. Direct detection of sparticles, measurements of their interactions and quantum numbers is the subject of this thesis.

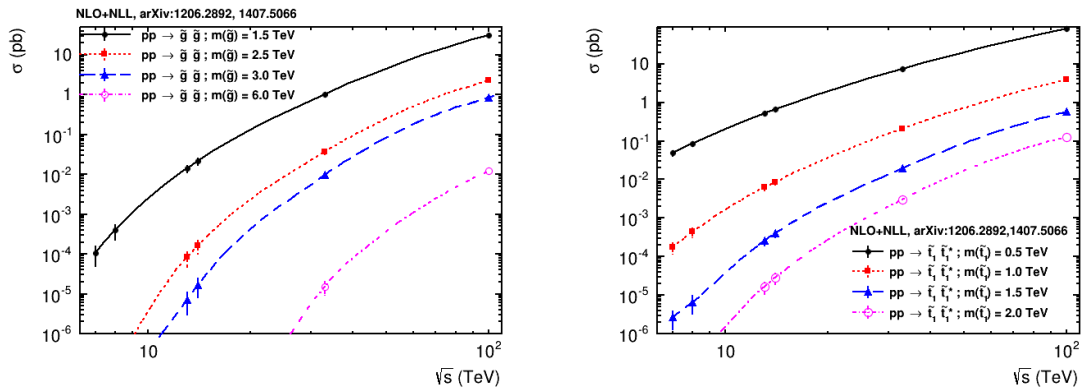


Fig. 3.6 Gluino (left) and scalar top (right) production cross sections in pp collisions at $\sqrt{s} = 13, 14, 33$ and 100 TeV [9]

⁴A τ has a mean lifetime of 2.906×10^{-13} seconds [31].

3.3.1 Production Mechanisms

In high-energy hadron colliders the production of SUSY particles is dominated by the strong nuclear force (QCD). Figure 3.6 shows the production cross section of pair produced gluinos and scalar top quarks as a function of centre-of-mass energy at a pp -collider. In scenarios where R-parity is conserved, the gluino pair production ($\tilde{g}\tilde{g}$), gluino-scalar-quark $\tilde{g}\tilde{q}$, scalar quark pair production $\tilde{q}\tilde{q}$ are by far the most dominant channels. Figure 3.7a and Figure 3.7b show Feynman diagrams that give the most dominant contributions to gluino and scalar quark production at hadron colliders. The cross section for pair production of third generation scalar quarks (\tilde{t}_1, \tilde{b}_1) is a fraction $10^{-3} - 10^{-1}$ of that of the first two generations of scalar quarks (for the same mass and centre of mass energy).

This is due to the fact that the parton distribution functions (PDFs) of the LHC and other hadron colliders do not contain any top quarks and negligible amounts of bottom quarks. Therefore the production of 3rd generation scalar quarks via the diagrams of the bottom row of Figure 3.7a and the middle and bottom rows of Figure 3.7b do not occur or are negligible. It is however theoretically well motivated that the first and second generation scalar quarks may be heavier than the third generation scalar quarks⁵, and therefore too heavy to be produced at the LHC.

3.3.2 Supersymmetry in Final States

Once SUSY particles have been produced they can decay leaving a signature of interest. Figure 3.8 shows two example of pair production of gluinos (left) and pair production of scalar tops (right) in a scenario where R-parity is conserved⁶. The gluino scenario leaves a final state with four b-quarks and two neutralinos, the second example results in a final state containing two b-quarks, a lepton-anti-neutrino pair and two quarks from a W decay. There are many more scenarios with a huge range of final states that has been explored by hadron colliders.

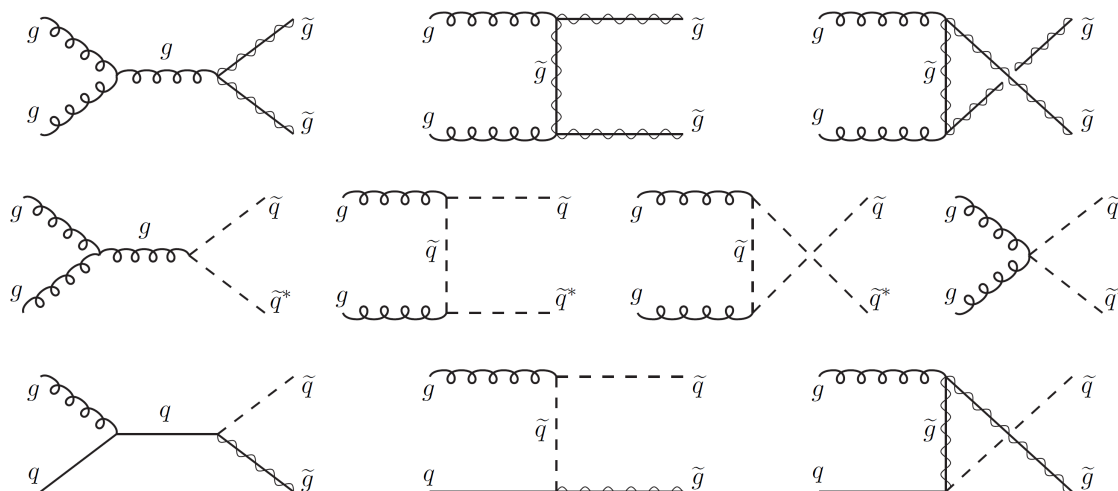
In the gluino pair-production example, the final state observed on the detector level is one containing four b -tagged jets and a large amount of E_T^{miss} , this is the signature for cases where the particles masses are:

$$m(\tilde{g}) > m(\tilde{b}_1) + m(b) > m(\tilde{\chi}_1^0) + m(b)$$

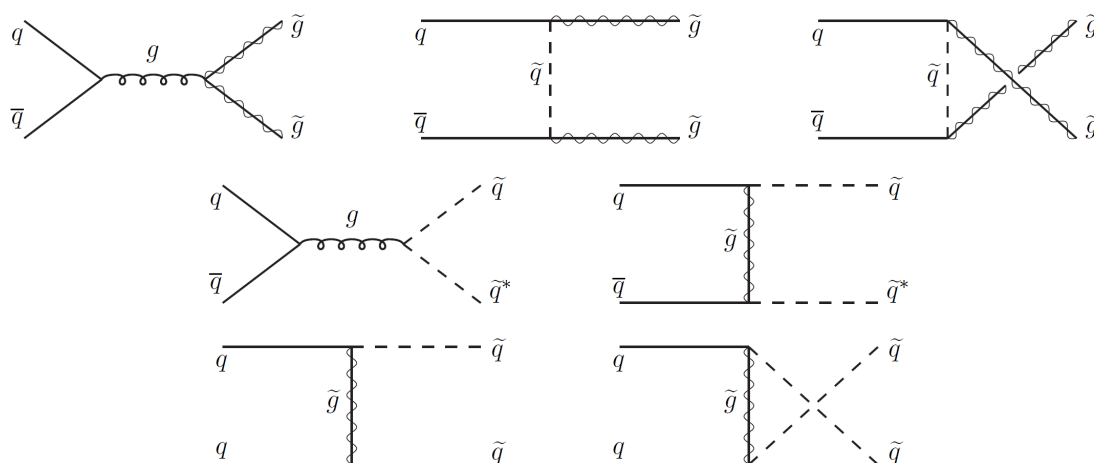
⁵due to their strong yukawa couplings to their SM partner

⁶If however, R-parity is not conserved, final states may not contain SUSY particles.

Fig. 3.7 QCD Feynman diagrams for pair production of gluinos and squarks



(a) Feynman diagrams for gluino and scalar quark pair production, the most dominant 1st order diagrams from gluon and gluon-quark fusion.



(b) Feynman diagrams for gluino and scalar quark pair production, the most dominant 1st order diagrams from quark-anti-quark annihilation and quark-quark scattering. The top row shows gluino production via quark-anti-quark fusion, the middle row shows production of scalar quarks via quark-anti-quark fusion and the bottom row shows scalar quark pair production via quark-quark scattering.

The same final state can arise from many different SM processes, the most dominant being $t\bar{t}$ production in association with a gluon (ISR/FSR, as seen in Figures 3.4a, 3.4b) which splits to give two b -tagged jets. This background, amongst others, can be reduced with the application of kinematic cuts. Figure 3.9 shows the signal in the case of gluino pair-production and another dominant SM background (Z+jets) which may lead to the same

experimental signature. In the case of the production of Z+jets, E_T^{miss} can arise from the decay of the Z boson to neutrinos.

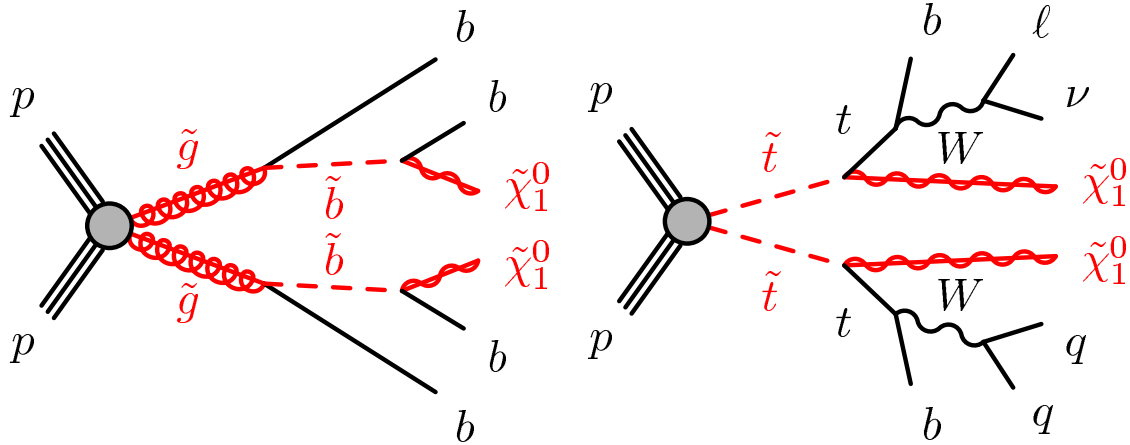


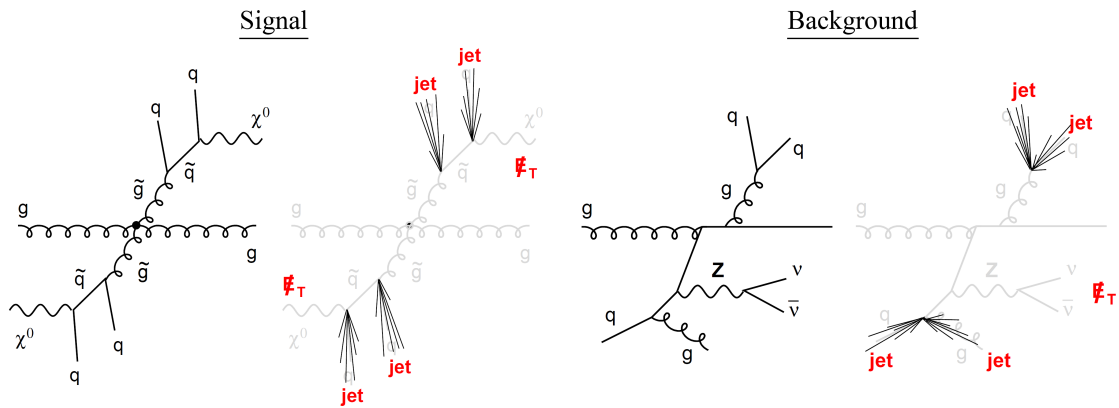
Fig. 3.8 Production diagrams showing two possible decay chains after sparticles have been pair produced. The left diagram shows pair production of gluinos decaying to scalar b-quarks (\tilde{b}_1) and b-quarks which subsequently decay to neutralinos ($\tilde{\chi}_1^0$) and b-quarks ($pp \rightarrow \tilde{g}\tilde{g} \rightarrow \tilde{b}\tilde{b} \rightarrow b\tilde{b} \rightarrow bbb\tilde{b} \rightarrow bbbb\tilde{\chi}_1^0\tilde{\chi}_1^0$). The right diagram shows pair production of scalar top quarks decaying to neutralinos and top quarks, which subsequently decay to W bosons either hadronically or leptonically.

3.3.3 Simplified Models

Figure 3.8 shows two example models with their corresponding final states. Experimental searches for SUSY at colliders target specific models like these, by assuming the initial SUSY particle, e.g. the scalar top, is the only SUSY particle directly produced by a hadron collider. The decay of the initial SUSY particle is assumed to follow a specific decay. These are referred to as “simplified models”.

Figure 3.10a shows a complex pMSSM model where many SUSY particles have masses $\mathcal{O}(1)$ TeV. Two simplified model scenarios are also shown for scalar top (Figure 3.10b) and scalar bottom pair-production (Figure 3.10c). The figures show the mass spectrum of the sparticles considered in the different models. The scenario in Figure 3.10b is one in which the lightest scalar top, lightest chargino and lightest neutralino are the only supersymmetric particles in existence. In this scenario the scalar top decays with an equal branching ratio to the neutralino and the chargino. The chargino state subsequently decays with a 100% branching ratio to the neutralino and a W boson. Figure 3.10c is a scenario where the lightest scalar bottom and lightest neutralino are the only two supersymmetric particles in existence. The scalar bottom decays exclusively into a b-quark and the lightest neutralino.

Fig. 3.9 Left: gluino pair production and its subsequent decay to scalar quarks and neutralinos; the experimental signature of multiple jets and E_T^{miss} is also shown. Right: the same signature is mimicked by the production of a Z boson in association with jets[10].



Searches for third generation scalar particles decaying into b-quarks are targeted in this thesis. As discussed in Chapter 2.4, in the majority of MSSM scenarios, the third generation scalar quarks are expected to mix to yield mass-degenerate states, which may be at a mass scale reachable by the LHC. In these scenarios the scalar particles are expected to be lighter than the gluinos, first- and second-generation scalar quarks.

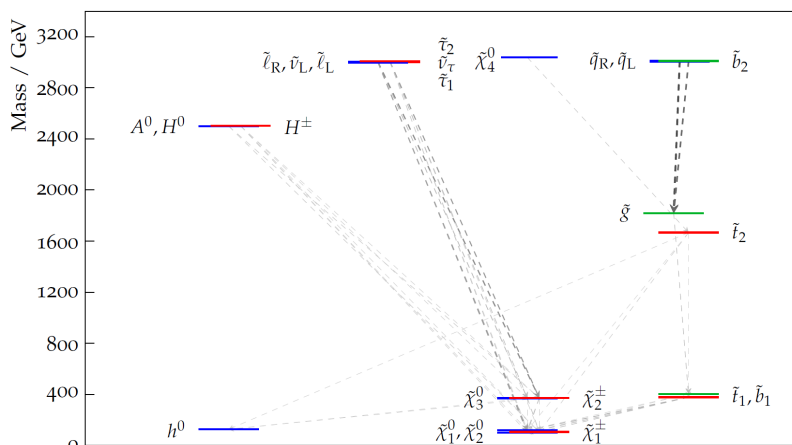
3.3.4 Searches for Supersymmetry at the LHC

Over the course of several years of operation, large datasets corresponding to $\mathcal{O}(20) \text{ fb}^{-1}$ and $\mathcal{O}(3) \text{ fb}^{-1}$ were collected at 8 and 13 TeV by both the ATLAS and CMS experiments at the LHC⁷. No significant deviations from the SM backgrounds were observed in searches for SUSY, this allowed the *exclusion limit* on various SUSY particles masses set by previous experiments at LEP [119–122] and the Tevatron [123–126] to be further improved. Figure 3.11 shows a summary of all direct production ATLAS searches for SUSY from Run-I and Run-II of the LHC, the mass limits on particular sparticles in the context of simplified model. The plot is split into distinct regions, from the top down: inclusive searches of pair produced gluinos and 1st, 2nd generation squarks; gluino pair production with decays mediated by third generation sparticles; 3rd generation direct pair production; electro-weak pair production, such as $pp \rightarrow \tilde{\chi}_1^+ \tilde{\chi}_1^-$; long-lived particles; *R*-parity violating (RPV) scenarios and other - a 2nd generation pair produced scalar charm search.

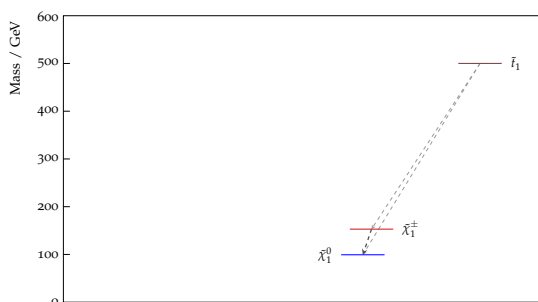
Likewise Figure 3.12 shows the limits obtained by the CMS experiment [127]. These are split into sections, from the top down: gluino pair production; second and third generation

⁷For more information on the datasets delivered by the LHC, see Chapter 4.8.1

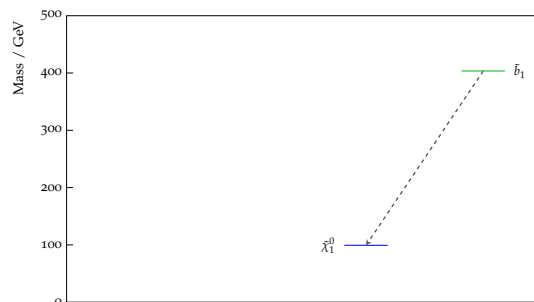
3.3 Supersymmetry at Hadron Colliders



(a) A complex model, taken from a pMSSM scenario in which a Naturalness argument has been applied.



(b) A simplified model scenario for the pair production of scalar top quarks.



(c) A simplified model scenario for the pair production of scalar bottom quarks.

Fig. 3.10 Pictorial representations of different SUSY models showing the masses of the sparticles and their decays. The arrows indicate the decay paths of the sparticles with the thickness of the arrow dependent on the branching ratio of the decay.

squark pair production; scalar top pair production; scalar bottom pair production; electroweak gaugino pair production; scalar lepton pair production and RPV scenarios.

The reader should be reminded of the context of these limits. The pMSSM is not representative of the full MSSM or the entire SUSY-phase space, similarly simplified models are even less so. If a particle in a simplified model has been excluded up to a certain mass, this does not necessarily mean that these particles cannot exist at energies lower than this.

Figure 3.13 shows the mass limits in the context of the pMSSM scan performed by ATLAS at the end of Run-I of the LHC, the z axis indicates the fraction of models excluded that predict certain sparticle masses.

ATLAS SUSY Searches* - 95% CL Lower Limits

Status: March 2016

ATLAS Preliminary
 $\sqrt{s} = 7, 8, 13 \text{ TeV}$

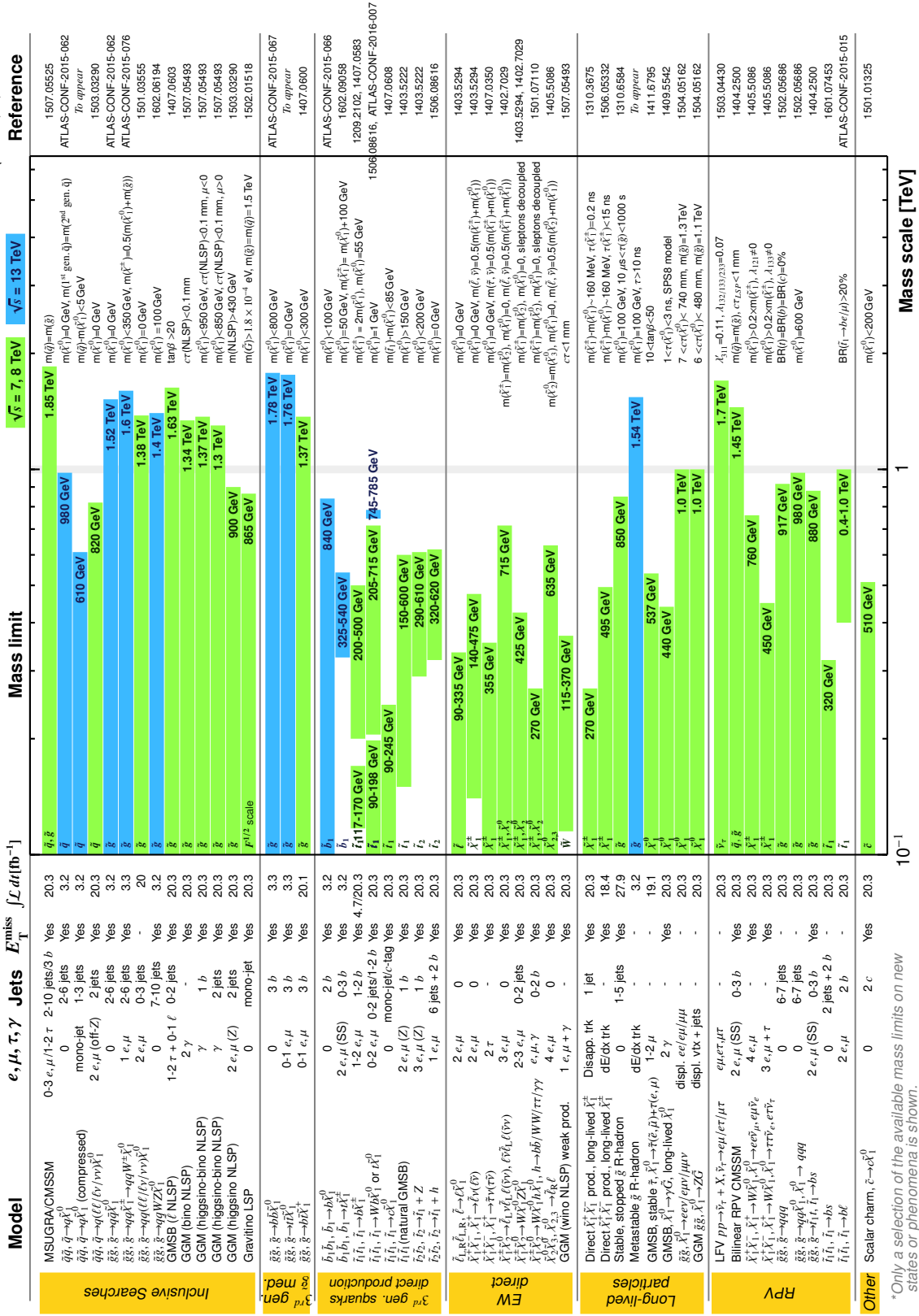


Fig. 3.11 A summary of all direct ATLAS searches for SUSY as of March 2016 [11].

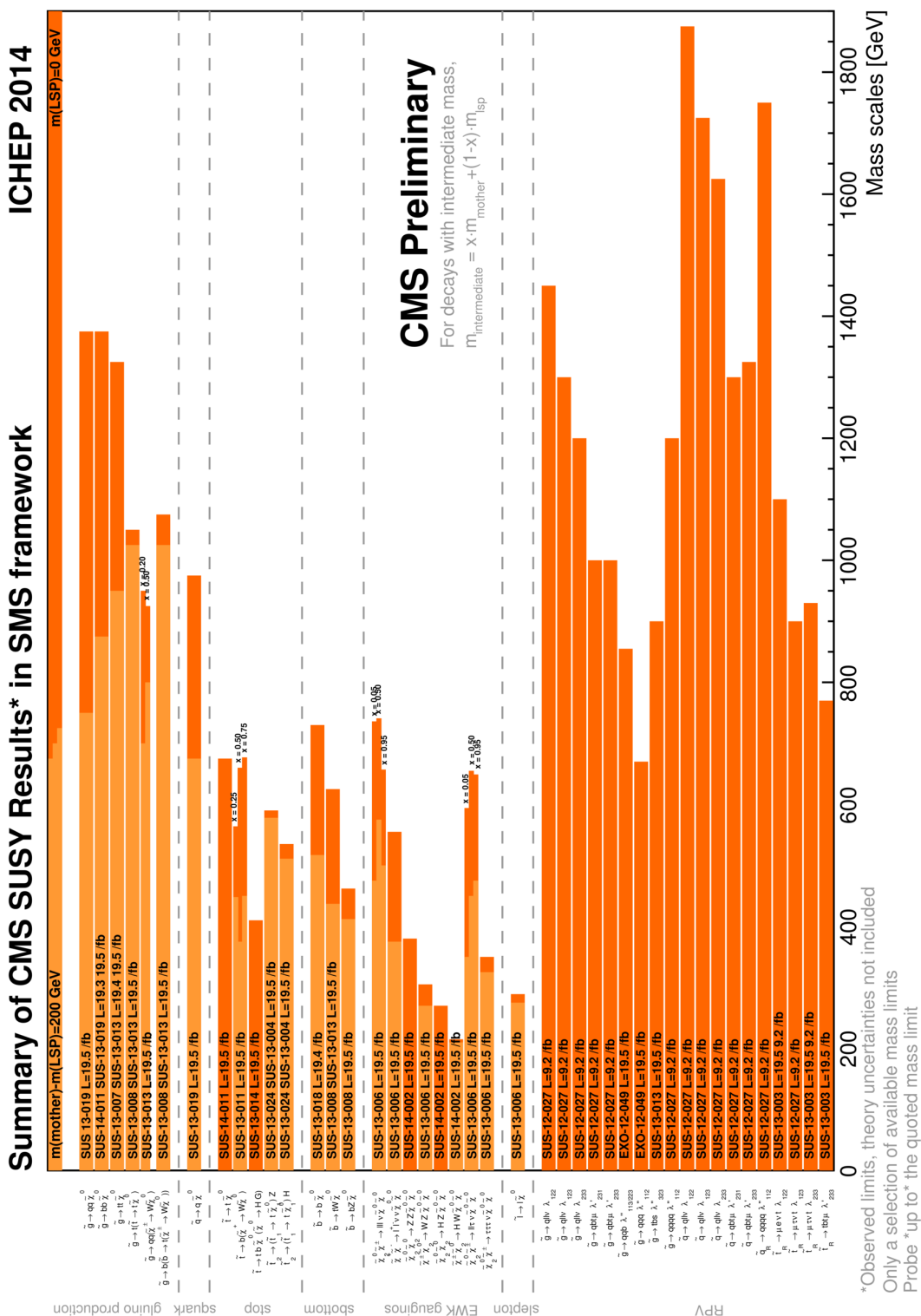


Fig. 3.12 Summary of CMS searches for SUSY as of the ICHEP 2014 conference [12].

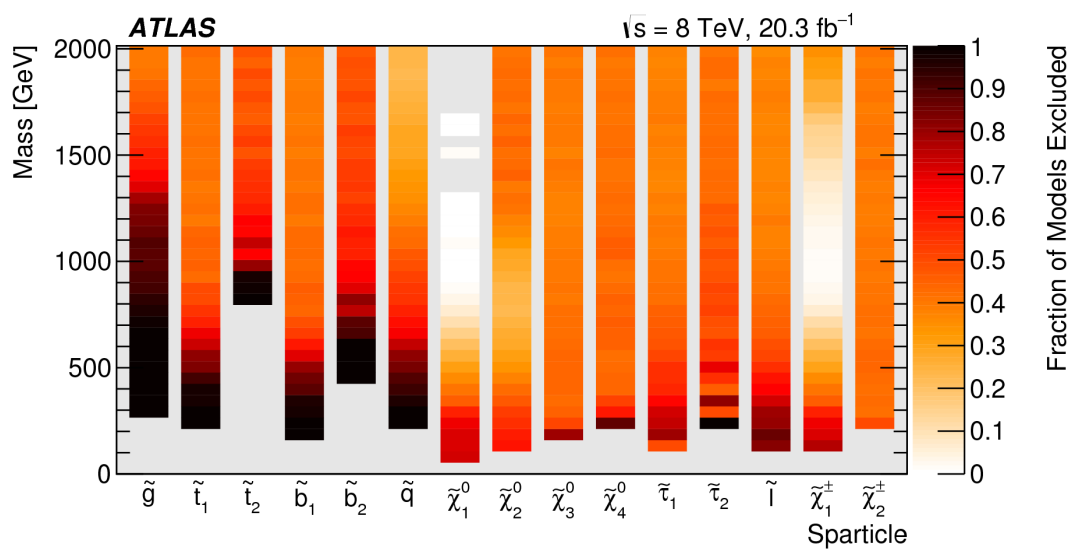


Fig. 3.13 A summary of the limits set on all sparticle masses in the context of the pMSSM, set by analyses contributing towards the Run-I pMSSM summary paper [11].

Chapter 4

The LHC and The ATLAS Detector

As of 2016, the largest hadron collider in the world is situated at CERN (Conseil Européen pour la Recherche Nucléaire), Geneva, Switzerland. It is named the Large Hadron Collider (LHC) and is designed to accelerate protons up to $\sqrt{s} = 14$ TeV. The following chapter details the LHC and the ATLAS detector, which thanks to the work of thousands of physicists and engineers over several decades, made this thesis possible.

With the ability to collide particles at ever increasing energies comes the need for detectors to accurately measure the products of energetic collisions without suffering greatly from radiation damage. The LHC has four main detectors for this purpose: ATLAS, CMS, LHCb and ALICE. This chapter will give a brief description of the LHC and a detailed description of the ATLAS detector and its sub-detectors.

4.1 The Large Hadron Collider (LHC)

Figure 4.1 shows a schematic diagram of the LHC complex [128], it is composed of many different sections. The main ring of the LHC is 27 km in diameter, it has been able to accelerate two proton beams up to 6.5 TeV and is designed to be able to accelerate the beams to 7 TeV. Run-II of the LHC started in 2015 with a centre-of-mass energy of $\sqrt{s} = 13$ TeV and collided pp collisions until the end of October 2016.

In the case of pp collisions, protons are first taken from a hydrogen bottle, stripped of their electrons with the application of an electric field before being injected into a linear accelerator (LINAC) [129] and accelerated to 50 MeV. The LINAC feeds protons into the Proton Synchrotron Booster (PSB) [130], reaching 1.4 GeV of energy. From there, they are passed to the Proton Synchrotron (PS) [131] increasing the energy to 26 GeV. Next the single

beam Super Proton Synchrotron (SPS) [132] accelerates the beam up to ≈ 450 GeV¹. Finally the SPS injects the proton beam into two different beam pipes along the LHC in opposite directions.

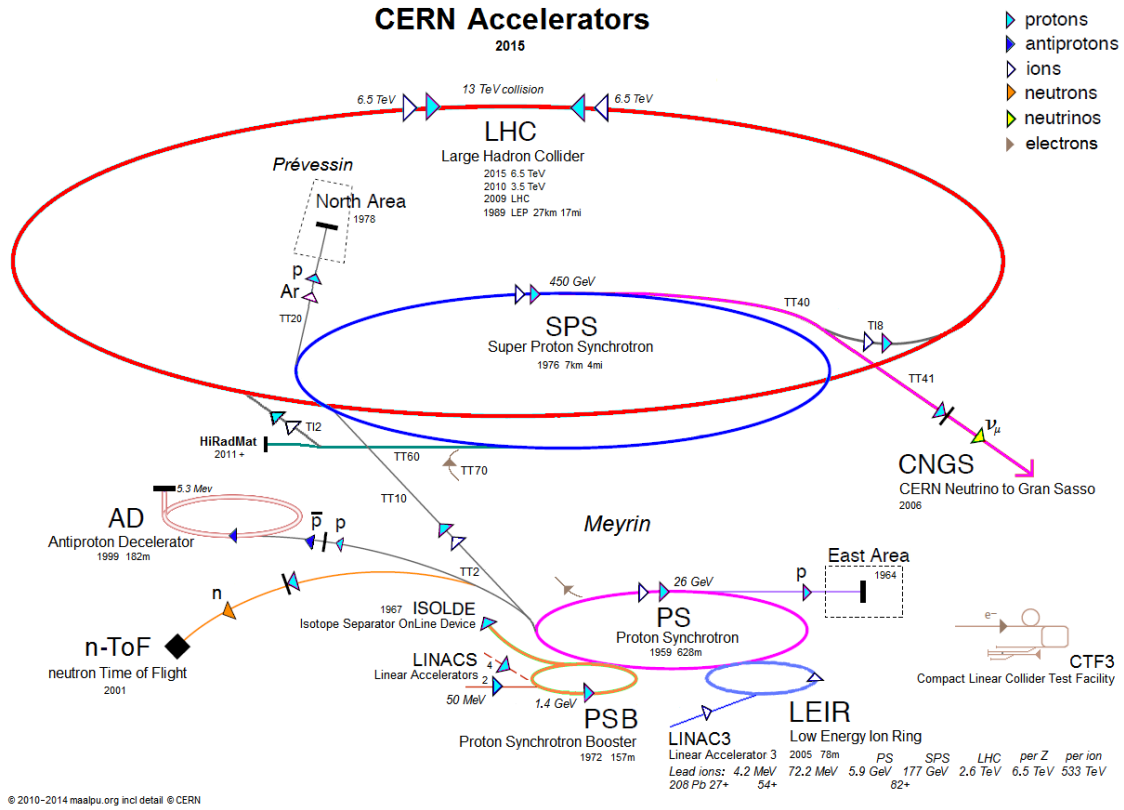


Fig. 4.1 Schematic diagram of the LHC site at CERN, Geneva [13].

4.2 The ATLAS Detector

In terms of physical size, A Toroidal Large Apparatus (ATLAS) is one of the largest experimental apparatus in the world. ATLAS and Compact Muon Solenoid (CMS) are designed as all purpose detectors capable of probing the frontiers of modern particle physics. The discovery of a scalar particle consistent with the Higgs boson in 2012 [80, 81] was one of the main goals of ATLAS and CMS. Many world leading measurements of SM processes have been made, as well as extensive searches for physics beyond the SM such as Z, W prime (Z', W') bosons [134] and searches for miniature black-holes [11].

¹The SPS was built in 1976 and originally its beams were used in the discovery of the W and Z bosons by the UA1 and UA2 experiments [133]

4.2.1 Overview of ATLAS

As with the majority of precision experiments based at colliders, ATLAS is a cylindrical shaped detector with onion like layers of sub-detectors. Figure 4.2 shows a diagram of ATLAS, the beam pipe runs horizontally through the middle of the experiment, the interaction point at the centre of the detector is surrounded by the inner detector (ID). The ID consists of three sub-detectors: Pixel Detector (Pixels), SemiConductor Tracker (SCT) and the Transition Radiation Tracker (TRT); all of which are used in the measurements of particles exiting the beam pipe. Outside of the ID, a solenoid magnet is used in the bending of charged particles in the inner parts of the detector. The electromagnetic calorimeter is the next layer, followed by the hadronic calorimeters, used for measuring electrons, photons and hadrons. Further out is the toroid magnet, this is used to bend charged particles in the muon chambers of ATLAS. Finally the Muon Spectrometer is the furthest layer from the centre of the detector, used for measuring muons. As can be also seen in Figure 4.2, ATLAS is not uniformly cylindrical, since the collision point is at the centre of the detector there are barrel and endcap sections of the inner detector, calorimeters, muon system and the magnets. The design enables the high precision reconstruction of particles with small angles to the beam pipe.

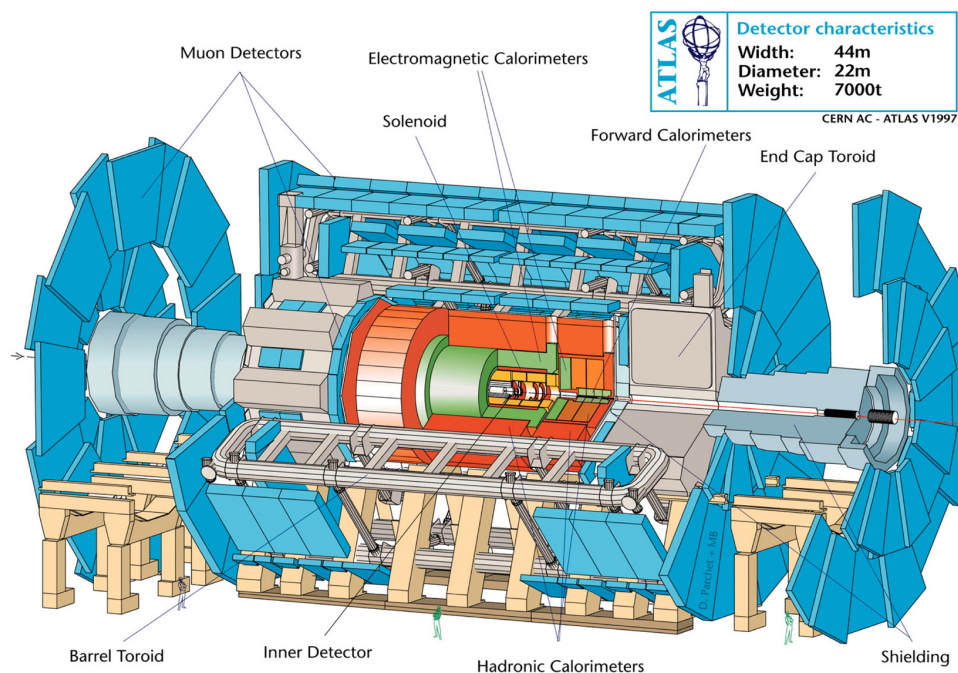


Fig. 4.2 Diagram of the ATLAS detector taken from [14].

4.2.2 ATLAS Coordinate System

As discussed in Chapter 3.2.4, the partons from the two beams collide at $z \approx 0$, where z is the direction along the beam axis from the centre of the detector, the top-right panel of Figure 4.3 shows the z - y plane where the beam pipe passes through the middle of the detector. The x -axis points in direction towards the centre of the LHC ring, the left panel of Figure 4.3 shows a transverse slice of the detector in the xy plane. Since ATLAS is cylindrical in shape, polar coordinates are typically used: where ϕ is the angle made in between the x - y coordinates and θ is the angle made between the z and y coordinates. Partons from two protons from colliding beams carry a fraction x_1 and x_2 of the energy of each proton, therefore their energy is generally not equal ($E_1 \neq E_2$), this boosts the centre-of-mass frame of the collision in the z -direction. The quantity of *pseudo-rapidity* is defined as:

$$\eta = -\ln \tan \left(\frac{\theta}{2} \right) \quad (4.1)$$

The difference $\Delta\eta$ between two points in the detector volume is therefore an invariant quantity with Lorentz boosts and is essential in the reconstruction of physics objects². Figure 4.3 is an event display for an event in which a pp collision has caused two energetic showers of particles in the ATLAS detector, clearly seen in the left and top-right panels. The bottom-right panel shows these two showers in the $\eta - \phi$ plane as a function of the transverse energy (E_T) deposits. See Chapter 5.1 for a complete overview of the reconstruction of physics objects.

4.3 Magnet System

Figure 4.4 shows the ATLAS magnet system. The inner solenoid is situated outside of the inner detector and provides a field of strength $2T$ - allowing for the measurement of momentum and charged particle identification by the ID. Encompassing the muon spectrometer, the toroid magnet is composed of 8 barrel and 2×8 endcap coil components. The toroid barrel field strength is approximately $0.5T$ and the endcap toroids are $\approx 1T$. As with the inner solenoid, the toroid magnet bends charged particles (muons) in order to measure their momentum.

²The quantity of rapidity y is sometimes used, defined as $y = \frac{1}{2} \ln \left(\frac{E+p_z}{E-p_z} \right)$; for $m \ll |\vec{p}|$, $\eta = y$.

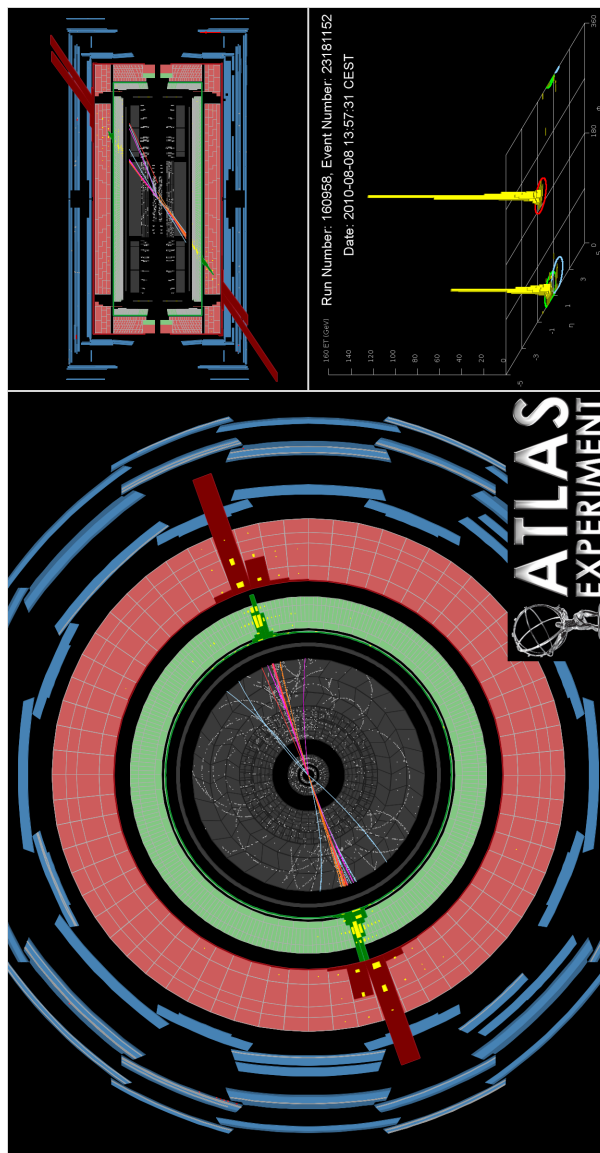


Fig. 4.3 Example of an ATLAS event display for a singular typical di-jet data event recorded in 2010. The ID is shown in light grey, the electromagnetic calorimeter is shown in green, the hadronic calorimeter is shown in red and the muon spectrometer is shown in blue. The left panel and top-right panel show a view of the detector in the $x - y$ plane and $z - y$ plane respectively. These displays show various tracks (in the ID) and various energy deposits in the calorimeters. The bottom-right panel shows the transverse energy (E_T) energy deposits as a function of η and ϕ , coloured lines show circles of radii 0.4 in the $\eta - \phi$ plane, demonstrating the reconstruction of energetic showers either as electromagnetic objects or jets, see Sections 5.1.4, 5.1.2.

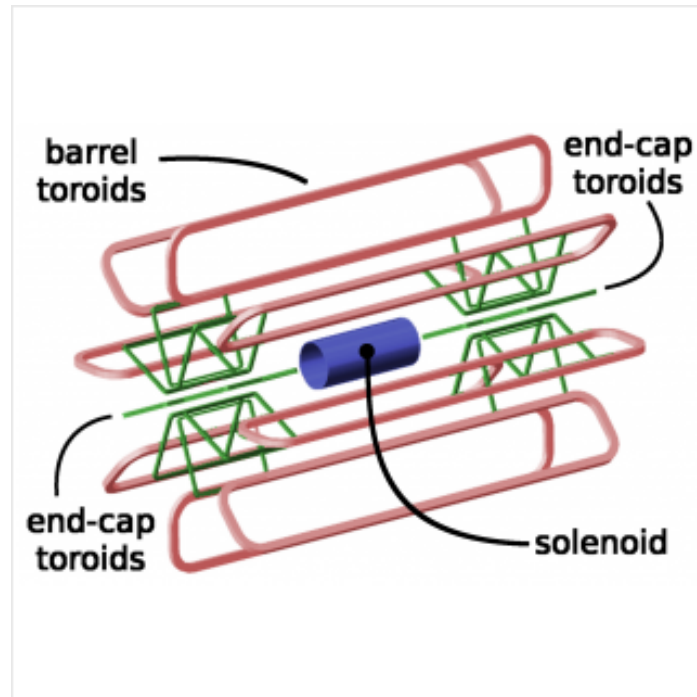


Fig. 4.4 ATLAS magnetic system: the inner detector is surrounded by a solenoid magnet; a toroid magnet system encompasses the muon spectrometer [15].

4.4 Inner Detector

A diagram of the ID is shown in Figure 4.7 with an indication of the distances from the beam pipe to each subsystem. The diagram includes the Insertable B-Layer (IBL) which was inserted at a radial distance of 33.25 mm from the beam pipe during the first shut-down of the LHC between Run-I and Run-II. The inclusion of the IBL greatly improved the identification of jets originating from B-hadrons (b-tagging), resulting in large sensitivity gains for searches for SUSY in final states containing b-tagged jets [135].

Figure 4.5 shows the radiation length³ (X_0) of the various components of the inner detector. ATLAS is designed in such a way to vary X_0 in the most suitable way for particle identification. A low value of X_0 in the ID is critical for the energy determination of particles in the outer layers of ATLAS.

The various ATLAS tracking systems, which cover the region $\eta < 2.5$, are designed to have a p_T (transverse momentum) resolution of tracks (see Section 5.1.1) given by $\sigma(p_T) = 0.05\% p_T \oplus 1\%$ [16].

³ X_0 is the characteristic radiation length (gcm^{-2}) of a material defined by its atomic and nucleon numbers (A,Z). An electron has a fraction $1/E$ of its energy left after traveling through X_0 .

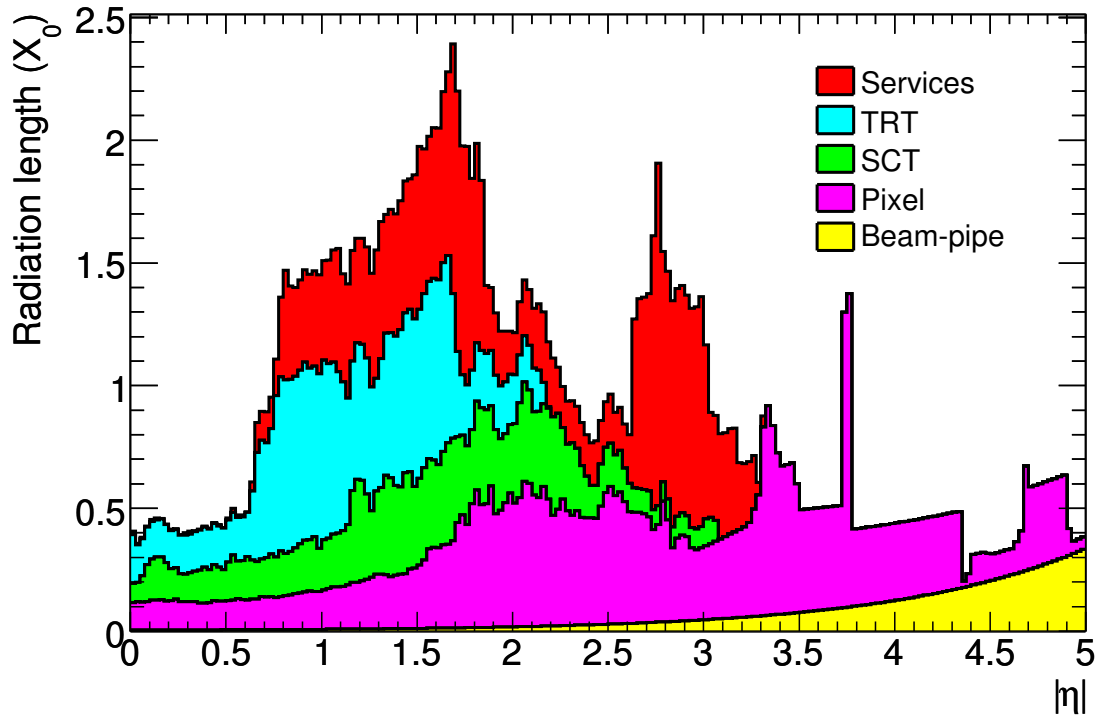


Fig. 4.5 Radiation lengths (X_0) in the Inner Detector (ID) (including the services) as a function of $|\eta|$ and averaged over ϕ . The breakdown indicates the contributions of external services and of individual sub-detectors. Taken from [16].

4.4.1 Insertable B-Layer

The IBL is a single layer of 14 staves, tilted by 14° for full ϕ coverage, consisting of FE-14 read out chips with an array of 80×336 silicon pixels of size $50 \times 250 \mu\text{m}^2$ [136]. The purpose of this was to improve the tracking, vertexing and b-tagging performance of ATLAS for Run-II of the LHC. It has been designed with a low *material budget*, and has a radiation length of $0.015X_0$ (for the layer at $z = 0$), in order to keep the detector mass low and reduce radiation damage to other systems.

Because of this low mass and small distance from the Interaction Point (IP), the impact parameter used in the reconstruction of tracks is vastly improved. Figure 4.6 demonstrates the improved resolution of the transverse impact parameter⁴ (d_0) [17].

⁴This variable is defined in Chapter 5.1.3 as the distance from the primary vertex to the closest approach of the track in the $R - \phi$ plane.

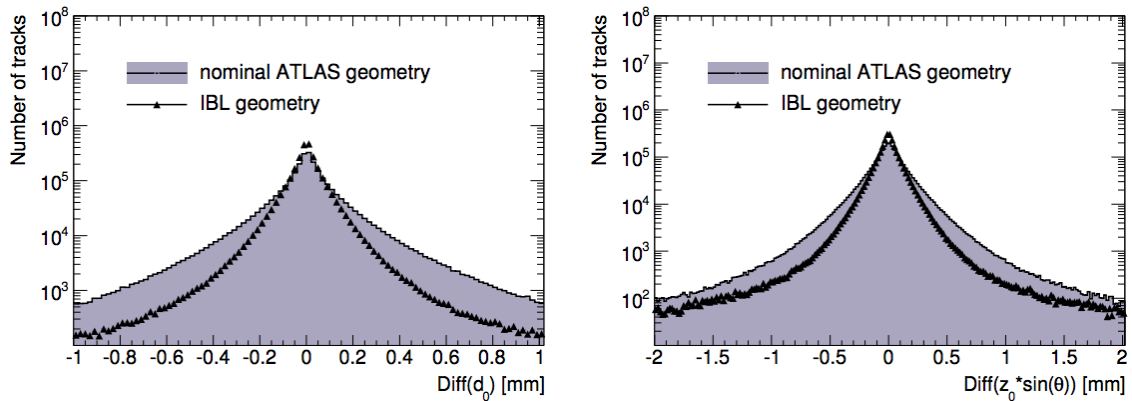


Fig. 4.6 Impact parameter distributions of reconstructed tracks with and without IBL for simulated $t\bar{t}$ events; (right) transverse impact parameter distribution d_0 and (left) longitudinal impact parameter distribution $z_0 \times \sin \theta$ with respect to the true values. Taken from [17]

For example, the rejection factor for light jets mis-tagged as b-jets in $t\bar{t}$ Monte-Carlo⁵ observes an increase in a factor of 2 with the IBL installed [136], the improved rejection factors are quoted in Table 4.1.

Table 4.1 Rejection of simulated light jets in $t\bar{t}$ events for a b -tagging efficiency of 60%, data obtained from [17]. For more details on the IP3D and IP3D+ SV1 algorithms see Section 5.1.3.

b -tagging Algorithm	Without IBL	With IBL	Ratio
IP3D	83 ± 1.5	147 ± 3.4	1.8
IP3D + SV1	339 ± 12	655 ± 32	1.9

4.4.2 The Pixel Detector

During Run-I the Pixel detector was the inner-most sub-detector, it is constructed from 60 million silicon pixels, with dimensions of $50 \times 400 \mu\text{m}^2$ [137]. These pixels, organised into modules, are arranged in 3 barrel layers as seen in Figure 4.7 as well as a total of 6 endcap disks, two on each side of the barrel, in order to cover higher η . As with the IBL, the Pixel detector is used in the immediate tracking of charged particles, vertex finding and b-tagging.

⁵See Section 5.1.3 for more detail.

4.4.3 SCT

Further away from the beam pipe is the SemiConductor Tracker (SCT), another silicon based tracking detector. The first barrel layer is situated at a distance of $R = 300$ mm away from the beam pipe. As with Pixels, it has multiple layers: 4 barrel layers and 2 sets of 9 endcap disks. The positions of various SCT disks and barrel sections are shown in Figure 4.7, the positive z side of the detector is referred to as “Side-A” of the detector and the negative z side is referred to as “Side-C”. Each barrel and disk layer are composed of many modules containing silicon strips and read-out electronics.

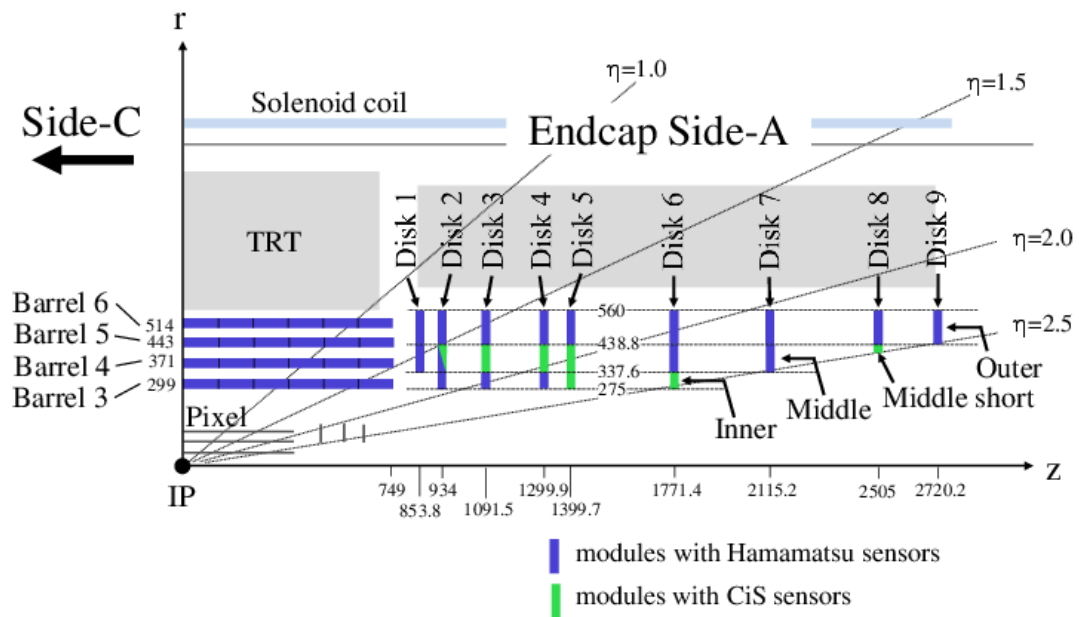


Fig. 4.7 Schematic diagram of the SCT quadrants. Two types of sensors are indicated in the diagram: Contact Image Sensors (CiS) and Hamamatsu. Taken from [18].

4.4.4 TRT

The Transition Radiation Tracker (TRT) is the third subsystem of the ID, it is the largest in size and situated between 554 – 1082 mm from the beam pipe as seen in Figure 4.7. Unlike the two other ID subsystems, the TRT is not composed of silicon pixels but rather $\sim 372,000$ gas straw tubes with a central anode wire and an outer cathode tube, filled with a xenon gas [138]. In total there are 73 barrel layers and 224 endcap layers, the straws being aligned axially in the barrel and radially in the endcaps. The TRT provides further tracking information of charged particles, it also provides a measurement of the transition radiation a

particle leaves in the detector which can be used to distinguish electron (positron) candidates from other charged particles.

As a charged particle passes through a straw tube it causes the ionisation of the noble gas, electrons drift towards the HV+ central anode wire and ions drift to the HV- cathode. From the timing of the signal pulse a drift circle of the possible positions of the passing charged particle can be made. When multiple drift circles from multiple straw tubes are combined and matched to an inner detector track, the path of a traversing charged particle can be determined. A diagram showing this can be seen in Figure 4.8. The TRT also has the capability to distinguish between electrons and pions since they emit different transition radiation (TR) [139]. The straw tubes are interleaved with polymer fibres and foils, electrons passing through these media radiate photons. The radiated photons cause increased ionisation in the straw tubes providing a characteristic enabling distinction between electrons and pions.

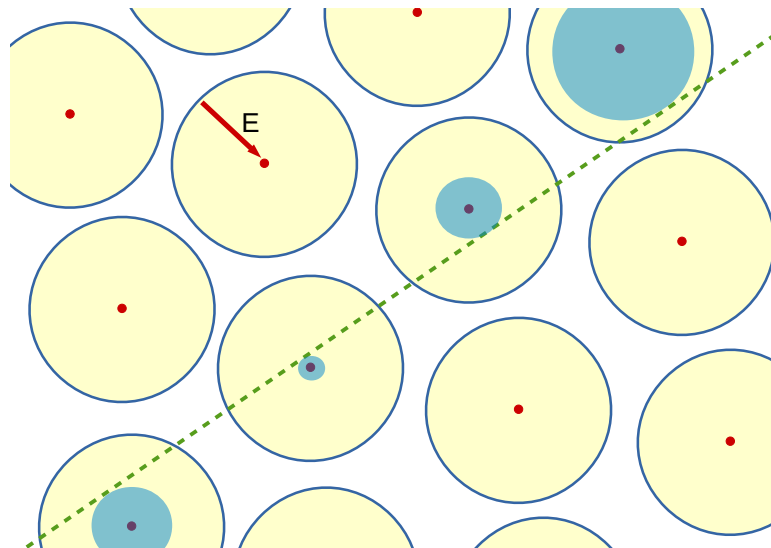


Fig. 4.8 Diagram of drift circles in an array of straw tubes of the TRT. The straw tubes are coloured yellow with the anode in the centre shown in red. An electric field is applied across the tube between the cathode shell and the inner anode. When an ionising particles travels through the noble gas a so-called *drift circle* can be inferred (grey-blue circles) from the drift time. When multiple drift circles are combined, taking into account the magnetic field, the particle track can be reconstructed (dashed-green line).

4.5 Calorimeters

In order to measure the energy of particles traversing the ID, calorimeters are situated outside of the inner solenoid magnet. Two types of calorimeters are used by ATLAS: the

ElectroMagnetic calorimeter (EMcal) and the Hadronic calorimeter (Hcal). The EMcal and Hcal are designed to measure deposited energy from electromagnetic showers and hadronic showers respectively. The coverage of the calorimeters, as seen in Figure 4.9, extends to $|\eta| < 4.9$. They are essential in the reconstruction of electrons, jets and E_T^{miss} .

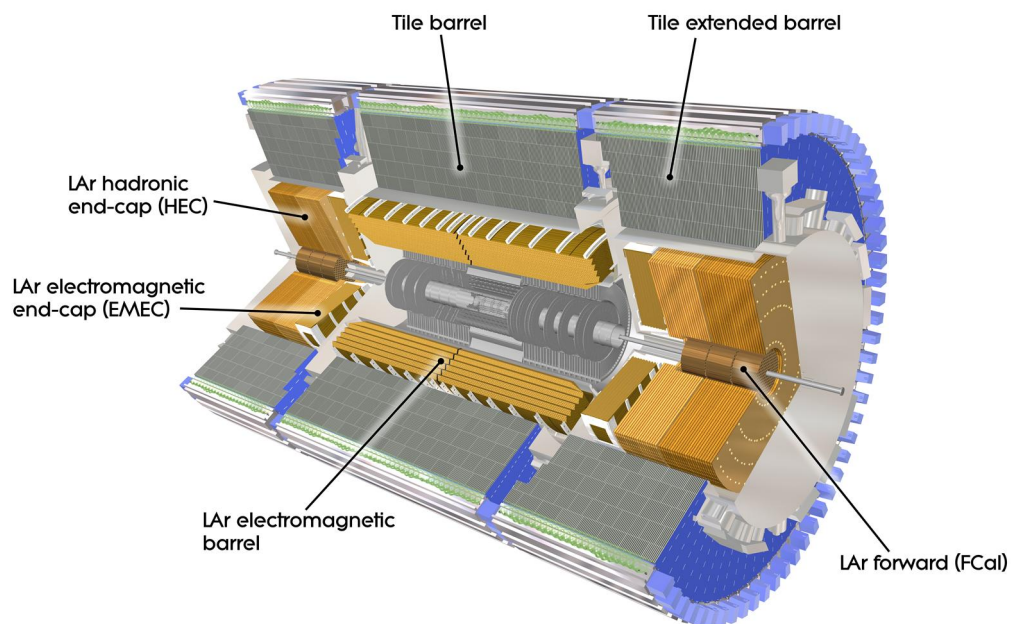


Fig. 4.9 ATLAS calorimeters: EM and hadronic section showing both barrel and endcap regions of the detector.

4.5.1 Electromagnetic Calorimeter

Increasing in radial distance outwards from the solenoid magnet, the EMcal causes the showering of high energy (> 1 GeV) electrons, positrons and photons via bremsstrahlung radiation and pair-production in the active area of the EMcal [140]. The radiation length (or material length), X_0 , is a characteristic of the active material defined as the length in which a EM particle is reduced to $1/E$ of its original energy. The EMcal is designed with a large X_0 in order to contain and measure high energy EM particles. X_0 is proportional to the inverse material density ($\propto \frac{1}{\rho}$), the proton number (Z) and nucleon numbers (A) of the material [141]. ATLAS uses Liquid Argon (LAr) alternated with plates of lead absorber as the active material in the EMcal, in both barrel and endcap sections, as seen in Figure 4.9. Both barrel and endcap sections of the EMcalo have an accordion geometry, this can be seen in Figure 4.10, to optimise the readout electrons and improve η coverage.

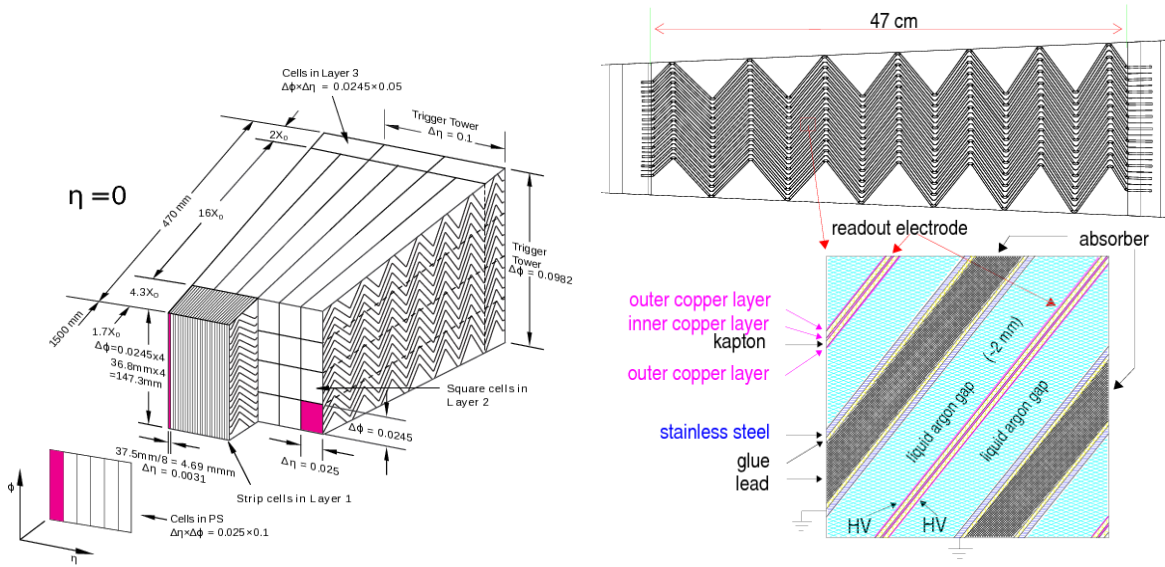


Fig. 4.10 Schematic diagram(s) of a EMcal barrel module located in the electromagnetic calorimeter.

4.5.2 Hadronic Calorimeter

Composed of two types of calorimeters, the Hcal is essential for the measurement of jets and E_T^{miss} . The barrel section or tile calorimeter, shown in Figure 4.10, covers $|\eta| < 1.0$ (Tile barrel) and $0.8 < |\eta| < 1.7$ (Tile extended barrel). Plastic scintillator and various metals⁶ are used for the active medium and absorber material, coverage of larger than $10X_0$ over all ϕ is obtained within the barrel ensuring hadronic showers are contained within the calorimeter up to large E [142]. Larger values of $1.5 < |\eta| < 3.2$ are covered by the LAr Hadronic EndCap (HEC). This calorimeter is of similar design to the EMcal endcaps, it is LAr based. Additionally the LAr forward calorimeter (FCal), composed of three separate modules per endcap, use copper and tungsten as absorber plates and provide coverage of $3.1 < |\eta| < 4.9$.

The ATLAS calorimeter systems are designed in such a way to ensure that hadronic particle showers are contained within the calorimetry. The interaction lengths of the material in each sub-system is shown in Figure 4.11, providing > 10 interaction lengths for $\eta < 4.9$.

The precise measurement of the energy of electro-magnetic and hadronic showers is critical. The reconstruction of these showers as either electron-magnetic objects or *jets* is discussed in Section 5.1.4 and Section 5.1.2 respectively. Chapter 6 discusses in detail the presence of a SM background originating from energy mis-measurement.

The designed energy resolution ($\sigma(E)$) of reconstructed objects as a function of energy (E), for the significant regions of the calorimetry is given in Table 4.2 [16].

⁶steel is used in the tile calorimeter, copper in endcaps and tungsten in the forward regions [142].

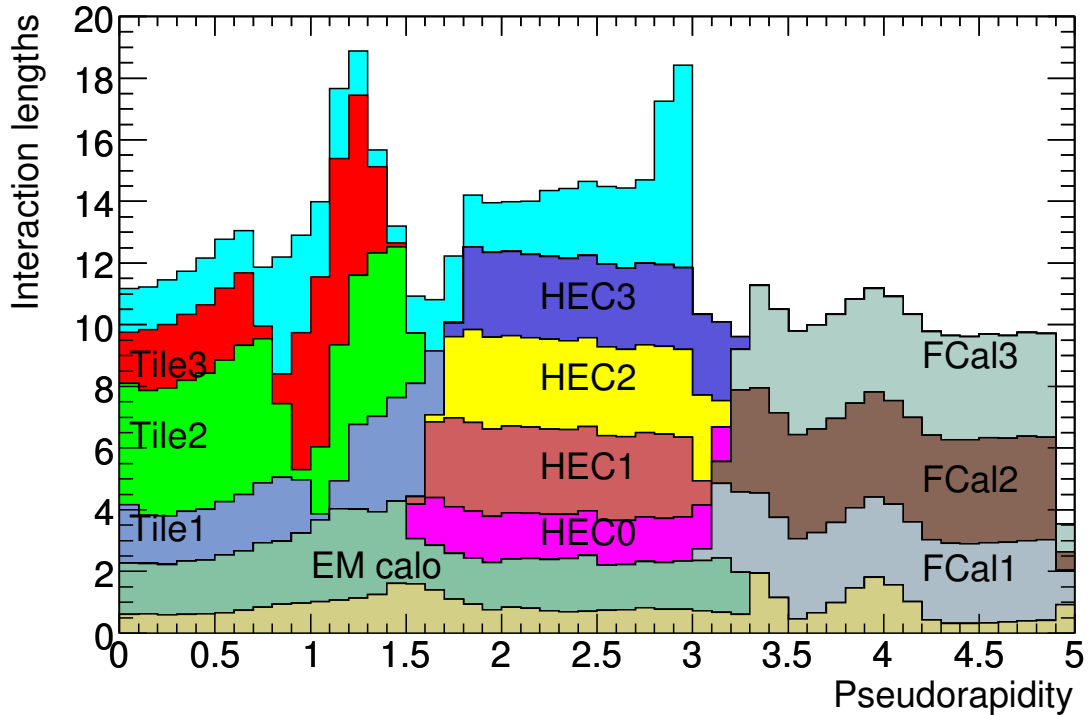


Fig. 4.11 Interaction lengths (I_0) in the calorimeter systems as a function of $|\eta|$ and averaged over ϕ . Taken from [16].

Table 4.2 ATLAS performance goals of the calorimeters. Taken from [16].

Calorimeter component	Resolution
EM	$\frac{\sigma(E)}{E} = \frac{10\%}{\sqrt{E}} \oplus 0.7\%$
Hadronic Barrel and Endcap	$\frac{\sigma(E)}{E} = \frac{50\%}{\sqrt{E}} \oplus 3\%$
Hadronic Forward	$\frac{\sigma(E)}{E} = \frac{100\%}{\sqrt{E}} \oplus 10\%$

4.6 Muon Spectrometer

The outermost layer of ATLAS is the Muon Spectrometer (MS). It is designed to measure the momentum of charged particles exiting the Hcal, covering the region of $|\eta| < 2.7$. Figure 4.12 depicts the side A of the muon spectrometer. It shows several barrel layers surrounded by the toroid magnet and several vertical wheels, the 4 big wheels (an additional two on side C) at located ~ 13 metres and ~ 21 metres from the centre of detector. The diagram also indicates the several types of gaseous detectors used in the MS, the main being Monitored

Drift Tubes (MDT), along with the Cathode Strip Chambers (CSC). These subsystems are used for tracking in the barrel and endcap regions. To trigger on muons in the barrel and endcap regions Resistive Plate Chambers (RPC) and the Thin Gap Chambers (TGC) are used. The muon chambers used for triggering cover a slightly smaller range of $|\eta| < 2.4$. The designed reconstructed p_T resolution of muons (see Section 5.1.5) measured in the MS is given by $\sigma(p_T) = 10\%$ for a muon p_T of 1 TeV [16].

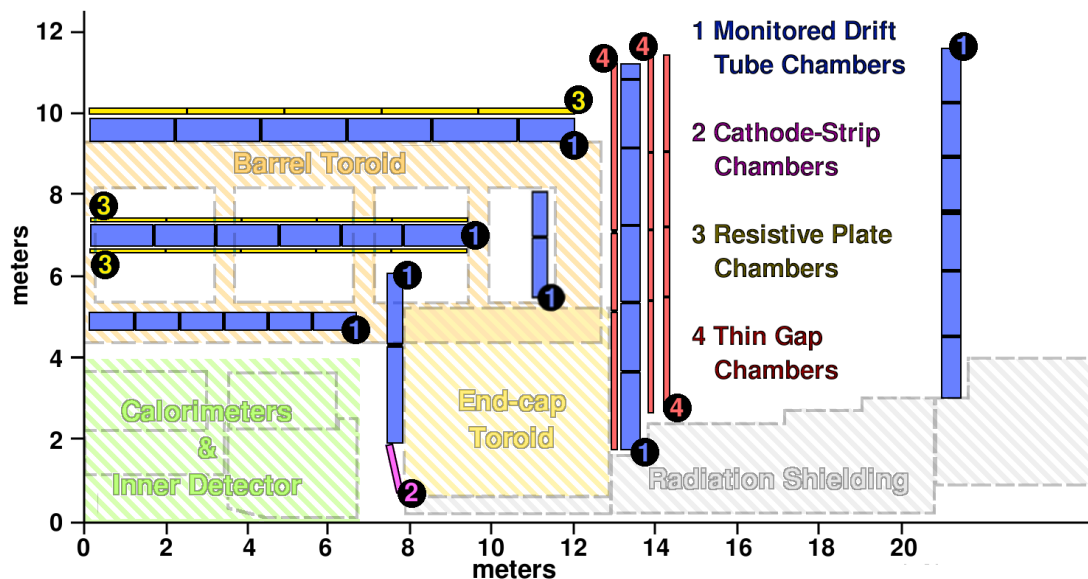


Fig. 4.12 Longitudinal diagram of the muon spectrometer (MS), side A of ATLAS. The x-axis indicates the distance from the IP along the beam pipe, the y-axis indicates the distance in height from the beam pipe.

4.7 Triggers

As mentioned in Chapter 3.2 at both $\sqrt{s} = 8$ TeV and $\sqrt{s} = 13$ TeV the cross section for inelastic collisions is $\mathcal{O}(10^{10})$ higher than the cross section for typical SUSY particle production. The collision rate of the LHC is 20(40) MHz during Run-I (Run-II), is much higher than storage and read-out capabilities of ATLAS. The need for a sophisticated trigger system capable of rapidly deciding which events are worth recording, is critical to physics analyses.

Figure 4.13 shows a schematic diagram of the ATLAS trigger system during Run-I and Run-II of the LHC. The Level 1 stage of the trigger system is hardware based and uses the calorimeters and MS to find *Regions Of Interest* (ROIs), reducing the rate to 70 kHz [143, 144] (100 kHz [145, 146]) in Run-I (Run-II). The Level 2 (L2) system is *seeded*

by the L1 system, these candidates are used by software to find physics objects - electrons, photons, muons, taus, jets, b-jets and E_T^{miss} with reduced event information. In Run-I the L2 information was passed to the *Event Filter* (EF), however in Run-II the L2 and EF are merged as a more complete event reconstruction based on the readout of additional subsystems of the detector. The L2 and EF make up the *High Level Trigger* (HLT), the rate after HLT acceptance in Run-I was 700 Hz and 1 kHz in Run-II.

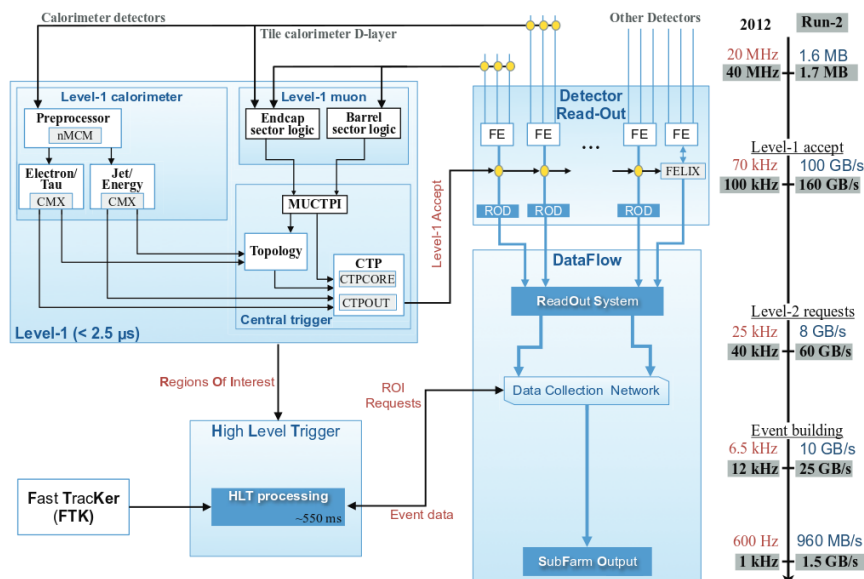


Fig. 4.13 Schematic diagram showing the overview of the ATLAS trigger system in Run-I and Run-II. Taken from [19].

A summary of the nomenclature of the trigger names is given in Table 4.3. Each trigger is *triggered* by a physics objects with some *online* threshold⁷. Some triggers are said to be *prescaled*, this means that only a fraction of events is recorded, for example, 1 in 10 events that pass a certain trigger will be recorded therefore the prescale value would be 10. Triggering on commonly produced physics objects such as photons and low p_T jets⁸ can take large prescale values since it is either not practical or undesirable to record every event produced by the LHC.

⁷online threshold - for example the p_T the initial L1/L2/HLT systems observe the object with, this will differ from the value measured after full reconstruction

⁸Hadronic showers.

Table 4.3 Summary of the most relevant ATLAS High Level Triggers. The naming convention and corresponding physics object are given, XX refers to an online threshold associated to the p_T of the triggered object.

Name	Corresponding Physics Object
HLT_xeXX	Missing transverse momentum (E_T^{miss})
HLT_jXX	At least one jet
HLT_eXX	At least one electron
HLT_muXX	At least one muon
HLT_gXX	At least one photon

4.8 Datasets and Simulation

A transverse slice of ATLAS in the barrel section, with all subsystems is shown in Figure 4.14. The reconstruction of the physics objects: muons; jets (protons, neutrons, other hadrons); electrons and photons; muons and E_T^{miss} (invisible particles e.g. neutrinos), is discussed in more detail in Chapter 5.1. ATLAS is needed to record these objects. The figure shows how the inner detector is used in the tracking of all charged particles which are bent by the inner solenoid magnet; electrons and photons shower in the EMcal; hadrons shower in the Hcal; muons are tracked through the entire detector and are detected by the muon spectrometer; and finally invisible particles such as neutrinos do not interact with the detector and are manifested as E_T^{miss} .

Information is collected by the various sub-detectors Data Acquisition instruments (DAQs), and is recorded to form data sets which can be used for analysis. In addition to this, simulation of the detector, the underlying physics and how produced particles interact with the detector is critical to the analyses in this thesis.

4.8.1 Datasets

The analyses in this thesis use two different data sets⁹: one recorded from April 2012 to December 2012 during Run-I of the LHC at a centre-of-mass energy of $\sqrt{s} = 8$ TeV; the other was recorded from June 2015 to November 2015 during Run-II of the LHC at $\sqrt{s} = 13$ TeV. Figure 4.15 summarises the amount of data delivered to ATLAS by the LHC and the amount of data ATLAS recorded. The total amount recorded in 2012 was 21.3 fb^{-1} , and the amount recorded in 2015 was 3.9 fb^{-1} . After the application of *Good Run Lists* (GRL), removing

⁹Which are not the total Run-I and Run-II data-sets discussed in Chapter 4.1.

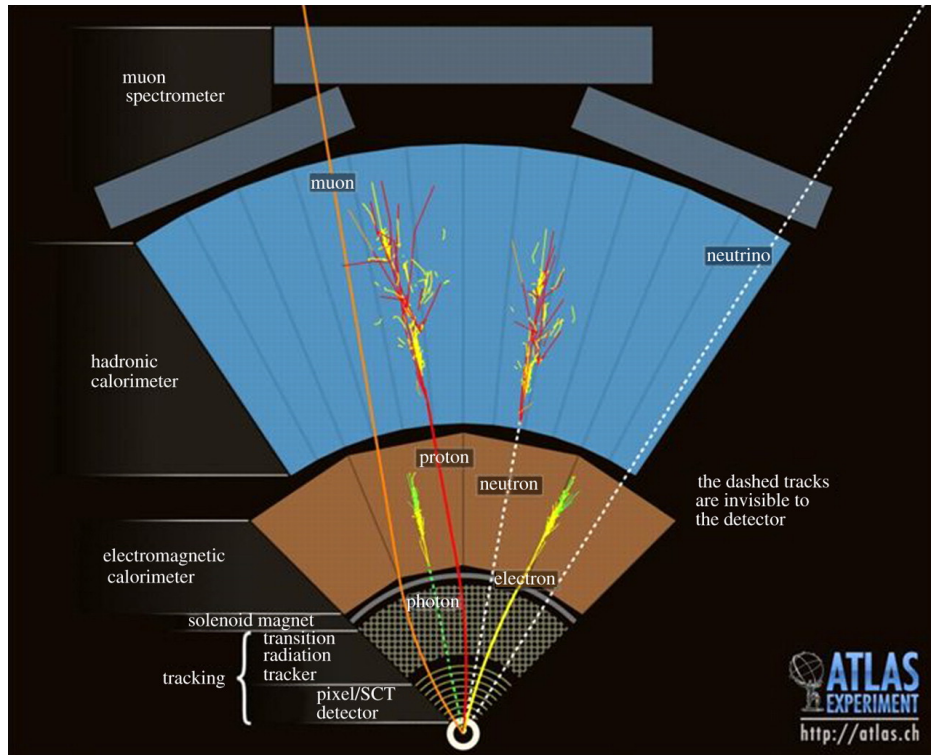
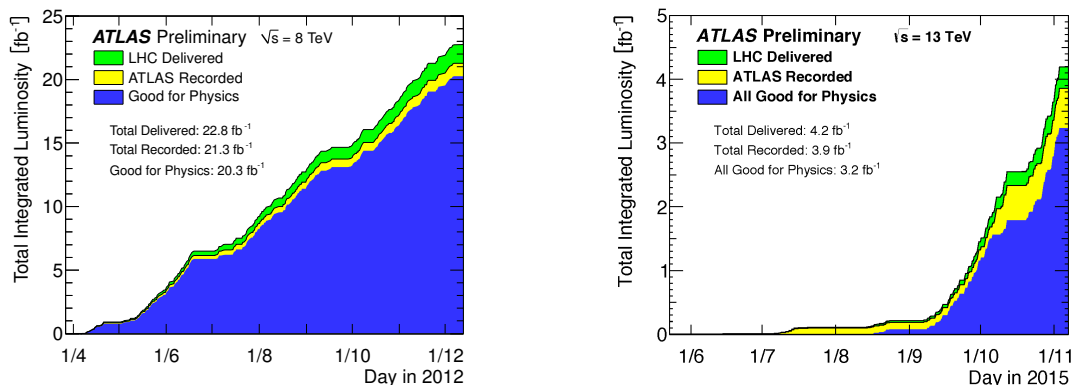


Fig. 4.14 Summary of different ATLAS sub-detectors and their purpose in terms of physics objects identification.

“runs” or sections of runs in which detector issues or downtime impeded the quality of the data, the 2012 data set was reduced to 20.3 fb^{-1} and the 2015 data set reduced to 3.2 fb^{-1} . The collision rate of the LHC given by Equation 3.1 is dependent on the number of bunches per beam, n_b . This number can be increased, hence increasing the luminosity, by decreasing the time between different bunches (bunch spacing). The LHC used a bunch spacing of 50 (25) ns, corresponding to a collision rate of 20 (40) MHz during Run-I (Run-II).

4.8.2 Simulating ATLAS

In the pursuit of physics beyond the SM a significant excess in the number of observed events is needed to claim the discovery of something new. Typically this is an excess with respect to a non-zero number of expected SM events, calculated with either data-driven techniques or with Monte-Carlo (MC) simulation. Many data-driven techniques, some of which were used in this thesis, still rely partially on MC at some level. The signal from BSM models needs to be simulated to find an expected rate. It is therefore of utmost importance to be able to correctly simulate all expected SM background and signal processes as well as model the



(a) Summary of the 2012 Run-I data set at $\sqrt{s} = 8$ TeV. It shows integrated luminosity versus time delivered to (green), recorded by ATLAS (yellow) and good for physics (blue). Plot taken from [147]

(b) Summary of the 2015 Run-II data set at $\sqrt{s} = 13$ TeV. It shows integrated luminosity versus time delivered to (green), recorded by ATLAS (yellow) and good for physics (blue). Plot taken from [148]

Fig. 4.15 Summary of the 2012 Run-I and 2015 Run-II data sets used in analyses.

detector accurately. Chapter 2 and Chapter 3 gave an overview of the underlying theory of particle physics and how this physics is manifested in hadron colliders.

The geometry of ATLAS is modelled using Geant4 [149] and accounts for all the material in the detector and the surrounding environment. MC samples are produced by many different *MC generators*, the most commonly used being: *Pythia* [150]; *MC@NLO* [151]; *Powheg* [152]; *MadGraph* [153]; and *Sherpa* [7]. *Generator level* information, commonly referred to as *truth information*, is essential in the calibration of physics objects.

The method for modelling high energy collisions can differ depending on the process being simulated. Generally the Underlying Event (UE) (see Chapter 3.2.3) is simulated using Pythia6 [154–156]. The Matrix Element (ME) calculation of the hard process is typically calculated to leading order, Next-to-Leading Order (NLO) and sometimes next-to-next-to-leading order. This is followed by the parton showering (PS) and the simulation of softer underlying processes, the result is then passed to the detector simulation which models the detector response. Referring back to Figure 3.5 of Chapter 3.2.3, the simulation of a $t\bar{t}h$ event in Sherpa [7] is pictorially represented. This generator is an example of a ME+PS generator - it performs both the matrix element and parton showering calculation.

Powheg+Pythia [152, 150] is an example of a NLO generator being interfaced with a PS. In the case of high jet multiplicity the more accurately the ME can be described then the more accurately the MC will describe data. *Matching procedures* [157, 158], are employed to match the matrix elements to the parton shower. This is needed to remove overlaps of the hard-process of interest and those which are related to the evolution of the PS. Figure 4.16

pictorially represents this and the important interplay between the ME (truth level), the parton showering and the detector level objects (reconstruction level). An event containing $N + 1$ jets may arise from two possible situations: collinear or soft-emission of a parton in a $N + 1$ parton state; or from N parton simulation where an extra jet is reconstructed from a hard-emission in the parton shower. This is an example of the double counting of events, see Figure 4.16 for a pictorial representation. Matching procedures remove the double counting by making decisions based on the p_T of the extra jet. In one such method the event is selected if the $N + 1$ jet p_T in the N parton state is below a certain threshold $p_T < Q_c$, otherwise it is removed. Events generated with $N + 1$ partons are then merged only keeping ones in which the $N + 1$ jet has $p_T > Q_c$.

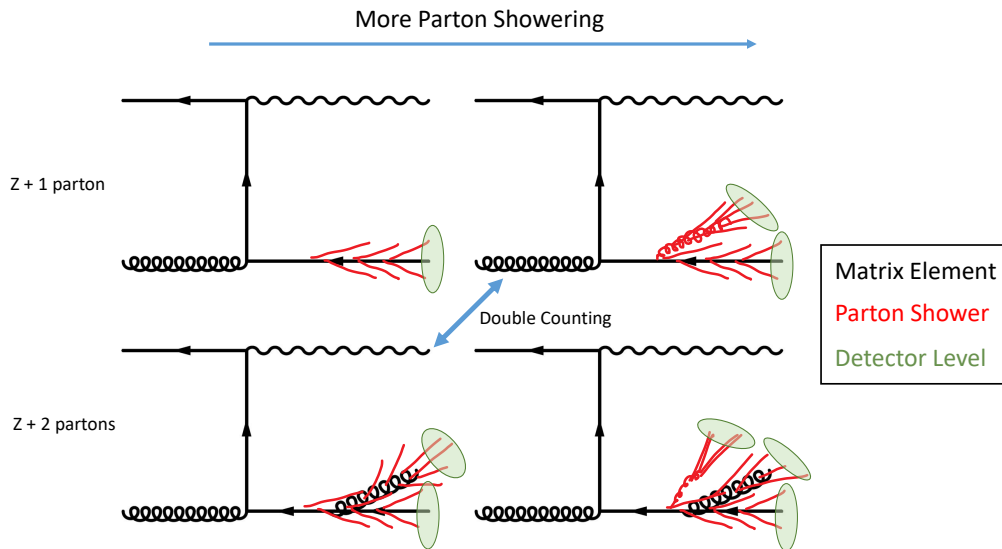


Fig. 4.16 Example of double-counting when matching ME+PS in MC simulation of multiple partons.

Fast Simulation As discussed in Chapter 4.8.2, Geant4 is used to perform a full simulation of ATLAS, the reconstruction time is long and uses a lot of CPU time, I/O¹⁰ and disk space. This can be improved with the use of *Fast Simulation* in which parametrisations of e.g. the ATLAS calorimeter cell response are used [159–161]. This greatly reduces computational resources with a loss in simulation accuracy. In the case of sub-dominant backgrounds and the calculation of theoretical uncertainties on the ME calculations and PS, fast simulation can be used.

¹⁰I/O - input/output communication between the disks and the computer

Scale Variations In the calculation of theoretical uncertainties on the MC predictions *scale variations* are also computed as well as the comparison between different ME+PS programs used in the generation of the MC. Various different PDF (see Chapter 3.1.2) sets have been used by ATLAS [162–166]. In addition to this variations on the generator parameters are used: h_{damp} parameter which controls the ME+PS matching, effectively regulating the high- p_T ISR/FSR radiation are used [156, 162]. Other variations include the renormalisation (μ_r) and factorisation (μ_f) scales which also control the amount of radiation [162]. The simulation of the UE can also be varied from the nominally used Pythia6 using the Perugia tunes [167].

Chapter 5

Analysis Tools

The previous Chapter detailed the ATLAS detector and how it is used to record collision data from the LHC. Chapter 4.8.2 introduced the concept of Monte-Carlo simulation of collision data and the ATLAS detector response. From this point the information from the detector and simulated detector needs to be reconstructed into so-called *physics* objects.

In Figure 5.1 a pictorial overview of the ATLAS data-flow is shown. The detector provides the collaboration with $\mathcal{O}(10)$ PBytes/year of data; simultaneously a huge Monte-Carlo production campaign provides $\mathcal{O}(100)$ PBytes of simulated data (simulated SM backgrounds and BSM signals).

As seen in Figure 5.1, both *raw data* and *simulated MC* are passed through the same reconstruction software using the software framework *Athena* [168]. The following chapter details this reconstruction stage; how raw data and simulation are transformed into so-called *physics objects* (jets, electrons etc.). Corrections to the Monte-Carlo, known as Scale Factors (SFs), are discussed as well as systematic uncertainties on the calibration of the Monte-Carlo performed at the reconstruction stage.

The final subsection of this Chapter details the use of the *HistFitter* [169] software package that is used to statistically interpret the analysis results of Chapters 7 and 8.

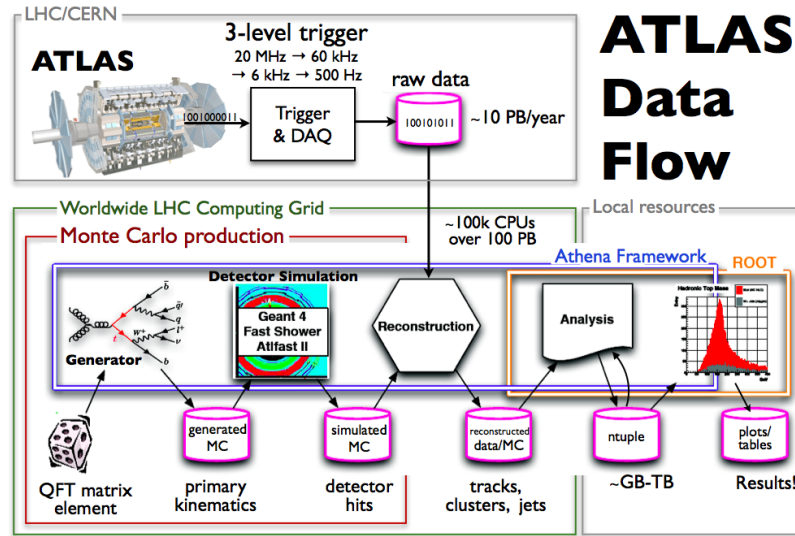


Fig. 5.1 An overview of the ATLAS data flow showing both data and simulation [20].

5.1 Physics Objects

The concept of electrons, photons, muons, jets and E_T^{miss} as detector level physics objects was briefly discussed in Section 3.2.4. This chapter provides a more detailed overview. Parton interactions in hadron colliders mostly produce large sprays of hadrons and mesons (π , K , n , ...) referred to as *Jets*. Figure 5.2 shows a pictorial example of this in which LEP produces a Z boson which decays to $q\bar{q}$, subsequent hadronisation of these quarks produces a spray of hadronic jets in the OPAL detector. Jets of particles can be tagged as originating from b quarks¹ and are referred to as b -jets. The b -tagging of jets is critical for analyses described in this thesis as the targeted signal models contain decays via b -quarks.

Electrons, positrons, muons and anti-muons are generally referred to as “leptons”; this term does not include taus and anti-taus. Taus decay 64.79% of the time hadronically via pions; 17.82% into tau neutrinos, electrons and electron anti-neutrinos; and 17.39% into tau neutrinos, muons and muon anti-neutrinos [170]. ATLAS observes leptonic tau decays as either electrons or muons and E_T^{miss} from the two neutrinos. Jets containing pions originating from taus can be tagged as originating from taus, referred to as tau jets.

5.1.1 Tracks

The purpose of the ID is to track charged particles as they exit the beam pipe at the centre of ATLAS. Although tracks are not used as *standalone* physics objects they are essential

¹It is also possible to tag them as c or t quarks

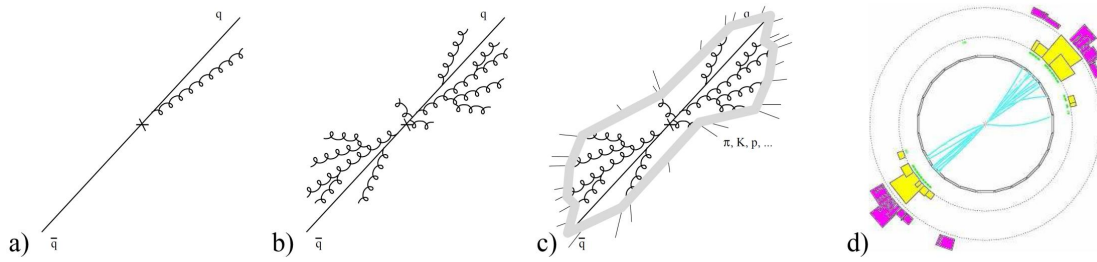


Fig. 5.2 a) The emission of a single gluon from the production of a $q\bar{q}$. (b) shows multiple emissions of gluons from a $q\bar{q}$, (c) then shows the hadronisation of these gluons forming bound states such as pions and kaons, (d) shows the event display from the OPAL detector for the production of $e^+e^- \rightarrow Z \rightarrow q\bar{q} \rightarrow \text{hadrons}$. Taken from [10].

in the reconstruction of leptons and jets. In the presence of large event pileup, there can be on average $\langle \mu \rangle > 20$ pp interactions per event resulting in large numbers of overlapping particle tracks. Tracks are constructed from space points in the various ID layers that point towards a common *vertex* at the centre of ATLAS, routes are built between them based on the most probable path, taking into account the effects of the B-field and multiple scattering. Once constructed multiple tracks can then be extrapolated to the beam axis to find vertices. The Primary Vertex (PV) is selected as the vertex with the largest sum of p_T of all tracks associated with the vertex. By finding the PV and additional large p_T vertices, contributions from pileup are reduced.

5.1.2 Jets

In 1973 the SPEAR e^+e^- [171] experiment at SLAC first observed evidence of showering of hadronic particles (jets) originating from quark-anti-quark pair production:

$$e^+e^- \rightarrow q\bar{q} \rightarrow j_1 j_2$$

It was demonstrated that the quark-anti-quark pair ($q\bar{q}$) had produced hadrons in the final states from the angular distribution and charge of the jets (j_1, j_2) [172]. This is also depicted in Figure 5.2. The jets observed at SPEAR appeared as two clusters of multiple charged particle tracks in the event displays [173]. Jets were also observed experimentally by PETRA [174] at DESY to originate from gluons. An electron-positron pair annihilation radiates a hard gluon in the final state, this was the first example of Final State Radiation (FSR),

described in Section 3.2.1:

$$e^+e^- \rightarrow q\bar{q}g \rightarrow j_1j_2j_3$$

With increased centre-of-mass energy and the use of hadron colliders comes the need to accurately measure the jet constituents and properly reconstruct them to perform quantitative analyses. Jet algorithms are used to cluster a large number of final state particles into a small number of jets depending on kinematic and angular distributions.

Jet input ATLAS reconstructs jets based on an input. Positive-energy topological clusters from the three-dimensional reconstruction of energy deposits (cells) in the calorimeters, known as “Topoclusters” are used. They are formed with the use of a nearest neighbour algorithm. To enter the cluster, cells must contain a significant level of signal above simulated noise [175]. The algorithm for simulating noise-level has been modified between Run-I and Run-II of the LHC to better match the observed noise levels during Run-I. The cluster algorithm itself has undergone modifications for Run-II data. Clusters are forbidden to grow from pre-sampler layers² of the calorimeter from neighbours in the same layers. By doing this, the amount of low-energy pileup deposits which only just reach the pre-sampler layers, do not form large topoclusters [176].

Jet Finding Many types of algorithms exist with the purpose of accurately reconstructing jets to probe the underlying partons. ATLAS uses multiple sequential recombination algorithms to find jets, the most popular being the anti- k_T ³ algorithm [177]. This jet algorithm is *infra-red safe* and *collinear safe* as demonstrated in Figure 5.3. The top two diagrams show how two jets can be incorrectly combined into a single jet if a soft particle is radiated between the two jets. The bottom two diagrams show how if a particle within the jet undergoes collinear splitting the reconstruction may not include all the jet constituents, an ideal jet algorithm is not susceptible to these effects. The algorithm used in this thesis is the anti- k_T algorithm. It proceeds as follows:

1. The constituent jet inputs (i) are ordered based on their transverse momentum to the power $2p$, $k_T^{2p}(i)$. The parameter $p = -1$ for the anti- k_T algorithm⁴.

²These are the layers with finest granularity at the closest radial distance to the interaction point

³ k_T refers to the transverse momentum (p_T) of an input object, this convention is kept in this sub-section to be consistent with the named algorithm.

⁴ $k_T^{-2} = \frac{1}{k_T^2}$

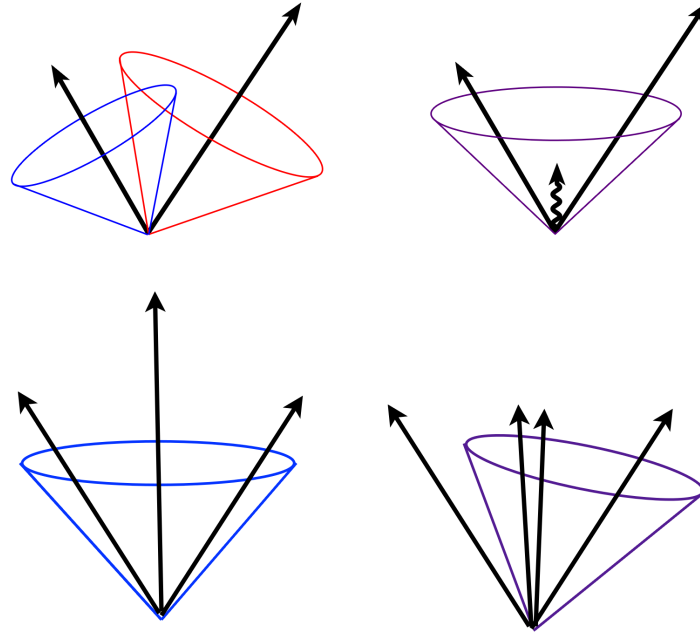


Fig. 5.3 Illustration of the infra-red sensitivity of a cursory designed jet algorithm (top). Illustration of the product of a collinear unsafe jet algorithm. A collinear splitting changes the number of jets (bottom). Taken from [21].

2. d_{ij} is the distance between the first ordered jet input (i) and additional jet inputs (j). The distance to with respect to the beam, d_{iB} , is also calculated.

These are defined as:

$$d_{ij} = \min\{k_T^{2p}(i), k_T^{2p}(j)\} \frac{\Delta R_{ij}^2}{R_C}$$

$$d_{iB} = k_T^{2p}(i)$$

where $\Delta R_{ij}^2 = \Delta y_{ij}^2 + \Delta \phi_{ij}^2$ and R_C is the cone radius⁵. A value of $R_C = 0.4$ is the most typical radius used in ATLAS.

3. If d_{ij} is the smallest distance, jet input j is combined with jet input i and d_{ij} is calculated for the next jet input in the list. If $d_{iB} < d_{ij}$ the jet input i is considered a jet and removed from the list, this occurs if $\Delta R_{ij}^2 > R_C$.

A Monte-Carlo (MC) level demonstration of the anti- k_T algorithm using $R_C = 1.0$ is shown in Figure 5.4, taken from [178]. An event has been simulated at parton level with $\mathcal{O}(10^4)$ random soft “ghost” particles and clustered with the algorithm detailed above. All

⁵ y is defined as the rapidity which differs from the pseudo-rapidity η

hard jets in the event are circular with a radius R_C and appear well reconstructed. However, the two jets seen at $\phi \sim 4.5 - 5.5$ and $y \sim 1 - 2$, shows how the harder right hand side jet (green) carves a crescent shape into two softer jet (pink). Preference in this algorithm is given to the harder jet perhaps overestimating its energy. A different jet finding algorithm (e.g. k_T with $p = 1$) or with a different value of R_C may better resolve these objects. In the case of a boosted top quark in the final state, the b-quark and W-boson decay products will also be boosted becoming collimated; in cases when the W-boson decays hadronic it can be advantageous to use a large $R_C \geq 1.0$ (fat-jet) to reconstruct the top quark mass.

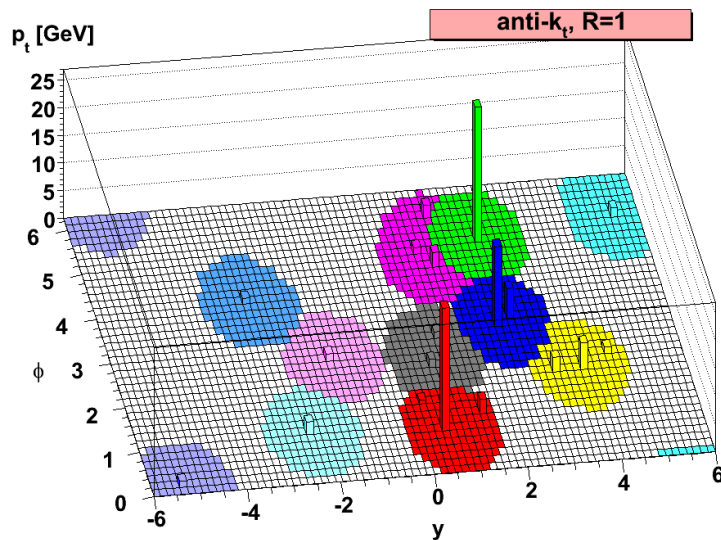


Fig. 5.4 Monte-Carlo level on jet clustering with the anti- k_T algorithm using $R_C = 1.0$ in the $y - \phi$ plane. Taken from [22].

Jet Energy Scale The topoclusters, used as inputs to jets, are reconstructed and calibrated to electro-magnetic showers [179] known as EM-jets. A second set of topoclusters can be built by performing a method known as *Local Cell Weighting* (LCW). This method classifies the topoclusters into EM or hadronic showers based on the energy density and shower depth. Topoclusters identified as hadronic showers have their re-calibrated. These objects are referred to as LCW-jets. Further calibration is applied *after* the jet finding procedure - *Jet Energy Scale* (JES). The Run-I analyses used the LCW+JES calibration scheme, the analyses performed with Run-II data used the EM+JES calibration scheme.

5.1.3 B-tagged jets

The accurate identification of jets originating from b-quarks is essential to the signal models of interest in this thesis. As discussed in Section 2.1.4, no isolated quark has ever been observed, b-quarks hadronise forming B-hadrons with lifetimes $\tau \approx \mathcal{O}(10^{-12})$ and masses $m_B \approx 5$ GeV. High p_T B-hadrons ($p_T > 20$ GeV) have a time of flight that can be used to distinguish them from lighter quark and gluon jets. A secondary vertex from the decay of the B-hadron can be detected as seen in Figure 5.5. The transverse impact parameter (d_0) is the distance from the primary vertex to the closest approach of the track in the $R - \phi$ plane. The longitudinal impact parameter (z_0) is the z coordinate of the track at the point of closest approach. These values can be used to separate jets originating from b-quarks from lighter quark and gluon jets.

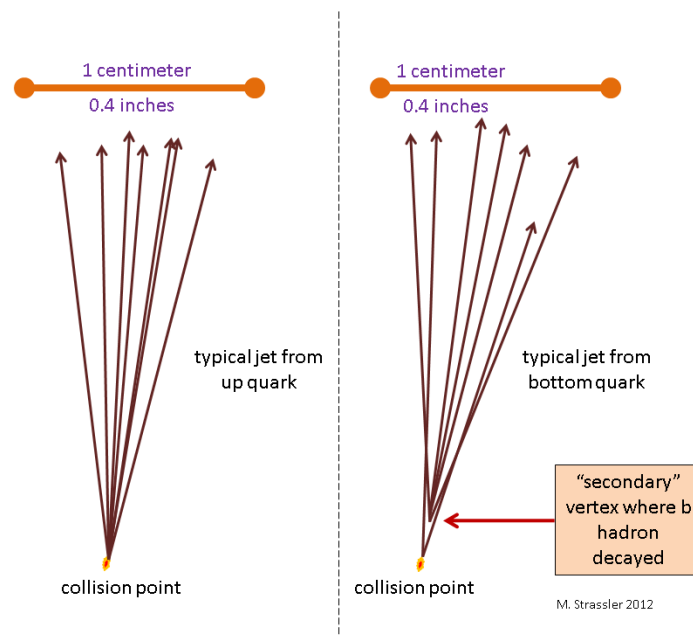
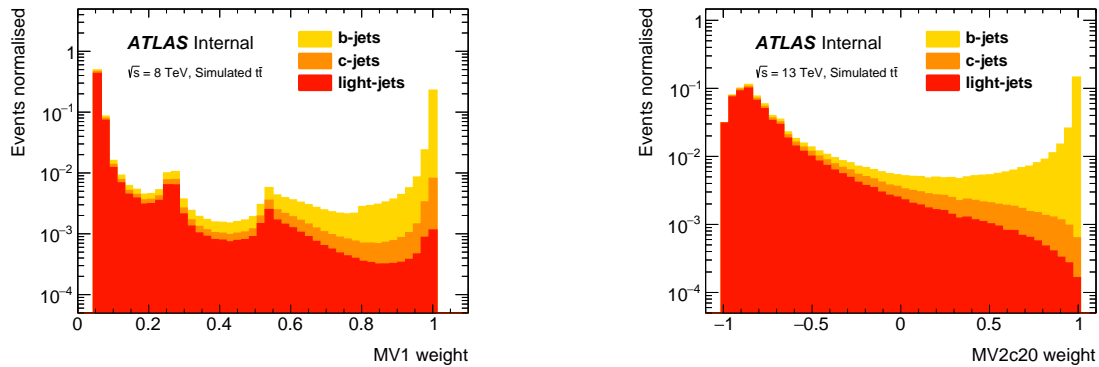


Fig. 5.5 Decay of a u-quark and a b-quark

To increase the discriminating power between jets originating from B-hadrons and all other sources, the output weights from multiple algorithms can be combined in a “neural network” using Multi-Variate (MV) algorithms. The b-tagging algorithm used in the Run-I analyses is named *MV1* [180], for Run-II the algorithm was updated, modified and is referred to as *MV2c20* [181]. Both MV algorithms use the outputs of three algorithms: Impact Parameter significance (IP3D), Secondary Vertex finding (SV1) and Multi-vertex fit (JetFitter) [182–184]. The IP3D algorithm takes d_0 and z_0 and calculates a tagger weight based on the log-likelihood ratio method (LLR) [182]. SV1 reconstructs a secondary vertex using displaced tracks that do not originate from a long lived particle or interaction with the

detector material [183]. JetFitter exploits the topology of the longer Heavy Flavour (HF) hadron decay chains⁶ inside a jet [184]. Jets originating from HF-hadrons will have a larger number of vertices (with at least two tracks) and a larger number of tracks from vertices (with at least two tracks). A Boosted Decision Tree (BDT) [185] combines the outputs of IP3D, SV1 and JetFitter. The default for the Run-II data set (MV2c20) is trained with b-jets as the *signal* and the *background* composed of 20% c-jets and 80% light jets.



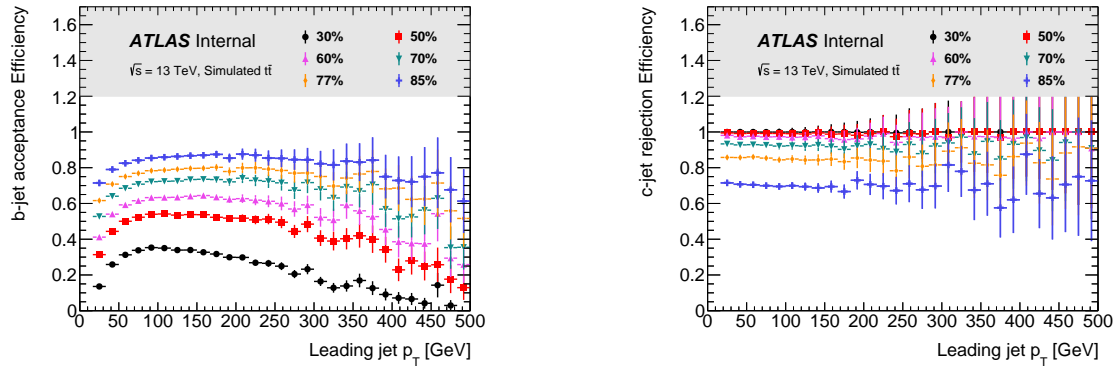
(a) MV1 weight for simulated $t\bar{t}$ MC showing b, c and light jets. This weight was used in Run-I for b-tagging.

(b) MV2c20 weight for simulated $t\bar{t}$ MC showing b, c and light jets. This weight was used in Run-II for b-tagging.

Fig. 5.6 MVx algorithms in simulated $t\bar{t}$ samples: MV1 was used for the Run-I analyses and MV2c20 was used for the Run-II analyses.

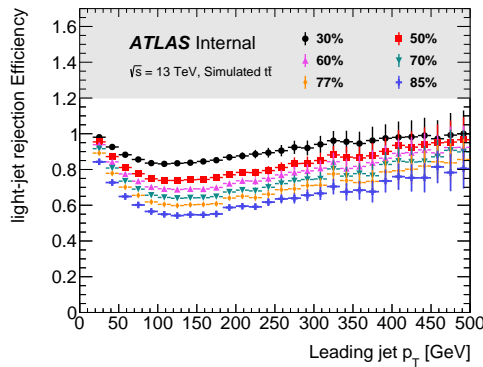
Figure 5.6a shows the MV1 weight used in Run-I in simulated $t\bar{t}$ at 8 TeV. Analogously, Figure 5.6b shows the output of the MV2c20 algorithm in simulated $t\bar{t}$ at 13 TeV. Both show the separation between true b-jets, c-jets and light-jets. In order to classify jets as b-tagged or not, the MV weights are cut on at certain *Working Points* (WPs) corresponding to specific MVX weight known as an *Operating Points* (OPs). WPs and OPs are determined from $t\bar{t}$ simulation. In the case of the MV2c20 algorithm, the OP $w_{MV2c20} > 0.4803$ corresponds to a 77% WP. The 77% refers to the b-tagged acceptance efficiency, meaning that for all true simulated b-jets in the $t\bar{t}$ sample, 77% of these will be correctly *tagged* as b-jets. The generator level information for c-jets (light-jets) can be also used to find the c-jet (light-jet) rejection efficiency - what percentage of jets originating from charmed hadrons (non-charmed- or non-b- hadrons) are incorrectly tagged as b-tagged jets. Figure 5.7 shows the b-jet acceptance efficiency, c-jet rejection efficiency and light-jet rejection efficiency for multiple OPs in simulated $t\bar{t}$ as a function of leading jet p_T at $\sqrt{s} = 13$ TeV.

⁶ c and b quarks have longer decay chains than lighter quarks.



(a) b-jet acceptance efficiency for multiple MVc20 working points in simulated $t\bar{t}$ MC

(b) c-jet rejection efficiency for multiple MVc20 working points in simulated $t\bar{t}$ MC



(c) light-jet rejection efficiency for multiple MVc20 working points in simulated $t\bar{t}$ MC

Fig. 5.7 MVc20 algorithm truth level acceptance and rejection efficiencies for a simulated $t\bar{t}$ MC sample. The various percentages corresponds to Working Points (WPs).

5.1.4 Electromagnetic Objects

Electrons, positrons⁷ and photons are measured by the EMCal as discussed in Section 4.5. These so called *Egamma* physics objects are formed in the same way - as reconstructed showers of deposited energy. They are distinguished by their association with a (positively or negatively) charged track or absence of a charged track.

A Sliding Window algorithm is used to group cells of deposited energy into clusters [186]. The EMCal has four active layers: the pre-sampler layer, S1, S2 and S3. S1 is a high granularity layer in η , this enables the distinction between overlapping objects. For example, two collimated photons from a pion decay. The mid-layer, S2, absorbs the majority of EM energy deposits. The final layer, S3, contains high energy showers. The algorithm reconstructs photons by locating a ‘‘Tower’’ of EM cells as a seed, and building a cluster

⁷electrons and positrons are both referred to as electrons.

around this seed depending on the transverse energy threshold. Tracks from the ID with $|\eta| < 2.47$ are matched to the clusters to reconstruct electrons; information from the TRT and SCT can also be used to determine if the object is an electron, see Section 4.4.4.

5.1.5 Muons

Muons are reconstructed from tracks in the muon chambers (see Section 4.3). Candidates are classified depending on additional track information as: Calorimeter-Tagged (CT), which have limited coverage in the Muon Spectrometer (MS) ($|\eta| < 0.1$)⁸; Stand-Alone (SA), extended beyond the ID track acceptance between $2.7 > |\eta| > 2.5$; ComBined (CB), full MS tracks and ID tracks; and Segment-Tagged (ST), only one segmented track in the MS and an ID track.

Different algorithms were used for the combination of the ID tracks, MS tracks and MS energy depositions in the Run-I and Run-II analyses. The Run-I analyses use the so-called *staco algorithm* [187] and Run-II analyses use a combined algorithm detailed in [188].

In the case of both muons and electrons, the terms refer to both particles and their anti-particles. The notation *SF* refers to Same Flavour and *OS* refers to Opposite Sign.

5.1.6 Missing Transverse Energy

In searches for R-parity conserving SUSY, the Missing Transverse Energy (E_T^{miss}) is key in the potential discovery of new particles. As discussed in Section 3.2.4, the majority of final observed states have large amounts of E_T^{miss} from the undetectable LSPs at the end of supersymmetric decay chains. Equation 5.1 defines E_T^{miss} as the magnitude of the negative sum of all \vec{p}_T objects. A more complete definition of E_T^{miss} is given by:

$$E_T^{\text{miss}} = |\mathbf{p}_T^{\text{miss}}| \quad (5.1)$$

$$\mathbf{p}_T^{\text{miss}} = \begin{pmatrix} E_x^{\text{miss}} \\ E_y^{\text{miss}} \end{pmatrix} \quad (5.2)$$

$$(\mathbf{p}_T^{\text{miss}}) = (\mathbf{p}_T^{\text{miss}})^{\text{Electrons}} + (\mathbf{p}_T^{\text{miss}})^{\text{Photons}} + (\mathbf{p}_T^{\text{miss}})^{\text{Muons}} + (\mathbf{p}_T^{\text{miss}})^{\text{Jets}} + (\mathbf{p}_T^{\text{miss}})^{\text{SoftTerm}} \quad (5.3)$$

The additional ‘‘soft term’’ $(\mathbf{p}_T^{\text{miss}})^{\text{SoftTerm}}$ differs between the Run-I and Run-II analyses. For Run-I analyses this includes all low momentum reconstructed jets ($p_T < 20$ GeV) and unmatched calorimeter clusters. In Run-II the soft term is built from tracks not associated to any reconstructed object.

⁸ID tracks are matched to small calorimeter energy deposits associated with minimally ionising particles

5.1.7 Signal Objects

An important concept in the analyses in this thesis is the definition of baseline and signal objects.

Baseline objects - electrons, photons, muons and jets are defined differently depending on the analyses described in this thesis (Run-I or Run-II). For example in the Run-II analyses, jets with $p_T > 20$ GeV and $|\eta| < 2.8$ are defined as baseline jets. Whereas in Run-I analyses, jets were said to be baseline jets if their $p_T > 20$ GeV and $|\eta| < 2.8$. Baseline jets tagged as originating from b-quarks (b-jets) are baseline jets with the additional criteria of: $|\eta| < 2.5$ and pass a loose b-tagging working point (85%).

Baseline electrons (muons) are defined with $|\eta| < 2.5$ (2.47), $p_T > 10$ GeV (Run-II) or $p_T > 7(8)$ GeV (Run-I) for electrons (muons). In both cases a loose identification of the leptons and photons is used [189, 187, 190].

Signal electrons, photons, muons and jets are isolated objects. Unless otherwise stated, the physics objects used, in the context of analyses, are signal objects. A signal jet is baseline jet passing a (Jet Vertex Tagger) JVT requirement⁹ [191] and bad jet removal¹⁰ [192]. Signal b-jets are signal jets with a typically tighter working point, all analyses in this thesis use a working point of 77% for signal b-tagged jets. Signal electrons are baseline electrons passing an isolation requirement¹¹ - $|d_0/\sigma(d_0)| < 5$, $|z_0 \sin \theta| < 0.5$, they are also required to pass tighter identification cuts. This identification differs between Run-I [193] and Run-II [189]. Similarly for muons, they are required to pass a tighter identification and $|d_0/\sigma(d_0)| < 3$, $|z_0 \sin \theta| < 0.5$.

A distinction is needed since the MC scale factors (see Section 5.4), used to match simulation to data, are calculated for the signal objects. For example, in zero lepton final state analyses (as will be presented in Section 7.1), it is advantageous to be able to veto on baseline leptons as opposed to signal leptons.

5.1.8 Truth Level Objects

As mentioned in Section 4.8.2, in the case of simulation, the generator level information can help understand the underlying physics behind the observed (reconstructed) physics objects. Throughout this thesis, generator level objects are referred to as *truth* objects. Figure 5.8 is a schematic diagram of a generator level $\tilde{t}\tilde{t}$ event produced by Sherpa [7] in a similar way to Figure 3.5. It illustrates both the generator level particle production and the detector level

⁹to remove pileup jets

¹⁰to remove badly reconstructed jets

¹¹ d_0 and z_0 are the transverse and longitudinal impact parameters defined in Section 5.1.3

measurement of the resultant particle fragments. Truth information is used to keep track of the underlying particles, decay products and hadronic fragments shown in this figure. Showers of truth level objects can be collected together as various radius jets using the same algorithms described in Section 5.1.2.

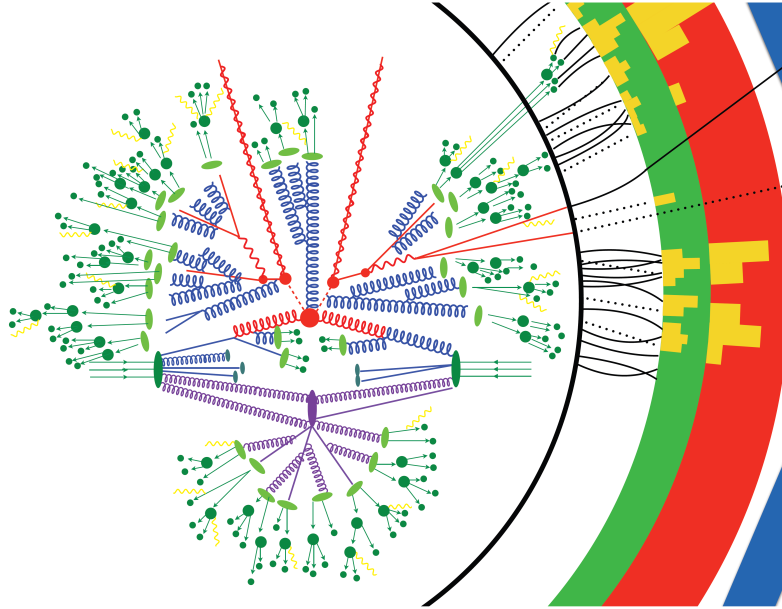


Fig. 5.8 Schematic diagram illustrating the interplay between the production at generator level and the measurement in the ATLAS detector of a scalar top event. Taken from [23].

5.2 Removing Overlapping Objects

In order to avoid double counting of final state objects, a procedure is followed to remove overlaps between final state objects. A common example of the need for this is the leptonic decay of a B-hadron resulting in a jet and muon in close proximity. Another example occurs when an isolated electron is reconstructed both as an electron and as a jet. The following lists the procedure to remove and select the most appropriate objects to be used:

- If an electron and a muon share a reconstructed track: if it is a Calo-Tagged (CT) muon, then the muon is removed, otherwise the electron is removed.
- If the distance between a jet and a baseline electron is $\Delta R < 0.2$ ¹², then the jet is removed.

¹²Here ΔR is defined as $\Delta R_{ij}^2 = \Delta\phi_{ij}^2 + \Delta\eta_{ij}^2$ where i is the first object and j is the second.

- In the case of the Run-II analyses if the jet is baseline b -tagged, instead the electron is removed.
- If the distance in ΔR between a jet and a baseline electron is $0.2 < \Delta R < 0.4$, then the electron is removed.
- If the distance in ΔR between a jet and a baseline muon is < 0.4 , then the muon is removed.
- Since no jets are tagged as originating from taus in any analyses described in this thesis, no overlap removal of tau-jets are performed.

5.3 Event Cleaning

All analyses performed in this thesis firstly remove any badly reconstructed objects, this is referred to throughout the text as *event cleaning*. The process of event cleaning removes any events which could potentially mimic any signal or warp data in regions of interest¹³. The following details various cleaning cuts that were applied to all data and simulated events:

Vertex selection Events with fewer than 2 tracks associated to the selected primary vertex are rejected.

Jet cleaning Fake jets can arise from non-collision backgrounds with a large muon energy deposit in the calorimeters. Fake signals in the calorimeter may also occur from noise bursts. A set of cuts are used to reject these jets. They are based on: the timing of the calorimeter signal with respect to that of the bunch crossing; on the quality of the fit to the calorimeter pulse shape; on the fraction of jet energy belonging to specific calorimeter samples; and on the amount of *jet charged fraction*¹⁴ - measured by the ID.

Muon cleaning Muons arising from cosmic background and badly reconstructed muons are rejected [194, 195].

For the Run-I $\sqrt{s} = 8$ TeV analyses additional cleaning of events was applied, due to the degradation of the detector over several years of previous LHC operations.

¹³The application of these so-called *cleaning cuts* differed between the Run-I and Run-II due to differences in the LHC conditions, the amount of pileup and the amount of degradation of the detector

¹⁴The jet charged fraction is defined as the ratio of the summed p_T of tracks associated to the jets divided by the jet's calibrated p_T .

Tile negative energy cleaning Cells and topoclusters in the Tile calorimeter can have large negative energy due to data corruption, leading to events with large fake missing transverse energy. Since these noisy cells with negative energy are not clustered in any jet, they are attributed to the soft E_T^{miss} term ($(\mathbf{p}_T^{\text{miss}})^{\text{SoftTerm}}$) of Equation 5.1. To reject events affected by noisy cells, the significance of the soft term contribution to the missing transverse energy is calculated. Events are rejected depending on the angular separation of $(\mathbf{p}_T^{\text{miss}})^{\text{SoftTerm}}$ and $\mathbf{p}_T^{\text{miss}}$ as well as the soft E_T^{miss} significance .

Tile hot cells In a portion of the 2012 Run-I dataset, a Tile calorimeter cell above the operating temperature was used in the reconstruction of objects. Events were removed if a jet points to the (η, ϕ) region close to the affected cell.

Dead Tile cells The Tile calorimeter had some non-operational sections during 2012 data taking affecting the jet reconstruction, jet energy response and resolution and is a source of fake missing transverse energy. These events are removed depending on various jet properties and the position of the jets [192].

5.4 Matching Simulation to Data

In order to correctly match simulation to data all simulated objects are passed through the same reconstruction software as data. In order to more correctly describe the data a series of *Scale Factors* are applied to a MC event depending on the properties of reconstructed physics objects. Typically for high enough p_T and central ($|\eta| < 2.5$) object scale factors are typically 0.9 – 1.0.

5.4.1 b-tagging SF

In the case of jets, scale factors are defined as the ratio between tagging efficiency in data (ϵ^{data}) and that in simulation (ϵ^{MC}), as measured in [196] and [197], in order to correct the tagging rate. The scale factors for b-tagged jets, c-tagged and light-quark jets are given by:

$$SF_b(p_T) = \frac{\epsilon_b^{\text{data}}}{\epsilon_b^{\text{MC}}}, \quad SF_c(p_T) = \frac{\epsilon_c^{\text{data}}}{\epsilon_c^{\text{MC}}}, \quad SF_l(p_T) = \frac{\epsilon_l^{\text{data}}}{\epsilon_l^{\text{MC}}}$$

The three weights are obtained per jet for $i = b, c, l$ and are given by:

$$w_{\text{jet}}^i = \begin{cases} SF_i(p_T) & \text{if jet is tagged with flavour } i \\ \frac{1-SF_i(p_T)\epsilon_i^{\text{MC}}}{1-\epsilon_i^{\text{MC}}} & \text{if jet is not tagged with flavour } i \end{cases} \quad (5.4)$$

The weight applied to the MC event is defined as:

$$w_{\text{event}} = \prod_j \prod_i^{n_{\text{jet } b,c,l}} w_j^i \quad (5.5)$$

5.4.2 Lepton SFs

Weights are also applied to events containing leptons, separately for muons and electrons. These SFs are p_T and η dependant, these measurements can be found in [189] and [198].

5.4.3 Other SFs

Additional weights are applied to account for any inefficiencies in the MC triggers with respect to data [199, 146, 200] as well as inefficiencies in the tagging of jets originating from pileup (JVT) [191].

5.4.4 Pileup weight

Knowing the exact pileup conditions is a difficult task as during the taking of data the LHC may be tuned to increase or decrease in-time pileup, manifested by the average number of interactions per bunch crossing ($\langle\mu\rangle$). When simulating either SM or BSM processes the effects of pileup on the MC have to be taken into account. Generally simulation is performed with an assumption on the range of $\langle\mu\rangle$. A reweighting procedure can then be applied to give more precedence to events with the correct value of $\langle\mu\rangle$.

5.5 Systematic Uncertainties

Many measurements are made in-situ in order to correctly calibrate the physics objects described in this section. With each measurement comes an uncertainty. These are referred to as detector systematic uncertainties throughout this thesis. When correcting reconstructed physics objects to truth level (calibration), values measured in data are used. All measurements have an associated uncertainty. When presenting physics results, these uncertainties

must be taken into account, by varying the MC simulation by $\pm 1\sigma$ of the measured values. These are the so-called *detector systematic uncertainties*. Other systematic uncertainties relating to *theory* are also evaluated.

5.5.1 Jet Energy Scale (JES)

The jet energy scale is used to calibrate reconstructed jets from an arbitrary energy scale to the true energy, as discussed in Section 5.1.2. This is essential in the search for new physics; for example, in searches for di-jet resonances, if jets are not calibrated to the correct scale then subsequent measurements of the invariant mass of a di-jet pair will give an incorrect value of the mass of a particle resonance.

This correction and its uncertainty are estimated using a combination of in-situ techniques exploiting the p_T balance between multi-jet events or the balance between a jet and a reference object (photon or a Z-boson) for $|\eta| < 4.5$ and $20 < p_T(\text{jet}) < 1000$ GeV. A series of techniques are used to extrapolate this to lower jet p_T , described in [201]. These measurements are also compared with a method where the jet energy scale is estimated from single-hadron (such as pions) response measurements. The single-hadron method is used for jets with $p_T(\text{jet}) > 1000$ GeV [202]. The JES uncertainty for EM-jets and LCW-jets is similar for jets of cone radius $R_C = 0.4$ [201].

As discussed in Section 5.1.2 LCW-jets were used in the Run-I analyses and EM-jets were used in the Run-II analyses. The calculation and application of the JES uncertainty differs between Run-I [201, 203] and Run-II [204]. In Run-I the uncertainty from the combination of in-situ and single-hadron measurements of the JES were combined into a single uncertainty of $\pm 1\sigma$ variations of the JES correction. However, in the 2015 Run-II dataset these measurements and combination were less complete [204], instead a method was employed to combine a number of these measured uncertainties into groups of three systematic uncertainties [205].

5.5.2 Jet Energy Resolution (JER)

Jets reconstructed in the calorimeters have some finite resolution describing how accurately the energy of the jet has been measured once they have been calibrated to the true jet energy scale (JES). MC simulation of the detector response smears the true jet energies measured in the calorimeters, the width of the Gaussian core of this smearing needs to accurately describe the real detector response. Measurements and corrections from Run-I data are described in [206], the resolution is primarily probed by the p_T balance of di-jet events. As

with the JES uncertainty this measurement and therefore the JER has an uncertainty which is taken into account.

5.5.3 B-tagging and Mis-tagging

The measured values in data are used to obtain the b-tagging SF as described Section 5.4.1. These are varied to create three b-tagging systematics depending on the b-tag rate, charm- and light-jet mis-tag rates. An additional systematic relates to the efficiency extrapolation at high p_T .

5.5.4 Missing Transverse Energy

E_T^{miss} is affected by systematic changes to calibrated physics objects entering the E_T^{miss} calculation. In addition to this a series of systematics relating to the calculation of the E_T^{miss} soft term are included. The definition of E_T^{miss} is different in the Run-I and Run-II analyses and therefore different systematic uncertainties apply. In Run-I the soft E_T^{miss} term is modified by soft term scale and resolution variations measured in data [207]. For Run-II soft track E_T^{miss} was used. Similarly, variations in the calculation of this quantity were applied. For more detail see [208].

5.5.5 Lepton Energy Scale and Resolution

As with jets, muons and electrons have an energy resolution and energy scale that is measured in data [198, 186]. Analogously to jets uncertainties on this calibration is taken into account. The efficiency of identifying electrons in the ID and muons in the ID and MS have associated efficiency with an error that is taken into account by three systematics varying the lepton scale factors defined in Section 5.4.2.

5.5.6 Pileup

A procedure for reweighting the simulated average interactions per bunch crossing to match the data distribution is applied. The measured value of pileup interactions in Run-I and Run-II data has an uncertainty. A systematic uncertainty accounts for this by altering the reweighting depending on the 1σ variations of this measured value ($\langle\mu\rangle_{\text{data}}$).

5.5.7 Theoretical Modelling Uncertainties

Another set of systematic uncertainties on the MC simulation arise from assumptions in the generation and showering of the MC¹⁵ as well as the cross-section of the simulated process. The uncertainty on the matrix element calculation, of a particular process, can be analysed by comparing the number of expected background events with two different MC generators with the same parton shower. Likewise, two samples using the same generator but with different parton showers can be used to estimate the uncertainty on the Parton Showering. There are additional prescriptions too where different parameters in the MC simulation are varied. For example, increasing the amount of ISR/FSR by varying the MC scales defined in Section 4.8.2.

5.6 Discriminant Variables

Once physics objects have been reconstructed, key kinematically based variables can be used for the purpose of separating the SM background from signal. They are also used for enhancing particular SM backgrounds to define control and validation regions (see Section 5.9).

The following lists the variables used in the analyses presented in this thesis, they are split into: physics objects based variables, variables sensitive to SM backgrounds and variables sensitive to signals of interest.

5.6.1 Object Based Variables

- N_X : Through this thesis, the number of physics objects¹⁶ described in Section 5.1 is denoted as so. This is key in picking out events where the signals of interest are expected to be present: regions with multiple b-jets and either zero or one lepton.
- $n_{extra\,jets}$: The number of non-*b*-tagged jets present in the event. This variable is specifically used to target the simplified supersymmetric model samples with short decay chains. Events from such scenarios are not expected to contain a high jet multiplicity.
- E_T^{miss} : The missing transverse momentum first defined in Section 3.2.4, Equation 5.1. As discussed previously, if SUSY is R-parity conserving then stable particles may be

¹⁵See Section 4.8.2.

¹⁶where X =baseline leptons, signal leptons, jets, b-jets, etc.

produced at the LHC. These particles would be manifested as large amounts of E_T^{miss} in an event.

- $\tilde{E}_T^{\text{miss}}$: Fake E_T^{miss} used in the estimation the $Z \rightarrow \nu\bar{\nu}$ background from $Z \rightarrow \ell\bar{\ell}$. The two well measured leptons can be used to mimic the E_T^{miss} from the two neutrinos. This variable is defined as:

$$\tilde{E}_T^{\text{miss}} = |\mathbf{p}_T^{\text{miss}} + \mathbf{p}_T(\ell_1) + \mathbf{p}_T(\ell_2)| \quad (5.6)$$

when two opposite sign signal leptons are present in the event their p_T is added vectorially to the missing transverse momentum.

- $(E_T^{\text{miss}})^\gamma$: Fake E_T^{miss} used in the estimation the $Z \rightarrow \nu\bar{\nu}$ background from γ events. Analogously to $\tilde{E}_T^{\text{miss}}$, the photon can be used to mimic the E_T^{miss} from the two neutrinos:

$$(E_T^{\text{miss}})^\gamma = |\mathbf{p}_T^{\text{miss}} + \mathbf{p}_T(\gamma)| \quad (5.7)$$

- ΣE_T : another important kinematic variable is the sum of the transverse energy, useful in determining how energetic an event is in the transverse plane. It is important for determining how significant the amount of E_T^{miss} is.
- H_T : The scalar sum of the p_T jets in an event. This variable is useful in separating signal from backgrounds. If there is a significant mass splitting between a SUSY particle decaying to another invisible SUSY particles and a visible SM particle then the latter particle can take large values of p_T . For scenarios in which SUSY particles have long decay chains, this quantity can be a useful discriminant.
- $\Delta\phi(X, Y)$: gives the angular separation between two physics objects (X, Y) . This can be important in picking out topologies of interest and reducing SM backgrounds.

5.6.2 Variables Sensitive to SM Backgrounds

- m_T : The transverse mass variable is defined in the case of one lepton as $m_T^2 = 2(E_T^{\text{miss}}E_T(\ell) - \mathbf{p}_T^{\text{miss}} \cdot \mathbf{p}_T(\ell))$. This variable separates SM backgrounds arising from W bosons decaying via a lepton and a lepton-neutrino. In these events the neutrino creates missing transverse energy and hence the value of m_T will be consistent with the mass of a W boson ($m_T < \sim 100$ GeV). This variable is also useful in rejecting events associated with fake-leptons.

- $m_{\ell\ell}$: The invariant mass of two leading leptons¹⁷. This variable is particularly useful in selecting events with leptonic decays of Z bosons ($Z \rightarrow \ell\ell$). The invariant mass of the lepton pair associated with the Z boson will be consistent with the Z boson mass.
- m_{bb} : The invariant mass of two leading b-tagged jets. This variable is useful for rejecting events which rise from $t\bar{t}$ backgrounds. If two high p_T b-jets are present, these are most likely to originate from the top and anti-top decay “legs”. Therefore the value of m_{bb} , for two high p_T b-jets ($p_T > 20$ GeV), will form a random distribution - peaked at values of $m_{bb} < 200$ GeV. In addition to this, events with b-jets arising from either ISR or FSR gluon splitting will be significantly reduced.
- m_{bj} : is also another invariant mass variable for the leading b-tagged jet and the leading non b-tagged jet. It can also be used to reduce the $t\bar{t}$ background for values < 200 GeV. A top quark will decay with a branching ratio of $\text{BR}(t \rightarrow Wb) \approx 1$. A W boson will then decay with a branching ratio of $\text{BR}(W \rightarrow \text{hadrons}) \approx 68\%$, forming hadronic jets. Therefore this variable can be used to reduce the number of events consistent with the top mass, $m_{bj} < 200$ GeV.
- $m_{b\ell}^{\min}$: The minimum invariant mass of a lepton and two b-tagged jets. Defined as $m_{b\ell}^{\min} = \min(m(b_1, \ell), m(b_2, \ell))$. In the case of $t\bar{t}$ production, if the invariant mass of a b-jet and a lepton is less than the top mass it can be considered that the pair is consistent with a top quark. By finding the minimum possible combination of the lepton with the two b-jets and applying a requirement for the quantity to be inconsistent with a top quark ($m_{b\ell}^{\min} > 170$ GeV) the $t\bar{t}$ background can be greatly reduced, and hence the SM background arising from single-top production can become more significant.
- $\min[\Delta\phi(\text{jet}_{1-4}, E_T^{\text{miss}})]$: The minimum azimuthal distance between the closest leading four jets (1 – 4) and the E_T^{miss} . As mentioned in the previous chapter this variable is a key discriminant for rejecting multi-jet events (QCD background). When a jet or multiple jets undergo p_T fluctuations creating E_T^{miss} , the E_T^{miss} is likely to be aligned with one of these jets.
- E_T^{miss} **Sig.:** The significance of the missing transverse energy.

$$E_T^{\text{miss}} \text{ Sig.} = \frac{E_T^{\text{miss}}}{\sqrt{X}} \quad (5.8)$$

¹⁷objects are ordered by p_T

where X can be taken as the variable H_T or ΣE_T . This variable is important in the selection of well measured multi-jet events which arise from QCD interactions. This variable is key for the method described in Section 6.1.

5.6.3 Variables sensitive to BSM signals

- m_{CT} : The contranverse mass kinematic variable [209] used to estimate the masses of pair-produced semi-invisibly decaying particles. m_{CT} is defined as:

$$m_{CT}^2(v_1, v_2) = [E_T(v_1) + E_T(v_2)]^2 - [\mathbf{p}_T(v_1) - \mathbf{p}_T(v_2)]^2 \quad (5.9)$$

where $E_T = \sqrt{p_T^2 + m^2}$. As shown in [209] the variable has a kinematical endpoint at:

$$m_{CT}^{\max} = \frac{m_i^2 - m_X^2}{m_i^2} \quad (5.10)$$

where i is the initially pair produced particle and X is the invisible particle they both decay into. This property is key in the variable's ability to discriminate between signal and particular SM backgrounds. In the case of the scalar bottom signal the two visible particles (v_1, v_2) are the b -tagged jets, the two invisible particles (X_1, X_2) are the two neutralinos ($\tilde{\chi}_1^0$). For $t\bar{t}$ decays, where the decay products of the W boson are soft or not reconstructed, v_1 and v_2 are again the b -tagged jets, X_1 and X_2 are the two W bosons from the two top decays. This gives a value of $m_{CT}^{\max} = 135$ GeV for $t\bar{t}$, for signals with small neutralino masses this endpoint becomes $m_{CT}^{\max} \approx m_{\tilde{b}}$. Hence this variable is used in rejection of the $t\bar{t}$ background, as well as increasing the significance (see Section 5.8) of pair produced semi-invisibly decaying heavy particles. As demonstration of this can be seen in Figure 5.9.

- am_{T2} : The asymmetric transverse mass [210, 211] is a kinematic variable which can be used to separate processes in which two decays giving missing transverse energy occur. m_{T2} is defined as follows:

$$m_{T2}^2(\chi) = \min_{\mathbf{q}_T^{(1)} + \mathbf{q}_T^{(2)} = \mathbf{p}_T} \left[\max \left\{ m_T^2(\mathbf{p}_T(v_1), \mathbf{q}_T^{(1)}; \chi), m_T^2(\mathbf{p}_T(v_2), \mathbf{q}_T^{(2)}; \chi) \right\} \right] \quad (5.11)$$

where $\mathbf{p}_T(v_i)$ are reconstructed transverse momenta vectors. $\mathbf{q}_T^{(i)}$ represent the missing transverse momenta from the two decays, with a total missing transverse momentum, \mathbf{p}_T . χ is a free parameter representing the unknown mass of the invisible particles. The

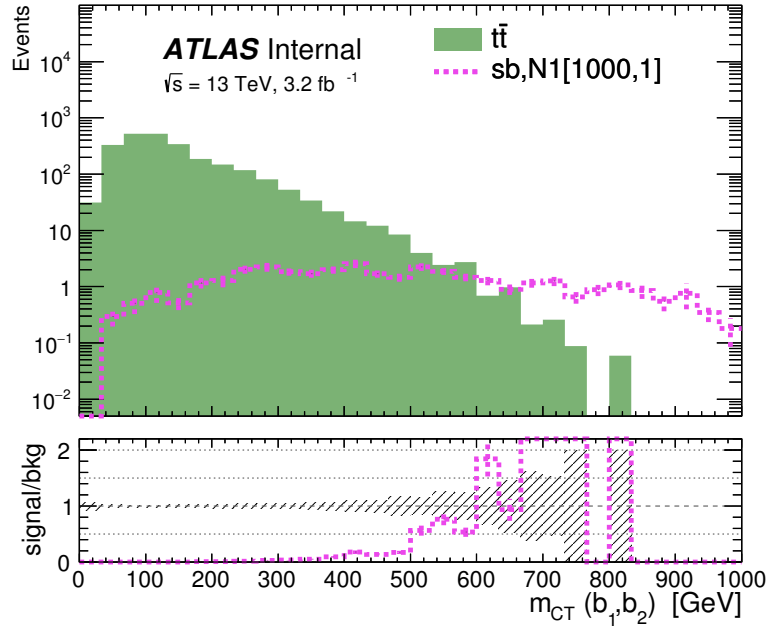


Fig. 5.9 Simulated distributions of the m_{CT} discriminant for $t\bar{t}$ and a supersymmetric signal model with a scalar bottom mass of 1000 GeV and a neutralino mass of 1 GeV.

a in am_{T2} indicates that the two visible decay legs are asymmetric, i.e. not composed of the same particles.

m_{T2} is calculated for different values of $\mathbf{p}_T(v_1)$ and $\mathbf{p}_T(v_2)$, since it is not known whether the lepton belongs to the decay leg of the first or the second b -tagged jet. This makes m_{T2} asymmetric. In practice, the lepton needs to be paired with one of the two b -jets, this choice is driven by the value of $m_{bl}(n)$ - the invariant mass of the n^{th} b -tagged jet and the lepton. If the two particles are correctly coupled, this value has an upper bound given by the top quark mass (see Table 2.2). The value of am_{T2} is thus computed accordingly:

- If $m_{bl}(1)$ and $m_{bl}(2)$ are both > 170 GeV, none of the two couplings is compatible with the b -jet and the lepton coming from a top decay.
- If $m_{bl}(1)$ is < 170 GeV and $m_{bl}(2)$ is > 170 GeV, m_{T2} is calculated with $v_1 = b_1 + \ell$ and $v_2 = b_2$. This is done because only the first pairing is compatible with a top quark decay.
- Similarly, if $m_{bl}(1)$ is > 170 GeV and $m_{bl}(2)$ is < 170 GeV, m_{T2} is calculated with $v_1 = b_1$ and $v_2 = b_2 + \ell$.

- If $m_{b\ell}$ (1) and $m_{b\ell}$ (2) are both < 170 GeV, m_{T2} is calculated in both configurations and its value is taken to be the minimum of the two. This must be done, since according to the $m_{b\ell}$ check both pairings would be acceptable.
- m_{eff} : The effective mass of an event is defined as the scalar sum of H_T and the E_T^{miss} . This is also a key variable in separating SM backgrounds from supersymmetric backgrounds. When supersymmetric particles decay, depending on mass splittings, they transfer large amounts of energy to their decay products. This results in large momentum boosts of visible particles (large values of H_T) or a large momentum boost to the invisible particles (large values of E_T^{miss}) or a mixture of the two. Therefore selections on m_{eff} instead of separate selections on H_T and E_T^{miss} can be a more powerful discriminant.

5.7 Statistical Tools

In experimental particle physics large data sets are analysed with great precision, in order to measure the properties of fundamental particles or to claim the discovery of a new particle, statistical interpretation of the data is needed.

In searches for SUSY, a *signal grid* is formed by varying parameters of a particular model. For example, varying the mass of the scalar bottom quark and the mass of the lightest neutralino. Multiple signal points on this grid are *optimised* by varying kinematic selections on both the background and signal. The statistical significance of the signal plus background hypothesis is tested by some function:

$$Z(s+b, b, \sigma_s, \sigma_b) \tag{5.12}$$

Where s is the number of signal events for a particular grid point, b is the number of SM background events and σ is the simulation uncertainty. The cuts associated with the best significance are then used to design Signal Regions (SRs). Once the analysis has been performed on data, the statistical interpretation of $Z(N_{\text{obs}}, b, \dots)$ versus $Z(s+b, b, \dots)$ (where N_{obs} is the number of observed events in data) is made in order to either claim a discovery or set exclusion limits on the signal model.

Additionally, statistical tools are used to evaluate the SM backgrounds in Control Regions (CRs) and Validation Regions (VRs). When using MC simulation as the SM background it is important to evaluate how well the SM background is modelled in a region close to the signal region - but is not contaminated by the signal. If the MC underestimates the amount of data this can lead to incorrect interpretation of the results, in order to avoid this many analyses

normalise MC in various CRs - this is a semi-data-driven technique. The use of VRs is to validate the normalisation obtained in the CRs in a region that may be closer to SR but with a much smaller number of expected signal events.

The statistical software framework used by multiple analyses in the search for SUSY with ATLAS is called *HistFitter* [212]. The software handles multiple SM backgrounds and signal samples in CRs, VRs, SRs; taking into account statistical, detector and theoretical uncertainties which may or may not be correlated between the various regions. Chapter 5.9 describes the framework in more detail.

5.8 Significance

Analyses may have multiple SRs, which are optimised for particular signal models by tuning cuts on observable quantities. It is important to have a figure of merit to quantify the significance of the signal versus background. The most basic form of significance is given by:

$$Z = \frac{s}{\sqrt{b + (\sigma_b b)^2}} \quad (5.13)$$

where s is the number of expected number signal events, b is the total number of background events and σ_b is the relative background uncertainty on the total background. This definition breaks down if either the raw MC statistics of either the signal or background become small or the overall total background yield becomes small (< 5 events). To account for this in the optimisation, minimum requirements on these numbers can be required, alternatively Equation 5.13 can be modified with $\sigma_b b \rightarrow \sigma_b b + 1$ to prevent the significance becoming too large with a small background yield. Optimisation scans are generally performed making an assumption on σ_b , e.g. 30% uncertainty.

Equation 5.13 is a first order approximation of the following significance definition in the limit of large $s + b$ [213, 214] :

$$Z = \phi^{-1} \left(1 - B \left(\frac{1}{1 + \tau}; s + b, \tau b \right) \right) \quad (5.14)$$

where $B(x; y, z)$ is an *incomplete beta function*¹⁸ [215], ϕ^{-1} is the inverse of the cumulative distribution of the standard Gaussian (quantile) using an approximation method [216] and $\tau = \frac{\sigma_b^2}{b}$. This definition of Z is available in the *RooStats* package [217] for ROOT [218] and can be used to obtain a more accurate value of Z with low background yields.

¹⁸ $B(x; y, z) = \int_0^x t^{y-1} (1-t)^{z-1} dt$

5.9 HistFitter

A typical analysis strategy flow using the HistFitter framework [212] is shown in Figure 5.10. The first step when using CRs for a semi-data-driven background estimate of multiple SM processes is to obtain normalisations via a likelihood fit in CRs dominated by the SM background processes. From this, *transfer factors* (TFs) for each normalised background (i) are obtained, this converts the observation of the number of events in the CRs to an SR estimates via:

$$N_i(SR, est.) = N_i(CR_p, obs.) \times \left[\frac{MC_i(SR, raw)}{MC_i(CR, raw)} \right] \quad (5.15)$$

$$= \mu_i \times MC_i(SR, raw) \quad (5.16)$$

where the square brackets indicate the TF, μ_i is the normalisation factor obtained from the background fit in the CRs.

Importantly, with the use TFs (and μ_i), systematic uncertainties on the background processes can be significantly reduced by cancellation if there is little extrapolation between a CR and a VR/SR. It is therefore necessary to keep the definitions of all the regions kinematically similar as possible - while remaining orthogonal and retaining a large total number of events. Using this semi-data-driven approach, the remaining uncertainty of the background estimate in the SR are the MC statistical uncertainty, theoretical uncertainties and residual systematic uncertainties from the extrapolation.

5.9.1 Likelihood Fit

The HistFitter software constructs a likelihood function of the analysis as a product of Poisson distributions of the number of events in the SR(s) and CR(s). Additionally, Gaussian distributions describing the systematic uncertainties are included in the likelihood function of the analysis [169]:

$$\begin{aligned} L(\vec{n}, \vec{\theta}^0 | \mu_{sig, s}, \vec{\mu}, \vec{b}, \vec{\theta}) &= P_{SR} \times P_{CR} \times C_{syst} \\ &= P(n_{SR} | \lambda_{SR}(\mu_{sig, s}, \vec{b}, \vec{\theta})) \times \prod_{i \in CR} P(n_i | \mu_i \cdot \lambda_i(\vec{b}, \vec{\theta})) \times C_{syst}(\vec{\theta}^0, \vec{\theta}) \end{aligned} \quad (5.17)$$

where $P(n, \lambda) = \frac{\lambda^n e^{-\lambda}}{n!}$ is a poissonian distribution, n_{SR} is the number of events in the signal region, n_i is the number of events in the control region, λ are functions describing the number of expected events, dependent on: the predictions for multiple backgrounds, \vec{b} ; the nuisance

parameters associated with systematic uncertainties¹⁹, $\vec{\theta}$; the normalisation factors for the background processes, μ_i ; and the signal strength parameter, μ_{sig} ²⁰.

The systematic uncertainties are represented by a product of Gaussian distributions:

$$C_{syst}(\vec{\theta}^0, \vec{\theta}) = \prod_{j \in S} G(\theta_j^0 - \theta_j) \quad (5.18)$$

where θ_j^0 are auxiliary measurements around which θ_j are varied to maximise the likelihood.

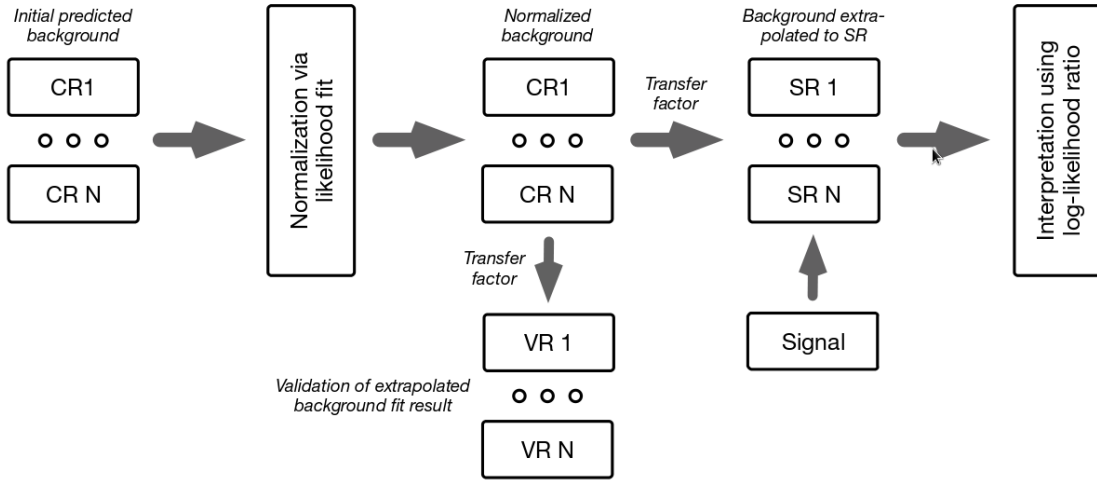


Fig. 5.10 A typical analysis strategy flow with HistFitter with N CRs, N VRs and N SRs. Taken from [24].

5.9.2 Profile Likelihood Ratio

Equation 5.17 is used to obtain probability values (p-values) from which a Confidence Level (CL) can be obtained for a discovery, model dependent exclusion and model independent exclusion as described in [219]. In cases where there is only one parameter of interest, e.g. μ_{sig} of Equation 5.17, a profile likelihood ratio is used. The profile log likelihood ratio is defined as [220, 24]:

$$q_{\mu_{sig}} = -2 \log \left(\frac{L(\mu_{sig}, \hat{\theta})}{L(\hat{\mu}_{sig}, \hat{\theta})} \right) \quad (5.19)$$

¹⁹e.g. $\theta_i = \pm 1$ for $\pm 1\sigma$ variations, $\theta_i = 0$ for the nominal template.

²⁰For $\mu_{sig} = 0$ the signal component is turned off and for $\mu_{sig} = 1$ the nominal value of the signal yield.

Here $\hat{\mu}_{sig}$ and $\hat{\theta}$ are fitted values which maximise Equation 5.17, using compressed notation $\theta = (\vec{\theta}, \vec{b})$. $\hat{\theta}$ maximises the likelihood function for a fixed value of μ_{sig} .

In the limit of a large statistics the likelihood distribution approaches a Gaussian and $q_{\mu_{sig}}$ follows a χ^2 distribution²¹ [220]. The importance of this is that confidence levels can be easily obtained on the profiled parameter.

The definition of the profile likelihood ratio differs depending on the type of fit being performed, as shown in Table 5.1.

Table 5.1 Types of fits performed by HistFitter.

Fit setup	background-only	model-dependent	model-independent
Samples	backgrounds ($\mu_{sig} = 0$) $\lambda_{SR} = b$	backgrounds + signal ($\lambda_{SR} = \mu_{sig} \cdot s + b$)	backgrounds + dummy signal
Fit Regions	CR(s)	CR(s) + SR(s)	CR(s) + SR(s)

5.9.3 Background-only Fit

When displaying tables showing the observed yields in CRs, VRs and SRs a simultaneous background-only fit has been performed in the CRs only. The fit of the CRs obtains the normalisation values μ_i which are firstly validated in the VRs before being used in the SRs. Once applied to the background processes of the SRs the discovery significance of the amount of observed data versus the expected background is determined. Setting $\mu_{sig} = 0$ in Equation 5.19 determines the probability that a background-only experiment is more signal like than observed. In the case of a positive signal²², Equation 5.19 becomes:

$$q_0 = \begin{cases} -2 \log \left(\frac{L(0, \hat{\theta})}{L(\hat{\mu}_{sig}, \hat{\theta})} \right) & \hat{\mu}_{sig} \geq 0 \\ 0 & \hat{\mu}_{sig} < 0 \end{cases} \quad (5.20)$$

The discovery p-value is defined as:

$$p_0 = \int_{q_0 \text{ obs.}}^{\infty} f(q_0|0) dq_0 \quad (5.21)$$

Where $f(q_0|0)$ is a *probability distribution function* (PDF²³) in the range $n_{SR} = \{0, \dots, \infty\}$ for a fixed value of $\mu_{sig} = 0$. $q_0 \text{ obs.}$ is the observed value of Equation 5.20 in data, per

²¹in the asymptotic limit

²²i.e. the signal cannot reduce the background

²³Not to be confused with a Parton Distribution Function.

SR. The particle physics community define a discovery to a p-value of $p \leq 2.87 \times 10^{-7}$, corresponding to a significance $Z \geq 5$.

In the case of large SR statistics the PDF, $f(q_0|0)$, is easily approximated using an *asymptotic limit*, see [219]. However, in the case of small statistics (less than $\mathcal{O}(10)$ events expected in the SR) the distributions is obtained by generating large numbers of *pseudo-experiments* or *toy-model* that randomise the central values (θ^0) of the auxiliary measurements and the number of observed events [169]. The use of the asymptotic approximation or toy-model is indicated in each analysis.

5.9.4 Model-dependent Fit

The purpose of a model-dependent fit is to set exclusion limits on the signal model of interest. A fit is performed per signal point on the signal grid with s equal to the number of expected signal events for that point. In the case of an observed excess in the signal region the model-dependent fit can be used to evaluate the probability the excess is consistent with the optimised signal.

A non-zero normalisation factor, μ_{sig} , is included in the likelihood fit with $\lambda_{SR} = \mu_{sig} \cdot s + b$. If $\hat{\mu}_{sig}$ is found to be negative, the best agreement between prediction and data is found for $\mu_{sig} = 0$. The profile likelihood ratio is given by:

$$q_{\mu_{sig}} = \begin{cases} -2 \log \left(\frac{L(\mu_{sig}, \hat{\theta}(\mu_{sig}))}{L(\hat{\mu}_{sig}, \hat{\theta})} \right) & \hat{\mu}_{sig} \geq 0 \\ -2 \log \left(\frac{L(\mu_{sig}, \hat{\theta}(\mu_{sig}))}{L(0, \hat{\theta}(0))} \right) & \hat{\mu}_{sig} < 0 \end{cases} \quad (5.22)$$

Analogous to the previous background-only fit, the p-value can be determined for the signal plus background hypothesis. The particle physics community define a signal sample to be excluded if a p value of $p \geq 0.05$ (i.e. 2σ , 95% CL exclusion) is found, corresponding to a significance of $Z < 1.64$.

5.9.5 Model-independent Fit

In the case of finding no significant SR excess it is useful to interpret the exclusion power of the analysis on any signal model, SUSY or not. The results of this type of fit can be used in future interpretations of the analysis with any kind of model. The fit is used to set *95% CL upper limits* on the number of signal events given the observed and expected background events (S_{obs}^{95} and S_{exp}^{95}), i.e. any model predicting more events in the SR would be excluded. A

similar definition to Equation 5.22 is used in upper limit setting instead with the number of expected signal events is unknown and is an additional maximised fit parameter.

Chapter 6

Jet Smearing

In searches for new physics final states containing multiple jets and large amounts of missing transverse momentum, the SM background arising from severe mis-measurement of multi-jet events¹ is particularly important to control and remove. Extensive studies [221, 222] have shown that at high values of E_T^{miss} the so called mis-measured multi-jet background is dominated by the mis-measurement of partons as they decay and shower. For analyses with multiple b-tagged jets in their final states, as presented in this thesis, the modelling of the mis-measurement of b-quarks as they decay is of key importance.

The following section describes a data-driven estimation technique, known as *JetSmearing* which was used by many searches for SUSY to estimate the multi-jet backgrounds during both Run-I and Run-II of the LHC.

The method is data-driven and hence provides an alternative estimation technique to simulating this background which is difficult and often inaccurate for several reasons. Firstly, the amount of simulated events needed to be generated in order to be mis-measured so significantly by detector effects is incredibly large. Secondly, simulation is often inaccurate (at large values of E_T^{miss}) due to the dependence on the jet energy resolution (JER). In fact, in-situ corrections to *gaussian core* of the JER from data are applied in simulations, but not applied to the *non-gaussian tails*. Thirdly, this background is a reducible background, meaning it is dependent on the pileup conditions of the LHC which can vary significantly over a data taking period. The data-driven approach of *JetSmearing* deals with these issues that arise in simulation of the multi-jet background.

In a nutshell, the *JetSmearing* technique is performed as follows: well measured data events are firstly selected, this is referred to the *seed selection* stage, more detail is provided in Section 6.3.1 ; every jet in these events are then smeared n times, see Section 6.3.2, by a predetermined jet response function (Section 6.2) which has been corrected to match

¹often referred to as the QCD background.

data (Section 6.4), for every seed event, n pseudo-data events are hence generated, some of which may have significant E_T^{miss} depending on the amount the jet responses have been altered; uncertainties on the pseudo-data from the seed selection and response corrections are evaluated; finally, to provide an estimate of this background in a signal region, the pseudo-data is normalised to a multi-jet rich region.

6.1 JetSmearing Technique

The ATLAS detector reconstructs physics objects with varying degrees of precision. Since the detector is not perfect all physics objects are associated with an intrinsic resolution, in the case of jets, this is referred to as the *jet energy response*, and is defined as:

$$R_{\text{MC}} = \frac{E^{\text{RECO}}}{E^{\text{TRUTH}}} \quad (6.1)$$

The response describes how accurately the ATLAS detector measures the reconstructed energy of a jet (E^{RECO}). It can be derived from MC as a function of the event generation level (truth) jet transverse momentum (p_T^{TRUTH}). If $R_{\text{MC}} < 1$ then it can be said that the jet has had its E_T under-measured, similarly if $R_{\text{MC}} > 1$ then its E_T has been over-measured. Figure 6.1 shows two examples of the b-veto² and b-tagged jet response for a slice in p_T of $\in [500, 1000]$ GeV jets. The response for b-veto and b-tagged jets are plotted separately due to heavy flavour decays containing real missing energy from neutrino decays. Two distinct regions can be seen: the Gaussian core; and the non-Gaussian low-side tail. In the case of b-tagged jets, the non-Gaussian low-side tail is much larger.

There are many sources of jet mis-measurement, for both the Gaussian core and the non-Gaussian parts of the jet response:

- Hadronic calorimeters are not perfect; there is some limit to granularity of calorimeters therefore they are not able to perfectly measure the energy of all particles. The broad Gaussian core of the jet response is dominated by the statistics of the calorimeter's resolution.
- Since jets are clusters of showering particles, it is possible that not all of these particles can be contained within the jet radius. Some of the showering particles may be lost due to interacting with non-detector material such as service cables. Additionally, background particles from various different sources may enter into a jet cone, although

²b-tagged jet veto

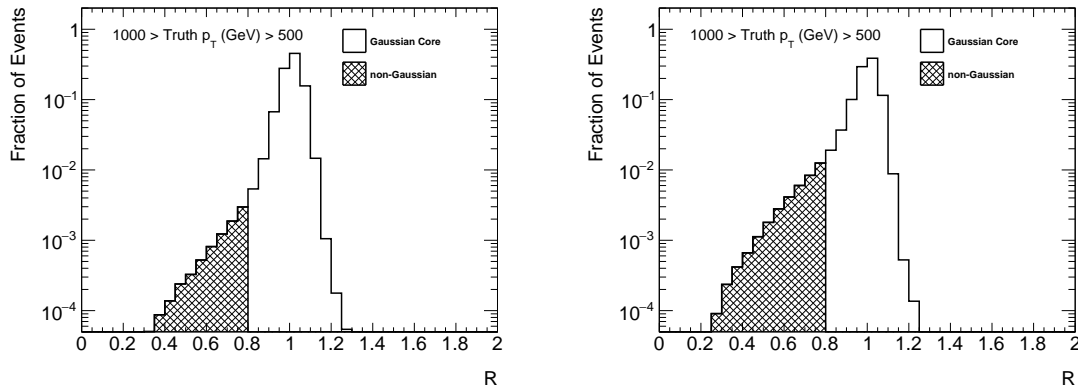


Fig. 6.1 Jet response, R_{MC} , for Truth jets with $500 < p_T < 1000$ GeV for b-veto jets on the left and b-tagged jets on the right. Two distinct regions of the jet response are shown: the main body of the response, known as the Gaussian core; and the non-Gaussian low-side tail.

this effect is reduced by cosmic background vetos and the overlap removal of other jets, photons, electrons and muons.

- Not all jets are fully contained within the calorimeter systems, if a jet has large amounts of energy, it can punch through to the muon system and potentially large amounts of the energy can be lost. This is one such source of the non-Gaussian part of the jet response; this effect always gives lost energy rather than an overestimation of the energy.
- Jets that are close to areas of large amounts of dead material are vetoed, however there are still regions with small amounts of dead material in the calorimeters which can cause particles to deposit their energy. The sources of dead material include damaged or inactive parts of the detector, services for running electronics to the detector and various non-instrumented regions from the support structure of ATLAS.
- In decays of heavy flavour quarks, particularly those of b-quarks, real missing energy can be present from neutrinos. Typically: $\approx 76\%$ of b-quark decays will be hadronic (including hadronic tau decays); leaving 12% of decays with muons and muon neutrinos; and 12% of decays with electrons and electron neutrinos. The decays involving neutrinos will carry a fraction of the jet energy with them, this gives a larger non-Gaussian tail in the case of b-tagged jets.

Motivation As seen in Figure 3.2 the production cross section for multi-jet events is of the order $10^5 - 10^7$ times larger than the production cross section of the signal models of many searches for SUSY. The production cross sections for the multi-jet events is so large

that a significant amount of multi-jet events with large amounts of jet mis-measurement are recorded. For example, Figure 6.1, with Truth jets of $1000 > p_T > 500$ GeV, has $\mathcal{O}(10^{-4})$ of events with a jet response of $R_{MC} \approx 0.4$. If a jet of $p_T = 500$ GeV is mis-measured by this amount it can give up to $E_T^{\text{miss}} = 300$ GeV.

Event Smearing The premise of the JetSmearing technique is that, if very well measured hadronic events can be selected, referred to as “seed” events, then each jet in the event can have its energy altered depending on the measured R_{MC} ³.

Considering a hadronic event with m jets, n pseudo-events can be created by smearing each jet with a random number chosen from the template of the R_{MC} distribution depending on the p_T of the jet. The process of smearing therefore requires $n \times m$ random numbers to be selected:

$$\begin{array}{c} \left(\begin{array}{c} E_0 \\ \vec{p}_0 \end{array} \right), \left(\begin{array}{c} E_1 \\ \vec{p}_1 \end{array} \right) \cdots \left(\begin{array}{c} E_m \\ \vec{p}_m \end{array} \right) \end{array} \longrightarrow \begin{array}{c} \left(\begin{array}{c} a_0 \cdot E_0 \\ a_0 \cdot \vec{p}_0 \end{array} \right), \left(\begin{array}{c} a_1 \cdot E_1 \\ a_1 \cdot \vec{p}_1 \end{array} \right) \cdots \left(\begin{array}{c} a_m \cdot E_m \\ a_m \cdot \vec{p}_m \end{array} \right) \\ \left(\begin{array}{c} b_0 \cdot E_0 \\ b_0 \cdot \vec{p}_0 \end{array} \right), \left(\begin{array}{c} b_1 \cdot E_1 \\ b_1 \cdot \vec{p}_1 \end{array} \right) \cdots \left(\begin{array}{c} b_m \cdot E_m \\ b_m \cdot \vec{p}_m \end{array} \right) \\ \vdots \\ \left(\begin{array}{c} n_0 \cdot E_0 \\ n_0 \cdot \vec{p}_0 \end{array} \right), \left(\begin{array}{c} n_1 \cdot E_1 \\ n_1 \cdot \vec{p}_1 \end{array} \right) \cdots \left(\begin{array}{c} n_m \cdot E_m \\ n_m \cdot \vec{p}_m \end{array} \right) \end{array}$$

(seed event) (pseudo events)

The random numbers (a_i, b_i, \dots, n_i) alter the jet energy. Assuming that the amount of real- E_T^{miss} in the seed event is small, the amount of E_T^{miss} in each pseudo-event can be much larger depending on the alignment of the jets. The vector sum of jet transverse momenta, smeared jet p_T s and post-smearing E_T^{miss} is given as:

$$\sum_i^m \vec{p}_T(j_i) = \vec{p}_T(0) + \vec{p}_T(1) + \cdots + \vec{p}_T(m) \quad (6.2)$$

$$\sum_i^m \vec{p}_T(j_i)' = a_0 \cdot \vec{p}_T(0) + a_1 \cdot \vec{p}_T(1) + \cdots + a_m \cdot \vec{p}_T(m) \quad (6.3)$$

$$\vec{p}_T^{\text{miss}'} = \vec{p}_T^{\text{miss}} + \sum_i^m \vec{p}_T(j_i) - \sum_i^m \vec{p}_T(j_i)' \quad (6.4)$$

Here, the primes indicate the pseudo-event after one event smear with m random numbers for m jets. This can be then repeated n times to generate n pseudo-events ($\sum_{a=0}^n$).

An overview of the method is shown in Figure 6.2.

³For a jet of cone size $R_C = 0.4$ it is assumed that $|\vec{p}| \gg m$

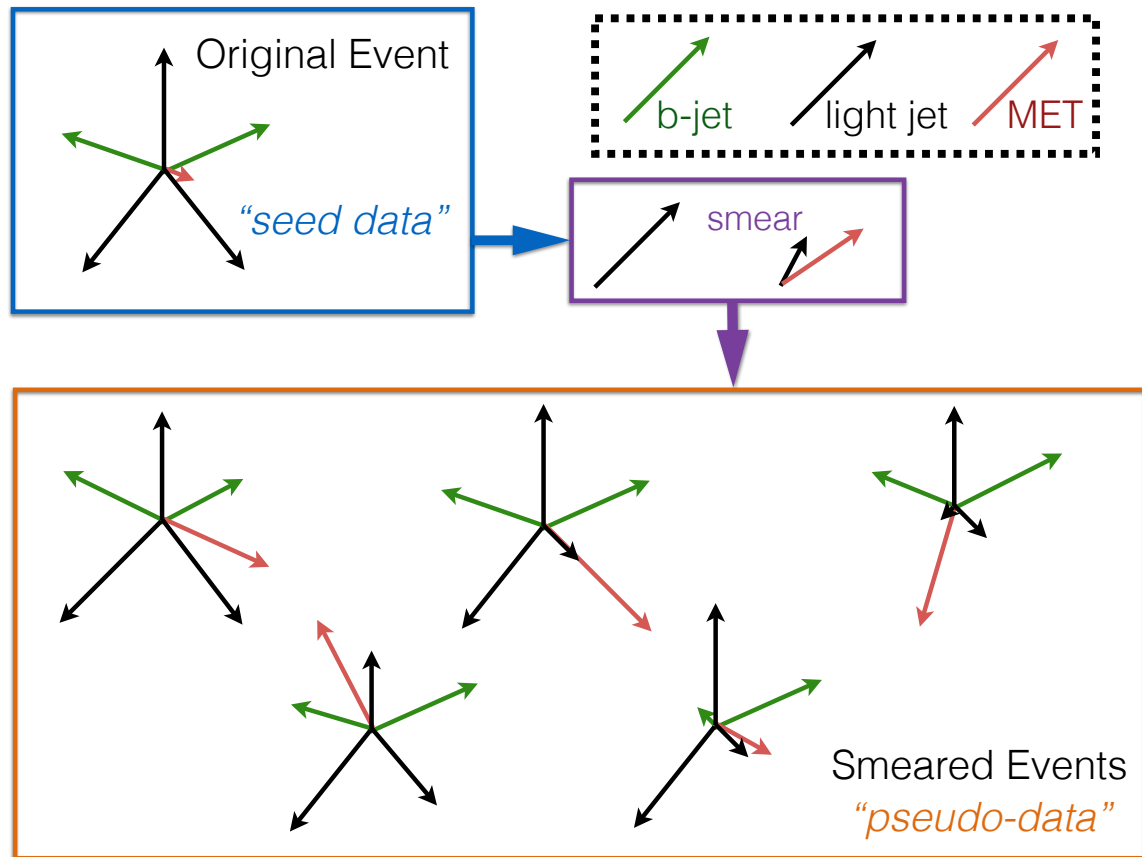


Fig. 6.2 A pictorial overview of the JetSmearing method in the transverse plane (p_x, p_y). Jets are indicated by the black arrows, b-jets by green arrows and E_T^{miss} (MET) indicated by red arrows. The size of the arrows indicates the magnitude of the transverse energy (momentum). Well measured events are first selected in data. Each jet in the event is then smeared n times to create n pseudo-events. This is performed via a smearing response map derived in MC and corrected for in data.

6.2 Constructing the Jet Response

The jet response, R_{MC} , is defined in Equation 6.1. Multi-jet events are simulated using *Pythia8* [223] monte-carlo. They are initially used to construct the jet response. The construction proceeds as follows:

1. *Pythia8* [223] MC events were used to simulate multi-jet events. Generator level (truth) jets reconstructed with the anti- k_T algorithm with a cone radius $R_C = 0.4$ and $p_T > 20$ GeV are selected.
2. Each truth jet is matched with a reconstructed jet of $p_T > 20$ GeV⁴. This is performed by finding the closest reconstructed jet in ΔR^5 to the truth jet.
 - (a) If no reconstructed jet is within $\Delta R < 0.3$ of the truth jet, the truth jet is skipped.
 - (b) If a second reconstructed jet is within $\Delta R < 0.6$ of the truth jet, the matching is not unique and the truth jet is skipped.
 - (c) If any other reconstructed jet is within $\Delta R < 0.6$ of the matched reconstructed jet, the jet is not isolated, therefore the jets are not used in the construction of R_{MC} .
 - (d) If any other truth jet is within $\Delta R < 0.6$ of the truth jet, the truth jet is not isolated, therefore both truth jets are skipped.
3. Truth muons are added to the four-momentum of the truth jet if they are within $\Delta R < 0.4$. This is because the generator level jets are electro-magnetic topoclusters (EMTopo) and therefore already include electrons. This way, leptonic decays within jets are modelled correctly, which is particularly important for Heavy Flavour (HF) decays.
4. For the same reasons, reconstructed muons are added to the four momentum of the reconstructed jet if they are within $\Delta R < 0.4$.
5. Finally, truth neutrinos are added to the four-momentum of the truth jet if they are within $\Delta R < 0.4$, accounting for the presence of real E_T^{miss} associated with jets. The amount of real E_T^{miss} associated with a jet is higher in Heavy Flavour (HF) decays.
6. Two separate response maps are built depending on whether or not the reconstructed jet is b-tagged⁶.

⁴No overlap removal of objects is performed

⁵Reminder: $\Delta R_{ij}^2 = \Delta\phi_{ij}^2 + \Delta\eta_{ij}^2$ is the distance in $\phi - \eta$ space between an object i and an object j .

⁶with a 77% OP, see Chapter 5.1.3

Figure 6.3a shows R_{MC} for non-b-tagged (b-veto) jets and Figure 6.3b shows R_{MC} for b-tagged jets as a function of jet p_T . A larger non-gaussian tail for all p_T in the case of b-tagged jets.

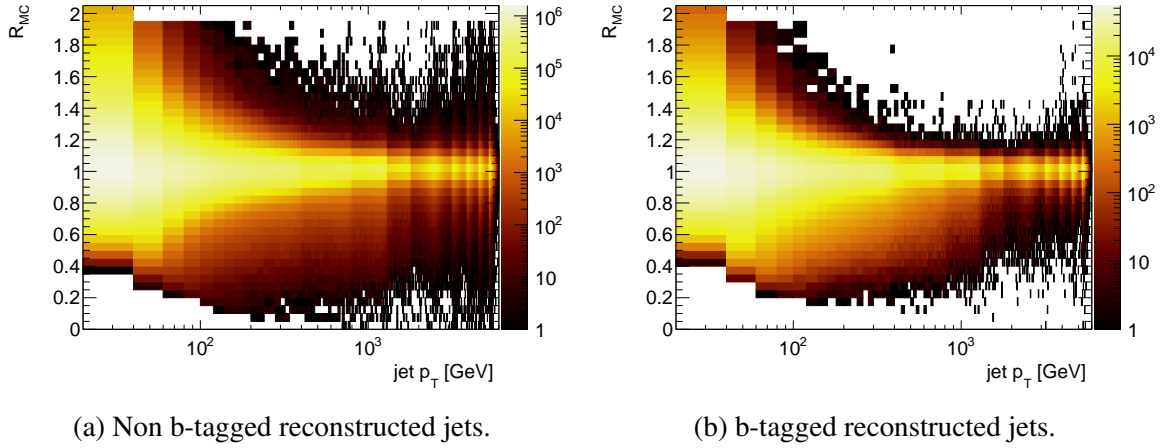


Fig. 6.3 Jet responses measured in di-jet Pythia MC (R_{MC}) as a function of truth jet p_T .

6.3 Performing JetSmearing

The smearing technique is first performed out-of-the-box using the template distribution of R_{MC} . The following describes the two key parts to the method: the selection of *seed* events and the *smearing* of the selected seed events.

6.3.1 Selecting Seed Events

In order for the technique to work in a robust manner, the selection of well measured data events - the so-called *seed events* is critical⁷. Selecting seed events without a bias in a key distribution is an absolute requirement of the method. The variable E_T^{miss} significance (E_T^{miss} Sig.) is known to be an invariant quantity over jet multiplicity due to its relation to the response of a calorimeter at significant p_T [224]. E_T^{miss} Sig., in the context of JetSmearing, is defined as:

$$E_T^{\text{miss}} \text{ Sig.} = \frac{E_T^{\text{miss}} - M}{\sqrt{\Sigma E_T}} \quad (6.5)$$

⁷A naive selection would be to select all events with $E_T^{\text{miss}} < \mathcal{O}(10)$ GeV, however from past Run-I knowledge [222] such a selection is known to create a bias in various distributions e.g. leading jet p_T (as seen by the blue markers in Figure 6.4a)

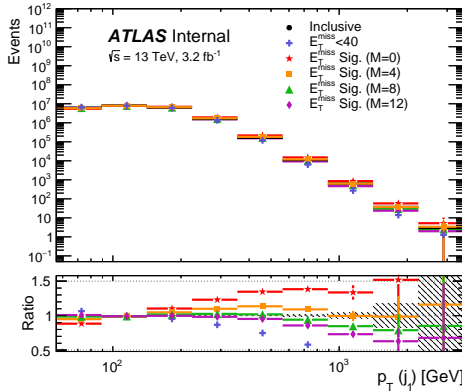
6.3 Performing JetSmearing

where E_T^{miss} is the missing transverse energy, ΣE_T is the sum of all transverse energy and M is some parameter that can be used to remove or compensate for any residual bias.

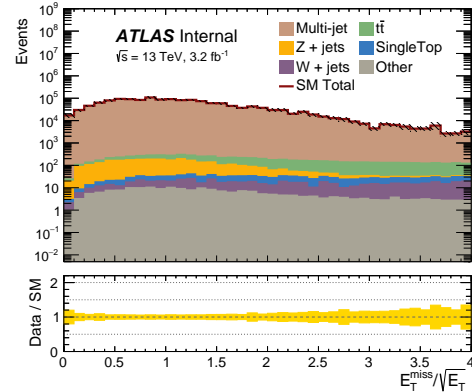
The leading jet p_T for an inclusive sample of jet events is shown in Figure 6.4a. Variations in the seed selection, normalised to the inclusive sample, are shown with variations in the value of M . A value of $M = 8$ GeV showed the least bias in the selection of well measured events as a function of the leading jet p_T , as can be seen by the orange points in Figure 6.4a. The average jet p_T ($\langle p_T(j) \rangle$) is defined as the scalar sum of the jets in the event (H_T) divided by the number of jets (N_{jet}) in the event, by applying a selection on this quantity removed a bias at large values of N_{jet} . Due to a larger amount of real E_T^{miss} present in heavy flavour decays, the cut of E_T^{miss} Sig. was made dependent on the number of b-tagged jets ($N_{\text{b-jets}}$). The selection value was derived from the approximate peak of the E_T^{miss} Sig. distribution in MC as shown in Figure 6.4b. The seed selection applied to the E_T^{miss} Sig. values of Figure 6.4a is given in Table 6.1 below:

Table 6.1 JetSmearing seed selections

Variable	Units	Cut Value
E_T^{miss} Sig.	$\text{GeV}^{\frac{1}{2}}$	$< 0.5 + 0.1 \cdot N_{\text{b-jets}}$
$\langle p_T(j) \rangle$	GeV	< 0.2



(a) Leading jet p_T distribution in data events with 0 leptons, inclusive jets with $p_T > 35$ GeV showing variations in seed selections. Events are data with non QCD SM processes subtracted. Only statistical errors are shown.



(b) MC events with 0 leptons, 2-4 jets (2 b-tagged) and $H_T > 500$ GeV. E_T^{miss} Sig. with $M = 0$ GeV. The multijet background and all other SM backgrounds are derived from MC.

Fig. 6.4 Key distributions in the choice of the JetSmearing *seed selection*.

6.3.2 Smearing Seed Events

Once seed events are selected using the selections detailed in Table 6.1 the process of JetSmearing, as described in Chapter 6.1, can be applied. Figure 6.5 shows an example of how seed events are used to generate *pseudo-data*. Figure 6.5a shows the jet p_T spectrum of the pseudo-data from a single jet of $p_T \approx 415$ GeV. Figure 6.5b shows how the leading pseudo-jet p_T spectrum builds up for multiple seed events. The black line in Figure 6.5c is an event with multiple jets and $E_T^{\text{miss}} \approx 26$ GeV, by smearing the jets in the event a broad pseudo- E_T^{miss} distribution is created (as seen in red). Finally, Figure 6.5d shows how from a relatively low number of seed events (black, at low values of E_T^{miss}) a smooth pseudo- E_T^{miss} distribution (red) is formed with potentially high values of E_T^{miss} .

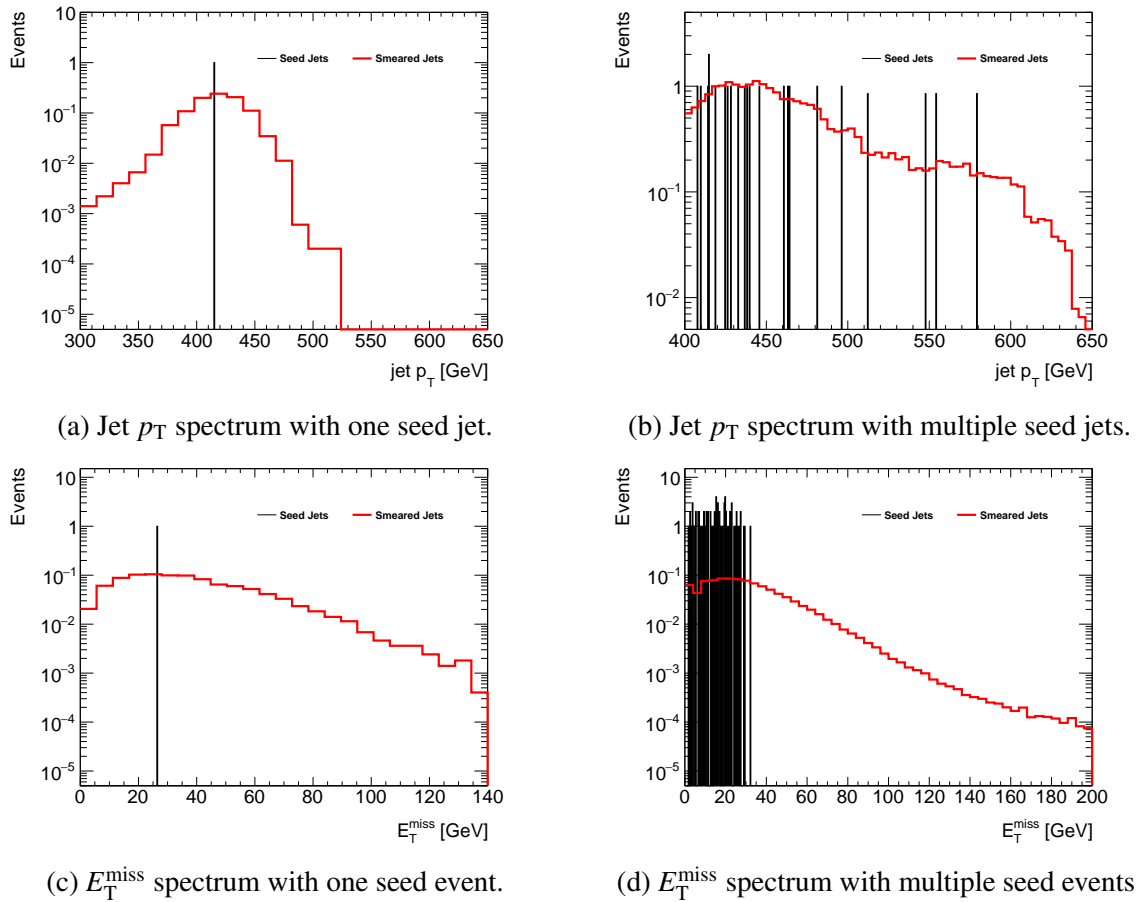
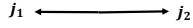
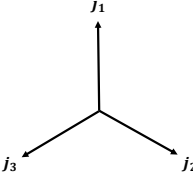

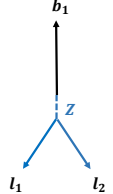


Fig. 6.5 Figure showing the building up of *pseudo-events* from the smearing of *seed events*. A value of $n_{\text{smears}} = 5000$ with 2015 data

6.4 Correcting the Jet Response

After producing *pseudo-data* with the *out-of-the-box* response maps these distributions are compared with data using analyses designed to probe the jet response with *balanced* physics objects. Table 6.2 details and pictorially represents the analyses performed to probe the jet response: di-jet balance; *Mercedes*⁸; γ -b-jet balance and Z-b-jet balance. Due to ambiguities in the construction of R_{MC} , its derivation from MC and the effects of the seed selection procedure, R_{MC} may not correctly describe the truth jet response. To compensate for this, corrections can be made based on observed data to further modify the Gaussian Core and Non-Gaussian Tail of R_{MC} .

Table 6.2 Analyses used to correct the R_{MC} map used in the JetSmearing procedure.

Jet	Region of R_{MC} to be probed	Analysis Name	Analysis Selection	
non b-tagged	Gaussian Core	di-jet balance	two back-to-back jets	
	Non-Gaussian Tail	Mercedes	three balanced jets	
b-tagged	Entire	γ -b-jet balance	Photon back-to-back with a jet	
	Entire	Z-b-jet balance	Z-boson back-to-back with a jet	

6.4.1 Di-jet Balance Corrections

The primary analysis to probe the Gaussian Core of R_{MC} is one in which aims to select back-to-back di-jet events in the detector. This can be obtained by requiring at least two jets above a p_T threshold with a large angle between the two jets, $|\Delta\phi(j_1, j_2)| > \pi - 0.25$, with only soft additional leptonic or hadronic activity in the event. With this configuration any E_T^{miss} in the event is assumed to originate from the mis-measurement of either or both hard p_T jets (j_1, j_2). From [225], if two jets have similar rapidity, the width of their jet p_T responses is the same, $\sigma(p_{T,1}) = \sigma(p_{T,2}) = \sigma(\langle p_T \rangle)$.

⁸This analysis was not performed in this thesis, it was however performed in [221] [222].

The p_T asymmetry for di-jet events is defined as:

$$A = \frac{p_{T,1} - p_{T,2}}{p_{T,1} + p_{T,2}} = \frac{p_{T,1} - p_{T,2}}{\frac{1}{2} \langle p_T \rangle} \quad (6.6)$$

where $p_{T,1}$ is the p_T of the leading jet, $p_{T,2}$ is the sub-leading jet p_T and $\langle p_T \rangle$ is the average di-jet p_T . The relation between $\sigma(A)$ and the fractional jet resolution is given by [225]:

$$\sigma(A) = \frac{\sqrt{\sigma^2(p_{T,1}) + \sigma^2(p_{T,2})}}{\langle p_{T,1} + p_{T,2} \rangle} \approx \frac{1}{\sqrt{2}} \frac{\sigma(\langle p_T \rangle)}{\langle p_T \rangle} \quad (6.7)$$

Hence by measuring the di-jet asymmetry the Gaussian width can be fitted as a function of the average di-jet p_T as:

$$\sigma(A) = \frac{N}{\langle p_T \rangle} + \frac{S}{\sqrt{\langle p_T \rangle}} + C \quad (6.8)$$

where N is a term representing the calorimeter noise, S is a stochastic term and C is a constant term.

6.4.1.1 Event selection

All data events in the 2015 data set passing a series of single jet triggers were used. A weight is applied to account for any trigger *prescales* depending on the leading jet p_T in the event and which triggers fired. These events were then required to pass the selection criteria detailed in Table 6.3. This is performed separately for non- b -tagged di-jets events and also for di-jets where both jets were b -tagged, as indicated in Table 6.3. The same data set was used as an input to the JetSmearing method to generate a pseudo-data distribution which required to pass the same selection.

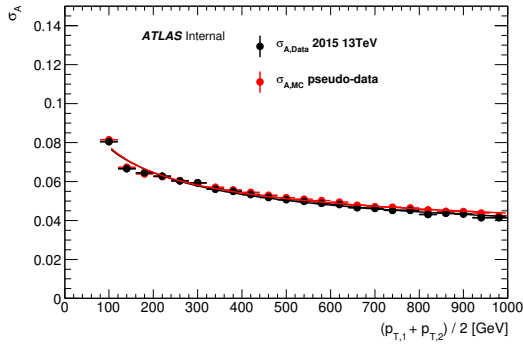
6.4.1.2 Results

Fitting $\sigma(A)$ to data and *pseudo-data* allows for a comparison between the post-smearing jet resolution and the actual jet resolution. The comparison for non- b -tagged jets and is shown in Figure 6.6a; the agreement between data and pseudo-data is good, therefore it was concluded that no corrections to the Gaussian core were needed to the R_{MC} for non b -tagged jets.

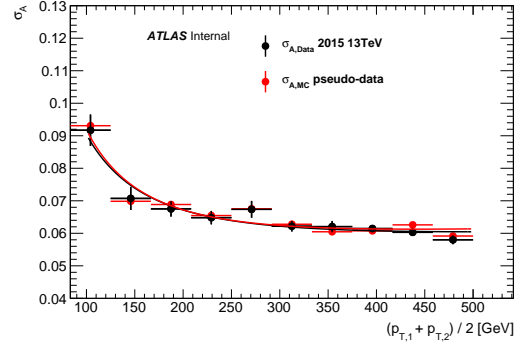
Figure 6.6b compares the Gaussian width in the case of balanced di- b -jets, showing good agreement between data and pseudo-data. In the case of b -tagged jets a di- b -jet balance is however hard for several reasons: a low number of events in 2015 data particularly at high average p_T ; larger non-Gaussian effects which may distort the approximation of the core

Table 6.3 Summary of analysis selection in the di-jet balance analyses.

Variable	di-jet balance	di-b-jet balance
N_{jets} ($p_T > 20 \text{ GeV}$, $ \eta < 2.5$)		2 – 3
$ \Delta\phi(j_1, j_2) $		$> \pi - 0.25$
Leading jet p_T [GeV]		100
Sub-leading jet p_T [GeV]		50
Third jet $E(j_3)$ [GeV]		$< E(j_1)$, $< E(j_2)$
Third jet $p_T/\langle p_T \rangle$		< 0.1
$N_{\text{baseline lep.}}$		0
$N_{\text{b-jets}}$	0	2



(a) non b-tagged jets



(b) b-tagged jets

 Fig. 6.6 Gaussian width of data (black) and pseudo-data (red) as a function of average di-jet p_T . Data points are fitted to the functional form given in Equation 6.8.

width; and contamination from other SM background processes such as $t\bar{t}$ production. For these reasons two alternative analyses were performed to probe the jet response of b-tagged jets, this is crucial for the analyses in this thesis since there are requirements of multiple b-tagged jets.

6.4.2 Photon-b-jet Balance Corrections

A photon (γ) balanced against a b-tagged jet is used to probe the b-jet response. The ATLAS photon reconstruction is known to be very efficient [190], the assumption is therefore that the photon's response is $R_\gamma = \frac{p_T^{\text{RECO}}}{p_T^{\text{TRUTH}}} \approx 1$, therefore any E_T^{miss} in the event is assumed to be associated with the b-jet only since the two objects are balanced in the detector. The approximation is that in order to conserve momentum in the transverse plane the negative

photon \vec{p}_T must be equal to the truth b-jet \vec{p}_T :

$$\vec{p}_T^{truth}(b) = \vec{p}_T^{miss} + \vec{p}_T(b) \quad (6.9)$$

$$\vec{p}_T(\gamma) = -\vec{p}_T^{truth}(b) \quad (6.10)$$

From this assumption and neglecting the mass of a b-hadron ($E_T \approx p_T$), two variables designed to probe the response were used: the photon response (R_b) and the momentum projection fraction (R_{MPF}). They are defined as:

$$R_b = \frac{p_T(b)}{p_T(\gamma)} \quad (6.11)$$

$$R_{MPF} = 1 + \frac{|\vec{p}_T^{miss} \cdot \vec{p}_T(\gamma)|}{|p_T(\gamma)|^2} \quad (6.12)$$

Table 6.4 shows a summary of the selections applied in this analysis in order to study Equations 6.11 and 6.12. A series of photon triggers are used to select events, correctly applying weights to each event to weight for any prescaled triggers that were used in the recording of the data.

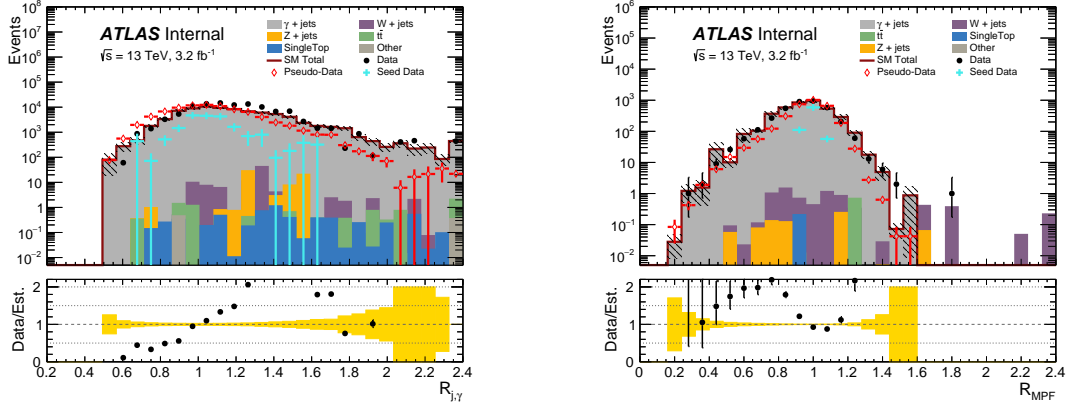
Table 6.4 Summary of analysis selection in the boson-b-jet balance analyses.

Variable	γ -b-jet balance	Z-b-jet balance
N_γ	1	0
$N_{\text{signal lep.}}$	0	2
$N_{\text{baseline lep.}}$	0	2
$m_{\ell\ell}$ [GeV]	0	[86,100]
N_{jets}		1 – 2
Leading jet p_T [GeV]		35
Second jet $E(j_2)$ [GeV]		$< E(j_1)$
Second jet $p_T(j_2)/p_T(j_1)$		< 0.1
$N_{\text{b-jets}}$		1
$ \Delta\phi(b, \gamma) $	$> \pi - 0.25$	-
$ \Delta\phi(b, l_1 + l_2) $	-	$> \pi - 0.25$

Results The top row of Figure 6.7 shows the variables R_b and R_{MPF} for two different p_T ranges, the Gaussian width in the case of $\sigma(R_b)$ is defined by fitting a Gaussian between $1.2 > R_b > 0.8$. In the case of R_{MPF} , the variable is more sensitive to the non-Gaussian tail of the jet response and hence is fitted between $1.15 > R_b > 0.85$. The sensitivity of R_{MPF} to the non-Gaussian tail of the b-tagged jet response allows for the adjustment of the non-Gaussian

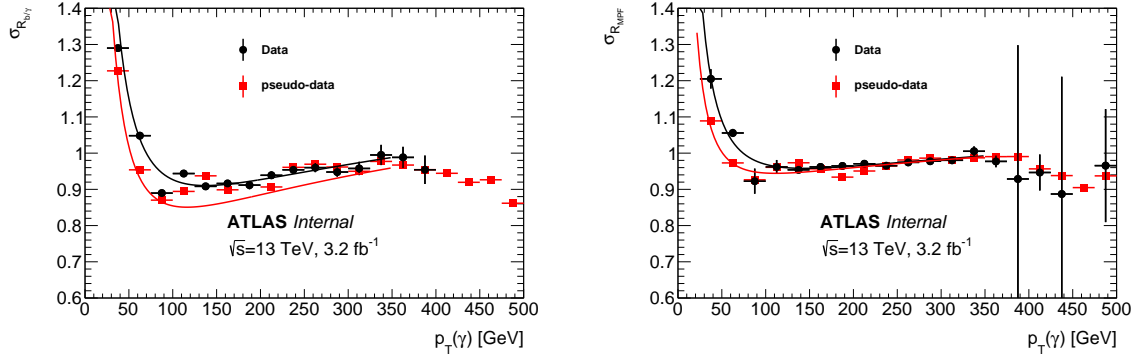
6.4 Correcting the Jet Response

tail region of R_{MC} to better describe this region - this can be used as an additional *systematic uncertainty* on the JetSmearing method. The bottom row of Figure 6.7, Figures 6.7c and 6.7d, show the dependence on photon p_T of the Gaussian core width. A good agreement is found between the width of the data and pseudo-data for photons⁹ with $p_T > 100$ GeV, further validating the method¹⁰.



(a) R_b for photons with $70 > p_T > 35$ GeV.

(b) R_{MPF} for photons with $200 > p_T > 130$ GeV.



(c) $\sigma(R_b)$ fitted as a function of photon p_T for data and pseudo-data.

(d) $\sigma(R_{MPF})$ fitted as a function of photon p_T for data and pseudo-data.

Fig. 6.7 (Top) two plots of the key variables for particular p_T ranges. (Bottom) width of photon-b-jet balance variables used to probe the Gaussian core of the b-tagged jet response as a function of photon p_T .

⁹ which corresponds to the truth level b-jet p_T as in Equation 6.9.

¹⁰For analyses with low jet multiplicity, high jet p_T and high requirements on the amount of E_T^{miss} , the multi-jet background will arise from significant p_T fluctuations of a small number of very high p_T jets. Therefore by observing a good agreement of the Gaussian core width of the pseudo-data for truth b-jets $p_T > 100$ GeV justifies the method.

6.4.3 Z-boson-b-jet Balance Corrections

The analysis described in Chapter 6.4.2 suffers from a lack of statistics. This affects the measurement of $\sigma(R_b)$ and $\sigma(R_{\text{MPF}})$ in the range $130 > p_T > 35$ GeV due to the lowest un-prescaled photon trigger being at a reconstructed p_T threshold of $p_T > 130$ GeV. To account for this an identical analysis was performed replacing the reconstructed photon with two opposite-sign, same-flavour leptons within the Z-boson mass window, the analysis selections are summarised in Table 6.4. Since the lowest un-prescaled photon lepton triggers allow a leading lepton of $p_T > 26$ GeV (sub-leading $p_T > 20$ GeV) the combined p_T of the lepton pair, $p_T(Z \rightarrow \ell_1 + \ell_2)$, can be used to probe lower truth b-jet p_T with greater statistics. Analogously to the γ -balance analysis, the Z-boson acts as an approximation of the truth b-tagged jet.

Figure 6.8 shows the two key variables used to probe the Gaussian core (R_b) and the non-Gaussian tail (R_{MPF}) of the b-jet response via the use of a Z-balance analysis. Figure 6.8a-6.8c-6.8e show the variation of the R_b variable for low p_T , medium p_T and high p_T Z-bosons. It can be seen that the Gaussian core region $1.1 > R_b > 0.85$ is well modelled in this range. The variable R_{MPF} , which is more sensitive to the non-Gaussian low-side-tail of the jet response, appears to under-shoot the data for low-medium Z-boson p_T values.

6.4.4 Balance Corrections Summary

For the method of JetSmearing to be able to correctly estimate the multi-jet background, it is important to make sure the response map (R_{MC}), derived in simulation, correctly matches data in the core of the distribution as well as the non-Gaussian tails. These two regions were probed for a range of p_T values by balancing a b-jet with a well measured object: a photon; and a Z boson (two leptons). The latter was used due to a lack of statistics for low p_T photon events because ATLAS highly prescales low p_T photon triggers.

The comparison of the gaussian core of the response for data and pseudo-data was observed to be fairly constant for b-tagged and non-b-tagged jets, particularly for $p_T > 50$ GeV, as seen in Figure 6.7 and Figure 6.8.

A disagreement was observed in the tail of the R_{MPF} distribution, the variable designed to probe the non-gaussian tails of R_{MC} , for p_T values < 200 GeV. This can be seen in Figure 6.8b and Figure 6.8d. The response can be corrected by increasing the size of tail of R_{MC} to best match the data. A systematic uncertainty on the final estimate could therefore be applied from the difference with and without this correction.

It is important to note that the analyses in this thesis which used this method for estimating the multi-jet background did not apply this variation uncertainty. It was found that the multi-

6.4 Correcting the Jet Response

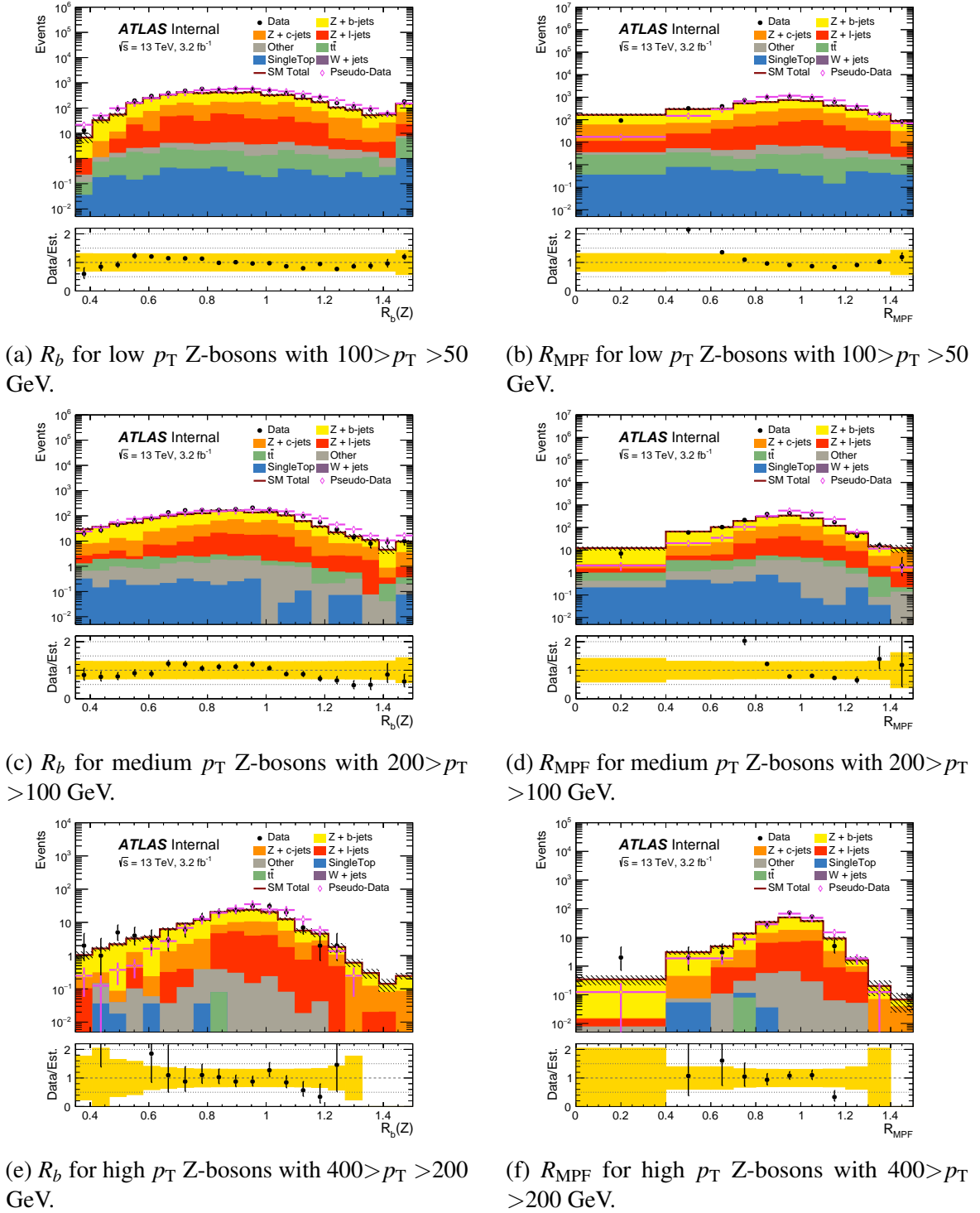


Fig. 6.8 Probing the b-jet jet response with variables R_b and R_{MPF} for b-jets balanced against a well measured Z-boson of low, medium and high p_T .

jet background, for the analyses in this thesis, was dominated by significantly higher b-jet p_T fluctuations where the agreement for balanced photons and balanced Z bosons is good.

6.4.5 Di-jet $\Delta\phi$ Corrections

The coordinates of a jet are determined by its central axis, if a jet is well measured this central axis should align with the truth jet central axis. However, when a jet is mis-measured it may not lie on its truth central axis. For example, some jet constituents may lie out of acceptance or within an area of dead-material. If this occurs, the jet coordinates may alter and the effect can be observed as a widening in the distribution of $\Delta\phi(j, E_T^{\text{miss}})$. This needs to be taken into account by the JetSmearing method. The variable $\Delta\phi(j, E_T^{\text{miss}})$ is used to reduce the multi-jet background, if the distribution is not well modelled by the method it would make the background prediction void. In the scenario of balanced di-jets the azimuthal distance between the di-jets ($\Delta\phi(j_1, j_2)$) can be used to correct the *pseudo-data* distribution to match data.

The selections detailed in Table 6.3, without the selection on $\Delta\phi(j_1, j_2)$ are applied to data and pseudo-data. Similarly to Equation 6.8, the width of the distribution is fitted as a function of the average di-jet p_T for both data and pseudo-data:

$$\sigma(\Delta\phi(j_1, j_2)) = \frac{a}{\langle p_T \rangle} + \frac{b}{\sqrt{\langle p_T \rangle}} + c \quad (6.13)$$

where a , b and c are some arbitrary values.

The correction applied to the pseudo-data is derived from the convolution of two Gaussians:

$$(\sigma_{\text{final}}(\phi))^2 = (\sigma_{\text{pseudo-data}}(\phi))^2 + (\sigma_{\text{correction}}(\phi))^2 \quad (6.14)$$

The requirement of $\sigma_{\text{final}}(\Delta\phi) = \sigma_{\text{data}}(\Delta\phi)$ forces the pseudo-data distribution to match the data. Therefore, the correction per jet becomes:

$$\sigma_{\text{correction}}(\phi) = \frac{1}{\sqrt{2}} \sqrt{\sigma_{\text{data}}(\Delta\phi)^2 - \sigma_{\text{pseudo-data}}(\Delta\phi)^2} \quad (6.15)$$

The correction is applied by rotating the seed jet about the z axis based on a random number generated from $\sigma_{\text{correction}}(\phi)$ as a function of the jet p_T . Figure 6.9 shows $\sigma(\Delta\phi(j_1, j_2))$ as a function of the average di-jet p_T in data, pseudo-data and corrected pseudo-data.

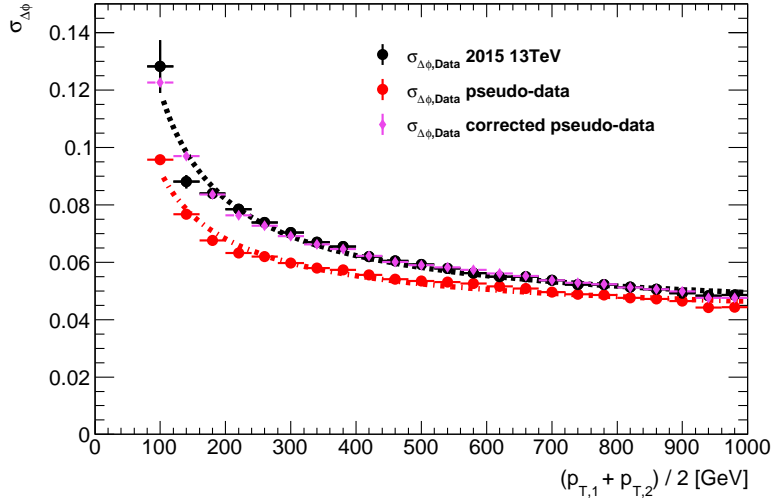


Fig. 6.9 $\sigma(\Delta\phi(j_1, j_2))$ as a function of average di-jet p_T for data (black), pseudo-data (red) and corrected pseudo-data (pink)

6.4.6 Effect of ϕ corrections on the Final Estimate

Table 6.5 shows two different selections at *pre-selection level* with significantly different jet kinematics and event topologies.

The first selection is based on a zero-lepton, multi-jet selection, referred to as “Multi-0L”. The selection has an inclusive number of jets, zero leptons high total jet p_T (H_T) and no selection on the number of b-jets.

Contrary to this, a second selection referred to as “Exclu-0L” has an exclusive selection on the number of jets and requires at least two jets to be b-tagged.

The effect of applying ϕ corrections to the JetSmearing method was tested by observing the $\min[\Delta\phi(\text{jet}_{1-4}, E_T^{\text{miss}})]$ distribution at pre-selection level in these analyses. In both analyses the $\min[\Delta\phi(\text{jet}_{1-4}, E_T^{\text{miss}})]$ variable is used to reduce the multi-jet background by applying an upper cut of > 0.4 . In the di-jet balance analysis, the measurement of $\sigma(A)$ in the case of b-tagged jets was found to be lacking in statistics. The measurement of $\sigma(\Delta\phi)$ for b-jets lacks statistics and is even more susceptible to $t\bar{t}$ contamination effecting the results. It is well motivated that the shape of R_{MC} in the case of non b-tagged jets and b-tagged jets should differ, however there is no substantial reason why the effect of increased ϕ resolution between well measured and mis-measured jets should be greatly different. Therefore, the ϕ corrections derived in the case of non b-tagged jets were also applied to b-tagged jets.

The $\min[\Delta\phi(\text{jet}_{1-4}, E_T^{\text{miss}})]$ distributions are seen in Figure 6.10 after applying the selections of Table 6.5. The multi-jet background is estimated from the JetSmearing method by

Table 6.5 Selections used at pre-selection level in the case of two different analyses using JetSmearing.

Variable	Multi-0L	Exclu-0L
Trigger	E_T^{miss} trigger	jet+ E_T^{miss} trigger
$N_{\text{baseline lep.}}$	0	0
N_{jets}	≥ 2	2
$N_{\text{b-jets}}$	-	2
jet p_T [GeV]	> 50	> 20
Leading jet p_T [GeV]	> 200	> 60
H_T [GeV]	> 200	-
E_T^{miss} [GeV]	> 200	> 150
Parabolic Trigger Plateau	-	$E_T^{\text{miss}} > \frac{150 \cdot p_T(j_1) - 11700}{p_T(j_1) - 85}$
$\min[\Delta\phi(\text{jet}_{1-4}, E_T^{\text{miss}})]$	< 0.5	< 0.4

creating pseudo-data which is normalised to the data minus non-QCD background. The top row shows the Multi-0L selection and the bottom row shows the Exclu-0L selection, the left column shows events before ϕ corrections and the right column shows after ϕ corrections. It is clear that the ϕ corrections greatly improve the agreement between the method and data in a region rich with multi-jet events. It is seen that this correction is important for both an inclusive jet and an exclusive b-jet selection.

6.5 Systematic Uncertainties

The variation of the non-Gaussian tail of R_{MC} to agree better with data can provide a systematic uncertainty. However this was not performed in this thesis, due to good agreement observed for high p_T of the balanced objects described. For low p_T a lack of statistics, contamination from fake¹¹ objects (photons and leptons) and other sources of E_T^{miss} (soft, photon and leptons) create difficulties in approximating the response. For more detail on modifying the jet response, using jets in a *mercedes* configuration see [35].

Based on results derived in Run-I on the LHC, an approximation of the non-Gaussian uncertainty of 30% was used throughout this thesis. Systematic uncertainties covering any residual bias in the selection of seed data were however applied. They are obtained via variation to the seed selection accounting for a tighter and looser selection of well-measured events. The statistical uncertainties are calculated based on the number of smears and number of seed events, more detail on smearing statistics can also be found in [35].

¹¹the incorrect reconstruction of an object, e.g. a jet can be mis-reconstructed as a photon and vice versa.

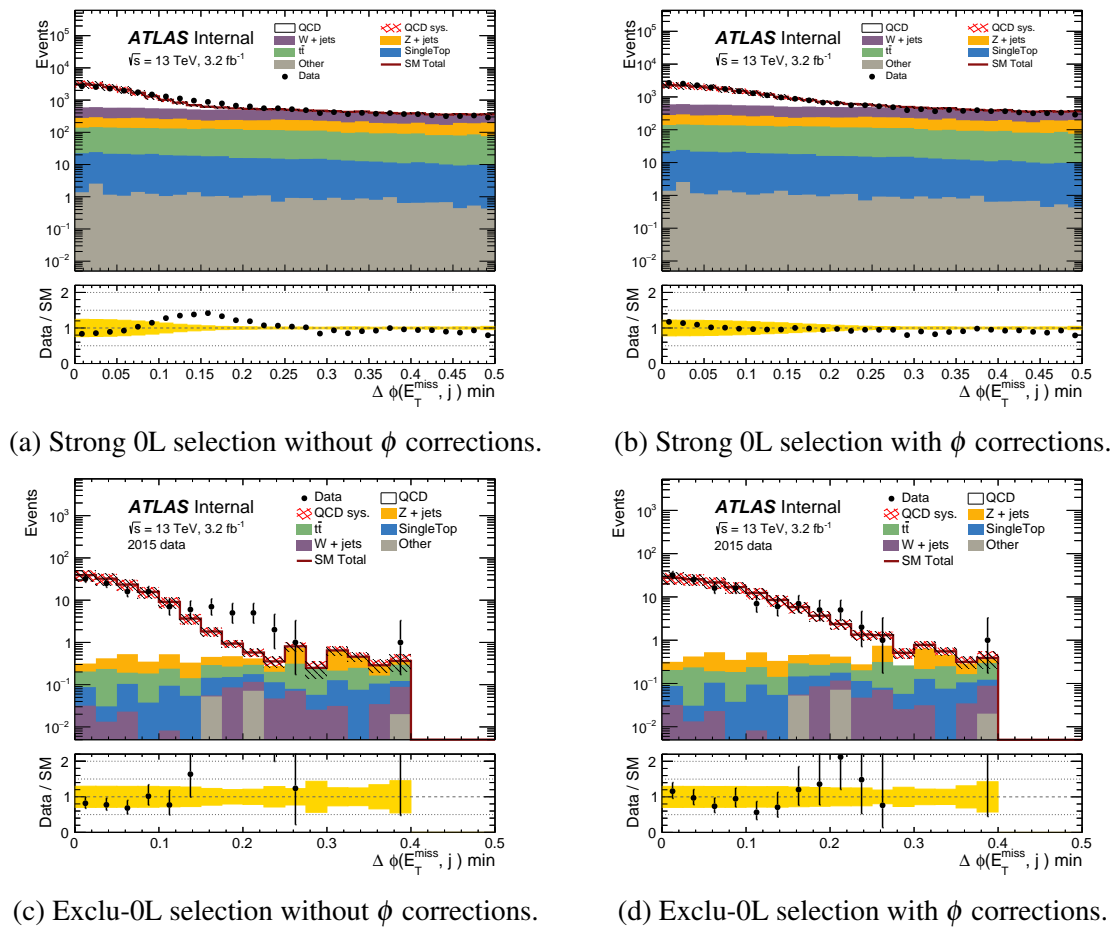


Fig. 6.10 $\min[\Delta\phi(\text{jet}_{1-4}, E_T^{\text{miss}})]$ distribution with different selections, the QCD background is estimated by the JetSmearing method.

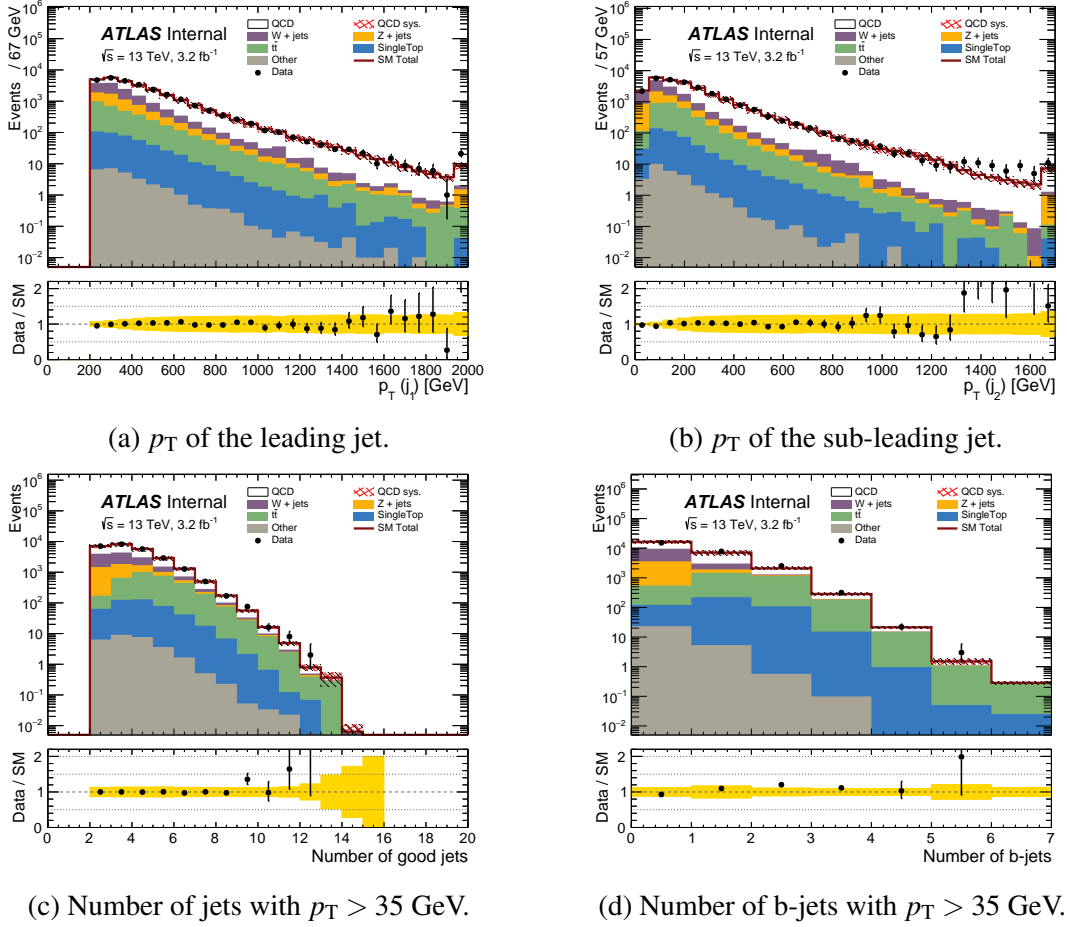


Fig. 6.11 Key distributions with the Multi-OL pre-selection.

6.6 Method Validation

In order to estimate the multi-jet background using the JetSmearing method pseudo-data is firstly normalised in a multi-jet rich control region (CR), once this normalisation is obtained the pseudo-data is firstly validated in validation regions (VRs) and then used to give an estimate of the background in signal regions (SRs). In order to obtain a good estimate of the background it is important that the variables which separate the CRs, VRs and SRs are well modelled by the method. As previously seen, the main discriminating variable between the SM background and the multi-jet background is $\min[\Delta\phi(\text{jet}_{1-4}, E_T^{\text{miss}})]$, which is typically used to separate the SRs from the CRs and VRs.

Figure 6.11 and Figure 6.12 show key variables after applying the Multi-OL and Exclu-OL selections, the multi-jet background in each distribution is well modelled by the JetSmearing method. The other SM background in the plot are generated by MC and only show statistical uncertainty, a conservative 30% systematic uncertainty is applied to the multi-jet background.

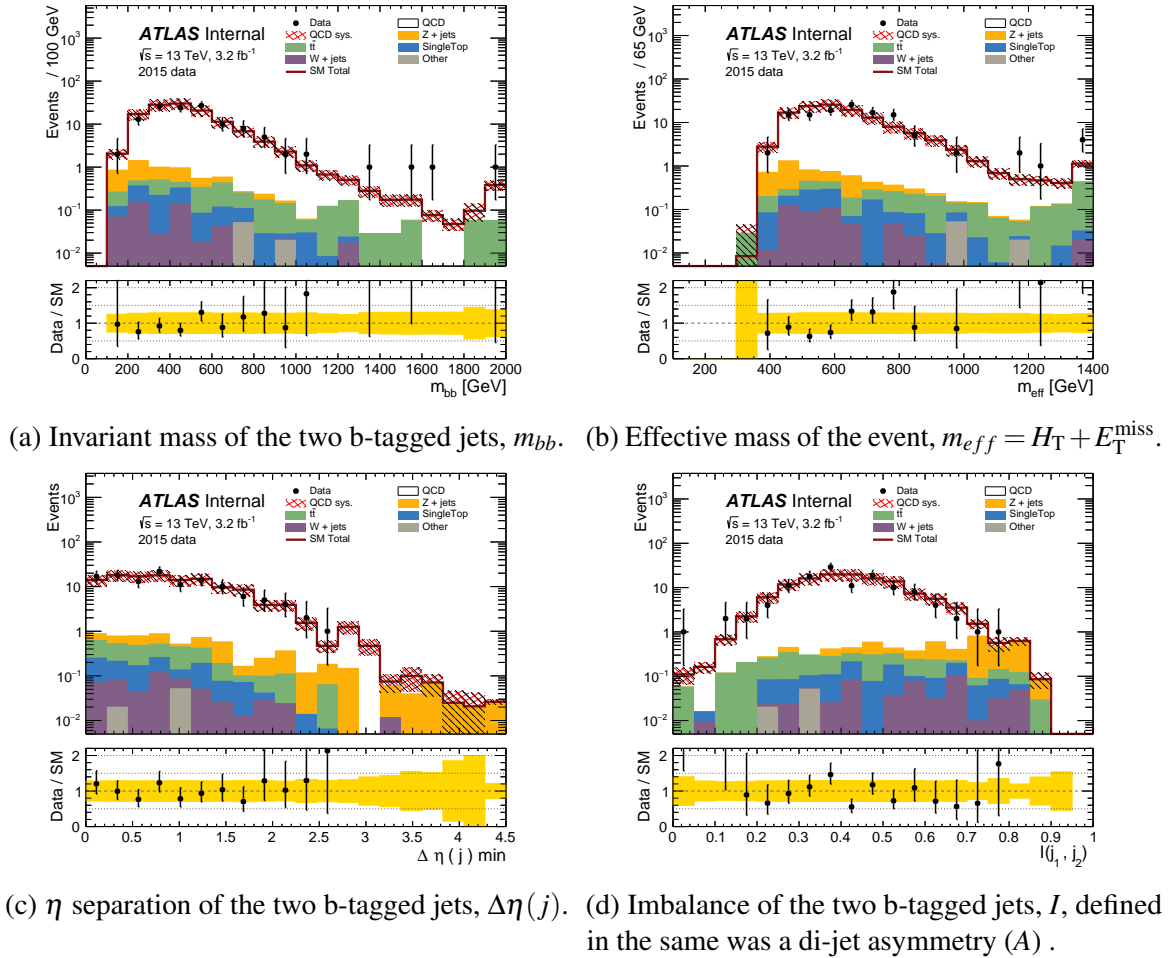
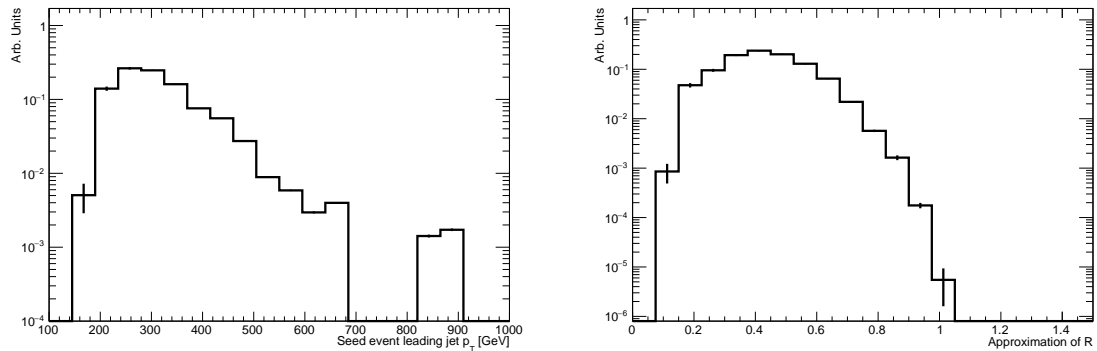


Fig. 6.12 Key distributions with the Exclu-0L pre-selection.



(a) The leading jet p_T of the seed events contributing toward the pseudo-data. (b) Approximation of the jet response from the seed event and post-smearing pseudo-events.

Fig. 6.13 Seed events for the pseudo-data passing the Exclu-0L selections. Seed events have prescales applied and are normalised to unit area.

As previously discussed, the low jet multiplicity and high E_T^{miss} requirement with the Exclu-0L selection results in the majority of the multi-jet events in this region arising from the severe mis-measurement of high p_T di-jet events. Figure 6.13a shows the leading jet p_T , arbitrarily normalised, of the well measured seed events which after smearing pass the Exclu-0L selection criteria. It can be seen that the majority of seed events have large leading jet p_T , such high p_T well measured events have good agreement in their Gaussian core and non-Gaussian between pseudo-data and data as measured by the balance analyses of Chapter 6.4.3. Figure 6.13b shows an approximation of the jet response, R_{MC} , obtained from the ratio of the seed event leading jet p_T divided its post-smearing pseudo- p_T . It can be clearly seen that for events passing this type of selection (multi- b -tagged jets, low jet multiplicity and high E_T^{miss}) that the multi-jet background is dominated by high p_T jets which undergo severe mis-measurement of their p_T leading to large E_T^{miss} .

6.7 Conclusion

This chapter detailed a robust data-driven method for estimating the Multi-jet (QCD) background in regions of high E_T^{miss} [221, 222]. The method relies on the assumption that the sources of $E_T^{\text{miss}} > 250$ GeV produced by QCD interactions arise from the mis-measurement of multiple jets. The term mis-measurement also refers to cases in which heavy-flavour decays result in reconstructed jets with significantly less energy than their parent heavy quark. For example, a b -quark may decay giving a jet, muon and a neutrino; the muon is overlap removed, this plus the neutrino may give large E_T^{miss} .

A jet response map for the jet mis-measurement is derived in Multi-jet MC on a jet-by-jet basis, and is corrected to match data with di-jet and γ -jet balance analyses. Well measured events (seed) are selected in data with selection of small values of E_T^{miss} Sig.; these events have very low E_T^{miss} and it is assumed that all the jets in the events are well measured. Each jet in the seed event is smeared based on random numbers from the jet response maps. This process is repeated $\mathcal{O}(10^3)$ times to create pseudo-data with potentially large E_T^{miss} . To estimate the multi-jet background in various regions, the pseudo-data is normalised to data in a multi-jet dominated region (typically low $\min[\Delta\phi(\text{jet}_{1-4}, E_T^{\text{miss}})]$). Once normalised, the distribution can be used to estimate the multi-jet background in signal regions (typically high $\min[\Delta\phi(\text{jet}_{1-4}, E_T^{\text{miss}})]$).

Section 6.6 showed how well the various shapes of key distributions with two different analysis selections (Multi-0L, Exlcu-0L) performed. Good agreement is observed in multiple distributions resulting in a robust data-driven estimation consistent with MC but with significantly greater statistics than MC.

Chapter 7

Searches for SUSY in Two b-jets + E_T^{miss} Final States

This chapter describes experimental searches for supersymmetry in events containing two b-jets and large amounts of missing transverse momentum (E_T^{miss}).

As discussed in Chapter 2.4.6, for SUSY to solve the Hierarchy problem in a simple way, *naturalness* favours light scalar top quark states:

$$m_S = \sqrt{m_{\tilde{t}_L} m_{\tilde{t}_R}} = \mathcal{O}(1 \text{ TeV})$$

The two states \tilde{t}_L and \tilde{t}_R mix to yield mass degenerate eigenstates \tilde{t}_1 and \tilde{t}_2 , as discussed in Chapter 2.4.2. Since the common mass parameter of the left handed squarks ($m_{\tilde{q}L3}$) drives the mass scale, the lightest mass eigenstate of the scalar bottom quark (\tilde{b}_1) may also be at a mass scale reachable by the LHC. If produced, the scalar particles are likely to decay into neutralinos via b-quarks, leaving a signature of b-jets and E_T^{miss} .

Previous searches for the direct pair-production of scalar bottoms were performed by the CDF and D0 experiments at the Tevatron [226, 227], with no significant excess above the SM background observed. During Run-I of the LHC, neither ATLAS nor CMS observed any significant deviations from the SM background in scalar bottoms searches, setting stringent limits on the masses of pair-produced scalar bottoms [27, 228–232].

A full summary of the ATLAS Run-I scalar bottom searches using 20.3fb^{-1} of LHC data collected at $\sqrt{s} = 8 \text{ TeV}$, is presented as part of a summary paper [25]. Figure 7.1 shows the limits obtained for three different simplified model scenarios involving scalar bottom quarks. The 95% CL limits on the \tilde{b}_1 and $\tilde{\chi}_1^0$ masses are shown in Figure 7.1a, for the simplified scenario where only \tilde{b}_1 are pair-produced and decay exclusively to $\tilde{\chi}_1^0$. Figure 7.1b shows limits obtained in the $(m_{\tilde{b}}, m_{\tilde{\chi}_2^0})$ mass plane for a simplified model scenario in which the second

lightest neutralino ($\tilde{\chi}_2^0$) is of a mass lower than the scalar bottom quark. In this model, pair produced scalar bottom quarks decay exclusively to the second lightest neutralinos which subsequently decay with a 100% branching ratio to the lightest neutralinos and a Higgs boson. Figure 7.1c shows limits obtained in the $(m_{\tilde{b}}, m_{\tilde{\chi}_1^\pm})$ mass plane for two different values of $m_{\tilde{\chi}_1^0}$ assuming exclusive decays of scalar bottoms to charginos and top-quarks. This chapter focuses on the simplified model scenario of Figure 7.1a which was previously depicted in Figure 3.10c.

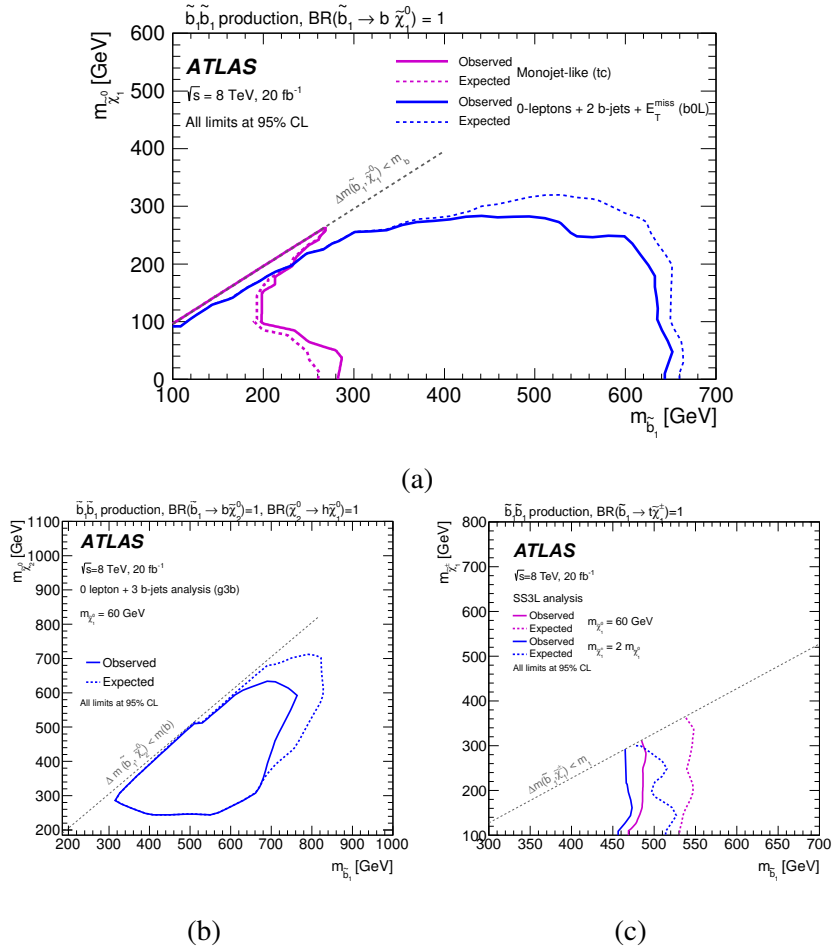


Fig. 7.1 The 95% CL limit obtained with the Run-1 pp collision data for direct sbottom pair production decaying with (a) 100% BR to neutralinos ($\tilde{\chi}_1^0$) in the $(m_{\tilde{b}}, m_{\tilde{\chi}_1^0})$ mass plane, (b) 100% BR to the 2nd heaviest neutralino ($\tilde{\chi}_2^0$), in the $m_{\tilde{b}} - m_{\tilde{\chi}_2^0}$ mass plane and (c) 100% BR to lightest chargino in the $m_{\tilde{b}} - m_{\tilde{\chi}_1^\pm}$ mass plane [25].

The increase in centre of mass energy of pp collisions from 8 to 13 TeV provides a large increase in sensitivity for searches targeting heavy scalar tops and scalar bottoms. The cross

7.1 A search for scalar bottoms with 3.2 fb^{-1} of data at $\sqrt{s} = 13 \text{ TeV}$

section as a function of the scalar bottom mass is shown in Figure 7.2 for the two energy regimes. For a scalar bottom with of mass 800 GeV it increases by almost a factor of 10 from 2.9 fb to 28 fb. Future Runs of the HL-LHC will reach up to 14 TeV.

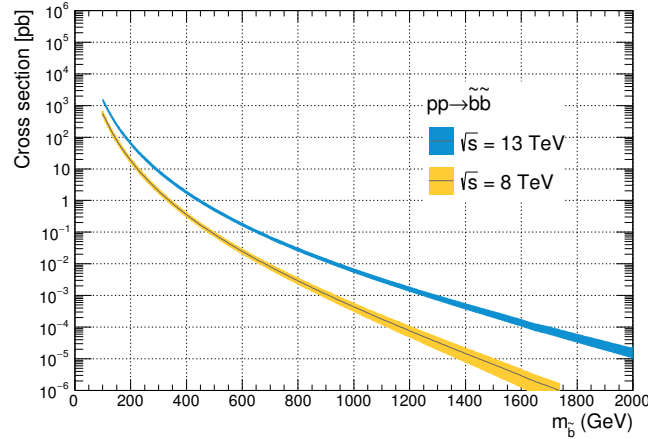


Fig. 7.2 Scalar bottom pair production cross section in pp collisions at $\sqrt{s} = 8 \text{ TeV}$ and $\sqrt{s} = 13 \text{ TeV}$ [26].

7.1 A search for scalar bottoms with 3.2 fb^{-1} of data at $\sqrt{s} = 13 \text{ TeV}$

The majority of this chapter summarises the results of a search for scalar bottom quarks with 3.2 fb^{-1} of data at a pp centre of mass energy of $\sqrt{s} = 13 \text{ TeV}$ published in [33, 28]. No significant deviation from the SM background was observed in any signal region. Exclusion limits were set on the scalar bottom and lightest neutralino in the simplified model scenario of pair produced scalar bottoms. The pair production in this scenario is depicted in Figure 7.3.

Analysis Overview The analysis performed was based on the Run-I searches for direct scalar bottom production [27]. A two-pronged search strategy was employed with two types of signal regions: SR_{Ax}, a series of SRs where x refers to the selection of the kinematic variable m_{CT} (see Chapter 5.6.3); and SR_B, a single SR designed to be sensitive to a high p_T ISR jet which boosts the scalar bottom quark pair system. The SR_{Ax} regions targeted the *bulk region* of the $m_{\tilde{b}} - m_{\tilde{\chi}_1^0}$ mass plane whereas the SR_B region targets the compressed scenarios $\Delta m(\tilde{b}, \tilde{\chi}_1^0) < 200 \text{ GeV}$. This is shown in Figure 7.4, the targetted regions have been superimposed onto the previous Run-I observed and expected limits from [27]. Both types

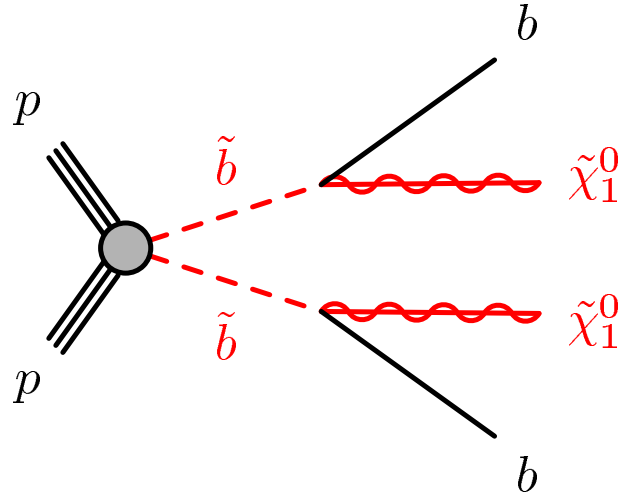


Fig. 7.3 Direct pair production of scalar bottom quarks, decaying exclusively to neutralinos.

of regions select events with no leptons in the final state and two b-jets; the backgrounds are derived from data-driven and semi-data-driven techniques with the use of MC simulation.

In total, four signal regions were used in the analysis: SRA250, SRA350, SRA450 and SRB. For each region, multiple CRs and VRs were defined to control and validate the background estimate in a semi-data-driven manner. Two data-driven methods were used as an alternative estimation of the Z+jets background in the SRs: Z+jets from γ +jets (Chapter 7.5.1) and Z+jets from an extrapolation over b-jet multiplicity (Chapter 7.5.2). The estimation of the multi-jet background was performed in data-driven way using a CR and VR.

Event Selection Events which are loosely signal-like were selected, as defined in Table 7.1. This selection, referred to as the preselection, was used as the baseline for defining various SRs, VRs and CRs for the analysis. For events with zero-leptons, a E_T^{miss} trigger was used applying a selection of $E_T^{\text{miss}} > 250 \text{ GeV}$ to be fully efficient¹. In events containing leptons - electron and muon triggers were used applying a selection on the leading lepton of $p_T(\ell_1) > 26 \text{ GeV}$ to be fully efficient. Single photon events were selected using a photon trigger with a selection of $p_T(\gamma) > 120 \text{ GeV}$.

Signal Regions The SR definitions were determined by an optimisation scan over a series of variables theoretically motivated to separate the SM backgrounds and supersymmetric signals. These variables included: m_{CT} , m_{bb} , p_T of the four jets and E_T^{miss} (for more detail, see

¹This means that all events above this threshold that should fire the E_T^{miss} trigger have fired the trigger.

7.1 A search for scalar bottoms with 3.2 fb^{-1} of data at $\sqrt{s} = 13 \text{ TeV}$

Fig. 7.4 Observed and expected exclusion limits on the lightest scalar bottom and neutralino masses set by Run-I searches for direct scalar bottom pair-production [27]. The areas on the $m_{\tilde{b}} - m_{\tilde{\chi}_1^0}$ mass plane targetted by the Run-II analysis are superimposed on top.

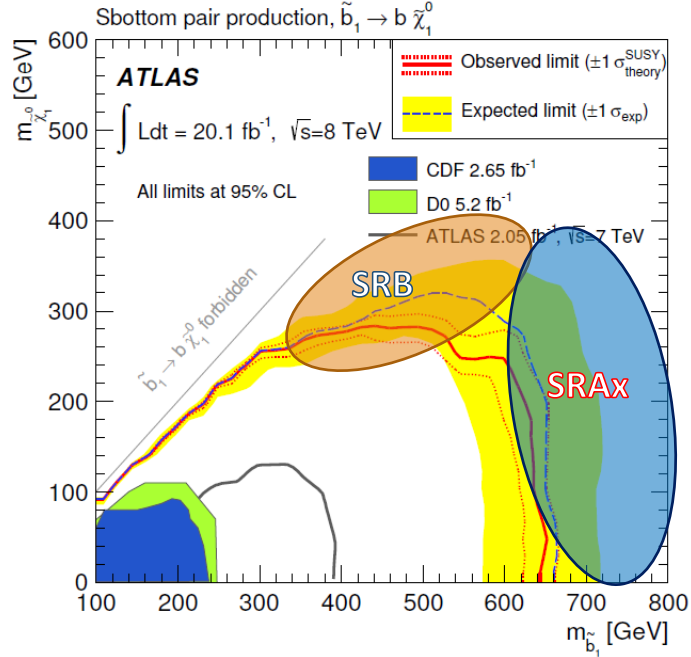


Table 7.1 Preselection criteria, common to all signal and control region of the analysis.

Leading two jets with $p_T > 50 \text{ GeV}$, $|\eta| < 2.8$
Veto on 4^{th} jet with $p_T > 50 \text{ GeV}$
At least one b -tagged jet, 77% working point

Table 7.2 Summary of the $bb + E_T^{\text{miss}}$ SR targets and their corresponding VRs and CRs

Signal Target	SR(s)	VR(s)	CR(s)
$m_{\tilde{b}} > 600 \text{ GeV}$	SRA250	VRmbbA	CRzA, CRttA
$\Delta m(\tilde{b}_1, \tilde{\chi}_1^0) > 200 \text{ GeV}$	SRA350	VRmctA	CRwA, CRst
	SRA450		
$m_{\tilde{b}} > 300 \text{ GeV}$	SRB	VRB	CRzB, CRtopB
$\Delta m(\tilde{b}_1, \tilde{\chi}_1^0) < 200 \text{ GeV}$			

Chapter 5.6). Additionally, selections on $\min[\Delta\phi(\text{jet}_{1-4}, E_T^{\text{miss}})]$ and $E_T^{\text{miss}}/m_{\text{eff}}$ are applied to remove the multi-jet background. The SRAX region optimisation targeted $m_{\tilde{\chi}_1^0} < 300 \text{ GeV}$,

$m_{\tilde{b}} \geq 700$ GeV, whereas the SRB optimisation targeted $m_{\tilde{b}} = 400$ GeV, $m_{\tilde{\chi}_1^0} = 300$ GeV. The selections that gave the best significance (see Chapter 5.8) were used to define the four signal regions.

Figure 7.5 shows the breakdown of the SM background contribution in SRAx and SRB. The SM background composition is similar in all SRAx regions. In order to correctly normalise the main backgrounds and reduce the impact of systematic uncertainties a semi-data-driven control region strategy was employed. This method is commonly used in many ATLAS searches and is described in detail in Chapter 5.9.

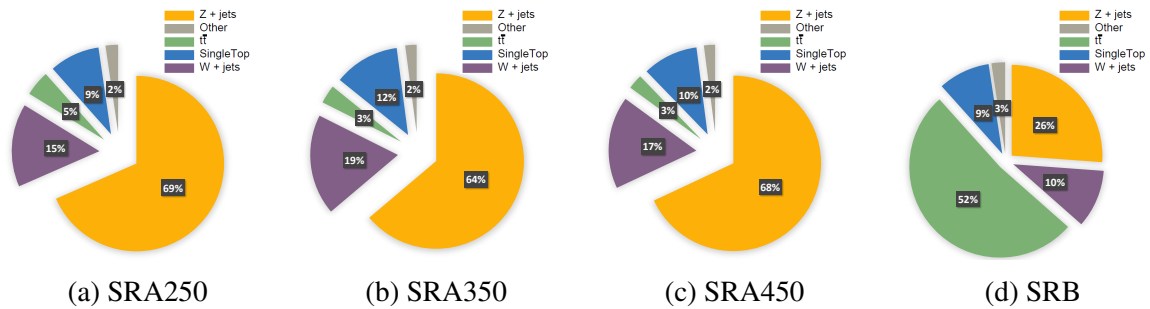


Fig. 7.5 SM backgrounds as a percentage of the total background in SRAx and SRB. The Z+jets background is the most dominant background in the SRAx regions and the $t\bar{t}$ background the most dominant in the SRB regions.

Control and Validation Regions Four orthogonal CRs were defined to normalise the Z+jets, $t\bar{t}$, W+jets and Single Top backgrounds in the three SRAx regions; the normalisation was validated in two VRs. For SRB, two CRs were defined for the Z+jets background and top backgrounds, one VR was used to check these estimates. Table 7.2 gives a summary of this strategy. This was motivated by the breakdown of the backgrounds in the four signal regions, shown in Figure 7.5.

Key variables, as detailed in Chapter 5.6, were used to make CRs, VRs and SRs orthogonal from each other, as can be seen in Figures 7.6 and 7.7. The full selections used in the SRAx regions are defined in Table 7.3 and Table 7.4 shows the full set of selections for the SRB regions.

7.2 MC samples

In order to evaluate the SM backgrounds and supersymmetric signal, MC simulation was used. A list of the MC samples used in the analysis is given in Table 7.5. Various different generators and parton showers were used in the modelling of the SM backgrounds depending

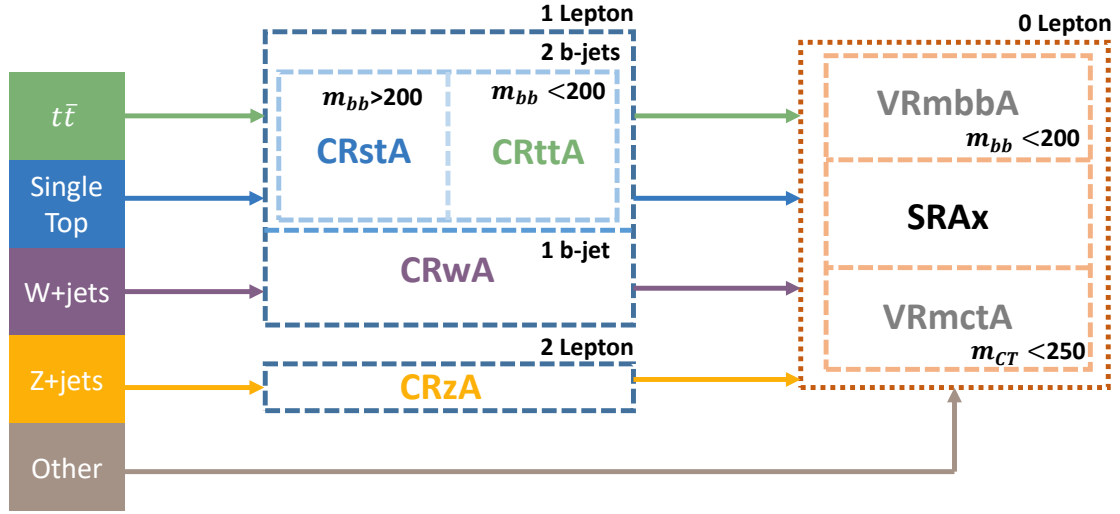


Fig. 7.6 Overview of the SRAx strategy. The four main backgrounds (solid boxes) are normalised in orthogonal control regions with a high purity of the SM background they attempt to normalise. The dashed boxes indicate the the various regions, indicating the selections which make them orthogonal. The other backgrounds in the VRs/SRs are not normalised in any control region.

Table 7.3 Definition of the control regions associated to SRAx. Four signal regions designed with high purity of Z+jets, $t\bar{t}$, Single-Top and W+jets backgrounds respectively. All regions are orthogonal to each other by the application of kinematic and object based selections.

Variable	Units	CRzA	CRttA	CRstA	CRwA	VRAmbb	VRAmct	SRAx
Pre-selection		✓	✓	✓	✓	✓	✓	✓
$N_{b\text{-jets}}$		2	2	2	1	2	2	2
Leading p_T jet b -tagged		✓	✓	✓	✓	✓	✓	✓
Sub-leading p_T jet b -tagged		✓	✓	✓	X	✓	✓	✓
Lepton selection ($\ell = e, \mu$)		2	1	1	1	0	0	0
Lepton p_T (ℓ_1, ℓ_2)	GeV	(> 90, > 20)	(> 26, -)	(> 26, -)	(> 26, -)	-	-	-
$m_{\ell\ell}$	GeV	[76 – 106]	-	-	-	-	-	-
m_T	GeV	-	-	-	> 30	-	-	-
Leading jet p_T	GeV	-	> 130	-	> 130	> 130	> 130	> 130
E_T^{miss}	GeV	< 100	> 100	> 100	> 100	> 250	> 250	> 250
$\tilde{E}_T^{\text{miss}}$	GeV	> 100	-	-	-	-	-	-
m_{bb}	GeV	> 200	< 200	> 200	$(m_{bj}) > 200$	< 200	> 200	> 200
m_{CT}	GeV	-	> 150	> 150	> 150	> 150	< 200	> x = 250, 350, 450
$m_{b\ell}^{\text{min}}$	GeV	-	-	> 170	-	-	-	-
$\min[\Delta\phi(\text{jet}_{1-4}, E_T^{\text{miss}})]$		-	-	-	-	> 0.4	> 0.4	> 0.4
$E_T^{\text{miss}}/m_{\text{eff}}$		-	-	-	-	> 0.25	> 0.25	> 0.25

on the process. For example, the generator Sherpa 2.1.1 [7] was used for the simulation of W or Z bosons with associated jets including heavy flavour jets. Whereas, Powheg+Pythia6 [233, 156] was used in the simulation of the top backgrounds.

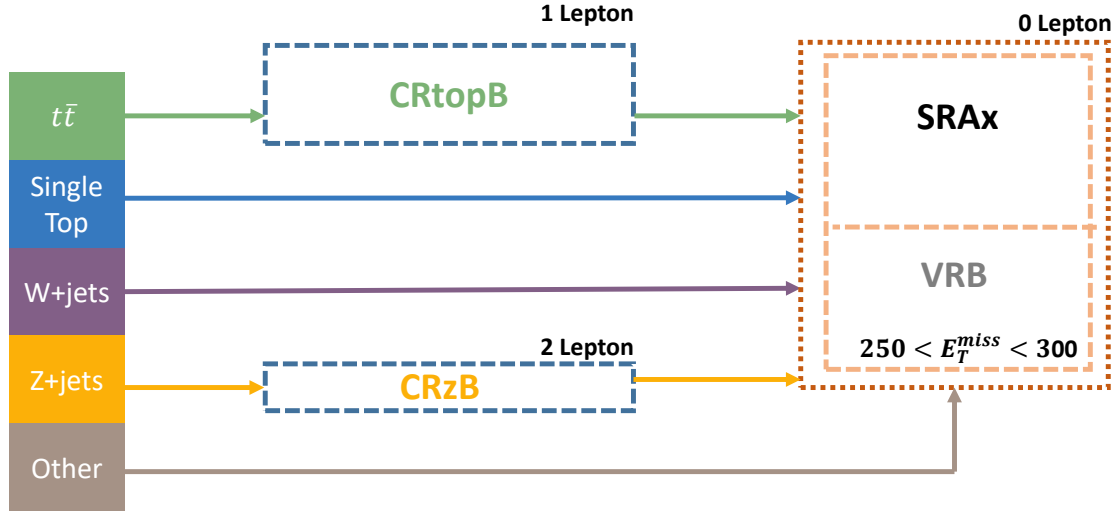


Fig. 7.7 Overview of the SRB strategy. The two main backgrounds (solid boxes) are normalised in orthogonal control regions with a high purity of the SM background they attempt to normalise. The dashed boxes indicate the the various regions, indicating the selections which make them orthogonal. In the B region case, the Single-Top, W+jets and other backgrounds are not normalised in any control regions.

Table 7.4 Control and validation regions associated to SRB.

Variable	Units	CRzB	CRtopB	VRB	SRB
Pre-selection		✓	✓	✓	✓
$N_{b\text{-jets}}$		2	2	2	2
Lepton selection ($\ell = e, \mu$)		2 SFOS	1	0	0
Lepton p_T (ℓ_1, ℓ_2)	GeV	(> 26, > 20)	(> 26, -)	-	-
Leading- p_T jet p_T	GeV	> 50	> 130	[100, 300]	> 300
Leading- p_T jet		not b -tagged	not b -tagged	not b -tagged	not b -tagged
Sub-leading- p_T jet		b -tagged	b -tagged	b -tagged	b -tagged
$\Delta\phi$ (1 st jet, E_T^{miss})		> 2.0	> 2.5	> 2.5	> 2.5
$m_{\ell\ell}$	GeV	[76 – 106]	-	-	-
$\tilde{E}_T^{\text{miss}}$	GeV	> 100	-	-	-
E_T^{miss}	GeV	< 100	> 200	[250, 300]	> 400
$\min[\Delta\phi(\text{jet}_{1-4}, E_T^{\text{miss}})]$		-	-	> 0.4	> 0.4
$E_T^{\text{miss}}/m_{\text{eff}}$		-	-	> 0.25	> 0.25

In cases where samples are generated with MadGraph5 + MC@NLO [153, 151], the program EvtGen 1.2.0 [234] is used to model the heavy flavour decays of b - and c -hadrons. The majority of the samples use a fully simulated detector response using Geant4 [149]; fast

7.3 Nominal Background Estimation

simulation [161] was used for theoretical uncertainty calculations. The simulation of pileup and the Underlying Event (UE) is performed by generating a series of interactions using Pythia 8.186 [223] with the MSTW2008LO [235] parton distribution function (PDF). For more detail see Chapter 3.1.2.

Table 7.5 MC samples used by the $bb+E_T^{\text{miss}}$ analysis in Run-II of the LHC.

SM background	MC generator(s)
scalar bottom signal $t\bar{t} + Z/W$	MadGraph5 + MC@NLO [153, 151]
Z+jets W+jets Di-bosons	Sherpa 2.1.1 [7]
γ +jets	Sherpa 2.1.0 [7]
$t\bar{t}$ Single Top (Wt-channel and s-channel)	Powheg-Box v2 + Pythia6 [233, 156]
Single Top (t-channel)	Powheg-Box v1 + Pythia6 [236, 156]

7.3 Nominal Background Estimation

Following the procedure detailed in Chapter 5.9, a semi-data-driven method to estimate the various SM backgrounds was employed as the nominal estimate. All backgrounds were simultaneously normalised via a likelihood fit of all CRs in Table 7.3 and all CRs in Table 7.4. As shown in Figures 7.6 and 7.7, the CRs are designed to best normalise a particular SM background. The likelihood fit takes into account all backgrounds in each region assigning a normalisation factor (μ_i) to each SM background to be normalised. In the CRs associated with the A region these are assigned to the $t\bar{t}$, Single Top, W+jets and Z+jets backgrounds; in the CRs associated with the B region only the $t\bar{t}$ and Z+jets backgrounds are assigned a normalisation factor. Backgrounds which are not given a normalisation factor are allowed to vary within their systematic uncertainties in the likelihood fit.

The simultaneous fits force the SM backgrounds to match the amount of observed data in the CRs since no signal is expected in these regions. The fit takes into account the effects of systematic uncertainties and correlations. The is performed with a *background-only* fit by maximising the likelihood functions of each fit, derived from Equation 5.17.

In the case of the fits performed for the SR_Ax and SR_B regions², the likelihood functions, maximised to find best values of μ_i , are mathematically represented as:

$$L_A(\vec{n}, \vec{\theta}^0 | \vec{\mu}, \vec{b}, \vec{\theta}) = \prod_{i \in [\text{CRttA}, \text{CRstA}, \text{CRzA}, \text{CRwA}]} P(n_i | \mu_i \cdot \lambda_i(\vec{b}, \vec{\theta})) \times C_{\text{sys}}(\vec{\theta}^0, \vec{\theta}) \quad (7.1)$$

$$L_B(\vec{n}, \vec{\theta}^0 | \vec{\mu}, \vec{b}, \vec{\theta}) = \prod_{i \in [\text{CRtopB}, \text{CRzB}]} P(n_i | \mu_i \cdot \lambda_i(\vec{b}, \vec{\theta})) \times C_{\text{sys}}(\vec{\theta}^0, \vec{\theta}) \quad (7.2)$$

Figure 7.8 and Figure 7.9 show key distributions in all A region CRs and all B region CRs respectively, before the values of μ have been obtained to scale the various SM backgrounds to match data in these regions.

7.4 Multi-jet Background Estimate

The JetSmearing method (Chapter 6) for estimating the background associated with jet mis-measurement was used in this analysis. The background is referred to as either the multi-jet background but is sometimes referred to as the QCD background in plots and region names. The procedure for selecting *seed events* and corrections to the azimuthal angle of the jets (ϕ) described in Chapter 6.4.5 were followed and applied. A value of $N_{\text{smears}} = 5000$ was used to generate *pseudo-events*. The pseudo-data was normalised to data in a QCD rich region (CRQCD) defined in Table 7.6. This control region is orthogonal to all SR_Ax and SR_B by inverting the selections on $\min[\Delta\phi(\text{jet}_{1-4}, E_T^{\text{miss}})]$ and $E_T^{\text{miss}}/m_{\text{eff}}$ so that the region is dominated by multi-jet (QCD) events. Figure 7.10a shows the $\min[\Delta\phi(\text{jet}_{1-4}, E_T^{\text{miss}})]$ distribution in CRQCD with a good shape agreement.

Before the method can be used to estimate the multi-jet background in all four SRs it is first tested in VRQCD, a region closer to the SRs but with increased SM backgrounds. VRQCD is also defined in Table 7.6, and is orthogonal to the SRs by only the inversion of the $\min[\Delta\phi(\text{jet}_{1-4}, E_T^{\text{miss}})]$ selection. Figure 7.10b shows the split between CRQCD and VRQCD, the $E_T^{\text{miss}}/m_{\text{eff}}$ variable is relatively well modelled. Figure 7.10c shows good agreement in the $\min[\Delta\phi(\text{jet}_{1-4}, E_T^{\text{miss}})]$ distribution in VRQCD, this is critical as this variable separates the validation region from all four SRs. It is clear that the multi-jet background is negligible for values $\min[\Delta\phi(\text{jet}_{1-4}, E_T^{\text{miss}})] > 0.4$ as seen in Figure 7.10c.

The background contribution from multi-jet fluctuations was found to be negligible in this analysis, selections on $\min[\Delta\phi(\text{jet}_{1-4}, E_T^{\text{miss}})]$ and $E_T^{\text{miss}}/m_{\text{eff}}$ were used aggressively to remove this background thoroughly.

²This will be referred to as the A and B region strategies.

7.4 Multi-jet Background Estimate

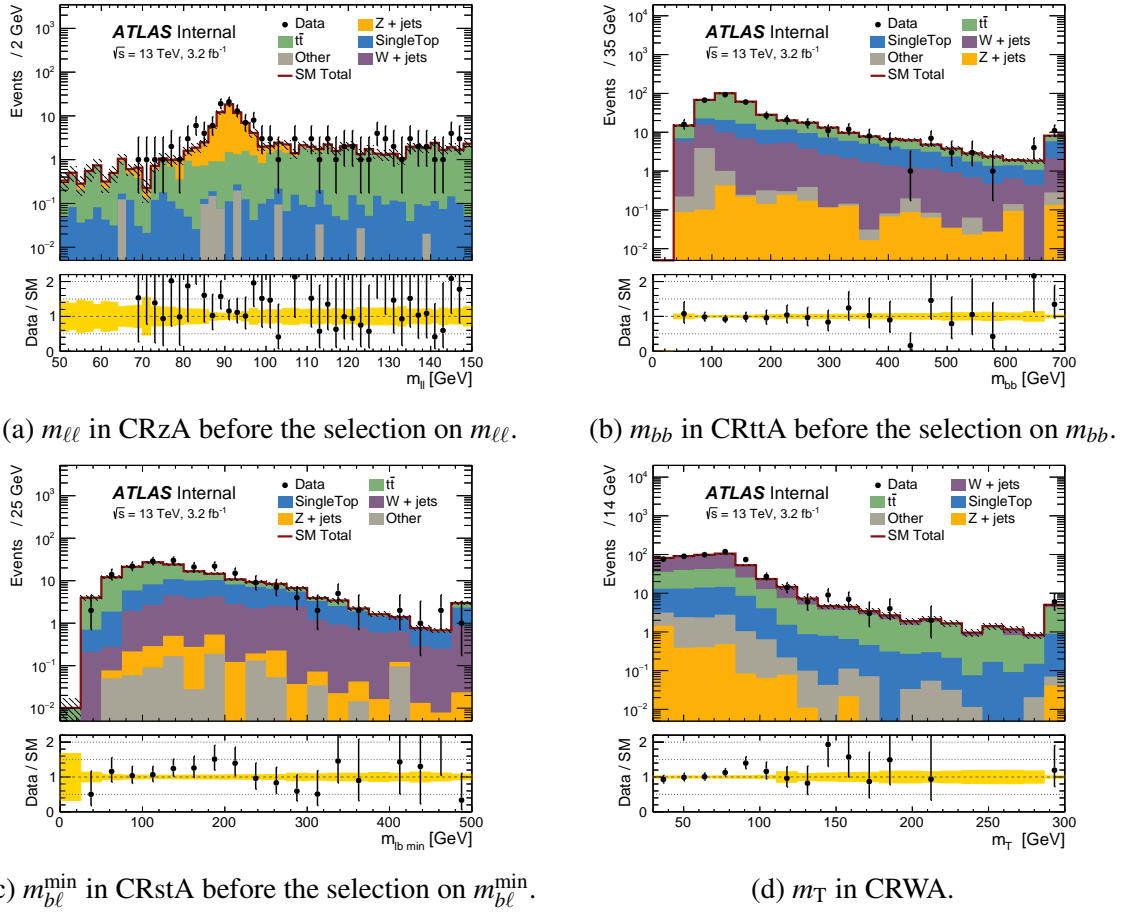


Fig. 7.8 SRAX control regions showing data and the total SM background before performing a likelihood fit. Four control regions, defined to have high purity of the Z (a), $t\bar{t}$ (b), Single Top (c) and W+jets (d) backgrounds are shown. The yellow uncertainty band only shows statistical errors.

Table 7.6 Definition of the multi-jet control (CRQCD) and validation (VRQCD) region for the jet smearing method.

CRQCD	VRQCD
$E_T^{\text{miss}}/m_{\text{eff}} < 0.25$	$E_T^{\text{miss}}/m_{\text{eff}} > 0.25$
0 baseline leptons with $p_T > 10$ GeV	
Leading two jets with $p_T > 50$ GeV	
Leading jet $p_T > 130$ GeV	
Veto on 4 th jet with $p_T > 50$ GeV	
At least two b -tagged jets (77% working point)	
$E_T^{\text{miss}} > 250$ GeV	
$\min[\Delta\phi(\text{jet}_{1-4}, E_T^{\text{miss}})] < 0.4$	

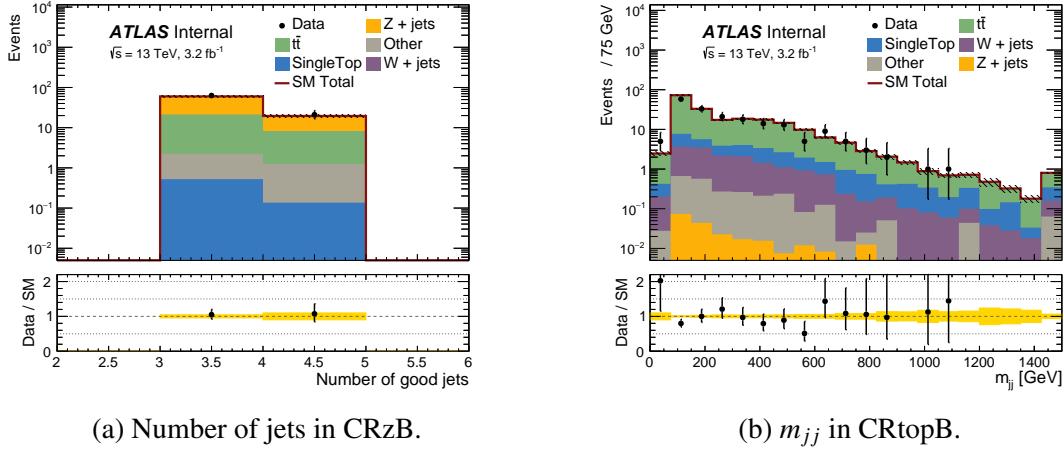


Fig. 7.9 SRB control regions showing data and the total SM background before performing a likelihood fit. (a) shows the Z+jets pure control region and (b) shows the top pure control region. The yellow uncertainty band only shows statistical errors.

7.5 Z+jets Background Estimate

The dominant background in the SRAx regions and the sub-dominant background in SRB is the SM background production of a Z boson and two b-tagged jets. The background is almost exclusively from $Z \rightarrow \nu\bar{\nu}$ decays. Figure 7.11 shows two Feynman diagram of Z-boson production in association with two jets. This background is notoriously difficult to model at low values of invariant mass of the two b-quarks. Figure 7.11a shows a Z boson production in association with quarks originating from $g \rightarrow q\bar{q}$. In the case of $g \rightarrow b\bar{b}$, leading-order and next-to-leading-logarithmic approximation calculations of the vertex depend on α_s and $m(b)$ leading to substantial theoretical uncertainties [237]. The selection of $m_{bb} > 200$ GeV in the three SRAx regions, requires a large virtual gluon mass, therefore gluon splitting diagrams become suppressed and diagrams such as Figure 7.11b become more dominant³. The selection of events in CRzA were also required to have a large b-jet invariant mass. In SRB the topology of a non-b-tagged leading jet back-to-back with the E_T^{miss} suppresses diagrams from gluon splitting.

Two alternative data-driven methods for estimating the Z + jets background were performed: exploiting the similarities between Z and γ bosons, (*Z from γ*); an extrapolation over b-jet multiplicity using $Z \rightarrow \ell\bar{\ell}$ data (*Z from $Z(\ell\bar{\ell})$*).

The electro-magnetic and weak nuclear forces are known to be manifestations of the same force above a certain energy, as described in Chapter 2.1.5. Equation 2.9 shows that the Z boson and γ are different mass eigenstates of the mixed W_μ^3 and B_μ boson eigenstates of

³Such diagrams become more dominant as the Z boson must be of high p_T to give large amounts of E_T^{miss} .

7.5 Z+jets Background Estimate

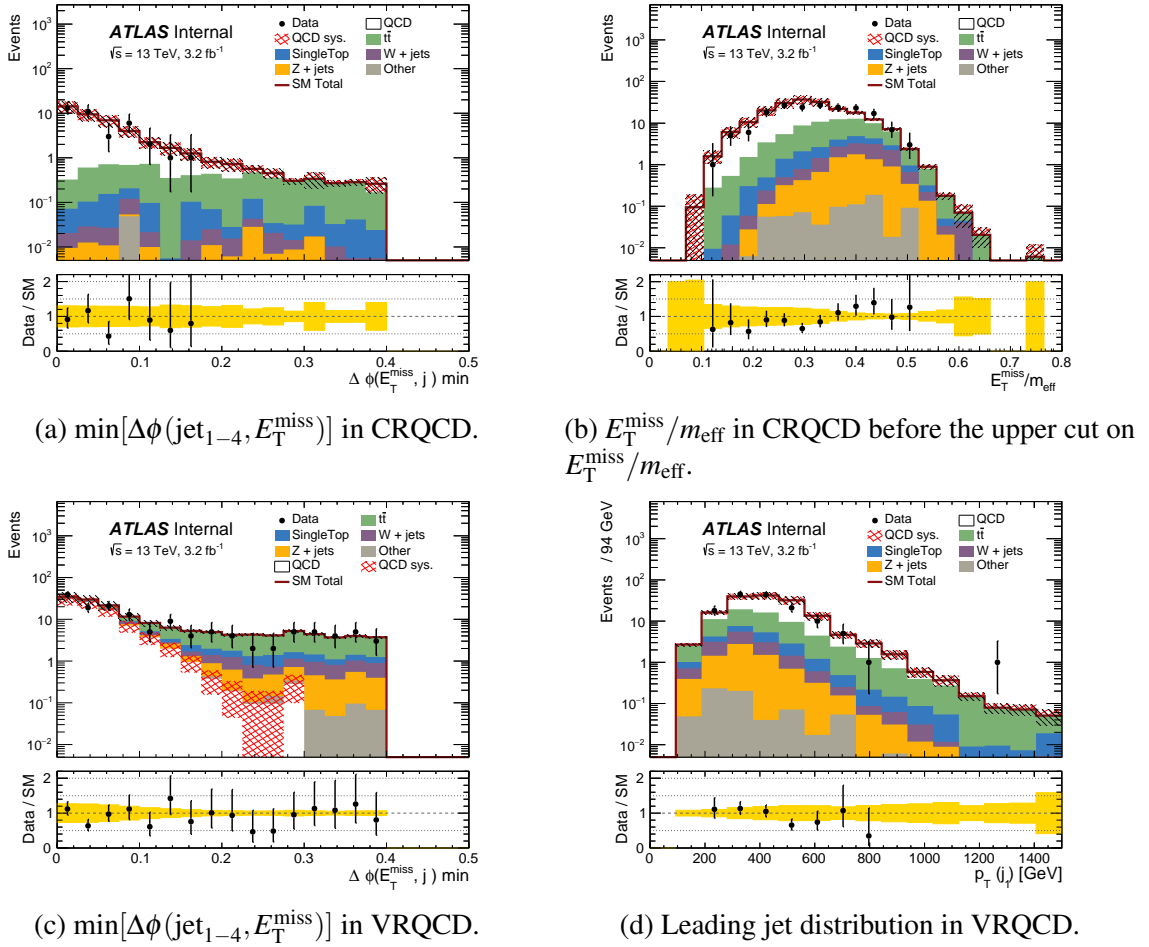


Fig. 7.10 Key distributions in the QCD (multi-jet) sbottom CR and VR.

electro-weak theory. The first data-driven method exploits an assumption that the Feynman diagrams for the production of γ or Z bosons in association with two b -quarks are almost identical. Z bosons have an additional longitudinal polarisation which produces additional Feynman diagrams. A Z boson may also couple to neutrinos adding additional NLO and NNLO diagrams - however these contribute a small amount to the total production cross section. Assuming the diagrams are the same, what remains is a kinematic difference between the final states in $\gamma + \text{jet}$ events and $Z(\nu\bar{\nu}) + \text{jets}$ due to the photon being massless and the Z boson being massive (Table 2.1).

The second method of fully emulating the SRs in $Z \rightarrow \ell\bar{\ell}$ events is a more idealised scenario. However, due to the fact that the branching ratio for Z boson decays to electron-anti-electron and muon-anti-muon pairs is smaller than the decay to invisibles⁴ [238] the statistical uncertainty becomes very large. In addition to this, the amount of background

⁴all three generations of neutrino-anti-neutrino pairs

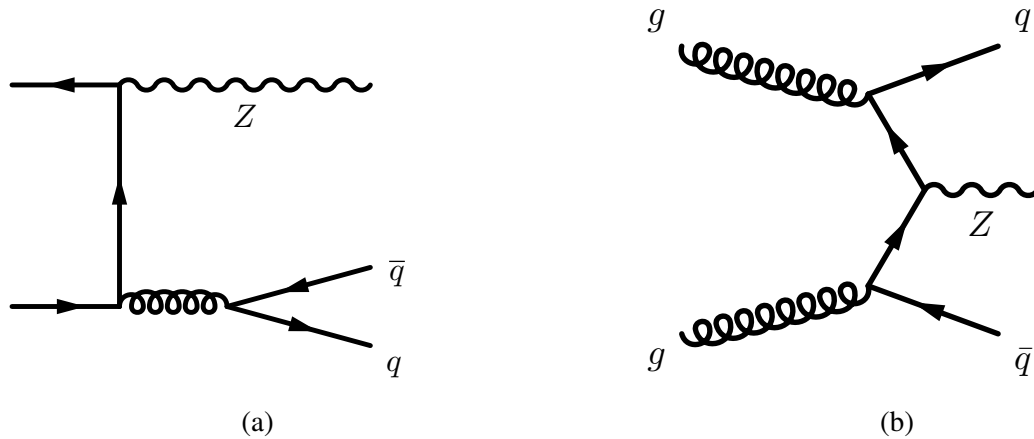


Fig. 7.11 Feynman diagrams showing the production of Z+jets. (a) The gluon splitting gives two quarks which can potentially result in a pair of b-tagged jets of typically low invariant mass. (b) two-additional parton diagram in which may lead to a final state with two b-tagged jets.

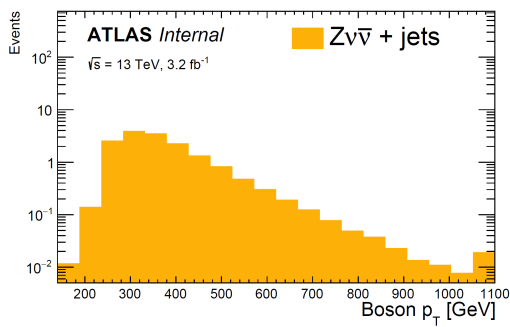
contamination from other SM backgrounds would reduce the effectiveness of the method. To counter these problems, a method was developed extrapolating over the b-tagged jet multiplicity from 0 b-tagged jets to 2 b-tagged jets. Due to the effects of gluon splitting and the inability to distinguish between gluon jets and light-quark jets, this method is only used in regions with large invariant mass of the leading jets, it is not used in SRB or VRAmbb.

To obtain a final estimate consistent with the nominal estimate, the likelihood fit was performed for both A and B strategies removing the CRzA and CRzB and replacing the Z+jets MC estimate with the data-driven estimates. Since these regions have a >99% purity of Z+jets and the other CRs have a small purity of Z+jets, the μ_i for the other backgrounds remained unchanged. This is referred to as the non-Z fit.

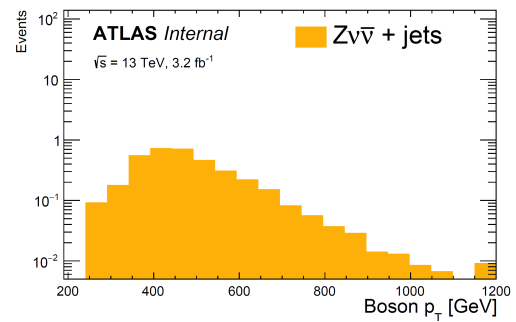
7.5.1 Data-Driven Z+jets from γ +jets

In the context of this analysis, where the Z decays into neutrinos, the boson p_T is approximately the missing transverse momentum, $p_T(Z) \approx E_T^{\text{miss}}$. The truth level Z boson p_T of the SRAX and SRB regions is shown in Figure 7.12.

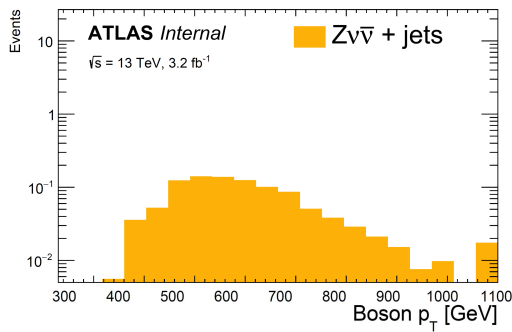
The spectrum in SRA250 peaks at $p_T(Z) \approx 300$ GeV, due to the E_T^{miss} cut of the SR, a value for which m_Z may cause a kinematic difference in Z + jets and γ + jets events. Due to this, a re-weighting procedure to correct for this difference is employed. An overview of the method is given below in Figure 7.13:



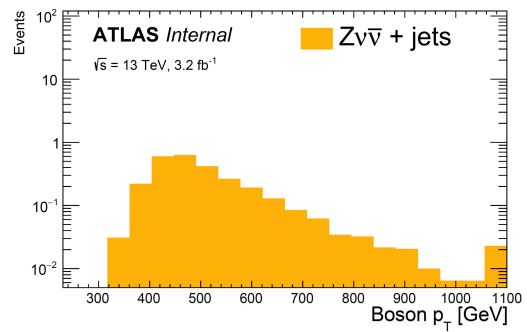
(a) Truth boson p_T in SRA250.



(b) Truth boson p_T in SRA350.



(c) Truth boson p_T in SRA450.



(d) Truth boson p_T in SRB.

Fig. 7.12 Truth boson p_T in the four signal regions as simulated using Sherpa MC.

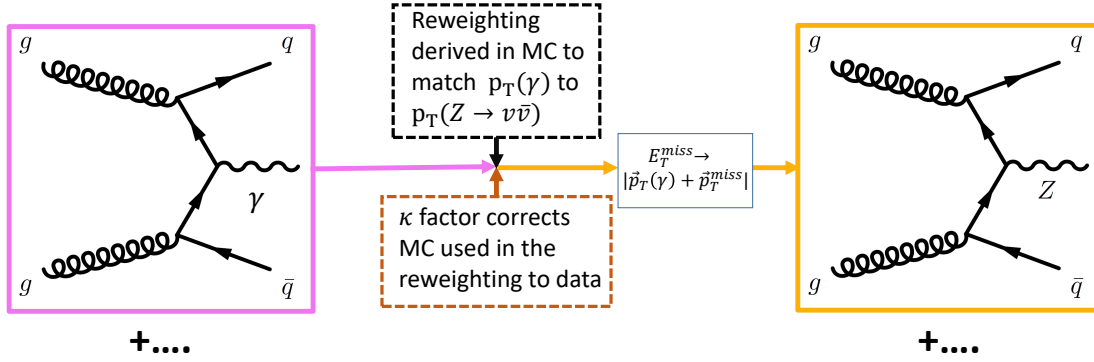


Fig. 7.13 γ +jets events are used for estimating the $Z \rightarrow \nu\bar{\nu}$ +jets background. Data containing a single photon and the same jet kinematics as the SRs are selected. These events are re-weighted to account for cross-sectional differences as a function of the boson p_T . The E_T^{miss} from the neutrino decays is mimicked by adding the photon p_T , finally the full SR selections are applied to estimate the $Z \rightarrow \nu\bar{\nu}$ background.

The method proceeds as follows:

1. Single photon data events with $p_T > 130$ GeV, $|\eta| < 2.37$ are selected using a photon trigger.
2. These events are then required to pass the SR Emulation Region (ER) defined in Table 7.7. The ERs are identical to the SRs but with a single photon whose four-vector has been added to the E_T^{miss} ⁵. The yields for the SM background and observed data can be found in Appendix B.3. A very high purity data sample of γ + jets events is obtained in these regions ($> 95\%$). The non- γ backgrounds are subtracted from the data, thus the shape of the m_{CT} distribution is given by $f_{ER\gamma}^{\text{data}} - f_{ER\gamma}^{\text{non-}\gamma\text{ MC}}$. Figure 7.14 shows the m_{CT} distributions in ER γ A and ER γ B for data and the SM background.
3. Next, the re-weighting factor ($R_{Z/\gamma}$) is determined from $Z\nu\bar{\nu}$ +jets and γ + jets MC in 50 GeV slices of the boson transverse momentum ($\Delta p_T(B)$) :

$$R_{Z/\gamma}\Delta p_T(B) = \frac{f_{\text{SR}}^{Z\nu\bar{\nu}+\text{jets MC}} \Delta p_T(\text{truth } Z)}{f_{ER\gamma}^{\gamma+\text{jets MC}} \Delta p_T(\text{reconstructed } \gamma)} \quad (7.3)$$

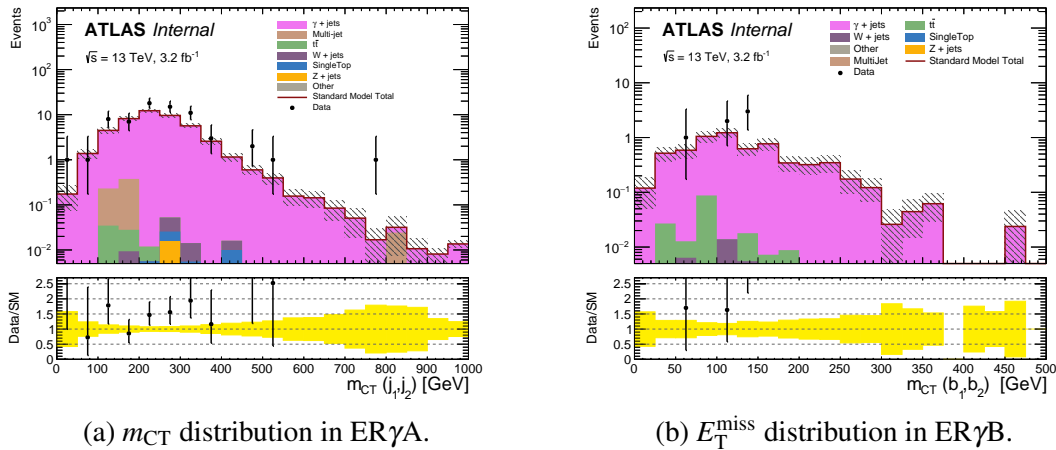
where f is a function describing the shape of a distribution in a particular region. Importantly, the reweighting is performed with the truth level $Z \rightarrow \nu\bar{\nu}$ boson p_T and

⁵All kinematic variables based on E_T^{miss} , such as $\min[\Delta\phi(\text{jet}_{1-4}, E_T^{\text{miss}})]$, use the modified E_T^{miss} .

Table 7.7 Definition of the emulation regions used as templates in the γ + jets data-driven method.

Selection	Units	ER γ A x	ER γ A-mbb	ER γ B
		<i>SRAx emulation</i>	<i>VRAmbb emulation</i>	<i>SRB emulation</i>
Pre-selection		✓	✓	✓
Photons		1 signal	1 signal	1 signal
Leading photon	[GeV]	> 130	> 130	> 130
Leptons (e or μ)		0 baseline	0 baseline	0 baseline
Leading jet p_T	[GeV]	> 130	> 130	> 300
$(E_T^{\text{miss}})^\gamma$	[GeV]	> 250	> 250	> 400
m_{bb}	[GeV]	> 200	< 200	-
m_{CT}	[GeV]	> x	> 150	-
b -jets		(1,2)	(1,2)	(2,3) or (2,4)

* The emulation of VRAmct is made with ER γ A x ; $x = 0$; with an upper cut on $m_{CT} < 150$.


 Fig. 7.14 m_{CT} distribution for data and MC background events in the two γ + jets control regions. Only statistical uncertainties are shown.

the reconstructed photon p_T . This accounts for an acceptance difference when selecting photons in data as well as the cross-section differences between these two processes.

The ratio between the two can be seen in Figure 7.15a. By definition, the reweighting matches the two processes, as shown in Figure 7.15b. The E_T^{miss} (m_{CT}) distribution before reweighting can be seen in Figure 7.15c (Figure 7.15e), after it is applied good agreement is observed between the two processes in Figure 7.15d (Figure 7.15f).

4. An additional factor, denoted as κ , is required to correct the modelling of the Z + jets MC and γ + jets MC used in the reweighting. This requires the addition of two control regions: CRzL and CR γ L. They are defined in Table 7.8 by loosening some of the selections of the ERs, importantly keeping the $(E_T^{\text{miss}})^\gamma > 250$ GeV to ensure that the boson p_T is not extrapolated over. κ is defined as:

$$\begin{aligned}
 \kappa &= \frac{\mu_{\gamma,\text{loose}}}{\mu_{Z,\text{loose}}} \\
 &= \frac{N_{\text{CR}\gamma\text{L}}^{\gamma+\text{jets,data}}}{N_{\text{CRzL}}^{Z+\text{jets,data}}} \cdot \frac{N_{\text{CRzL}}^{Z+\text{jets,MC}}}{N_{\text{CR}\gamma\text{L}}^{\gamma+\text{jets,MC}}} \\
 &= \frac{N_{\text{CR}\gamma\text{L}}^{\text{data}} - N_{\text{CR}\gamma\text{L}}^{\text{non-}\gamma\text{ MC}}}{N_{\text{CRzL}}^{\text{data}} - N_{\text{CRzL}}^{\text{non-Z MC}}} \cdot \frac{N_{\text{CRzL}}^{Z+\text{jets,MC}}}{N_{\text{CR}\gamma\text{L}}^{\gamma+\text{jets,MC}}} \quad (7.4)
 \end{aligned}$$

The calculation of κ is obtained from the yields of CRzL and CR γ L which can be found in Appendix B.3. The result is quoted below:

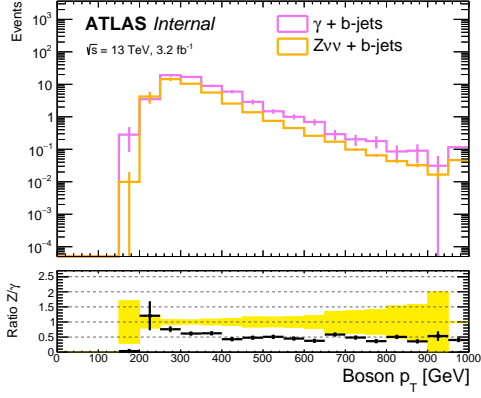
$$\begin{aligned}
 \kappa &= \mu_{\gamma,\text{loose}} / \mu_{Z,\text{loose}} \\
 &= (1.54 \pm 0.09) / (1.21 \pm 0.25) \\
 &= 1.27 \pm 0.27 \quad (7.5)
 \end{aligned}$$

5. The final expected number of $ZV\bar{V}$ + b-jets in the SRs is therefore given by:

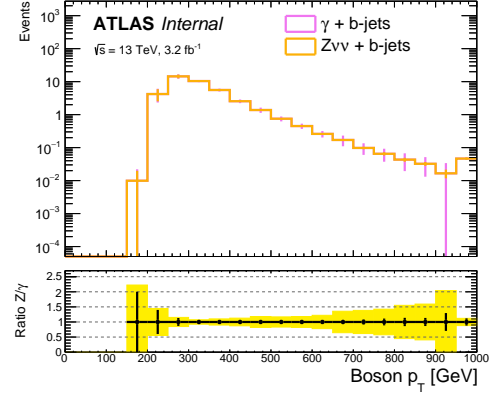
$$N_{\text{SRAx}}^{ZV\bar{V}} = \int_x^\infty \left(f_{\text{ER}\gamma\text{Ax}}^{\text{data}} - f_{\text{ER}\gamma\text{Ax}}^{\text{non-}\gamma\text{ MC}} \right) \cdot \frac{1}{\kappa} \cdot R_{Z/\gamma}(p_T(\gamma)) \, dm_{CT} \quad (7.6)$$

$$N_{\text{SRB}}^{ZV\bar{V}} = \int_0^\infty \left(f_{\text{ER}\gamma\text{B}}^{\text{data}} - f_{\text{ER}\gamma\text{B}}^{\text{non-}\gamma\text{ MC}} \right) \cdot \frac{1}{\kappa} \cdot R_{Z/\gamma}(p_T(\gamma)) \, dm_{CT} \quad (7.7)$$

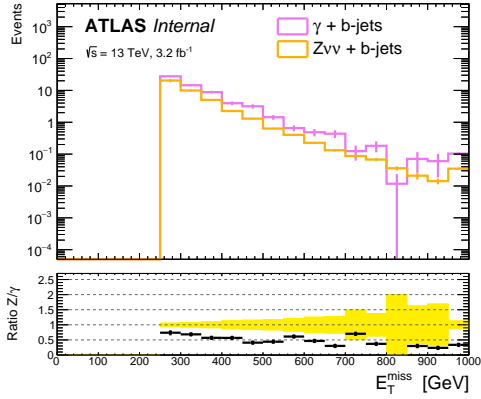
7.5 Z+jets Background Estimate



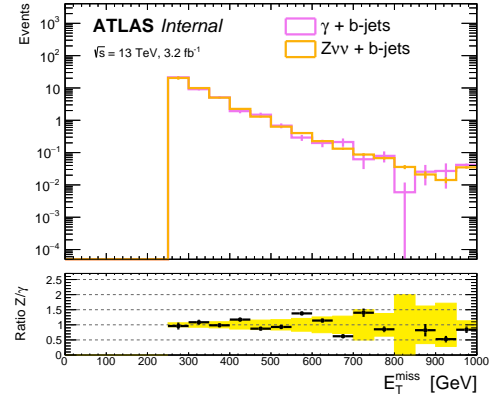
(a) Truth boson p_T of $Z \rightarrow \nu\nu$ MC compared with reconstructed boson p_T γ MC.



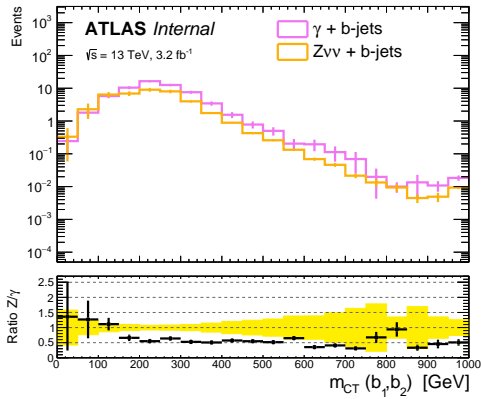
(b) Truth boson p_T of $Z \rightarrow \nu\nu$ MC compared with reconstructed boson p_T γ MC after applying p_T re-weighting.



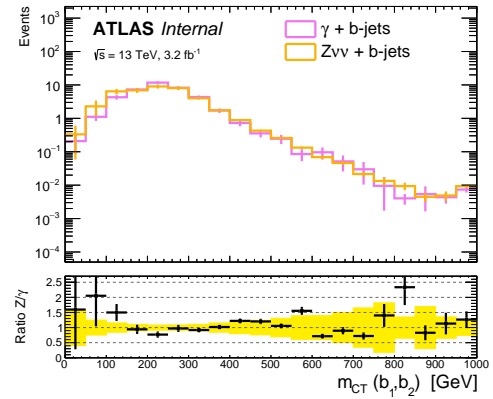
(c) Corrected E_T^{miss} in $Z \rightarrow \nu\nu$ MC compared with γ MC.



(d) Corrected E_T^{miss} in $Z \rightarrow \nu\nu$ MC compared with γ MC after p_T re-weighting.



(e) m_{CT} in $Z \rightarrow \nu\nu$ MC and γ MC.



(f) m_{CT} in $Z \rightarrow \nu\nu$ MC and γ MC after p_T re-weighting.

Fig. 7.15 Comparisons of $Z \rightarrow \nu\nu + b$ -jets and $\gamma + b$ -jets Monte-Carlo events after applying the SRA selections to the $Z \rightarrow \nu\nu + b$ -jet and the ER γ A selections to the $\gamma + b$ -jets. The left column shows the comparison before p_T re-weighting and the right column shows after p_T re-weighting, as described in 3. By construction the p_T re-weighting procedure matches up the reconstructed photon p_T in ER γ A to the truth vector boson p_T in SRA (Figure 7.15b) Only statistical uncertainties are shown. 135

7.5 Z+jets Background Estimate

Table 7.8 Definition of the loose control regions used in estimation of the κ factor in the γ + jets data-driven method.

Selection	Units	CR γ L	CRzL
Pre-selection		✓	✓
Photons		1 signal	-
Leading photon	[GeV]	> 130	-
Leptons (e or μ)		0 baseline	2 signal
Leading jet p_T	[GeV]	> 50	> 50
$(E_T^{\text{miss}})^\gamma$	[GeV]	> 250	-
$\tilde{E}_T^{\text{miss}}$	[GeV]	-	> 250
E_T^{miss}	[GeV]	-	< 100
$m_{\ell\ell}$	[GeV]	-	[76, 106]
b -jets		any 2	any 2

The final estimate obtained from Equation 7.6 and Equation 7.7 is given in Table 7.11, a plot of m_{CT} in SRA is shown in 7.21. Figure 7.16 show additional plots of the E_T^{miss} and leading jet p_T in SRA250 as well as the m_{CT} in VRAmbb and m_{bb} in VRAmct.

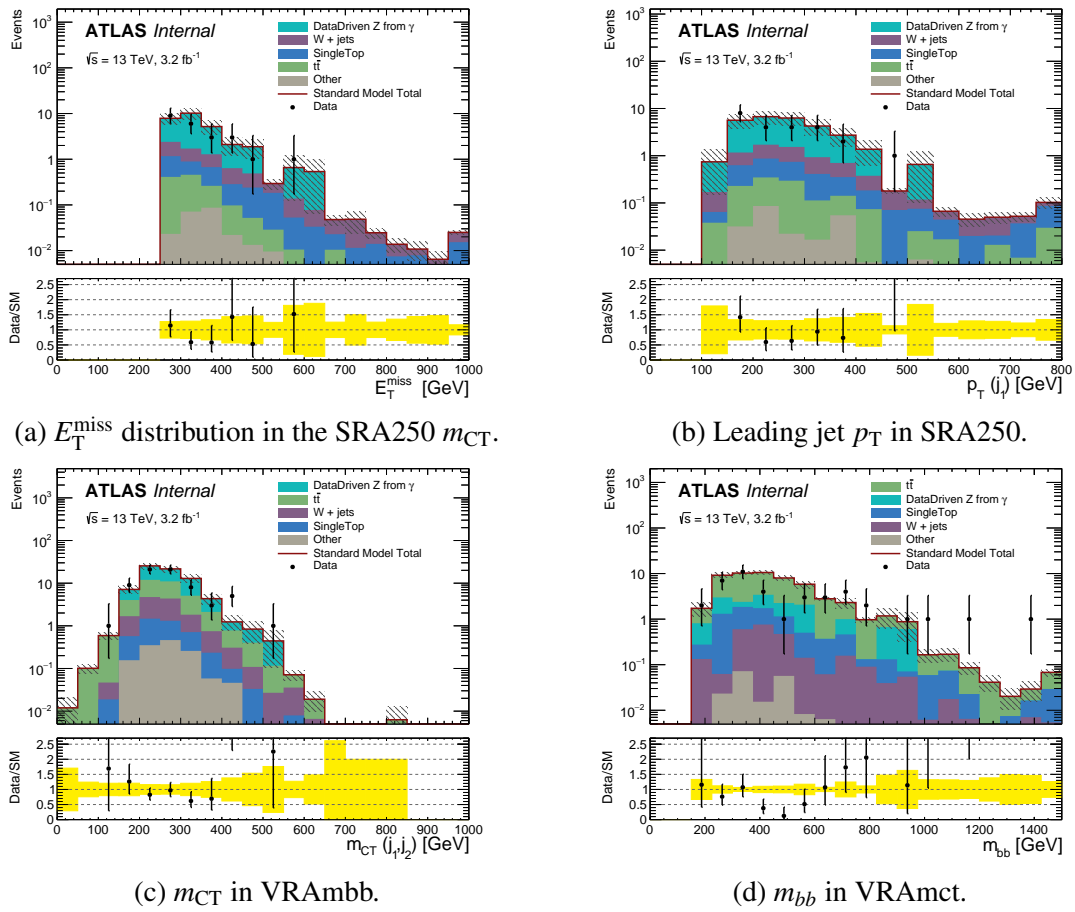


Fig. 7.16 Various VR/SR plots with the Z + jets background estimated using the data-driven technique described in this section. All other SM backgrounds show only MC statistical uncertainties.

7.5.2 Data-Driven Z+jets Extrapolating Over b-jet Multiplicity

The second data-driven method for estimating $Z \rightarrow \nu\bar{\nu} + b$ -jets events relies on the hypothesis that, for an equivalent selection, the shape of the m_{CT} is invariant under changes of the b -jet multiplicity. This was found to hold well for events with high invariant mass of the two leading jets and low jet multiplicity. In such events the effects of gluon splitting and higher order diagrams are suppressed, therefore gluon and light-quark jets can be used to model b -quark jets. The VRAmbb region was defined with an inverted selection on m_{bb} , therefore breaking the hypothesis of sub-dominant contributions from gluon splitting and soft gluon-jets. Due to the different kinematics in SRB, and selection on m_{bb} , this method was only applied for the SRAX regions. Analogously to the previous method, the reconstructed Z (lepton pair) is added to any real E_T^{miss} to form $\tilde{E}_T^{\text{miss}}$. In the case of two leptons, E_T^{miss} and all E_T^{miss} biased variables are replaced with $\tilde{E}_T^{\text{miss}}$. An overview of the method is given below in Figure 7.17.

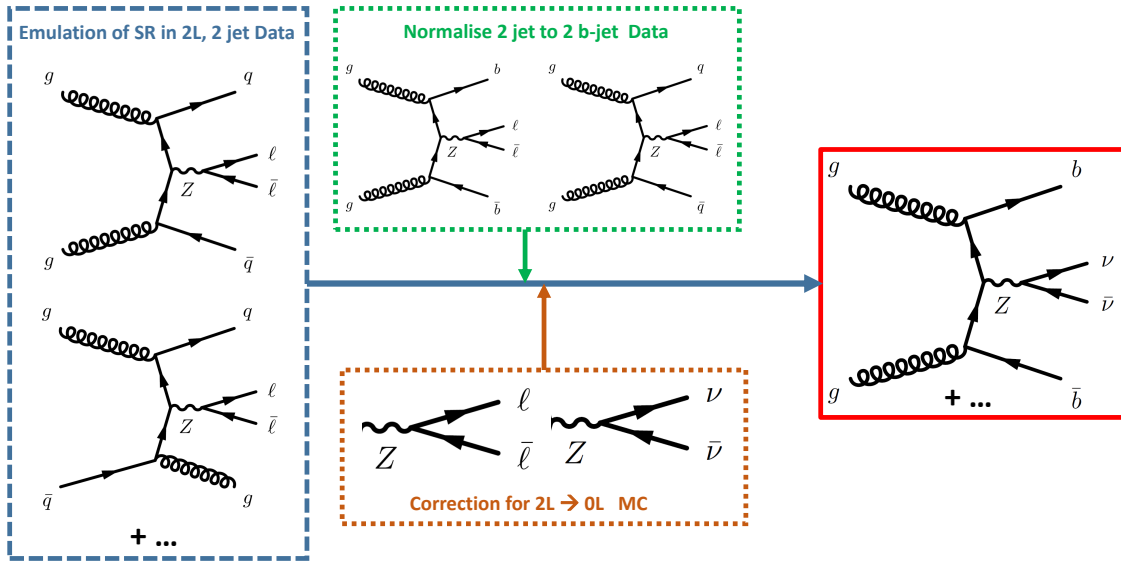


Fig. 7.17 $Z \rightarrow \ell\bar{\ell} + \text{light-jets}$ events are used for estimating the $Z \rightarrow \nu\bar{\nu} + b$ -jets background. Data with two leptons consistent with a Z boson and no b -tagged jets are used as a template. The lepton pair is used as fake- E_T^{miss} and the same jet kinematic selections as the SRs are applied. These events are normalised to events with two b -tagged jets in data. Corrections derived from MC accounting for the lepton reconstruction efficiency and the ratio of $\text{BR}(Z \rightarrow \ell\bar{\ell}) / \text{BR}(Z \rightarrow \nu\bar{\nu})$ are applied. A final estimate of the $Z \rightarrow \nu\bar{\nu} + b$ -jets in the SRs can hence be obtained.

The quantity $f_{Z\nu\nu;2b}(m_{CT})$ defines the distribution of the m_{CT} variable for $Z \rightarrow \nu\bar{\nu}$ events in SRAX. The total number of $Z \rightarrow \nu\bar{\nu}$ events can hence be expressed as:

$$N_{Z\nu\nu}^{SR} = \int_X^\infty f_{Z\nu\nu;2b}^{\text{data}}(m_{\text{CT}}) dm_{\text{CT}} \quad (7.8)$$

$$= \frac{\Gamma_{Z\ell\ell;2b}^{\text{data}}}{\Gamma_{Z\ell\ell;0b}^{\text{data}}} \times \int_X^\infty f_{Z\ell\ell;0b}^{\text{data}}(m_{\text{CT}}) \times C_{\text{lep}} dm_{\text{CT}} \quad (7.9)$$

where

$$\Gamma_{Z\ell\ell;2b}^{\text{data}} = \int_0^\infty f_{Z\ell\ell;2b}^{\text{data}}(m_{\text{CT}}) dm_{\text{CT}} = N_{\text{CR};2b}^{\text{data}} - N_{\text{CR};2b}^{\text{non-Z MC}} \quad (7.10)$$

$$\Gamma_{Z\ell\ell;0b}^{\text{data}} = \int_0^\infty f_{Z\ell\ell;0b}^{\text{data}}(m_{\text{CT}}) dm_{\text{CT}} = N_{\text{CR};0b}^{\text{data}} - N_{\text{CR};0b}^{\text{non-Z MC}} \quad (7.11)$$

$$C_{\text{lep}} = \frac{f_{Z\nu\nu;2b}^{\text{MC}}(m_{\text{CT}})}{f_{Z\ell\ell;2b}^{\text{MC}}(m_{\text{CT}})} \quad (7.12)$$

In this expression:

- $\Gamma_{Z\ell\ell;2b}^{\text{data}}$ is the number of $Z \rightarrow \ell\bar{\ell}$ events in a Z control region similar to the SRA with additional Z purity selections, with two leptons and two b -tagged jets. This can be obtained from the data after subtraction of the non-Z component derived from MC. The region is referred to as CRzA-2b2l and is defined in Table 7.9.
- $\Gamma_{Z\ell\ell;0b}^{\text{data}}$ is the number of $Z \rightarrow \ell\bar{\ell}$ events in a Z control region similar to the SRA with additional Z purity selections, with two leptons and zero b -tagged jets. This can be obtained from the data after subtraction of the non-Z + jets backgrounds which are derived from simulation. The region is referred to as CRzA-0b2l and is also defined in Table 7.9.
- $f_{Z\ell\ell;0b}^{\text{data}}$ is the shape of the m_{CT} distribution obtained from the fully emulated SRA in events with 2 leptons and no b -tagged jets. The region is named ERzA-0b2l and is defined in Table 7.9. Note that this region is extremely pure in Z + jets; yields can be found in Appendix B.2 as well as yields for CRzA-2b2l and CRzA-0b2l .
- C_{lep} is a correction that takes into account any m_{CT} shape difference between $Z \rightarrow \ell\bar{\ell}$ and $Z \rightarrow \nu\bar{\nu}$ due to the branching ratio of a Z boson into electrons and muons or neutrinos, acceptance and efficiency of the leptons. This correction factor is obtained purely from MC in SRax and the emulation of SRax in 2 lepton 2 b-jet events named ERzA-2b2l . The kinematic selections of this region are defined in Table 7.9. Due to the lack of statistics this factor was calculated in a single histogram bin for $m_{\text{CT}} > 200$ GeV.

Figure 7.18a shows a MC level validation of the hypothesis that the m_{CT} shape is independent of the number of required b -jets. It can be seen from this plot that this statement does not hold true for high values of m_{CT} (> 450); therefore the final estimate in SRA450 may over predict the Z background in this region, if the high m_{CT} $Z\nu\bar{\nu}$ MC is assumed to be modelled accurately⁶.

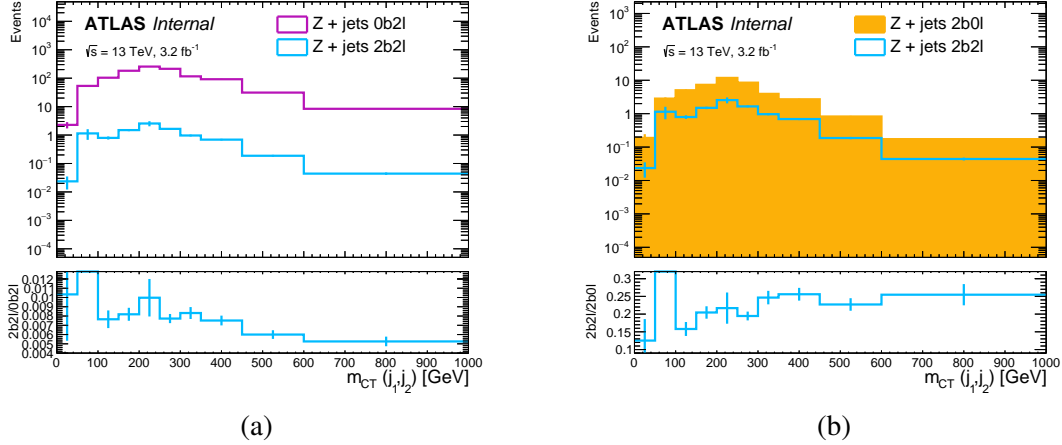


Fig. 7.18 (a) Comparison of the m_{CT} shape for $Z \rightarrow \nu\bar{\nu}$ events with no and two b -jets. (b) Comparison of the m_{CT} shape for events with two b -jets and either no or two leptons.

The distributions from which the factor $\frac{f_{Z\nu\nu;2b}^{MC}(m_{CT})}{f_{Z\ell\ell;2b}^{MC}(m_{CT})}$ is computed are shown in Figure 7.18b. The ratio is relatively flat above $m_{CT} > 200$ GeV, but the MC lacks statistics. A value of ≈ 3 is expected from the ratio between the branching ratios of $Z \rightarrow \nu\bar{\nu}$ and $Z \rightarrow \ell\bar{\ell}$, this factor also takes into the account the effects of efficiency and acceptance in selecting the two leptons in a kinematically similar region to the SRs.

A consistent correction factor is obtained using Sherpa (v2.1) ($C_{lep} = 4.73 \pm 0.43$) and MadGraph+Pythia8 ($C_{lep} = 4.66 \pm 0.70$) for the integral above $m_{CT} > 200$ GeV. For the final estimate given in this section, the percentage errors from MadGraph and Sherpa are added in quadrature and a single correction factor of $C_{lep} = 4.73 \pm 0.83$ is used.

The template distribution $f_{Z\ell\ell;0b}^{data}(m_{CT})$ is extracted from data in ERZA-0b2l. The m_{CT} distribution is shown in Figure 7.19a. The region has a small contamination from non-Z events. This contamination is estimated as a function of m_{CT} from the MC, and subtracted bin-by-bin from the data. The distribution after this subtraction is shown in Figure 7.19b.

The calculation of the $\frac{\Gamma_{Z\ell\ell;2b}^{data}}{\Gamma_{Z\ell\ell;0b}^{data}}$ factor used for the normalisation to two b -jet events is performed with data observed in CRZA-2b2l and CRZA-0b2l.

⁶There is a doubt in the modelling of high p_T b -jets which may mean the high values of m_{CT} for the Z+b-jets MC may not be well modelled. This is why alternative methods were used.

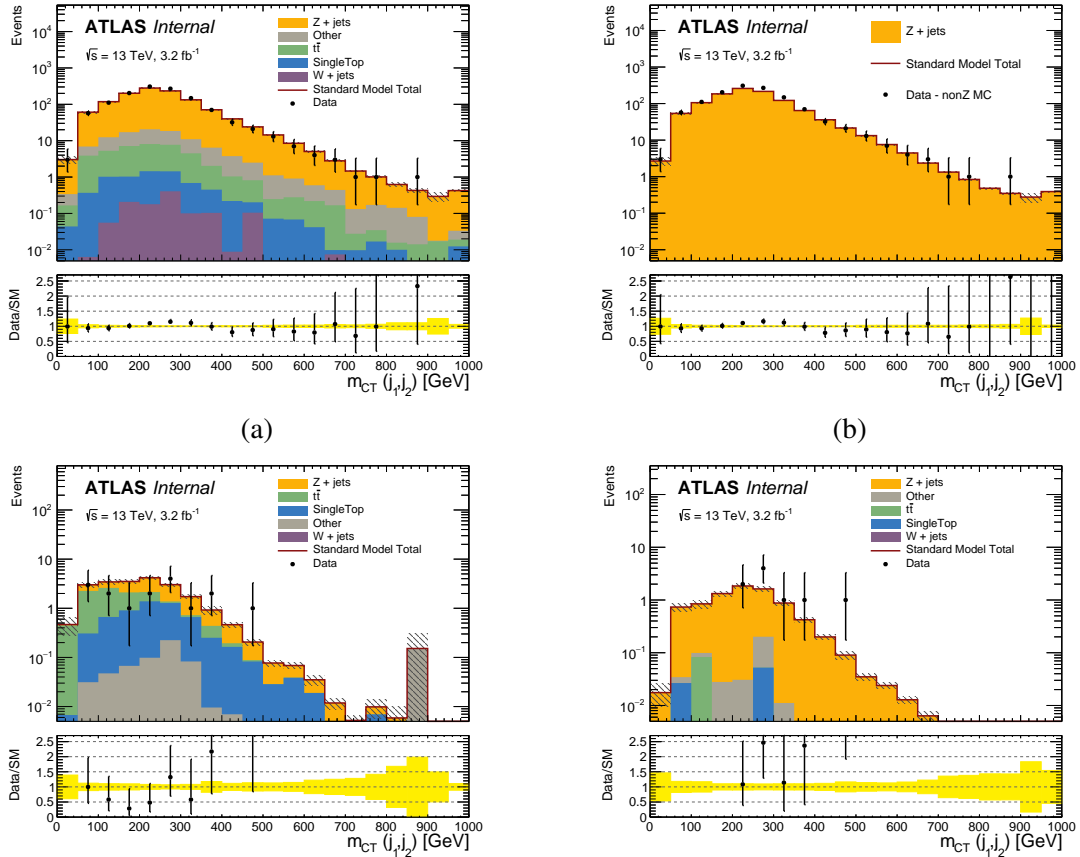


Fig. 7.19 m_{CT} distributions for (a) ERZA-0b2l raw (b) ERZA-0b2l with non-Z MC background subtraction. In the case of two b -tagged jets, m_{CT} is shown in ERZA-2b2l (c) before apply a selection on the original E_T^{miss} and (d) after applying a selection of original $E_T^{\text{miss}} < 100$ GeV and a Z mass window selection of $106 \text{ GeV} > m_{\ell\ell} > 76 \text{ GeV}$. The shaded bands show the Monte Carlo statistical uncertainties.

Table 7.9 Definition of the various 2-lepton emulation (ERzA) and normalisation (CRzA) regions.

		ERzA-0b2l	ERzA-2b2l	CRzA-0b2l	CRzA-2b2l
Pre-selection		✓	✓	✓	✓
Leptons (e or μ)		2 SF	2 SF	2 SF	2 SF
Leading jet p_T	GeV	> 130	> 130	> 130	> 130
$\tilde{E}_T^{\text{miss}}$	GeV	> 250	> 250	> 250	> 250
m_{bb}	GeV	> 200	> 200	> 200	> 200
$m_{\ell\ell}$	GeV	-	-	[76, 106]	[76, 106]
E_T^{miss}	GeV	-	-	< 100	< 100
b -jets (MV2c20 77%)		0	(1, 2)	0	(1, 2)

The resultant factor is obtained in data is shown below in Table 7.10. The table also shows the value obtained in MC as a closure test.

Table 7.10 Calculation of $\frac{\Gamma_{Z\ell\ell;2b}^{\text{data}}}{\Gamma_{Z\ell\ell;0b}^{\text{data}}}$ from CRzA-0b2l and CRzA-2b2l. The superscript, Γ^{data} , refers to the Data with non-Z Monte-Carlo subtracted.

Factor	Value
$\frac{\Gamma_{Z\ell\ell;2b}^{\text{data}}}{\Gamma_{Z\ell\ell;0b}^{\text{data}}}$	$(0.88 \pm 0.31) \cdot 10^{-2}$
$\frac{\Gamma_{Z\ell\ell;2b}^{\text{MC}}}{\Gamma_{Z\ell\ell;0b}^{\text{MC}}}$	$(0.87 \pm 0.06) \cdot 10^{-2}$

The final estimate of the Z + jets background in SRA using this method are shown in Table 7.11, with the b-jet normalisation obtained from data in CRzA-2b2l and CRzA-0b2l, as quoted in Table 7.10. The estimate of the data-driven method agrees well with that of the nominal prediction from the fit strategy within uncertainties. A comparison of the total MC background prediction and the data in the signal region SRA250 is shown in Figure 7.20 for some selection variables. A good modelling of the data is observed in all cases using the Z + jets data-driven estimate.

7.5.3 Data-Driven Z + jets Summary

A full comparison of the expected yields for all SRs and VRs is given in Table 7.11. Two plots of the m_{CT} variable in SRax is shown in Figure 7.21.

7.5 Z+jets Background Estimate

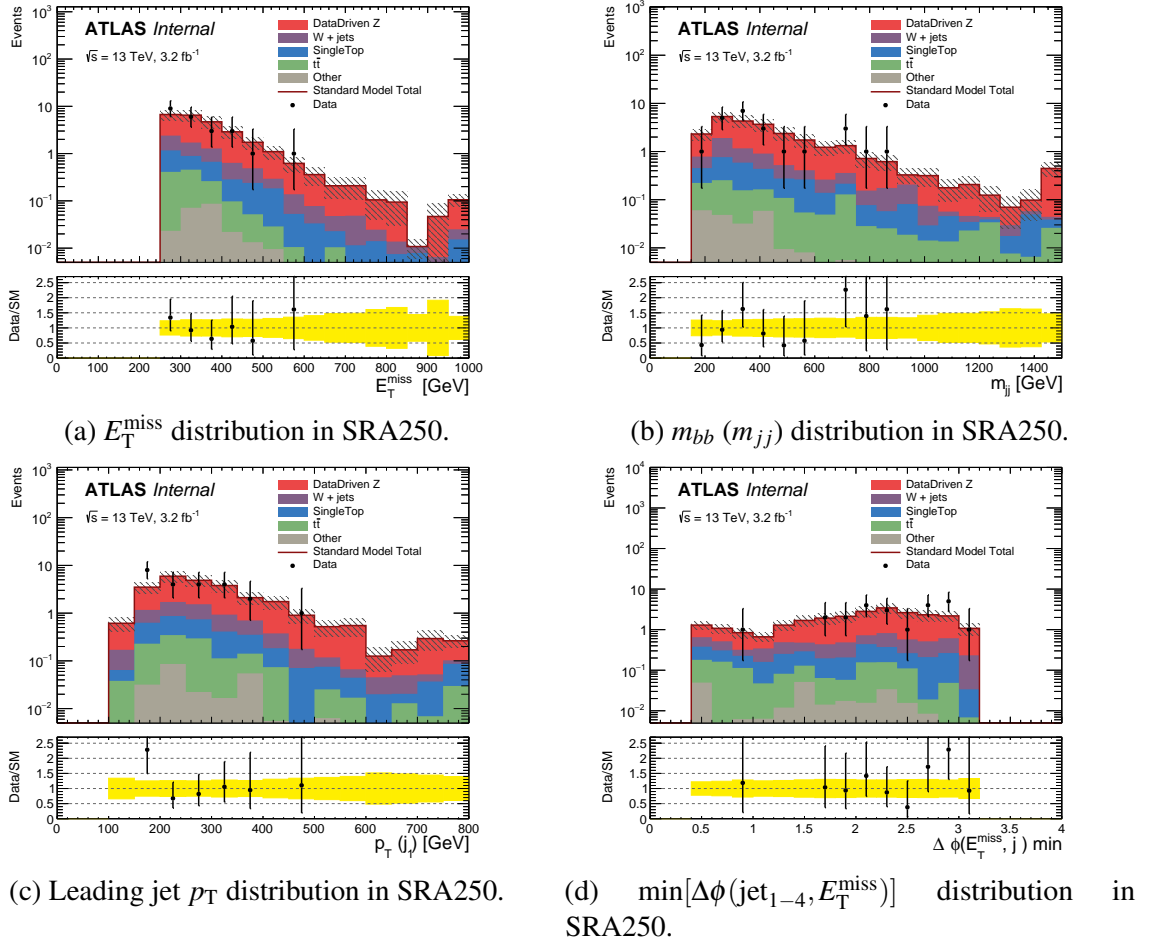


Fig. 7.20 Key distributions after applying the full data driven from Z+light-jets method in SRA.

Table 7.11 Expected Z + jets background in VRAmct, SRA250, SRA350 and SRA450 for two different data-driven Z + jets estimation methods.

Data-Driven fit	VRAmct	VRAmbb	SRA250	SRA350	SRA450	SRB
Data-Driven Z from γ events	7.69 ± 2.56	33.10 ± 8.24	18.24 ± 4.93	3.69 ± 1.54	1.84 ± 1.01	2.22 ± 1.04
Data-Driven Z from $Z(\ell\bar{\ell})$ events	5.21 ± 1.94	N/A	17.56 ± 6.41	4.28 ± 1.60	1.29 ± 0.52	N/A

A good agreement between the two data-driven methods is observed (within statistical + systematic errors).

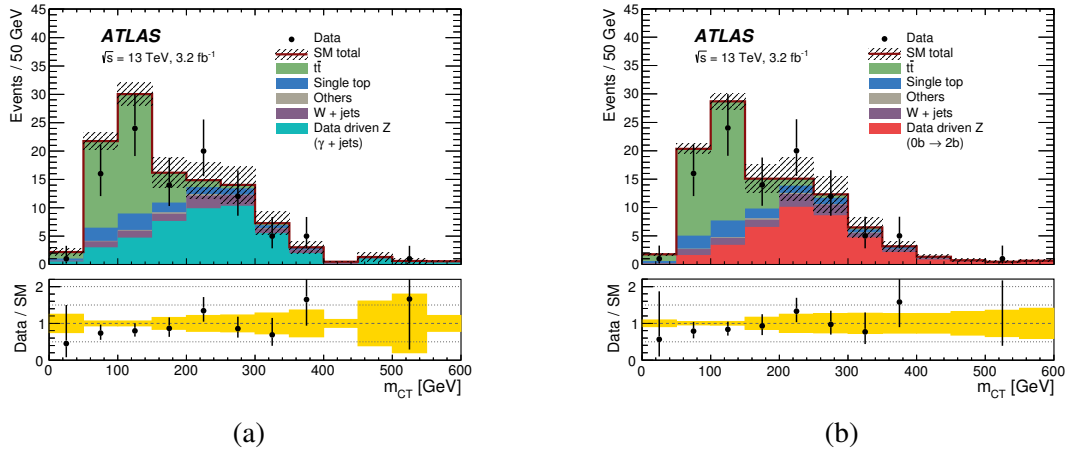


Fig. 7.21 Comparison between data and SM predictions for the m_{CT} variable in the SRAX regions. Non Z+jets backgrounds are estimated from MC and normalised in the CRs and only show MC statistical uncertainties. The left plot (a) shows the Z+jets background estimated using the data-driven method derived from γ +jets and the right plot (b) shows the data-driven prediction derived using Z+light jets processes.

7.6 Systematic Uncertainties

Several sources of experimental and theoretical uncertainties were evaluated in this analysis. These uncertainties take into account various aspects of physics object reconstruction, simulation conditions and detector conditions. As discussed in Chapter 5.9, the normalisation of the MC backgrounds in CRs kinematically close to the SRs reduces the impact of these uncertainties.

Theoretical Modelling Uncertainty The uncertainties in the modelling of the SM background processes - the simulation in MC and their theoretical cross-section is taken into account. For the W/Z + jet backgrounds alternative samples were generated with different renormalisation, factorisation, merging and resummation scales; for a more detailed overview of this see Chapter 4.8.2. The uncertainty of the $t\bar{t}$ and single top backgrounds are computed from samples differing in generators and settings: MadGraph5 [239] generation is used to evaluate the generator uncertainty against the nominal generation using Powheg-Box v2 [233]; Herwig++ v2.7.1 [240] showering instead of Pythia6 [156] is used to evaluate the Parton Shower (PS) uncertainty; and ISR/FSR uncertainties are estimated by tuning parameters in Powheg-Box v2 [233]. The systematic uncertainty is evaluated as the difference between the estimate from these different scales, settings and generation. The errors are added in quadrature.

7.6 Systematic Uncertainties

Table 7.12 summarises the total uncertainty for the four most dominant backgrounds in all signal regions. The numbers are quoted as a percentage relative to the total uncertainty of the background. These errors may be correlated and therefore do not necessarily add in quadrature to the total background uncertainty.

Table 7.12 Theoretical uncertainty as a percentage relative to the total uncertainty for the Z + jets, W + jets, $t\bar{t}$ and Single Top backgrounds in all SRs. The individual uncertainties can be correlated and do not necessarily add in quadrature to the total background uncertainty.

Background	SRA250	SRA350	SRA450	SRB
Z + jets	37%	28%	25%	11%
W + jets	7%	7%	6%	16%
$t\bar{t}$	8%	5%	4%	77%
Single Top	14%	15%	15%	14%

Jet Energy Resolution (JER) The dominant detector systematic in all SRs is the JER, see Chapter 5.5.2 for more detail. The measured values of JER in 13 TeV data as a function of jet η and p_T are detailed in [241], the systematic uncertainty is evaluated from $\pm 1\sigma$ variations of the JER in detector reconstruction. The JER uncertainty accounted for 35%, 31%, 21% and 26% of SRA250, SRA350, SRA450 and SRB of the total background uncertainty.

Jet Energy Scale (JES) The value of JES was estimated in Run-II data at a centre-of-mass energy of $\sqrt{s} = 13$ TeV [204] and applied in the calibration of jets. For a more detailed description of the JES refer to Chapter 5.5.1. The percentage of the total uncertainty associated with JES ranged from 15% – 30% in SRA and 3% in SRB.

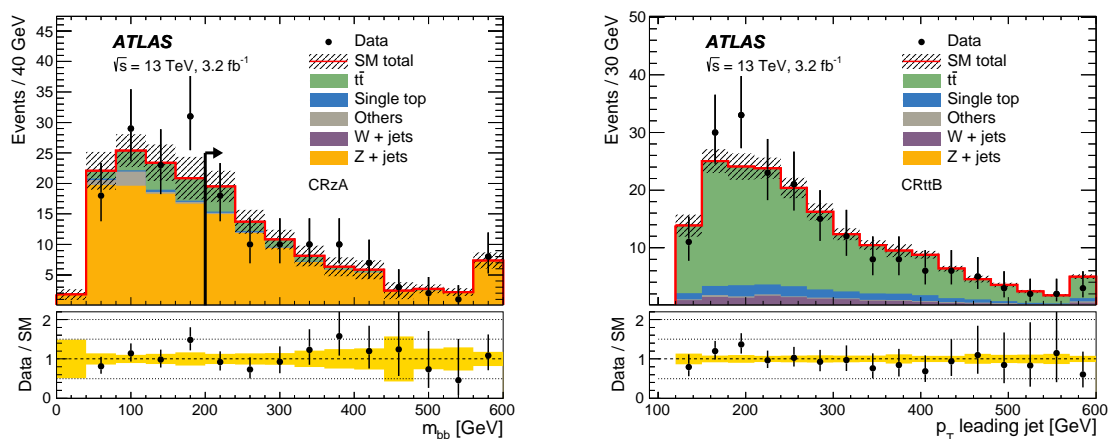
b-tagging and mis-tagging rates Variations to the flavour-dependent jet scale factors (see Chapter 5.4.1) depending on the measured tagging efficiencies and mis-tag rates are calculated. The measured values were obtained in Run-I data at 8 TeV and extrapolated to 13 TeV. b-tagging uncertainties account for between 25-45% of the total systematic uncertainty in the three SRAs and 15% in SRB.

E_T^{miss} soft term In addition to the propagation of uncertainties of the reconstruction of jets and leptons into the E_T^{miss} calculation, a further set of uncertainties relating to the track based soft E_T^{miss} calculation are applied (see Chapter 5.5.4). The systematic uncertainties associated with E_T^{miss} as a percentage of the total systematic uncertainty are $< 10\%$.

Lepton reconstruction The smallest uncertainties due to the high statistics in the lepton CRs and lack of leptons in the SRs came from the reconstruction of leptons. More detail is given in Chapter 5.5.5. These uncertainties relate to the resolution, energy scale, identification and scale factors associated with lepton physics objects. These uncertainties as a percentage of the total systematic uncertainty are $< 10\%$ of the total uncertainty.

7.7 Results

Figure 7.22 shows two plots of the m_{bb} distribution in CRzA before applying the $m_{bb} > 200$ GeV selection and the leading jet p_T distribution in CRtopB.



(a) m_{bb} distribution in CRzA before the $m_{bb} > 200$ GeV selection. The errors represent statistical and systematic uncertainties on the SM background. (b) Leading jet p_T distribution in CRtopB. The errors represent statistical and systematic uncertainties on the SM background.

Fig. 7.22 CR plots for the 2015 $bb+E_T^{\text{miss}}$ analysis published in [28]

Results from performing a CR background-only-fit for the four most dominant SM backgrounds in the SRx regions, as well as the validation regions, are shown in Table 7.13. Table 7.14 shows the background normalisation values (μ_i) of Equation 5.15. The uncertainties on the SM backgrounds, and hence the total background, include all detector and theoretical systematic uncertainties, these errors may be correlated and do not necessarily add in quadrature. For more detail on the statistical interpretation of the results refer to Chapter 5.9.

The background-only-fit results for the singular SRB regions are shown in Table 7.15, with the normalisation values obtained in CRtopB and CRzB shown in Table 7.16.

Table 7.13 Fit results in the control and validation regions associated to the SRA selection for an integrated luminosity of 3.2 fb^{-1} . The results are obtained from the control regions using the background-only fit (see text for details). The errors shown are the statistical plus systematic uncertainties.

CR/VR channels	CRzA	CRwA	CRttA	CRstA	VRmctA	VRmbbA
Observed	78	543	260	56	41	68
Total Background (fit)	78.01 ± 8.82	543.00 ± 23.29	260.11 ± 16.12	55.88 ± 7.42	54.25 ± 7.44	75.61 ± 7.50
Z + jets	67.65 ± 8.98	3.76 ± 0.64	1.38 ± 0.23	0.94 ± 0.17	10.78 ± 3.35	35.34 ± 6.30
W + jets	0.00 ± 0.00	327.54 ± 43.47	45.04 ± 14.19	20.24 ± 5.71	2.94 ± 0.84	11.36 ± 4.05
$t\bar{t}$	9.01 ± 1.63	153.71 ± 26.17	180.97 ± 22.66	11.15 ± 2.09	35.60 ± 6.88	20.76 ± 3.82
Single Top	0.75 ± 0.36	50.01 ± 22.42	27.19 ± 12.19	23.03 ± 10.22	4.65 ± 2.12	2.60 ± 1.20
Dibosons	0.27 ± 0.06	7.02 ± 1.11	4.84 ± 0.62	0.37 ± 0.08	0.18 ± 0.06	5.29 ± 0.59
$t\bar{t} + Z$	0.32 ± 0.03	0.56 ± 0.14	0.41 ± 0.04	0.06 ± 0.01	0.08 ± 0.01	0.22 ± 0.07
$t\bar{t} + W$	0.01 ± 0.00	0.39 ± 0.03	0.26 ± 0.03	0.10 ± 0.01	0.03 ± 0.00	0.03 ± 0.01
Total Background (MC expected)	61.41	502.99	266.58	57.47	53.71	66.21
Z + jets	50.45	2.81	1.03	0.70	8.04	26.35
W + jets	0.00	270.54	37.20	16.72	2.43	9.38
$t\bar{t}$	9.45	161.22	189.94	11.69	37.34	21.78
Single Top	0.91	60.45	32.88	27.83	5.62	3.15
Dibosons	0.27	7.03	4.85	0.37	0.18	5.29
$t\bar{t} + Z$	0.32	0.56	0.41	0.06	0.08	0.22
$t\bar{t} + W$	0.01	0.39	0.26	0.10	0.03	0.03

Table 7.14 Normalization factors obtained from the background-only fit with 3.2 fb^{-1} , for each of the main backgrounds in SRA. The uncertainties include both statistical and systematic sources.

μ_{st}	0.83 ± 0.37
μ_{top}	0.95 ± 0.13
μ_W	1.21 ± 0.18
μ_Z	1.34 ± 0.18

Table 7.15 Fit results in the control and validation regions associated to the SRB selection for an integrated luminosity of 3.2 fb^{-1} . The results are obtained from the control regions using the background-only fit (see text for details). The errors shown are the statistical plus systematic uncertainties.

CR/VR channels	CRzB	CRtopB	VRB
Observed	59	188	76
Total Background (fit)	59.00 ± 7.66	188.01 ± 13.71	71.81 ± 6.71
Z + jets	43.10 ± 7.86	0.30 ± 0.12	13.96 ± 3.17
W + jets	0.00 ± 0.00	12.91 ± 4.74	6.42 ± 3.42
$t\bar{t}$	14.24 ± 1.95	155.98 ± 14.97	46.64 ± 5.95
Single Top	0.42 ± 0.07	16.62 ± 2.13	3.95 ± 0.61
Dibosons	0.83 ± 0.36	1.31 ± 0.20	0.50 ± 0.16
$t\bar{t} + Z$	0.38 ± 0.04	0.57 ± 0.09	0.28 ± 0.06
$t\bar{t} + W$	0.03 ± 0.01	0.31 ± 0.03	0.05 ± 0.01
Total Background (MC expected)	45.05	190.92	68.10
Z + jets	28.88	0.20	9.36
W + jets	0.00	12.92	6.43
$t\bar{t}$	14.52	158.97	47.53
Single Top	0.42	16.63	3.95
Dibosons	0.83	1.31	0.50
$t\bar{t} + Z$	0.38	0.57	0.28
$t\bar{t} + W$	0.03	0.31	0.05

Table 7.16 Normalization factors obtained from the background-only fit with 3.2 fb^{-1} , for each of the main backgrounds in SRB. The uncertainties include both statistical and systematic sources.

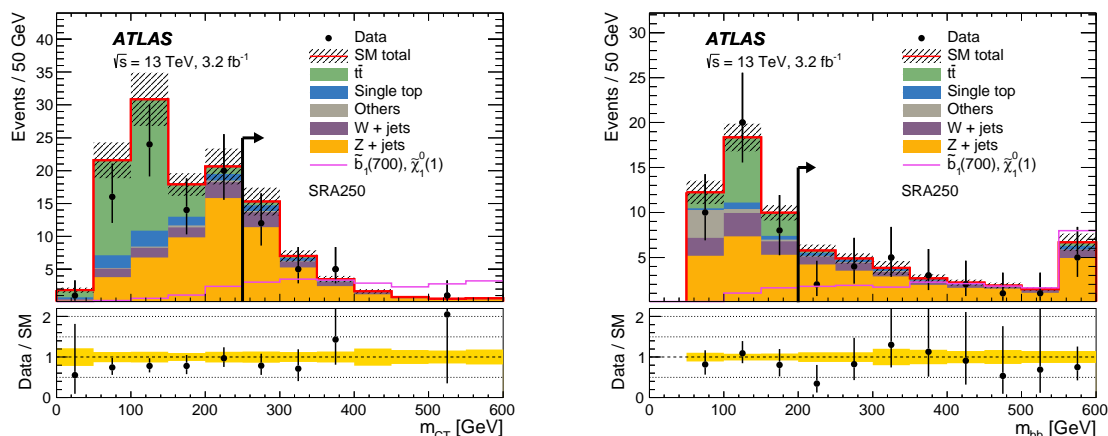
μ_{top}	0.98 ± 0.10
μ_Z	1.49 ± 0.27

A summary of the final signal region results for the background-only fits are shown in Table 7.17.

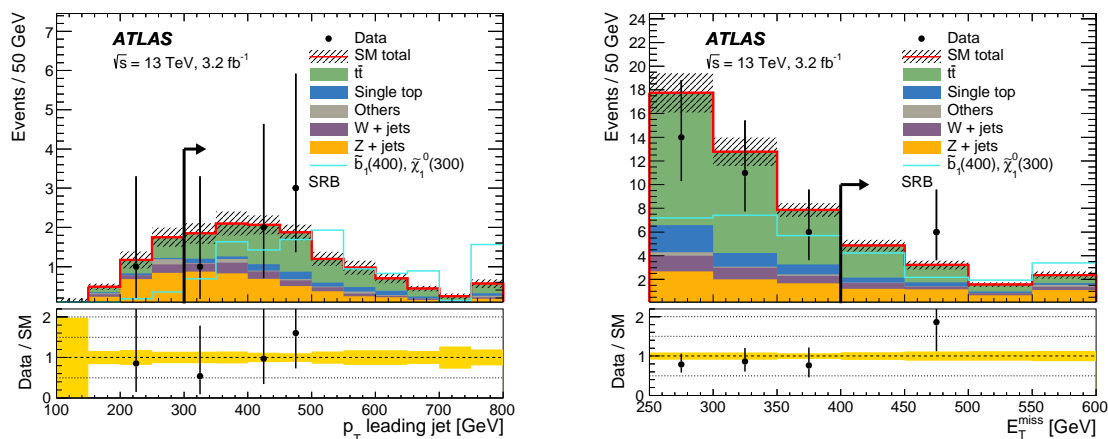
Table 7.17 Observed data and post-fit results in SRAx and SRB signal regions for an integrated luminosity of 3.2 fb^{-1} . The results are obtained from the A and B region CRs using the background-only fit (see text for details). The errors shown are the statistical plus systematic uncertainties, they are not necessarily added in quadrature due to the correlation between certain uncertainties. Additionally two background-only fits were performed, without fitting the $Z + \text{jets}$ backgrounds, these are referred to as non- Z fits. The results using the two data-driven estimates of the $Z + \text{jets}$ background are therefore also shown. The original MC yields before the background-only fit was performed are shown as pre-fit MC yields..

Signal Regions		SRA250	SRA350	SRA450	SRB
Observed Data		23	6	1	6
Total Background	Full fit	29.15 ± 4.71	6.95 ± 1.23	1.84 ± 0.39	12.02 ± 2.50
	Non- Z fit (D.D. Z from $Z(\ell\ell)$)	25.22 ± 6.63	6.28 ± 1.68	1.80 ± 0.54	-
	Non- Z fit (D.D. Z from γ)	25.90 ± 5.21	5.69 ± 1.63	2.35 ± 1.02	10.10 ± 2.34
Data-Driven	Multi-jet	0.00 ± 0.00	0.00 ± 0.00	0.00 ± 0.00	0.00 ± 0.00
	$Z + \text{jets}$ from $Z(\ell\ell)$	17.56 ± 6.41	4.28 ± 1.60	1.29 ± 0.52	-
	$Z + \text{jets}$ from γ	18.24 ± 4.93	3.69 ± 1.54	1.84 ± 1.01	2.22 ± 1.04
Post-fit MC	$Z + \text{jets}$	21.58 ± 4.30	4.96 ± 1.08	1.34 ± 0.36	4.19 ± 1.30
	$W + \text{jets}$	4.36 ± 1.33	1.19 ± 0.41	0.30 ± 0.12	1.11 ± 0.57
	$t\bar{t}$	1.05 ± 0.45	0.17 ± 0.08	0.04 ± 0.02	5.46 ± 2.03
	Single Top	1.80 ± 1.01	0.53 ± 0.30	0.13 ± 0.07	0.99 ± 0.36
	Dibosons	0.21 ± 0.05	0.07 ± 0.04	$0.02^{+0.02}_{-0.02}$	0.19 ± 0.05
	$t\bar{t} + Z$	0.13 ± 0.02	0.03 ± 0.00	0.01 ± 0.00	0.06 ± 0.01
	$t\bar{t} + W$	0.02 ± 0.00	0.01 ± 0.00	0.00 ± 0.00	0.01 ± 0.00
Pre-fit MC	$Z + \text{jets}$	16.09	3.70	1.00	2.81
	$W + \text{jets}$	3.60	0.98	0.25	1.11
	$t\bar{t}$	1.10	0.18	0.04	5.57
	Single Top	2.18	0.64	0.15	0.99
	Dibosons	0.21	0.07	0.02	0.19
	$t\bar{t} + Z$	0.13	0.03	0.01	0.06
	$t\bar{t} + W$	0.02	0.01	0.00	0.01

Figure 7.23 shows some key distributions in the SRAx signal regions and the SRB signal regions. The yield obtained in data, the SM background post-fit and different supersymmetric models are shown.



(a) m_{CT} distribution in SRAx before the $m_{CT} > x$ GeV selection. (b) m_{bb} distribution in the SRAx regions before the $m_{bb} > 200$ GeV selection.



(c) Leading jet p_T distribution in SRB.

(d) E_T^{miss} distribution in SRB

Fig. 7.23 SR plots for the 2015 $bb+E_T^{\text{miss}}$ analysis published in [28]. The errors represent statistical and systematic uncertainties on the SM background. Signal samples for varying scalar bottom and neutralino masses are shown. No significant deviation from the SM background can be seen.

7.7.1 Model-dependent Limits

The concept of a model-dependent fit is discussed in Chapter 5.9.4. A fit of the analysis likelihood function is performed for signal grid point of the simplified model grid, injecting the expected signal yield, s , into the function of form Equation 5.17. The model-dependent *profile likelihood*

*ratio*⁷, of the form of Equation 5.22, is evaluated by the *HistFitter* software package [169] using an asymptotic approximation for large event yields, and a *toy monte-carlo* for small event yields⁸.

As described in Chapter 5.9.4, a p-value is obtained from the profile likelihood ratio. If a small p-value under the background-only hypothesis is obtained ($s = 0$) and an equally small p-value is also obtained with $s \ll b$, then the model-dependent hypothesis is meaningless. To solve this problem, the so called CL_s method [242] is used. The p-value is *regulated* as:

$$CL_s = \frac{CL_{s+b}}{CL_b} \quad (7.13)$$

Where CL_{s+b} is the confidence level⁹ interval of the p-value obtained through the model-dependent fit ($s \neq 0$) and CL_b is the value obtained through the background-only fit ($s = 0$).

The CL_s method ensures that if both the null hypothesis (background-only) and the signal hypothesis both give small p-values, then a value CL value is still obtained. All CL values obtained through this thesis were hence calculated using the CL_s method.

Figure B.3 shows the expected and observed limits at a 95% CL for a range of scalar bottom and neutralino masses. The excluded region is contained within the bands. For example, in this simplified model scenario with a massless neutralino, pair production of scalar bottom quarks up to a mass of ~ 850 GeV are excluded.

7.7.2 Model-independent Limits

Limits were also set for a model-independent scenario, described in Chapter 5.9.5. It is useful to quote numbers relating to the numbers of signal models for *any* scenario that would have been excluded by this analysis. These numbers are supplied by running the likelihood fit for the analysis with s as a free parameter. From this, values for the expected and observed number of signal events which are model-independent can be quoted. This information is useful for evaluating the exclusion power of this analysis in more complex scenarios.

Upper limits on the number of signal events and the visible cross-section¹⁰ for the model independent scenario in each signal region are given in Table 7.18. These model independent limits are derived with 5000 pseudo-experiments. All systematic uncertainties are included, Appendix B.1 provides a complete breakdown of these uncertainties.

⁷Often referred to as a test statistic

⁸Random generation of $n_{\text{toys}} = 5000$ when using the *frequentist calculator* of the package RooStats [217] used to sample the test statistic distribution.

⁹95% CL is used through this thesis.

¹⁰Signal production cross-section times acceptance times efficiency.

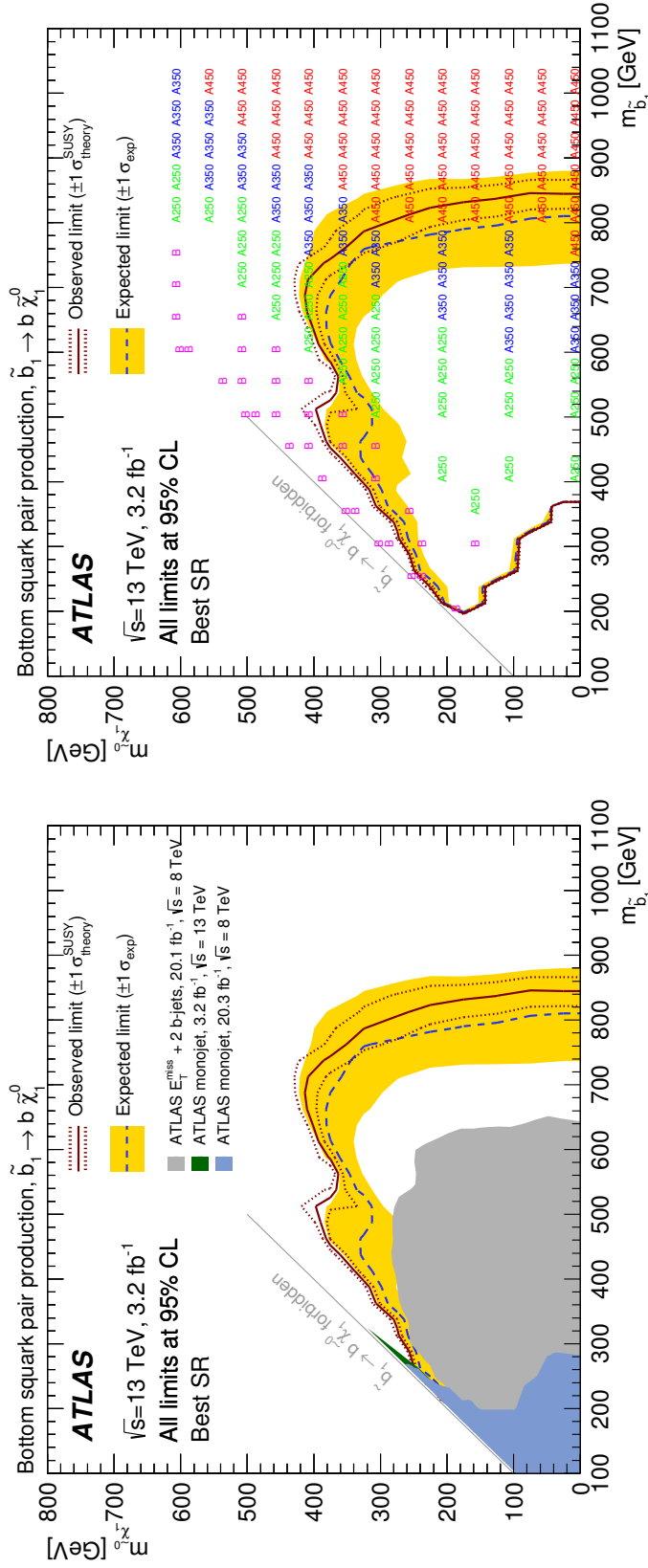


Fig. 7.24 Combined expected and observed exclusion limits at 95% CL in the $(m_{\tilde{b}_1}, m_{\tilde{\chi}_1^0})$ plane (a). For each signal point, the signal region which leads to the best expected limit is chosen, indicated in (b). The dashed black and solid bold red lines show the 95% CL expected and observed limits respectively, including all uncertainties except the theoretical signal cross-section uncertainty. The shaded (yellow) bands around the expected limits show the impact of the experimental uncertainties while the dotted red lines show the impact on the observed limit of the variation of the nominal signal cross-section by 1σ theoretical uncertainty [28].

Table 7.18 Left to right: 95% CL upper limits on the visible cross section ($\langle \epsilon \sigma \rangle_{\text{obs}}^{95}$) and on the number of signal events (S_{obs}^{95}). The third column (S_{exp}^{95}) shows the 95% CL upper limit on the number of signal events, given the expected number (and $\pm 1\sigma$ excursions on the expectation) of background events. The last two columns indicate the CL_B value, i.e. the confidence level observed for the background-only hypothesis, and the discovery p -value ($p(s=0)$).

Signal Channel	$\langle \epsilon \sigma \rangle_{\text{obs}}^{95}$ [fb]	(S_{obs}^{95})	(S_{exp}^{95})	CL_B	$p(s=0)$
SRA250	3.38	10.8	$13.7^{+6.0}_{-3.3}$	0.21	0.86
SRA350	1.93	6.2	$6.5^{+3.2}_{-1.0}$	0.38	0.94
SRA450	1.23	3.9	$4.1^{+1.9}_{-0.5}$	0.29	0.69
SRB	1.90	6.1	$8.8^{+3.0}_{-2.4}$	0.08	0.49

7.8 Conclusions

The results of a search for scalar bottom quark pair production using the data set corresponding to 3.2 fb^{-1} of pp collisions at $\sqrt{s} = 13 \text{ TeV}$ collected by the ATLAS experiment at the LHC in 2015 are presented. Scalar bottom quarks are searched for in events containing large missing transverse momentum and up to three jets, exactly two of which have been identified as having originated from a b -quark. Four dedicated signal regions optimised to give the best sensitivity for varying masses of scalar bottom quarks and their decay products (neutralinos) were utilised.

Three of the signal regions, the SRAx regions, were overlapping, differing by a selection on the m_{CT} of the leading two b -tagged jets. Four control regions were used to normalise the four most dominant SM backgrounds in the SRAx regions using a likelihood fit: $Z + \text{jets}$, in CRzA; $t\bar{t}$, in CRttA; Single Top in CRst; and $W + \text{jets}$ in CRwA. The normalisations obtained were validated in two validation regions designed to be close to the SR with little signal contamination and large yields of $Z + \text{jets}$ and $t\bar{t}$. Background events arising from severe mis-measurement of multi-jet events were validated as negligible with the JetSmearing method. The semi-data-driven $Z + \text{jets}$ background obtained via MC normalised in CRzA was validated by two independent data-driven techniques found to be within 1σ agreement. The variation between the nominal estimate and the two data-driven background estimates was added as an additional systematic uncertainty on the final result.

The data-driven method of using light-jets to model b -jets is a new method developed by the author of this thesis, significant improvement in the method is expected with a changing in the b -tagging strategy discussed in Chapter 5.1.3. The b -tagging efficiency as a function of

7.9 Future Prospects for Scalar Bottom Pair Production at the HL-LHC

jet p_T is shown in Figure 5.7, the tagging efficiency drops as a function of p_T . The method was originally designed for a b-tagging algorithm that has a flat efficiency as a function of p_T .

Normalisation of two dominant backgrounds in SRB, a signal region targeting a compressed scalar bottom - neutralino scenario, was obtained in two control regions. CRtopB was used to normalise the background estimated from MC arising from top quarks and CRzB was used to normalise Z + jets. A singular validation region (VRB) was used to verify this normalisation. The multi-jet background was found to be negligible in this SR. γ + jets were also used in a data-driven method as an alternative estimation of the Z + jets events, good agreement between this estimate and the nominal estimate was found and a systematic uncertainty was added to account for this.

No excess above the expected Standard Model background yields is found in any signal region. Exclusion limits at 95% confidence level on the mass of the scalar bottom quark are derived in a simplified model in which the \tilde{b}_1 is the lightest squark and is assumed to decay via $\tilde{b}_1 \rightarrow b\tilde{\chi}_1^0$, where $\tilde{\chi}_1^0$ is the lightest supersymmetric particle and is stable. Scalar bottom quark masses up to 800 GeV are excluded for $\tilde{\chi}_1^0$ masses below 400 GeV (860 GeV for $\tilde{\chi}_1^0$ masses below 10 GeV) whilst differences in mass above 100 GeV between \tilde{b}_1 and $\tilde{\chi}_1^0$ are excluded up to \tilde{b}_1 masses of 500 GeV.

7.9 Future Prospects for Scalar Bottom Pair Production at the HL-LHC

If any indication of new physics BSM is found during Run-II of the LHC the High-Luminosity-LHC (HL-LHC) will further probe the properties of the underlying physics and a large programme of measurements will be undertaken. This section focuses on the discovery and exclusion reach of the LHC and HL-LHC in the case of direct sbottom pair production with $\sim 300 \text{ fb}^{-1}$ LHC and $\sim 3000 \text{ fb}^{-1}$ of data respectively at $\sqrt{s} = 14 \text{ TeV}$. These results are publically available in [34].

The study was performed using generator level (truth level) Monte Carlo samples for both the background and the signal processes, no control regions or data-driven methods were considered, an assumption of a 30% systematic uncertainty of the background and signal is assumed from past analyses. A procedure of truth smearing was performed on the detector response based on existing data samples and full high pile-up Monte Carlo simulations of the upgraded detector, as described in [243, 244]. The smearing is based on the resolution

7.9 Future Prospects for Scalar Bottom Pair Production at the HL-LHC

and the reconstruction efficiencies of electrons, muons, jets, b -jets¹¹ and E_T^{miss} measured in Run-I of the LHC at $\sqrt{s}=8$ TeV. Simple definitions of signal physics objects were chosen, for jets a p_T threshold of 20 GeV and $|\eta| < 2.8$ was used for all post-smearred truth jets and $p_T > 50$ GeV, $|\eta| < 2.5$ for post-smearred truth b -jets.

This parametrisation of truth level information also accounts for the effect of pileup ranging between $140 > \langle \mu \rangle > 60$ with a 25ns bunch spacing. No triggers are used in this analyses, the cut on the E_T^{miss} and p_T of the leading jet was assumed to be high enough to be fully efficient with a E_T^{miss} or jet+ E_T^{miss} trigger.

7.9.1 Signal Regions

Signal Regions (SRs) were designed based on the Run-I strategy using the kinematic variable m_{CT} . Selections to reject the multi-jet background and $t\bar{t}$ background were kept the same as Run-I and additional cuts on leading jet p_T and E_T^{miss} were optimised for the increased centre-of-mass energy and 300fb^{-1} of data. m_{CT} thresholds of 300, 350, 450, 550, 650 and 750 GeV were chosen, a maximum value of 750 GeV was used since the MC statistical uncertainties become dominant in the tail of the m_{CT} distribution beyond this value, as can be seen in Figure 7.25. A summary of the SRs is given in Table 7.19. The number of expected events for the 300fb^{-1} luminosity scenario is shown in Table 7.20. The dominant backgrounds are Z +jets and single top production, with sub-leading contributions from W +jets and $t\bar{t}V$.

Table 7.19 Summary of selection requirements for the bottom squark pair production signal regions. The value of x notes the selection of the variable m_{CT} .

Selection	SR x
Lepton veto	No e/μ with $p_T > 7(6)$ GeV for $e(\mu)$
E_T^{miss}	> 350 GeV
Leading jet $p_T(j_1)$	> 150 GeV
Third jet $p_T(j_3)$	veto if > 50 GeV
b -tagging	leading 2 jets ($p_T > 50$ GeV, $ \eta < 2.5$)
$\min[\Delta\phi(\text{jet}_{1-4}, E_T^{\text{miss}})]$	> 0.4
$E_T^{\text{miss}}/m_{\text{eff}}(2)$	$E_T^{\text{miss}}/m_{\text{eff}}(2) > 0.25$
m_{CT}	$> x$ GeV
m_{bb}	> 200 GeV

¹¹including the mis-identification of c -jets and light-jets.

7.9 Future Prospects for Scalar Bottom Pair Production at the HL-LHC

Table 7.20 Expected numbers of events for SM background and three bottom squark pair signal points, for different m_{CT} thresholds and an integrated luminosity of 300fb^{-1} . The uncertainties shown are statistical only.

	SRA300	SRA350	SRA450	SRA550	SRA650	SRA750
$(m_{\tilde{b}}, m_{\tilde{\chi}_1^0}) = (1000, 1)$	216 ± 4	200 ± 4	161 ± 4	118.5 ± 3.2	78.6 ± 2.6	44.0 ± 1.9
$(m_{\tilde{b}}, m_{\tilde{\chi}_1^0}) = (1400, 1)$	19.3 ± 0.9	18.4 ± 0.9	16.8 ± 0.8	14.9 ± 0.8	12.8 ± 0.7	10.2 ± 0.6
$(m_{\tilde{b}}, m_{\tilde{\chi}_1^0}) = (1600, 1)$	6.04 ± 0.28	5.84 ± 0.28	5.55 ± 0.27	5.19 ± 0.26	4.57 ± 0.25	3.78 ± 0.22
$t\bar{t}$	32.6 ± 3.0	14.8 ± 2.0	4.3 ± 1.1	1.5 ± 0.7	0.6 ± 0.4	0.29 ± 0.29
single top	146 ± 12	83 ± 8	41 ± 6	25 ± 5	12.7 ± 3.2	8.9 ± 2.5
Z+jets	508 ± 8	249 ± 5	70.5 ± 2.7	23.1 ± 1.5	9.1 ± 1.0	4.1 ± 0.7
W+jets	92 ± 5	44 ± 4	9.3 ± 1.7	2.9 ± 0.9	1.6 ± 0.8	0.9 ± 0.6
Other	5.4 ± 0.5	3.3 ± 0.4	1.59 ± 0.28	0.50 ± 0.16	0.18 ± 0.09	0.15 ± 0.08

7.9.2 Results and Limits

Exclusion limits are set in the $m_{\tilde{b}_1} - m_{\tilde{\chi}_1^0}$ plane using the best expected signal region as shown in Figure 7.26. The 5σ discovery curves are also shown on the same plot. Bottom squark masses up to 1400 GeV can be excluded at 95% CL with 300fb^{-1} of integrated luminosity, for a massless $\tilde{\chi}_1^0$. For the HL-LHC a luminosity of 3000fb^{-1} is hoped to be obtained, the exclusion reach improves by an additional 150 GeV with the same selection criteria. Bottom squarks with masses of $\sim 1100\text{ GeV}$ (1300 GeV) may be discovered with 5σ significance with 300fb^{-1} (3000fb^{-1}).

With an improved analysis strategy the actual results that may be obtained at the HL-LHC will extend the exclusion and discovery limits further than those found in this study. It is however clear that with a greater centre-of-mass energy and 100-1000 times more luminosity the increase in exclusion/discovery potential is not of the same order - much less. This will therefore be a challenge for future generations of particles physicists - if supersymmetry is to be discovered at very high energies with hadron colliders.

7.9 Future Prospects for Scalar Bottom Pair Production at the HL-LHC

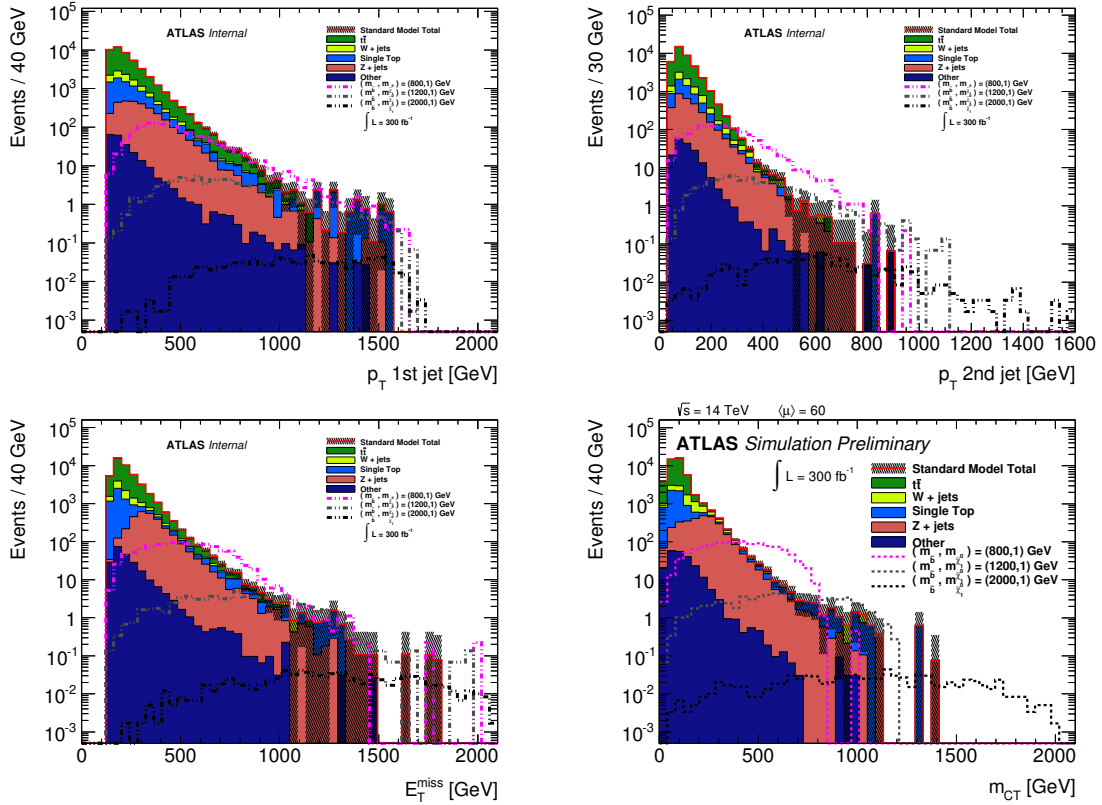


Fig. 7.25 Distributions of the leading two jet $p_{T,S}$, E_T^{miss} and m_{CT} for 300 fb^{-1} before any selection on the variable. Three signal points and the SM backgrounds are shown.

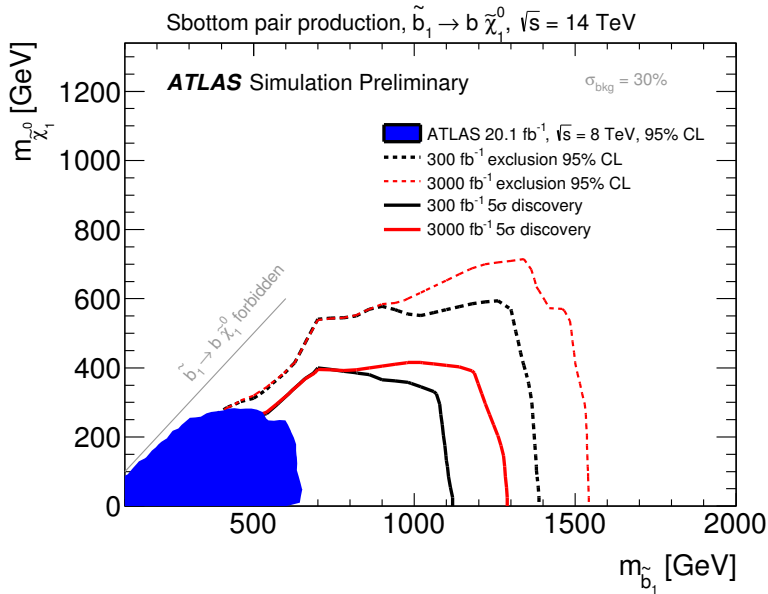


Fig. 7.26 Expected reach of the HL-LHC for 95% level exclusion (dashed lines) and 5σ discovery potential for 300 and 300 fb^{-1} of data.

Chapter 8

A Search for SUSY in a Realistic pMSSM Scenario

If SUSY exists in nature it is most likely to manifest itself in multiple decay chains and mixed branching ratios (BR). As previously discussed, the majority of searches for SUSY in colliders are optimised for a particular sparticle decay with 100% branching ratio. As seen in Chapter 7, a search for scalar bottom quarks targeted a signal model assuming the scalar bottom quarks are pair produced and decay with 100% BR to bottom quarks and neutralinos ($\tilde{b}_1 \rightarrow b\tilde{\chi}_1^0$).

In realistic MSSM scenarios, such as the pMSSM, there are often multiple decay modes of the third generation scalar quarks¹. The exclusion limit reaches obtained at the LHC for scalar quarks are weakened if multiple decay modes occur in nature. In addition to this, mixed decay chains give rise to alternative discovery channels for third generation scalar quarks.

The following chapter details an analysis performed at the end of Run-I of the LHC which was inspired by requiring Naturalness on the pMSSM. It was performed after the 2012 data taking period and published alongside a summary of simplified third generation scalar quark searches [25]. The results were also interpreted in the context of a full pMSSM scan performed by ATLAS [32].

The analysis targeted sparticle masses for two more realistic manifestations of SUSY in nature: a mixed decay model and a naturally inspired pMSSM model. Both of which result in a potential excess in Single Top + E_T^{miss} final states.

¹There are also multiple decay modes of other scalar quarks, gluinos and electro-weakinos.

8.1 Single Top + E_T^{miss} Final States

In Chapter 2.4.6, the concept of Naturalness was discussed. Imposing this phenomenological constraint on the MSSM may lead to *split SUSY* [245], i.e. light scalar top and scalar bottom quarks. Depending on the gaugino mass spectrum, the scalar bottoms (scalar tops) can decay either directly to a neutralino ($\tilde{b}_1 \rightarrow b + \tilde{\chi}_1^0$, $\tilde{t}_1 \rightarrow t + \tilde{\chi}_1^0$) or via intermediate decay into charginos ($\tilde{b}_1 \rightarrow t + \tilde{\chi}_1^\pm$, $\tilde{t}_1 \rightarrow b + \tilde{\chi}_1^\pm$). Final states with a Single Top + E_T^{miss} signature may be populated by the production and mixed decays of scalar bottom and scalar top quarks. A pictorial representation of the Single Top + E_T^{miss} signature originating from either scalar top or scalar bottom decays can be seen in Figure 8.1.

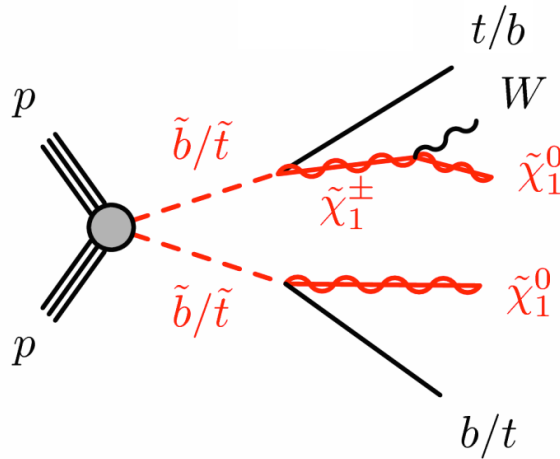


Fig. 8.1 Feynman diagrams of the single top + E_T^{miss} final state signature produced by asymmetric decays of the stop or sbottom into the neutralinos and charginos.

8.2 Searches for SUSY in Single Top + E_T^{miss} Final States in 2012 data at $\sqrt{s} = 8$ TeV

The following details an analysis of Single Top + E_T^{miss} final states from asymmetric decays of scalar top and scalar bottom quarks. The analysis assumed the chargino and neutralino are almost mass degenerate, this is partly motivated by theory but additionally motivated by the fact that scenarios involving additional hard products are well covered by other analyses searching for squarks and gluinos in multi-object final states [246] [32].

The dataset recorded by ATLAS in 2012, at a centre-of-mass energy of $\sqrt{s} = 8$ TeV, totalling 20.3 fb^{-1} of recorded data was used in the analysis and was published in [25].

8.2 Searches for SUSY in Single Top + E_T^{miss} Final States in 2012 data at $\sqrt{s} = 8$ TeV

The leptonic and hadronic decays of the top quark were studied to find the best sensitivity to the signal models of interest. The leptonic channel, giving a final state of two b -jets, one lepton and E_T^{miss} , is found to give the best signal to background ratio over the two main signal models considered. In this case, the dominant SM background processes in the signal regions (SRs) are semileptonic $t\bar{t}$ and single top production as well as W +jets production.

The analysis strategy is to target two signal phenomenologies: a Natural pMSSM (phenomenological Minimum Supersymmetric Standard Models) and two simplified models with mixed decays of the top squark and a small $\Delta m(\tilde{\chi}_1^\pm, \tilde{\chi}_1^0)$.

8.2.1 Simplified Signal Models

In the simplified model scenario, the only parameters of interest considered are: the scalar top quark, neutralino and chargino masses. The branching ratio of the chargino decays are chosen to lead to the signature of interest, a single top final state. This was motivated by studies performed in [247], which showed that ATLAS supersymmetry searches did not perform well for pMSSM models in which a single top final state, opposed to models with two bottom or two top final states.

The scalar top quark mass is varied from 300 to 800 GeV, and the neutralino mass is varied between a lower limit of 100 GeV to an upper limit which is dependent upon the top squark mass considered (where it is required that the top quark from the decay is real). Two signal grids are investigated with either $\Delta m(\tilde{\chi}_1^\pm, \tilde{\chi}_1^0) = 5$ GeV or $\Delta m(\tilde{\chi}_1^\pm, \tilde{\chi}_1^0) = 20$ GeV. In order to generate realistic decays for these scenarios a combination of three types of signal samples, $\tilde{t}_1\tilde{t}_1 \rightarrow t\tilde{\chi}_1^0t\tilde{\chi}_1^0$, $\tilde{t}_1\tilde{t}_1 \rightarrow b\tilde{\chi}_1^\pm b\tilde{\chi}_1^\pm$ and asymmetric decay mode $\tilde{t}_1\tilde{t}_1 \rightarrow t\tilde{\chi}_1^0b\tilde{\chi}_1^\pm$, is required. The total number of events expected is also dependent upon the branching ratios of the available decays. The calculated total number of events for the combination is shown in Eq. 8.1, where k is the branching ratio of the $\tilde{t}_1 \rightarrow t + \tilde{\chi}_1^0$ decay.

$$N_{Total} = k^2 N_{t\tilde{\chi}_1^0t\tilde{\chi}_1^0} + 2k(1-k)N_{t\tilde{\chi}_1^0b\tilde{\chi}_1^\pm} + (1-k)^2 N_{b\tilde{\chi}_1^\pm b\tilde{\chi}_1^\pm} \quad (8.1)$$

Events are generated using MadGraph [239] interfaced to Pythia 6 [155] for the asymmetric and $\tilde{t}_1 \rightarrow b + \tilde{\chi}_1^\pm$ simplified models, and Herwig++ for the Natural pMSSM and simplified scalar top models.

8.2.2 pMSSM Inspired Model

The pMSSM is a constrained subset of the MSSM with 19 free parameters (see Chapter 2.4.5), this number can be further reduced using Naturalness arguments of Chapter 2.4.6. This

8.2 Searches for SUSY in Single Top + E_T^{miss} Final States in 2012 data at $\sqrt{s} = 8$ TeV

particular model is referred to throughout the text as the Natural pMSSM model (NatpMSSM). The Natural pMSSM model is generated by performing a scan over two free parameters (see Table 2.7): μ , the Higgsino mass parameter; and $m_{\tilde{q}_{L,3}}$, the common mass of the top and bottom squarks. Other parameters related to the third generation squarks are constrained by requirements on maximal stop mixing and the Higgs mass. Finally the m_2 parameter is set to 3μ in order to produce models with almost degenerate $\tilde{\chi}_1^0, \tilde{\chi}_1^\pm$ and $\tilde{\chi}_2^0$. In this signal model, SUSY particles are primarily produced in pairs, mixed sparticle pair production occurs but is suppressed. An example of the sparticle masses, decay width ($\Gamma \propto \frac{1}{\tau}$) and their decays for the grid point $\mu=110$ GeV, $m_{\tilde{q}_{L,3}} = 400$ GeV is detailed in Table 8.1. For this particular mass point however the overwhelming majority of signal events originate from either direct scalar top or direct scalar bottom pair production. The total direct scalar bottom pair production ($\tilde{b}_1 \tilde{b}_1$) cross section for this signal point is $\sigma(pp \rightarrow \tilde{b}_1 \tilde{b}_1) = 0.3406$ pb and $\sigma(pp \rightarrow \tilde{t}_1 \tilde{t}_1) = 0.5441$ pb for direct stop pair production ($\tilde{t}_1 \tilde{t}_1$), as with the sparticle masses, the direct production cross subsection of the \tilde{b}_1 and \tilde{t}_1 is dependent on the common mass parameters $m_{\tilde{q}_{L,3}}$.

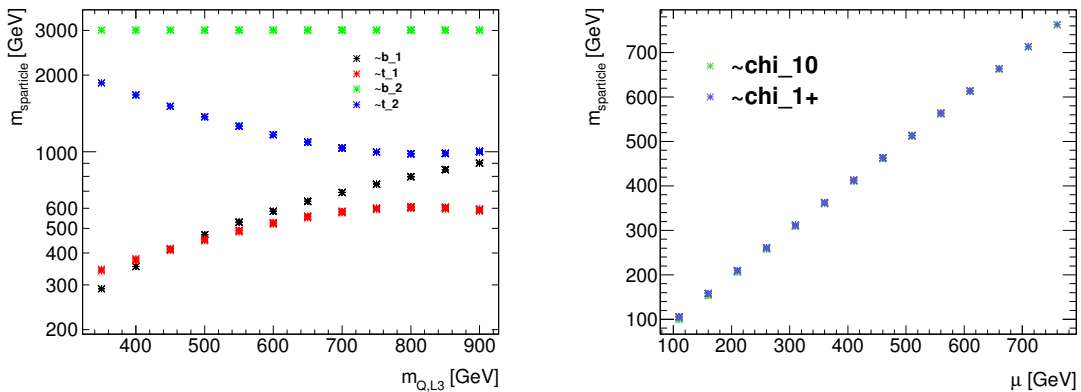


Fig. 8.2 The dependence of the masses of the third generation squarks (left), the lightest chargino and the lightest neutralino (right) on the pMSSM parameters μ and $m_{\tilde{q}_{L,3}}$ in the Natural pMSSM grid. A small mass difference between the $\tilde{\chi}_1^0$ and $\tilde{\chi}_1^\pm$ can be seen in the right plot.

A consequence of naturalness in this particular pMSSM model is that the theory becomes decoupled. The mass parameters of the decoupled particles are set to an arbitrary high scale of 3 TeV, so they are unreachable by the LHC. The mass of the gluinos are set to ~ 1.5 TeV which is also assumed effectively unreachable by the $\sqrt{s} = 8$ TeV LHC. This leaves the mass eigenstates of the mixed Higgsinos and gauginos (neutralinos and charginos) as well as the lightest bottom squark (\tilde{b}_1), lightest top squark (\tilde{t}_1) and the heaviest top squark (\tilde{t}_2) as the only particles dependant on the pMSSM parameters μ and $m_{\tilde{q}_{L,3}}$. The decoupling

8.2 Searches for SUSY in Single Top + E_T^{miss} Final States in 2012 data at $\sqrt{s} = 8$ TeV

Table 8.1 A list of various supersymmetric particles; their masses, decay widths and decays with branching ratios in the Natural pMSSM model with $\mu=110$, $m_{\tilde{q}_{L,3}} = 400$.

Mass[GeV]	Decay Width [GeV]	Decays (BR)
\tilde{t}_1 (377.14)	3.59	36.4 % ($\tilde{t}_1 \rightarrow \tilde{\chi}_2^0 t$) 32.8 % ($\tilde{t}_1 \rightarrow \tilde{\chi}_1^0 t$) 30.7 % ($\tilde{t}_1 \rightarrow \tilde{\chi}_1^\pm b$) <0.1 % ($\tilde{t}_1 \rightarrow \tilde{\chi}_2^\pm b$)
\tilde{b}_1 (403.55)	4.12	69.9 % ($\tilde{b}_1 \rightarrow \tilde{\chi}_1^\pm t$) 16.4 % ($\tilde{b}_1 \rightarrow \tilde{\chi}_1^0 b$) 12.5 % ($\tilde{b}_1 \rightarrow \tilde{\chi}_2^0 b$) 1.1 % ($\tilde{b}_1 \rightarrow \tilde{\chi}_3^0 b$)
$\tilde{\chi}_1^0$ (99.30)	stable	stable
$\tilde{\chi}_1^\pm$ (105.30)	<0.01	100% ($\tilde{\chi}_1^\pm \rightarrow W + \tilde{\chi}_1^0$)
$\tilde{\chi}_2^0$ (118.59)	$2.58 \cdot 10^{-6}$	33 % ($\tilde{\chi}_2^0 \rightarrow W + \tilde{\chi}_1^\pm$) 67% ($\tilde{\chi}_2^0 \rightarrow Z + \tilde{\chi}_1^0$)
\tilde{t}_2 (1666.72)	110.81	28.2 % ($\tilde{t}_2 \rightarrow \tilde{b}_1 W^+$) 20.6 % ($\tilde{t}_2 \rightarrow \tilde{\chi}_1^\pm b$) 14.8 % ($\tilde{t}_2 \rightarrow \tilde{t}_1 h$) 13.5 % ($\tilde{t}_2 \rightarrow \tilde{t}_1 Z$) 11.6 % ($\tilde{t}_2 \rightarrow \tilde{\chi}_2^0 t$) 9.6 % ($\tilde{t}_2 \rightarrow \tilde{\chi}_1^0 t$) 1.2 % ($\tilde{t}_2 \rightarrow \tilde{\chi}_2^\pm b$) 0.5 % ($\tilde{t}_2 \rightarrow \tilde{\chi}_3^0 t$)
\tilde{b}_2 (3010.01)	100.23	many
\tilde{g} (1818.24)	69.10	some
$\tilde{q}_{1,2}$ (3000)	-	many
Gauginos (3000)	-	many
$\tilde{l}_{1,2,3}, \tilde{\nu}_{1,2,3}$ (3000)	-	many

8.2 Searches for SUSY in Single Top + E_T^{miss} Final States in 2012 data at $\sqrt{s} = 8$ TeV

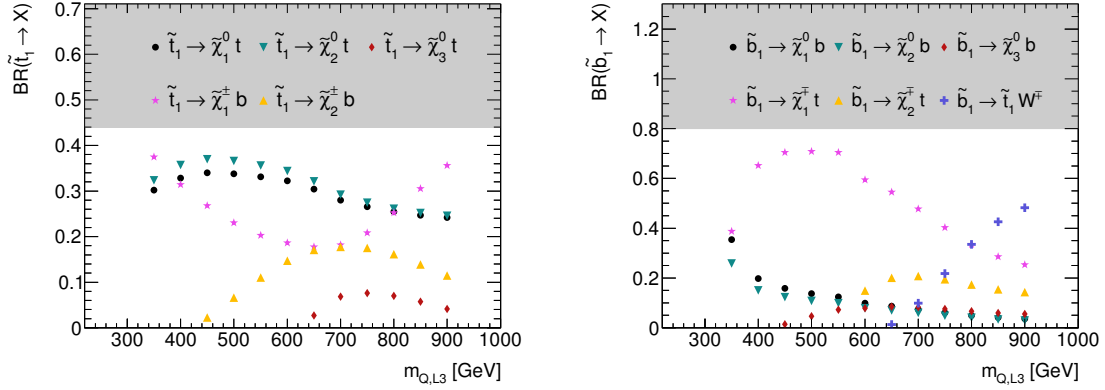


Fig. 8.3 Branching ratios of the dominant decays of scalar top (left) and scalar bottom (right) quarks in the Naturally inspired pMSSM signal scenarios as a function of the left-handed third generation common mass parameter ($m_{\tilde{q}_{L,3}}$).

of the sparticle masses can be seen in Table 8.1 for a model in which $\mu=110$ and $m_{\tilde{q}_{L,3}} = 400$ GeV. The dependence on the pMSSM parameters μ and $m_{\tilde{q}_{L,3}}$ can be seen in Figure 8.2, the y-axis shows the mass of various sparticles and the x-axis shows either the μ or $m_{\tilde{q}_{L,3}}$ value. For high $m_{\tilde{q}_{L,3}}$ masses, those above ~ 700 GeV, the mixing between the left-handed and right-handed third generation squarks ($\tilde{q}_{3,R}$, $\tilde{q}_{3,L}$) becomes smaller causing the mass of the \tilde{t}_1 to level off and begin to drop for $m_{\tilde{q}_{L,3}}$ masses greater than ~ 800 TeV, the mass of the \tilde{t}_2 also decreases with $m_{\tilde{q}_{L,3}}$. The effect of these phenomena and the weak dependence of the top squark mass on the μ parameter is a reduced sensitivity to the $tb+E_T^{\text{miss}}$ signal. It also causes an effect, seen later, in which the expected signal significance decreases with $m_{\tilde{q}_{L,3}}$, then increases slightly for very high $m_{\tilde{q}_{L,3}}$ masses (800-900 GeV).

8.2.3 Analysis Strategy

The key discriminant variables of Chapter 5.6 were used to form SRs both sensitive to the simplified and pMSSM models. The presence of a lepton originating from a single top quark in the chosen signal provides a unique phase-space. The variables; am_{T2} , m_T , E_T^{miss} , m_{eff} and E_T^{miss} Sig. were found to give good separation between SM backgrounds and the signal models. The figure-of-merit used to define the significance of the signal was a modified version of Equation 5.13, given by:

$$Z = \frac{s}{\sqrt{b + (0.3 \cdot b + 1)^2}} \quad (8.2)$$

s is the number of SUSY signal events, b is the total number of background MC events, 0.3 is an estimate of a 30% systematic uncertainty, the +1 ensures that Z does not become large

8.2 Searches for SUSY in Single Top + E_T^{miss} Final States in 2012 data at $\sqrt{s} = 8$ TeV

for small values of b . An additional condition of a minimum of 5 signal events ($s \geq 5$) was also applied.

For the pMSSM model the presence of higher mass neutralino, charginos and scalar top states, for particular values of $m_{\tilde{q}_{L,3}}$ and μ , reduces the effectiveness of a selection based on the number of jets ($n_{\text{extra jets}}$). Signal regions designed to be sensitive to these pMSSM scenarios are referred to as the inclusive SRs (SRinX). Three inclusive SRs were designed based on benchmark points in different regions of the pMSSM phase space: a low mass point $m_{\tilde{q}_{L,3}} = 400$ GeV, $\mu = 110$ GeV; an intermediate mass point $m_{\tilde{q}_{L,3}} = 500$ GeV, $\mu = 210$ GeV; and a high mass point $m_{\tilde{q}_{L,3}} = 700$ GeV, $\mu = 110$ GeV. In contrast, the phenomenology of the simplified models is such that the W bosons from the chargino decays are generally *soft* due to the mass degeneracy. As a consequence of this the $n_{\text{extra jets}}$ variable is used as an additional discriminant between the signal samples and the SM background, this signal region is referred to as the exclusive SR (SRexA). The optimisation has been performed targeting the low $m_{\tilde{t}}$ diagonal region, $\tilde{t}_1 \rightarrow t + \tilde{\chi}_1^0$ decay is on the limit of kinematic availability, focusing specifically on the $m_{\tilde{t}} = 300$ GeV, $m_{\tilde{\chi}_1^0} = 100$ GeV point for $\Delta m(\tilde{\chi}_1^\pm, \tilde{\chi}_1^0) = 5, 20$ GeV. A branching ratio of 50% was used in the exclusive SR optimisation with $k = 0.5$ in Equation 8.1.

8.2.4 MC samples

The Monte Carlo samples used in this analysis are simulated with the ATLAS full Geant4 simulation [248, 149] or fast simulation AF-II [161]. A complete list of samples used for the various SM background processes considered are summarised in Table 8.2. Where more than one generator or parton shower is indicated, the first sample in the list is the nominal sample used in the analysis, whilst the others are used in the calculation of theoretical systematic uncertainties.

8.2.5 Signal Region Definitions

Table 8.3 provides a summary of the three inclusive signal regions, optimised for the pMSSM scenario and the exclusive signal region optimised for the simplified model scenario. Figure 8.4 shows the best expected significance (and corresponding SR) for all four SRs over the Natural pMSSM grid in the μ - $m_{\tilde{q}_{L,3}}$ mass plane, the significance is calculated from Equation 5.14. Figure 8.5 shows the best expected significance for two simplified models with $\Delta m(\tilde{\chi}_1^\pm, \tilde{\chi}_1^0) = 5$ GeV and $\Delta m(\tilde{\chi}_1^\pm, \tilde{\chi}_1^0) = 20$ GeV. Figure 8.6 shows the discriminating power between the SM backgrounds and the Natural pMSSM signal by the am_{T2} and m_T variables in the SRinA.

8.2 Searches for SUSY in Single Top + E_T^{miss} Final States in 2012 data at $\sqrt{s} = 8$ TeV

Table 8.2 Summary of all MC simulation used in the Single Top + E_T^{miss} analysis. The programs used in the ME+PS associated with the SM background process are indicated as well as the type of simulation used.

Process	Simulation Software	Simulation Type
$t\bar{t}$	Powheg+Pythia [236, 150]	AF-II
	MC@NLO+Jimmy [249, 250]	AF-II
	Powheg+Jimmy [236, 250]	AF-II
	MadGraph+Pythia [239, 150]	AF-II
Single Top	(s-channel) MC@NLO+Jimmy [249, 250]	AF-II
	(s-channel) Powheg+Pythia [236, 150]	AF-II
	(t-channel) AcerMC+Pythia [251, 150]	Full-Sim
	(Wt-channel) Powheg+Pythia [236, 150]	AF-II
	(Wt-channel) Powheg+Jimmy [236, 250]	AF-II
Z/W+jets	Sherpa [7]	AF-II
Di-Boson	Sherpa [7]	AF-II
$t\bar{t} + Z/W$	MadGraph+Pythia [239, 150]	AF-II

Table 8.3 Summary of the selections used to design the SRs.

Variable	Units	SRinA	SRinB	SRinC	SRexA
$N_{\text{b-jets}}$				2	
N_{Lepton}				1	
E_T^{miss}	GeV	> 200	> 120	> 220	> 160
m_T	GeV		> 140	> 180	> 120
m_{eff}	GeV	> 300	> 450	> 650	> 300
E_T^{miss} Sig.	GeV ^{1/2}	> 8	> 12	> 5	> 10
am_{T2}	GeV	> 180	> 200		> 180
m_{bl}^{min}	GeV			< 170	
$\Delta\phi_{\text{min}}^b$				> 0.4	

8.2.6 Background Estimation

The favoured approach in this analysis was to exclusively implement a semi-data-driven background estimation. The *HistFitter* method of Chapter 5.9 was used - SM backgrounds were estimated using MC and normalised in control regions (CRs) via a likelihood fit performed by the HistFitter software [169]. This normalisation was first tested in validation regions (VRs) before performing a background-only-fit (see Chapter 5.9.3) to give an estimate of the number of SM background events to be compared with data. A model-dependent-fit,

8.2 Searches for SUSY in Single Top + E_T^{miss} Final States in 2012 data at $\sqrt{s} = 8$ TeV

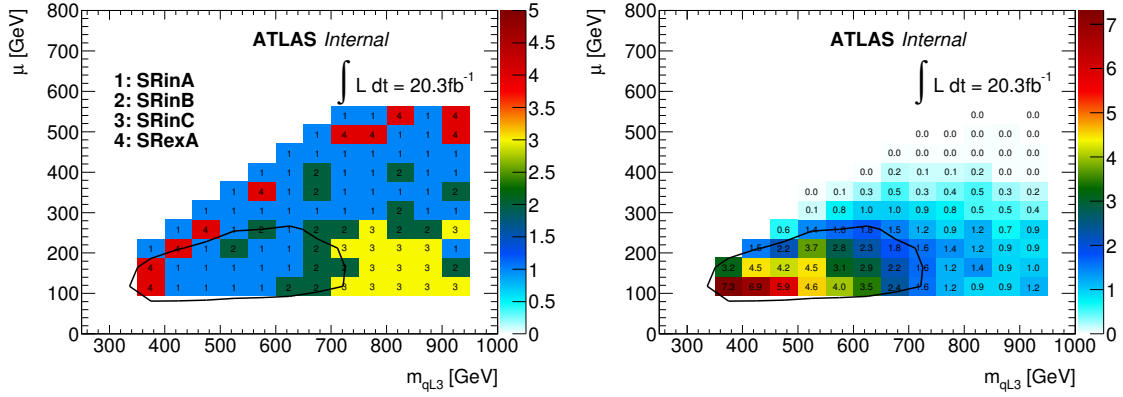


Fig. 8.4 Plots showing the best SRs and significances over the Natural pMSSM μ $m_{\tilde{q}_{L,3}}$ grid. The left plot shows the best SR, three inclusive SRs (labelled: 1, 2, 3) and one exclusive SR (labelled: 4), at each grid point. The plot on the right shows the corresponding combined best significance values from the best SRs. The significance in these plots has been calculated using the Z_N -function of Equation 5.14. The solid black line shows the expected exclusion limit contour ($Z_N = 1.64$).

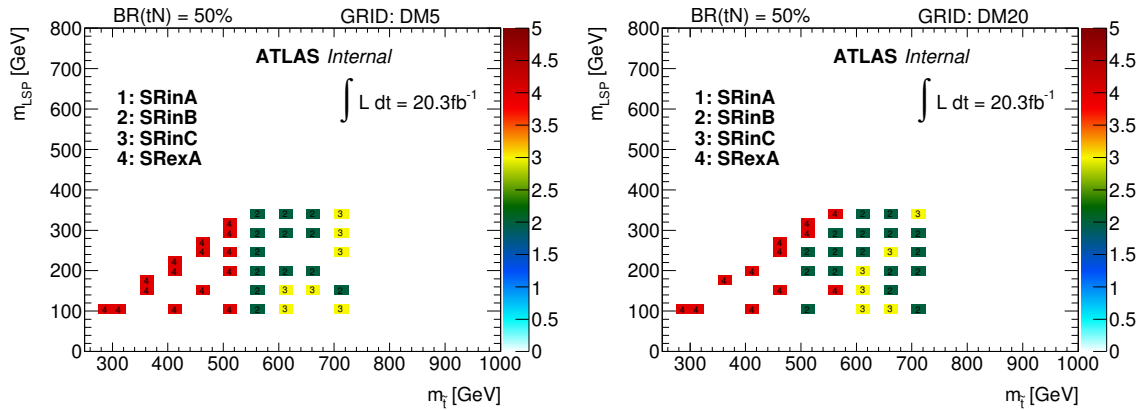


Fig. 8.5 Best signal regions obtained in the asymmetric grid $\Delta m(\tilde{\chi}_1^\pm, \tilde{\chi}_1^0) = 5\text{GeV}$ and $\Delta m(\tilde{\chi}_1^\pm, \tilde{\chi}_1^0) = 20\text{GeV}$ for a branching ratio of $k = 0.5$ (50%).

Chapter 5.9.4, was alternatively performed taking into account the signal from the Natural pMSSM scenarios and from the simplified model scenarios. A model-independent-fit, Chapter 5.9.5, was finally performed using the CRs and SRs to set limits on any BSM model.

The am_{T2} variable provides good discrimination for $t\bar{t}$ events, and similarly the m_T variable provides discrimination for W +jets events. This can be seen in Figure 8.6. CRs and VRs are defined in regions that are enhanced in the background under consideration. Top production (pair and single), are the dominant backgrounds in this analysis. Hence CRT (top control and validation regions) and CRW (W +jets control and validation regions) are defined. The general recipe followed is described below:

8.2 Searches for SUSY in Single Top + E_T^{miss} Final States in 2012 data at $\sqrt{s} = 8$ TeV

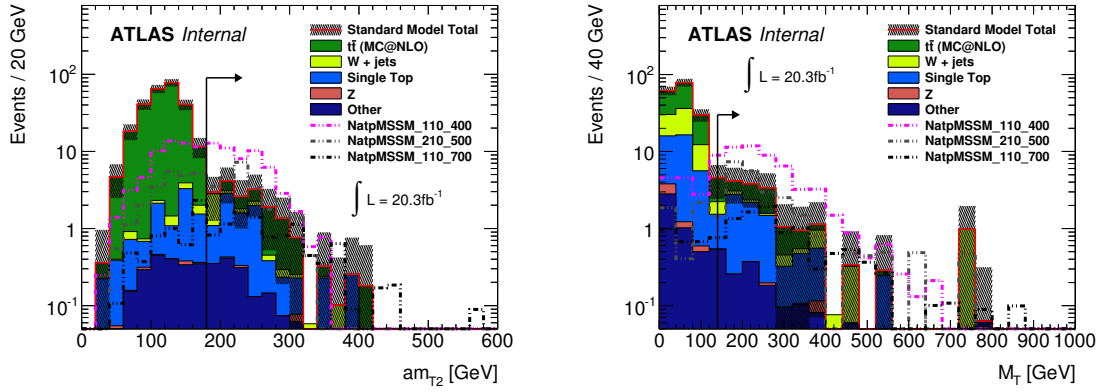


Fig. 8.6 Distributions the two of the main discriminating variables that were used in the SRinA, before the final selection of the variable is applied. The left plot shows the kinematic variable am_{T2} , the right plot shows the m_T distribution.

- Top validation regions are defined by inverting the am_{T2} selections in the SR.
- W + jets validation regions are defined by inverting the m_T selections in the SR.
- The CR and VR definitions differ depending on which SR is under consideration:
 - For CRs associated with SRinA, SRinC, the E_T^{miss} in the VRs is inverted with a lower cut of $E_T^{\text{miss}} > 100$ GeV. In addition to this, in the CRTs the am_{T2} selection is decreased to < 160 GeV to reduce signal contamination in the interval [160,180] GeV. Furthermore, to increase the W + jets purity in the CRWs, events with only 1 b-jet are also included.
 - For CRs associated with SRinB the E_T^{miss} Sig. in the VRs is instead inverted because of a low $E_T^{\text{miss}} > 120$ GeV cut. Additionally, a cut on E_T^{miss} Sig. of > 6 GeV is applied to reduce fake-leptons. The am_{T2} selection is decreased to < 160 GeV in the CRT and 1 b-jet events are allowed in the CRW.
 - For the CRs associated with SReXA, the m_{eff} selection is removed from the VR selections, the E_T^{miss} selection is lowered to > 100 GeV and the E_T^{miss} Sig. inverted to ensure orthogonality.

Finally, an additional E_T^{miss} Sig. $> 5 \text{ GeV}^{\frac{1}{2}}$ cut is added to each region to further protect from fake-lepton backgrounds.

The summary of the CRs and VRs are shown in Appendix C which also shows distributions of key variables in all CRs and VRs before a likelihood fit of the regions is performed.

8.2.7 Systematic Uncertainties

Systematic uncertainties based on measured properties entering the object reconstruction were evaluated as in Chapter 7.6. A similar set of uncertainties based on JER, JES, b-tagging, pileup, E_T^{miss} and lepton reconstruction were used. The uncertainties in these measurements were taken from earlier data taking periods with centre-of-mass energies of $\sqrt{s} = 7$ TeV and $\sqrt{s} = 8$ TeV. Chapter 5.5 gave a full overview of the systematic uncertainties associated with object reconstruction and the differences between Run-I and Run-II.

Theoretical uncertainties on the generation and showering of the MC were evaluated. In the case of $t\bar{t}$ and single top, Powheg+Pythia was used: Powheg for generation; and Pythia for the parton shower. The generator uncertainty was evaluated from the comparison between Powheg+Jimmy and MC@NLO+Jimmy. Similarly, the uncertainty associated with the parton shower was evaluated as the difference between Powheg+Pythia and Powheg+Jimmy.

For Sherpa samples, W/Z + jets and DiBoson, generator and various other settings are evaluated based on truth level information of the number of jets. Additionally, the flavour content of the W/Z samples is evaluated by increasing the cross section of the samples containing c-quarks and samples containing b-quarks by 24%.

The Feynman diagrams of $t\bar{t}$ and Single Top Wt -channel productions interfere at next-to-leading order, their diagrams become quantum mechanically identical. To evaluate the uncertainty associated to the treatment of the interference terms, the combination of the Powheg+Pythia $t\bar{t}$ and Single Top (Wt -channel only) samples were compared with a $WWbb$ process simulated by AcerMC and composed of $q q \rightarrow WWbb$ and $g g \rightarrow WWbb$ diagrams [252]. Samples with more or less ISR/FSR are used analogously to Chapter 7.6 to evaluate ISR/FSR uncertainties on $t\bar{t}$ and Single Top.

8.2.8 Results

The $t\bar{t}$ and W backgrounds were normalized in the corresponding control regions for each SR, yielding the scale factors summarised in Table 8.4.

Table 8.4 Background scale factors for the $t\bar{t}$ and W samples, as obtained by the background fit.

	SRinA	SRinB	SRinC	SRexA
$\mu_{t\bar{t}}$	1.06 ± 0.07	1.12 ± 0.09	0.94 ± 0.21	1.06 ± 0.07
μ_W	0.92 ± 0.20	0.61 ± 0.23	0.93 ± 0.27	1.10 ± 0.34

8.2 Searches for SUSY in Single Top + E_T^{miss} Final States in 2012 data at $\sqrt{s} = 8$ TeV

8.2.8.1 Background only fit

A summary of the number of observed events in each signal region, after performing a background-only-fit hypothesis are shown in Table 8.5. Figure 8.7 shows the backgrounds and various signals for key discriminant variables in the four SRs after the fit.

Table 8.5 Summary of the background-only-fit results for the Single top + E_T^{miss} analysis.

SR		SRinA	SRinB	SRinC	SRexA
Observed Data	$n_{\text{obs.}}$	38	20	10	46
Total Background	b	27.0 ± 6.73	14.1 ± 2.84	7.12 ± 2.93	31.3 ± 6.82
Post-fit MC	$t\bar{t}$	10.7 ± 5.64	4.98 ± 1.40	2.04 ± 1.96	13.2 ± 3.01
	Single Top	9.08 ± 2.88	5.24 ± 2.07	3.22 ± 2.14	9.96 ± 5.34
	W + jets	3.21 ± 1.24	1.24 ± 0.65	0.56 ± 0.26	4.35 ± 1.65
	Z + jets	0.09 ± 0.02	0.05 ± 0.01	0.03 ± 0.00	0.07 ± 0.01
	DiBoson	1.04 ± 0.18	0.72 ± 0.11	0.29 ± 0.06	1.48 ± 0.29
	$t\bar{t}$ + W/Z	2.92 ± 0.92	1.88 ± 0.61	0.98 ± 0.32	2.30 ± 0.72

8.2.8.2 Limits

Limits were set by performing a model-dependent-fit for multiple signal models. Figure 8.8a shows the expected and observed exclusion limit in the Natural pMSSM grid for the pMSSM parameters $m_{\tilde{q}_{L,3}}$ and μ . The observed limit at each signal point is taken as the value given by the SR giving the best expected exclusion at that point. Figures 8.8b-8.8c show the limits obtained on the scalar top and neutralino masses in the simplified model scenarios with $\text{BR}(\tilde{t} \rightarrow t\tilde{\chi}_1^0) = \text{BR}(\tilde{t} \rightarrow b\tilde{\chi}_1^\pm) = 0.5$, for $\Delta m(\tilde{\chi}_1^\pm, \tilde{\chi}_1^0) = 5$ GeV and $\Delta m(\tilde{\chi}_1^\pm, \tilde{\chi}_1^0) = 20$ GeV respectively. Figure C.3 of Appendix C.1.4 shows the limits obtained on these grids with alternative branching ratios of scalar top decays.

The limits on the model-independent hypothesis are given in Table 8.6. These numbers show for each signal region the visible cross section and number of signal events for a generic signal model which would be excluded by this analysis.

8.2 Searches for SUSY in Single Top + E_T^{miss} Final States in 2012 data at $\sqrt{s} = 8 \text{ TeV}$

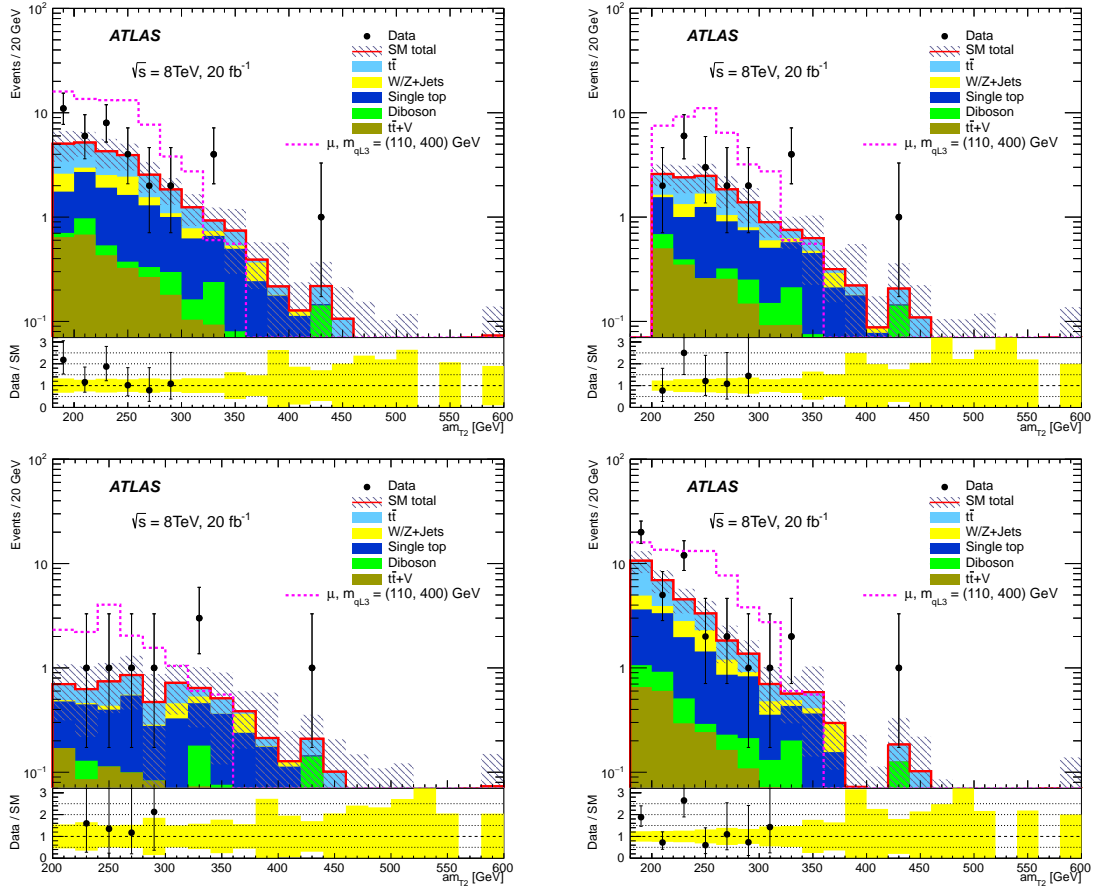


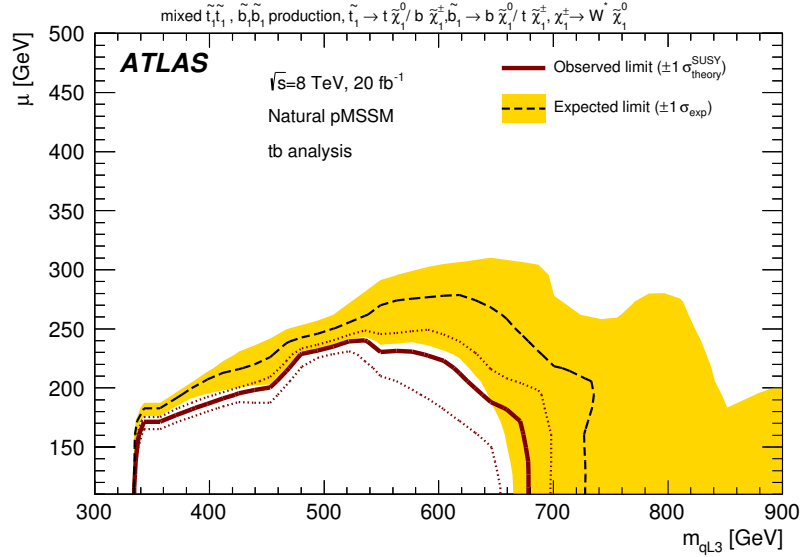
Fig. 8.7 Post-fit key kinematic distributions of am_{T2} for SRinA (top-left), SRinB (top-right), SRinC (bottom-left) and SReXA (bottom-right). Both statistical and systematic uncertainties are shown.

Table 8.6 Breakdown of upper limits calculated by the asymptotic calculation method. Left to right: 95% CL upper limits on the visible cross section ($\langle \epsilon \sigma \rangle_{\text{obs}}^{95}$) and on the number of signal events (S_{obs}^{95}). The third column (S_{exp}^{95}) shows the 95% CL upper limit on the number of signal events, given the expected number (and $\pm 1\sigma$ excursions on the expectation) of background events. The last two columns indicate the CL_B value, i.e. the confidence level observed for the background-only hypothesis, and the discovery p -value ($p(s=0)$).

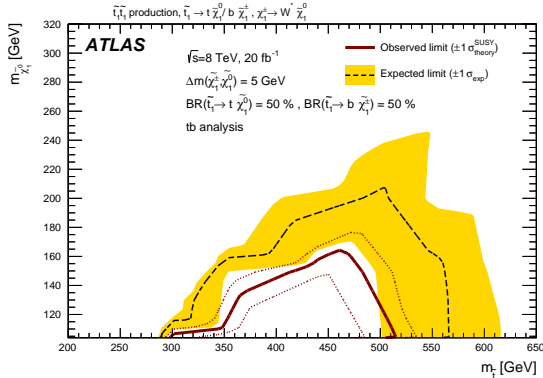
Signal channel	$\langle \epsilon \sigma \rangle_{\text{obs}}^{95} [\text{fb}]$	S_{obs}^{95}	S_{exp}^{95}	CL_B	$p(s=0)$
SRinA	1.35	27.4	$18.6^{+7.6}_{-5.6}$	0.88	0.11
SRinB	0.79	15.9	$11.0^{+4.8}_{-3.1}$	0.85	0.13
SRinC	0.57	11.5	$9.7^{+3.9}_{-2.7}$	0.69	0.27
SReXA	1.53	31.1	$20.3^{+7.8}_{-5.6}$	0.91	0.07

8.3 Interpretation in the ATLAS pMSSM scan

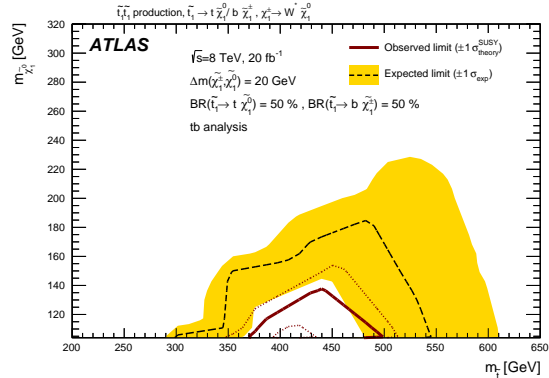
Fig. 8.8 Single Top + E_T^{miss} analysis limits on the Natural pMSSM and simplified model grids



(a) Limits obtained in the Natural pMSSM grid. The x-axis indicates the common mass parameter of the left-handed third generation scalar quarks, the y-axis indicates the higgsino mass parameter which govern the LSP mass.



(b) Limits obtained in the simplified model grid for $\Delta m(\tilde{\chi}_1^\pm, \tilde{\chi}_1^0) = 5$ GeV with $\text{BR}(\tilde{t} \rightarrow t\tilde{\chi}_1^0) = \text{BR}(\tilde{t} \rightarrow b\tilde{\chi}_1^\pm) = 0.5$.



(c) Limits obtained in the simplified model grid for $\Delta m(\tilde{\chi}_1^\pm, \tilde{\chi}_1^0) = 20$ GeV with $\text{BR}(\tilde{t} \rightarrow t\tilde{\chi}_1^0) = \text{BR}(\tilde{t} \rightarrow b\tilde{\chi}_1^\pm) = 0.5$.

8.3 Interpretation in the ATLAS pMSSM scan

The analysis was also considered in a large scan performed by ATLAS on the pMSSM[32], as described in Chapter 2.4.5. The results of a generator level (truth) analysis were used with the results of the model-dependent fit to interpret the exclusion power for many models, not just those constrained further by a Naturalness argument.

8.3.1 Overview of the Signal Models Considered

The MSSM can be constrained to a smaller sub-set of possible models via phenomenological constraints imposed by particle physics and cosmology. This constrained MSSM known as the pMSSM is described in Chapter 2.4.5 results in a reduced set of 19 free parameters.

A set of models was simulated at truth level using MadGraph+Pythia6 [253, 150] using the range of values listed in Table 8.7. For a complete description of the choice of values used in the scan see [32]. Table 2.7 provides a description of each of the 19 parameters.

Table 8.7 Range of the free pMSSM parameters considered in the ATLAS pMSSM summary scan[32].

Lower limit	pMSSM parameter	Upper limit
90 GeV \leq	$m_{\tilde{L}_1} (= m_{\tilde{L}_2})$	≤ 4 TeV
90 GeV \leq	$m_{\tilde{e}_1} (= m_{\tilde{e}_2})$	≤ 4 TeV
90 GeV \leq	$m_{\tilde{L}_3}$	≤ 4 TeV
90 GeV \leq	$m_{\tilde{e}_3}$	≤ 4 TeV
200 GeV \leq	$m_{\tilde{Q}_1} (= m_{\tilde{Q}_2})$	≤ 4 TeV
200 GeV \leq	$m_{\tilde{u}_1} (= m_{\tilde{u}_2})$	≤ 4 TeV
200 GeV \leq	$m_{\tilde{d}_1} (= m_{\tilde{d}_2})$	≤ 4 TeV
100 GeV \leq	$m_{\tilde{Q}_3}$	≤ 4 TeV
100 GeV \leq	$m_{\tilde{u}_3}$	≤ 4 TeV
100 GeV \leq	$m_{\tilde{d}_3}$	≤ 4 TeV
0 GeV \leq	$ M_1 $	≤ 4 TeV
70 GeV \leq	$ M_2 $	≤ 4 TeV
200 GeV \leq	$ M_3 $	≤ 4 TeV
80 GeV \leq	$ \mu $	≤ 4 TeV
0 GeV \leq	$ A_t $	≤ 8 TeV
0 GeV \leq	$ A_\tau $	≤ 4 TeV
0 GeV \leq	$ A_b $	≤ 4 TeV
100 GeV \leq	M_A	≤ 4 TeV
1 \leq	$\tan \beta$	≤ 60

The model set was based on the study performed in [254], with several changes. Modifications were made considering new ATLAS exclusion limits from $\sqrt{8}$ TeV data as well as updated constraints and better signal simulation.

8.3.2 Categorisation

From the scan of the pMSSM parameters resulted in a set of 312537 signal models² which also passed the pre-ATLAS SUSY constraints. The resultant set of models was subdivided into three categories:

1. The LSP is mostly a bino like state. $N_{11}^2 > \max(N_{12}^2, N_{13}^2 + N_{14}^2)$, see Chapter 2.4.2 for more detail on neutralino mixing governed by Equation 2.41. This corresponds to 105,329 models.
2. The LSP is mostly a wino like state. $N_{12}^2 > \max(N_{11}^2, N_{13}^2 + N_{14}^2)$. This corresponds to 80,292 models.
3. The LSP is mostly a higgsino like state. $N_{13}^2 + N_{14}^2 > \max(N_{11}^2, N_{12}^2)$. This corresponds to 126,916 models.

8.3.3 Truth Level Implementation

The three inclusive and single exclusive $tb+E_T^{\text{miss}}$ signal regions were implemented at truth level in order to approximate the number of expected signal events at full reconstruction level for many pMSSM points. The plots in Figure 8.9 show the efficiency (ϵ) as the ratio of the number of expected signal events at reconstruction level to the number of expected signal events at truth level as a function of the truth acceptance for the signal models analysed in Chapter 8.2. The mean efficiency and 1σ bands are also shown.

The expected number of events at reconstruction level therefore can be approximated as the following:

$$N_{\text{reco}}^{\text{exp.}} = \frac{N_{\text{reco}}^{\text{exp.}}}{N_{\text{truth}}^{\text{exp.}}} \cdot N_{\text{truth}}^{\text{exp.}} \quad (8.3)$$

$$= \epsilon \cdot N_{\text{truth}}^{\text{exp.}} \quad (8.4)$$

In the case of pMSSM models multiple production modes may be present. Therefore the total number of expected events in a signal region, at truth level, is given by:

$$N_{\text{truth}}^{\text{SR exp.}} = \mathcal{L} \times \sum_{\text{process } i} A_i^{\text{SR}} \cdot \sigma_i \quad (8.5)$$

²Rather than just one signal model as in the original analysis

8.3 Interpretation in the ATLAS pMSSM scan

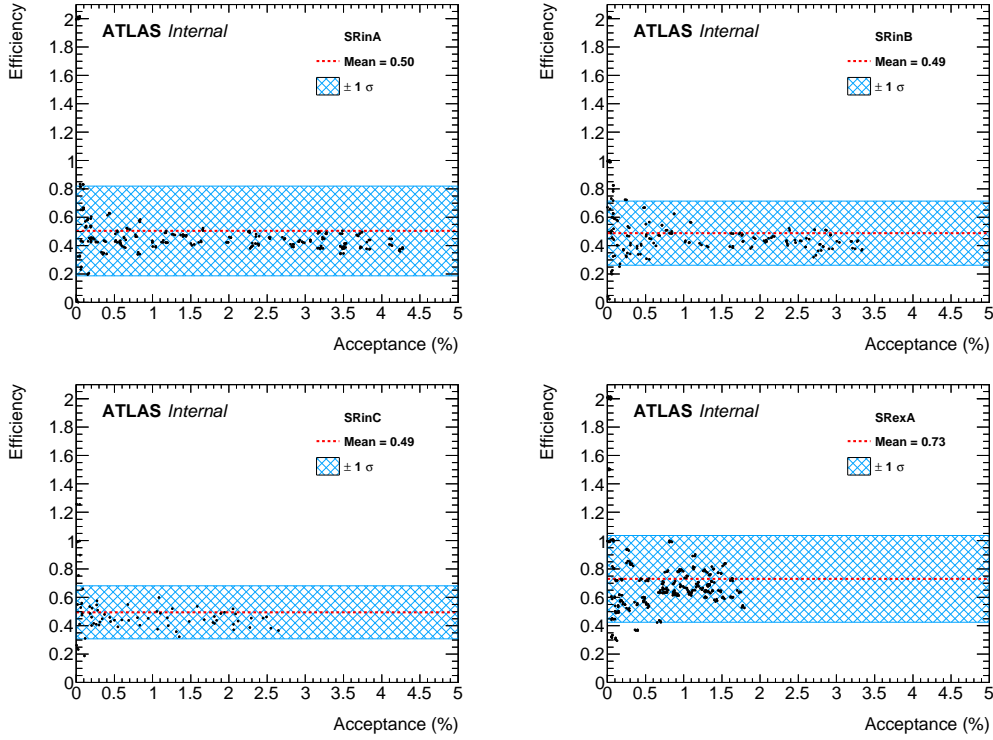


Fig. 8.9 Efficiency vs truth acceptance plots for all four tb+MET SRs .

where \mathcal{L} is the luminosity of the analysis, in the case of the Single Top + E_T^{miss} analysis this is 20.3fb^{-1} . A_i^{SR} is the acceptance of signal events at truth level and σ_i is the production cross section for a given process i .

Models generated in the pMSSM scan at truth level can be classified for the analysis SRs based on the quantity r^{SR} . This is performed by comparing the expected yields to the observed model-independent limit at full reconstruction level, see Section 5.9.5 for more detail on model-independent limits. The ratio is calculated as:

$$r^{\text{SR}} = \frac{\epsilon^{\text{SR}} \cdot N_{\text{truth}}^{\text{SR exp.}}}{N_{\text{UL}}^{\text{SR obs.}}} \quad (8.6)$$

here ϵ^{SR} is the average reconstruction efficiency per SR, as measured in Figure 8.9 for the four SRs of the Single Top + E_T^{miss} analysis. The value of the Upper Limit number of observed events, $N_{\text{UL}}^{\text{SR obs.}}$, for the Single Top + E_T^{miss} analysis can be found in Table 8.6, quoted as S_{obs}^{95} for all four signal regions.

All pMSSM models generated at truth level were passed through the truth level Single Top + E_T^{miss} 8 TeV analysis to obtain a value for $N_{\text{truth}}^{\text{SR exp.}}$ and hence values for r^{SR} . Models were classified based on the following:

$$\begin{aligned}
 r^{SR} \leq 0.5 & & : \text{Category 1} \\
 0.5 < r^{SR} \leq 2 & & : \text{Category 2} \\
 2 \leq r^{SR} & & : \text{Category 3}
 \end{aligned}$$

If a model is within Category 1 this is to say the model is highly likely to not be excluded. Category 2 models are possibly excluded and Category 3 models are almost certainly excluded. The values of 0.5 and 2 are used allowing for the truth level prediction to be off by a factor of 2.

Models that were found to be within Category 2, for any of the signal regions, were fully reconstructed (using MadGraph+Pythia8) and were interpreted by the full analysis of Chapter 8.2. For each Category 2 model, a model-dependent confidence level of the exclusion potential was obtained.

8.3.4 Results and Interpretation

A summary of the effective exclusion power of multiple analyses, including the Single Top + E_T^{miss} analysis [25], in the context of the ATLAS pMSSM scan [32] is summarised in Table 8.8.

Figure 8.10 shows various mass-plane plots of the exclusion power of the Single Top + E_T^{miss} analysis. Figure 8.10 shows the fraction of models which were observed to be excluded by the Single Top + E_T^{miss} analysis, many of these models were also excluded with better exclusion power by the analyses listed in Table 8.8. It can be clearly seen that the analysis excludes many models in which the scalar top and scalar bottom are of similar mass, this is also observed in Figure 8.10a for the 2.04% combined models in which the Single Top + E_T^{miss} analysis had the best expected exclusion power.

When scalar top and scalar bottom quarks have similar mass then their production cross section are similar, this results in the mixed scenarios in which scalar tops and scalar bottoms are simultaneously pair produced at similar rates, therefore the Single Top + E_T^{miss} analysis becomes sensitive to these scenarios particularly when the branching ratio of scalar top and scalar bottom decays to neutralinos and charginos is mixed. Figure 8.11 shows the branching ratios of scalar tops and scalar bottoms to the lightest neutralino and chargino states. Figure 8.12 provides more detail of the branching ratio of the decays in these models by showing the combined branching ratios to the lightest neutralino and chargino states and the branching ratios to the second lightest neutralino and chargino states. Importantly, it can be seen in Figure 8.12 that most of these models have a small BR of $(\tilde{t}_1, \tilde{b}_2 \rightarrow X$, where $X = \tilde{\chi}_{3,4}, \tilde{g}, \dots$). In addition to this, the signal models the analysis is most sensitive to, are the ones in which the $\Delta m(\tilde{\chi}_1^\pm, \tilde{\chi}_1^0)$ is small. This is not a surprise as the analysis was optimised for

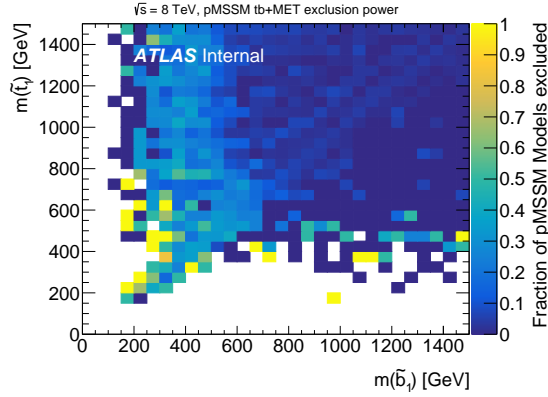
Analysis Name	Combined	Bino-like	Wino-like	Higgsino-like
0 ℓ , 2-6 jets[255]	30.91%	33.84%	28.71%	32.20%
0 ℓ , 7-10 jets[256]	6.66%	3.96%	6.41%	6.92%
1 ℓ , 2-6 jets[257]	3.12%	1.85%	2.36%	3.64%
1-2 τ , jets[258]	0.28%	0.11%	0.39%	0.22%
2 ℓ SS/3 ℓ [259]	0.77%	0.62%	0.46%	0.96%
3 b -jet [260]	7.17%	3.96%	5.43%	8.38%
Stop 0 ℓ [261]	4.35%	2.90%	3.48%	4.95%
Stop 1 ℓ [262]	4.36%	1.78%	3.25%	5.16%
Stop 2 ℓ [263]	0.22%	0.34%	0.34%	0.14%
Stop to charm [264]	3.82%	11.20%	3.19%	3.96%
Stop with Z boson [265]	0.30%	0.80%	0.24%	0.32%
Two b -jet [29]	2.46%	2.58%	1.67%	2.96%
tb+MET [25]	2.04%	0.88%	1.35%	2.51%
2 ℓ , electro-weak [266]	0.45%	0.90%	0.16%	0.61%
2 τ , electro-weak [267]	0.00%	0.00%	0.00%	0.00%
3 ℓ , electro-weak [268]	0.29%	0.45%	0.39%	0.22%
4 ℓ [269]	0.35%	0.55%	0.37%	0.32%
Disappearing Track [270]	9.74%	0.31%	25.57%	0.06%
Exotics mono-jet [271]	4.96%	11.26%	4.49%	5.04%
$H/A \rightarrow \tau^+ \tau^-$ [272]	1.86%	2.12%	0.88%	2.47%
Total	37.73%	38.04%	41.33%	35.45%

Table 8.8 Fraction of models excluded by the individual analyses, the total does not equal the sum of all analyses since multiple analyses may exclude the same model. All ATLAS analyses included in the pMSSM interpretation are cited. Table has been taken from [32].

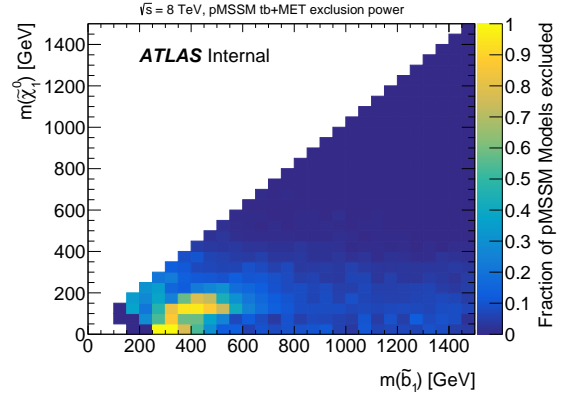
this type of final state. As seen in Table 8.8 this scenario is one in which is significant in the context of the pMSSM. The analysis is found to be very competitive with other long-standing third generation searches for SUSY, such as the Run-I Two b -jets analysis (direct scalar bottom [29] at $\sqrt{s} = 8$ TeV, discussed in Chapter 7), particularly for scenarios in which the LSP is Higgsino-like.

8.4 Conclusions

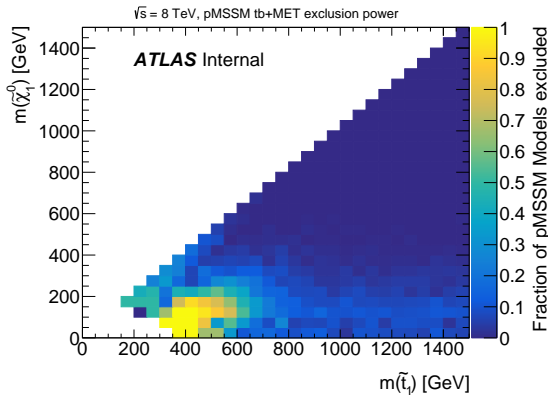
This chapter detailed an analyses performed at the end of Run-I of the LHC which attempted to cover a phase-space missed by the simplified signal model approaches. If SUSY exists in nature mixed decays of multiple supersymmetric particles are likely to populate final states observed in hadron colliders. The single top + E_T^{miss} analysis was a unique analysis



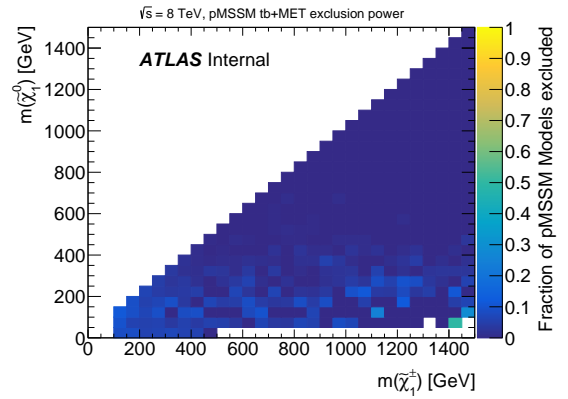
(a) Fraction of pMSSM models observed to be excluded by the Single Top + E_T^{miss} analysis in the scalar top - scalar bottom mass plane.



(b) Fraction of pMSSM models observed to be excluded by the Single Top + E_T^{miss} analysis in the scalar bottom - lightest neutralino mass plane.



(c) Fraction of pMSSM models observed to be excluded by the Single Top + E_T^{miss} analysis in the scalar top - lightest neutralino mass plane.



(d) Fraction of pMSSM models observed to be excluded by the Single Top + E_T^{miss} analysis in the light chargino - lightest neutralino mass plane.

Fig. 8.10 Exclusion power of the Single Top + E_T^{miss} analysis interpreted in the context of the pMSSM.

inspired by requiring a naturalness constraint on the pMSSM with low mass scalar top quarks, resulting in a single top final state due to mixed decay of scalar top and bottom quarks.

The analysis results were used as a part of the ATLAS pMSSM summary paper which interpreted many analyses in the context of a full scan over the 19 parameters of the pMSSM. The analysis was competitive with other third generation scalar quark searches showing the importance of targeting more complicated and models inspired by phenomenological constraints.

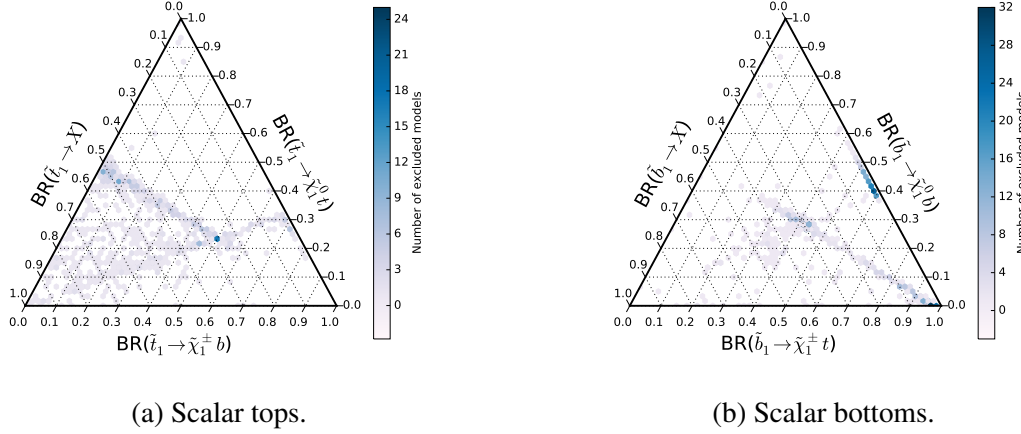


Fig. 8.11 Number of pMSSM models where the best expected exclusion was the Single Top + E_T^{miss} analysis. The axes represent the two decay modes of the scalar top and scalar bottom quarks to the highest neutralino and chargino states, the third axis show the remaining fraction of decays to higher neutralino and chargino mass states denoted as X .

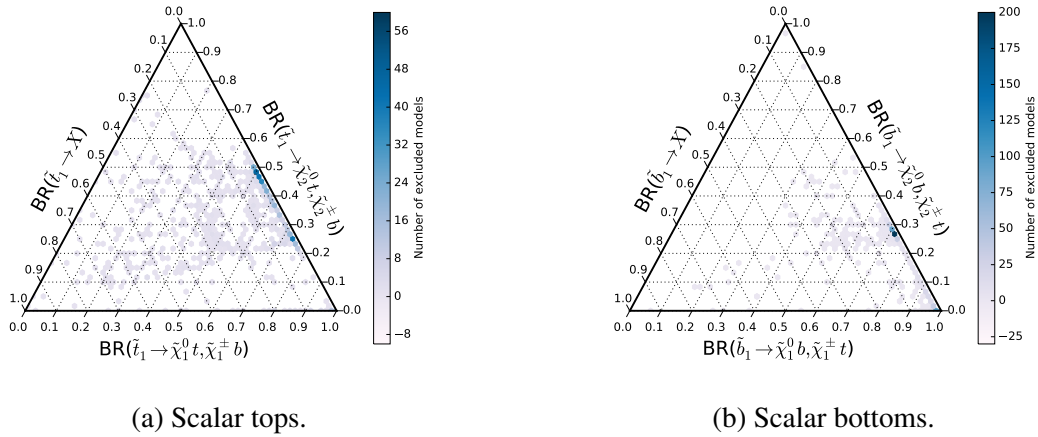


Fig. 8.12 Number of pMSSM models where the best expected exclusion was the Single Top + E_T^{miss} analysis. The bottom axis shows the combined branching ratio of scalar tops (sbottoms) to the highest neutralino and chargino states, the right axis shows the combined branching ratio of scalar tops (sbottoms) to the second lightest neutralino and chargino states and the left axis show the remaining fraction of decays to higher neutralino and chargino mass states denoted as X .

Chapter 9

Conclusions

No significant excess above the Standard Model background was observed in any of the analyses performed in this thesis. This has been the case for the majority of ATLAS and CMS searches¹ for supersymmetry as of 2016. The two analyses discussed set exclusion limits on SUSY particle masses and parameters in multiple simplified scenarios. The search for scalar bottom quarks of Chapter 7 has set a 95% CL limit on scalar bottom quarks of up to 800 GeV for low mass (< 200 GeV) neutralinos using 3.2 fb^{-1} of $\sqrt{s} = 13$ TeV data. Chapter 8 presented a search for asymmetric decays of third generation supersymmetric particles with 20.3 fb^{-1} of pp -collision data at $\sqrt{s} = 8$ TeV. In the context of a Natural pMSSM scenario, the common mass parameter of the left-handed scalar quarks is excluded with a 95% CLs for a mass of up to 680 GeV for low mass higgsino like neutralino and charginos². The search for supersymmetry in a Single Top + $E_{\text{T}}^{\text{miss}}$ final state was also used to set limits in the context of simplified asymmetric models with varying branching ratios of the scalar top decay and in the context of a full pMSSM scan performed by ATLAS.

The background estimation techniques performed, developed and improved upon in this thesis were the key work performed by the author. The JetSmearing technique described in Chapter 6 has proven to be one of the most robust and best estimates of the Multi-jet background in high $E_{\text{T}}^{\text{miss}}$, zero lepton final states. The technique has been used by multiple analyses in searches for supersymmetry as well as exotic particle searches. Being able to understand and control backgrounds arising from mis-measurement jets will become increasingly more important as the regions of search phase-space are widened particularly in searches for compressed decays of a variety of theorised particles.

Two data-driven methods for estimating the $Z(\rightarrow \nu\bar{\nu}) + 2$ b-jets were extensively discussed in Chapter 7. A method using $\gamma + 2$ b-jet events has been widely used by ATLAS

¹and previous Tevatron/LEP searches.

² $\mu < 150$ GeV

and CMS previously. The second method, exploiting the similarities in key variable shapes of $Z(\rightarrow \ell\bar{\ell}) + 2$ b-jets and $Z(\rightarrow \ell\bar{\ell}) + 2$ light-jets is a new novel approach to estimating this background. The method was found to work well for low jet multiplicities and may be used by many more analysis with b-jet final states. Data-driven methods provide an alternative estimate of the SM backgrounds from MC simulation, additionally detector systematic uncertainties are mostly negligible³.

The interpretation of an analysis in the context of a multiple parameter scan is a key study for future interpretations. As discussed in Chapter 8, simplified models (such as Chapter 7) may not be likely manifestations of SUSY, if it exists in nature. The MSSM has 120 free parameters, there simply is not enough computing power in the world to be able to interpret all of these models. Additionally, N-MSSM models add an even larger phase-space for SUSY to be manifested in. To be able to probe this huge sea of possibilities, the techniques described in Chapter 8.3 will be used to reduce down the model sizes. Quoting exclusion limits on a scalar quark mass in a simplified model does not provide a clear summary of what has been excluded. Combining analysis, targeting more complex scenarios and performing these studies provides a much more informative summary of what has or has not yet been excluded by multiple experiments.

The LHC, and its detectors, have performed exceptionally well over several years of data taking at centre-of-mass energies as high as $\sqrt{s} = 13$ TeV. A number claimed discoveries of new particles, particle states and unusual phenomena by ATLAS, ALICE, CMS and LHCb have been popularised by the media. The discovery of the Higgs Boson in 2012 was a ground-breaking discovery, it is a step on the road in attempting to understand this universe we live in. History teaches us that scientific discoveries tend to develop the human race in unforeseeable ways.

The discovery of supersymmetry may lead us down the next path of our understanding of the universe, the theoretical framework predicts a vast zoo of particles that might be discovered by the LHC and the HL-LHC. As seen in Chapter 7.9, the HL-LHC will reach a centre-of-mass energy of $\sqrt{s} = 14$ TeV with an expected luminosity of $\approx 3000 \text{ fb}^{-1}$ to be delivered by 2035. Supersymmetry may not exist in nature, or it may and the LHC may never discover it. There are however many more theories predicting new exotic particles and phenomena that may be discovered.

Some see a lack of discovery of any new particle states of masses above the top quark mass an interesting result in itself. Which it is. From a theoretical point of view it would require a rethink, as the Standard Model would remain incomplete. In reality however, from a personal and funding point of view, the discovery of exotic high mass particles will always

³depending on the construction of the method

be a more significant result. The LHC and other particle physics experiments are probing the frontiers at the pinnacle of human knowledge which is why they are perceived by many to be so inspiring.

References

- [1] D. Griffiths, *Introduction to elementary particles*, 2008.
- [2] S. P. Martin, *A Supersymmetry primer* (1997), [hep-ph/9709356](https://arxiv.org/abs/hep-ph/9709356).
- [3] L. J. Hall *et. al.*, *A Natural SUSY Higgs Near 126 GeV*, **JHEP** (2012) 131, [1112.2703](https://arxiv.org/abs/1112.2703).
- [4] I. Melzer-Pellmann *et. al.*, *Lessons for SUSY from the LHC after the first run*, **Eur. Phys. J.** (2014) 2801, [1404.7191](https://arxiv.org/abs/1404.7191).
- [5] A. D. Martin *et. al.*, *Parton distributions for the LHC*, **Eur. Phys. J.** (2009) 189–285, [0901.0002](https://arxiv.org/abs/0901.0002).
- [6] K. M. C. Anastasiou, L.J. Dixon *et. al.*, *High precision QCD at hadron colliders: Electroweak gauge boson rapidity distributions at NNLO*, **Phys. Rev.** (2004) 094 008, [hep-ph/0312266](https://arxiv.org/abs/hep-ph/0312266).
- [7] T. Gleisberg *et. al.*, *Event generation with SHERPA 1.1*, **JHEP** (2009) 007, [0811.4622](https://arxiv.org/abs/0811.4622).
- [8] T. Gleisberg *et. al.*, *Event generation with SHERPA 1.1*, **JHEP** (2009) 007, [0811.4622](https://arxiv.org/abs/0811.4622).
- [9] C. Borschensky *et. al.*, *Squark and gluino production cross sections in pp collisions at $\sqrt{s} = 13, 14, 33$ and 100 TeV*, **Eur. Phys. J.** (2014) (12) 3174, [1407.5066](https://arxiv.org/abs/1407.5066).
- [10] G. P. Salam, *Elements of QCD for hadron colliders*, in *High-energy physics. Proceedings, 17th European School, ESHEP 2009, Bautzen, Germany, June 14-27, 2009*, 2010, False, [1011.5131](https://arxiv.org/abs/1011.5131), <https://inspirehep.net/record/880643/files/arXiv:1011.5131.pdf>.
- [11] [online] <https://twiki.cern.ch/twiki/bin/view/AtlasPublic>.
- [12] [online] <http://cms-results.web.cern.ch/cms-results/public-results/publications/>.
- [13] [online] https://cds.cern.ch/record/1700455/files/fig_LHC_area_overview.png.
- [14] [online] http://www.atlasexperiment.org/photos/atlas_photos/selected-photos/full-detector/.
- [15] *ATLAS magnet system: Technical design report* (1997).
- [16] *The ATLAS Experiment at the CERN Large Hadron Collider*, **JINST** (2008) S08 003.

-
- [17] M. Capeans *et. al.*, *ATLAS Insertable B-Layer Technical Design Report, Technical Report CERN-LHCC-2010-013. ATLAS-TDR-19* (2010), <https://cds.cern.ch/record/1291633>.
- [18] [online] https://atlas.web.cern.ch/Atlas/GROUPS/INNER_DETECTOR/SCT/.
- [19] Y. Nakahama, *The ATLAS Trigger System: Ready for Run-2, Technical Report ATL-DAQ-PROC-2015-006. 8*, CERN, Geneva (2015), <https://cds.cern.ch/record/2015211>.
- [20] [online] <http://reece.scipp.ucsc.edu/>.
- [21] B. Isildak, *Measurement of the differential dijet production cross section in proton-proton collisions at $\sqrt{s} = 7$ TeV* (2011), 1308.6064, <https://inspirehep.net/record/1251416/files/arXiv:1308.6064.pdf>.
- [22] M. Cacciari *et. al.*, *The Anti-k(t) jet clustering algorithm*, *JHEP* (2008) 063, 0802.1189.
- [23] B. Nachman *et. al.*, *Investigating the Quantum Properties of Jets and the Search for a Supersymmetric Top Quark Partner with the ATLAS Detector*, Ph.D. thesis, Stanford U., Phys. Dept. (2016), presented 2016, <http://cds.cern.ch/record/2204912>.
- [24] M. Baak *et. al.*, *HistFitter software framework for statistical data analysis*, *Eur. Phys. J.* (2015) 153, 1410.1280.
- [25] G. Aad *et. al.* (ATLAS Collaboration), *ATLAS Run 1 searches for direct pair production of third-generation squarks at the Large Hadron Collider*, *Eur. Phys. J.* (2015) (10) 510, [Erratum: *Eur. Phys. J.*C76,no.3,153(2016)], 1506.08616.
- [26] C. Borschensky *et. al.*, *Squark and gluino production cross sections in pp collisions at $\sqrt{s} = 13, 14, 33$ and 100 TeV*, *Eur.Phys.J.* (2014) (12) 3174, 1407.5066.
- [27] Georges Aad and others (ATLAS Collaboration Collaboration), *Search for direct third-generation squark pair production in final states with missing transverse momentum and two b-jets in $\sqrt{s}=8$ TeV pp collisions with the ATLAS detector*, *JHEP* (2013) 189, 1308.2631.
- [28] M. Aaboud *et. al.* (ATLAS Collaboration), *Search for bottom squark pair production in proton-proton collisions at $\sqrt{s} = 13$ TeV with the ATLAS detector*, *Eur. Phys. J.* (2016) (10) 547, 1606.08772.
- [29] G. Aad *et. al.* (ATLAS Collaboration Collaboration), *Search for direct third-generation squark pair production in final states with missing transverse momentum and two b-jets in $\sqrt{s} = 8$ TeV pp collisions with the ATLAS detector*, *J. High Energy Phys.* (2013) 189. 51 p, 1308.2631.
- [30] K. A. Olive *et. al.* (Particle Data Group Collaboration), *Review of Particle Physics*, *Chin. Phys.* (2014) 090 001.
- [31] R. B. Mann, *An introduction to particle physics and the standard model*, 2010, http://www.taylorandfrancis.com/shopping_cart/search/search.asp?search=9781420082982.

- [32] *Summary of the ATLAS experiment's sensitivity to supersymmetry after LHC Run 1 - interpreted in the phenomenological MSSM*, submitted to *JHEP* (2015), 1508.06608.
- [33] *Search for Bottom Squark Pair Production with the ATLAS Detector in proton-proton Collisions at $\sqrt{s} = 13$ TeV*, Technical Report ATLAS-CONF-2015-066, CERN, Geneva (2015), <https://cds.cern.ch/record/2114833>.
- [34] *Search for Supersymmetry at the high luminosity LHC with the ATLAS experiment*, Technical Report ATL-PHYS-PUB-2014-010, CERN, Geneva (2014), <http://cds.cern.ch/record/1735031>.
- [35] G. T. Fletcher *et al.*, *A data-driven method for measuring the mismeasured jet background for missing transverse energy searches in multijet, Z+jet and γ +jet events.*, Technical Report ATL-COM-PHYS-2014-1243, CERN, Geneva (2014), <https://cds.cern.ch/record/1950335>.
- [36] G. Aad *et al.* (ATLAS Collaboration), *Search for pair production of gluinos decaying via stop and sbottom in events with b-jets and large missing transverse momentum in pp collisions at $\sqrt{s} = 13$ TeV with the ATLAS detector*, *Phys. Rev.* (2016) (3) 032 003, 1605.09318.
- [37] *Search for Dark Matter production associated with bottom quarks with 13.3 fb^{-1} of pp collisions at $\sqrt{s} = 13 \text{ TeV}$ with the ATLAS detector at the LHC*, Technical Report ATLAS-CONF-2016-086, CERN, Geneva (2016), <https://cds.cern.ch/record/2206279>.
- [38] S. L. Glashow, *Partial Symmetries of Weak Interactions*, *Nucl. Phys.* (1961) 579–588.
- [39] S. Weinberg, *A Model of Leptons*, *Phys. Rev. Lett.* (1967) 1264–1266.
- [40] A. Salam, in *Elementary Particle Theory*, p. 367, Almqvist and Wiksell, Stockholm, 1968.
- [41] B. Odom *et al.*, *New Measurement of the Electron Magnetic Moment Using a One-Electron Quantum Cyclotron*, *Phys. Rev. Lett.* (2006) 030 801, <http://link.aps.org/doi/10.1103/PhysRevLett.97.030801>.
- [42] S. G. Karshenboim, *Guide for atomic and particle physicists to CODATA's recommended values of the fundamental physical constants*, *Lect. Notes Phys.* (2008) 35–53, 0711.4567.
- [43] G. Gabrielse *et al.*, *New Determination of the Fine Structure Constant from the Electron g Value and QED*, *Phys. Rev. Lett.* (2006) 030 802, <http://link.aps.org/doi/10.1103/PhysRevLett.97.030802>.
- [44] M. Levi, *UA1 Results on W^\pm and Z^0 Production*, in *International Europhysics Conference on High-Energy Physics Bari, Italy, July 18-24, 1985*, 1985, <http://alice.cern.ch/format/showfull?sysnb=0074674>.
- [45] A. R. Weidberg (UA2 Collaboration), *W and Z production and decay results from UA2*, *Conf. Proc.* (1989) 266–273.

- [46] G. Aad *et al.* (ATLAS Collaboration), *Observation of a new particle in the search for the Standard Model Higgs boson with the ATLAS detector at the LHC*, **Phys. Lett.** (2012) 1–29, [1207.7214](#).
- [47] S. Chatrchyan *et al.* (CMS Collaboration), *Observation of a new boson at a mass of 125 GeV with the CMS experiment at the LHC*, **Phys. Lett.** (2012) 30–61, [1207.7235](#).
- [48] J. Ellis *et al.*, *The Super-GUT CMSSM Revisited* (2016), [1608.05370](#).
- [49] N. Sakai, *Naturalness in Supersymmetric GUTs*, **Z. Phys.** (1981) 153–157.
- [50] J. C. Pati *et al.*, *Lepton number as the fourth "color"*, **PRD** (1974) 275–289.
- [51] H. Georgi *et al.*, *Unity of All Elementary-Particle Forces*, **Phys. Rev. Lett.** (1974) 438–441, <http://link.aps.org/doi/10.1103/PhysRevLett.32.438>.
- [52] A. Buras *et al.*, *Aspects of the grand unification of strong, weak and electromagnetic interactions*, **Nuclear Physics B** (1978) (1) 66 – 92, ISSN 0550-3213, <http://www.sciencedirect.com/science/article/pii/0550321378902146>.
- [53] Y. Golfand *et al.*, *Extension of the Algebra of Poincare Group Generators and Violation of p Invariance*, **JETP Lett.** (1971) 323–326.
- [54] D. V. Volkov *et al.*, *Is the Neutrino a Goldstone Particle?*, **Phys. Lett.** (1973) 109–110.
- [55] J. Wess *et al.*, *Supergauge Transformations in Four-Dimensions*, **Nucl. Phys.** (1974) 39–50.
- [56] J. Wess *et al.*, *Supergauge Invariant Extension of Quantum Electrodynamics*, **Nucl. Phys.** (1974) 1.
- [57] S. Ferrara *et al.*, *Supergauge Invariant Yang-Mills Theories*, **Nucl. Phys.** (1974) 413.
- [58] A. Salam *et al.*, *Supersymmetry and Nonabelian Gauges*, **Phys. Lett.** (1974) 353–355.
- [59] P. A. M. Dirac, *The Quantum Theory of the Electron*, **Proceedings of the Royal Society of London A: Mathematical, Physical and Engineering Sciences** (1928) (778) 610–624, ISSN 0950-1207, <http://rspa.royalsocietypublishing.org/content/117/778/610.full.pdf>, <http://rspa.royalsocietypublishing.org/content/117/778/610>.
- [60] E. Majorana, *Teoria simmetrica dell'elettrone e del positrone*, **Il Nuovo Cimento (1924-1942)** (2008) (4) 171, ISSN 1827-6121, <http://dx.doi.org/10.1007/BF02961314>.
- [61] S. Dell'Oro *et al.*, *Neutrinoless double beta decay: 2015 review*, **Adv. High Energy Phys.** (2016) 2162 659, [1601.07512](#).
- [62] F. Halzen *et al.*, *QUARKS AND LEPTONS: AN INTRODUCTORY COURSE IN MODERN PARTICLE PHYSICS*, 1984, ISBN 0471887412, 9780471887416.
- [63] M. D. Schwartz, *Quantum Field Theory and the Standard Model*, Cambridge University Press, 2014, ISBN 1107034736, 9781107034730, <http://www.cambridge.org/us/academic/subjects/physics/theoretical-physics-and-mathematical-physics/quantum-field-theory-and-standard-model>.

- [64] C. P. Burgess *et al.*, *The standard model: A primer*, Cambridge University Press, 2006, ISBN 9780511254857, 9781107404267, 9780521860369.
- [65] O. Klein, *Quantentheorie und fünfdimensionale Relativitätstheorie*, *Zeitschrift für Physik* (1926) (12) 895–906, ISSN 0044-3328, <http://dx.doi.org/10.1007/BF01397481>.
- [66] E. Schrödinger, *Quantisierung als Eigenwertproblem*, *Annalen der Physik* (1926) (4) 361–376, ISSN 1521-3889, <http://dx.doi.org/10.1002/andp.19263840404>.
- [67] C. D. Anderson, *Energies of Cosmic-Ray Particles*, *Phys. Rev.* (1932) 405–421.
- [68] Proca, Al., *Sur la théorie ondulatoire des électrons positifs et négatifs*, *J. Phys. Radium* (1936) (8) 347–353, <http://dx.doi.org/10.1051/jphysrad:0193600708034700>.
- [69] G. J. Blunar *et al.*, *Measurement of $\psi(3.1)$ Meson Production by Pions and Protons*, *Phys. Rev. Lett.* (1975) 346–349, <http://link.aps.org/doi/10.1103/PhysRevLett.35.346>.
- [70] G. Feldman *et al.*, *Has ψ_4 Already Been Observed at Stanford Linear Accelerator Center?*, *Phys. Rev. Lett.* (1975) 344–346, <http://link.aps.org/doi/10.1103/PhysRevLett.35.344>.
- [71] G. Feldman *et al.*, *The Discovery of Colored Kaons?*, *Phys. Lett.* (1976) 353–355.
- [72] R. Giese, *Photoproduction of rho Mesons from Hydrogen and Deuterium from 9-GeV to 16-GeV*, Ph.D. thesis, SLAC (1974), <http://www-public.slac.stanford.edu/sciDoc/docMeta.aspx?slacPubNumber=slac-r-178>.
- [73] J. E. Augustin *et al.* (SLAC-SP-017 Collaboration), *Discovery of a Narrow Resonance in $e^+ e^-$ Annihilation*, *Phys. Rev. Lett.* (1974) 1406–1408, [Adv. Exp. Phys.5,141(1976)].
- [74] J. J. Aubert *et al.*, *Discovery of the New Particle J*, *Nucl. Phys.* (1975) 1–18.
- [75] R. C. Giles *et al.*, *Vibrational States in a Heavy Quark Bound System*, *Phys. Lett.* (1978) 30–32.
- [76] S. Abachi *et al.* (D0 Collaboration), *Observation of the top quark*, *Phys. Rev. Lett.* (1995) 2632–2637, [hep-ex/9503003](http://arxiv.org/abs/hep-ex/9503003).
- [77] E. Mazzucato *et al.*, *Precise measurement of neutral-pion photoproduction on the proton near threshold*, *Phys. Rev. Lett.* (1986) 3144–3147, <http://link.aps.org/doi/10.1103/PhysRevLett.57.3144>.
- [78] e. a. C. S. Wu, *Experimental Test of Parity Conservation in Beta Decay*, *Phys. Rev.* (1957) 1413 – 1415, <https://link.aps.org/doi/10.1103/PhysRev.105.1413>.
- [79] C. Rubbia, *The Discovery of the W and Z bosons*, *Phys. Rept.* (1994) 241–284.
- [80] G. Aad *et al.* (ATLAS Collaboration), *Observation of a new particle in the search for the Standard Model Higgs boson with the ATLAS detector at the LHC*, *Phys. Lett.* (2012) 1–29, [1207.7214](https://arxiv.org/abs/1207.7214).

-
- [81] S. Chatrchyan *et al.* (CMS Collaboration), *Observation of a new boson at a mass of 125 GeV with the CMS experiment at the LHC*, *Phys. Lett.* (2012) 30–61, [1207.7235](#).
- [82] S. A. Thomas *et al.*, *Upper Bound of 0.28 eV on Neutrino Masses from the Largest Photometric Redshift Survey*, *Physical Review Letters* (2010) (3) 031301, [0911.5291](#).
- [83] N. Agafonova *et al.* (OPERA Collaboration), *Observation of a first ν_τ candidate in the OPERA experiment in the CNGS beam*, *Phys. Lett.* (2010) 138–145, [1006.1623](#).
- [84] L. J. Hall *et al.*, *Supergravity as the Messenger of Supersymmetry Breaking*, *Phys. Rev.* (1983) 2359–2378.
- [85] H. P. Nilles, *Phenomenological aspects of supersymmetry*, in *Gauge theories, applied supersymmetry, quantum gravity. Proceedings, Workshop, Leuven, Belgium, July 10-14, 1995*, 1995, 81–105, [hep-ph/9511313](#).
- [86] <https://home.cern/about/physics/extra-dimensions-gravitons-and-tiny-black-holes>, <https://home.cern/about/physics/extra-dimensions-gravitons-and-tiny-black-holes>.
- [87] J. H. Oort, *The force exerted by the stellar system in the direction perpendicular to the galactic plane and some related problems*, *bain* (1932) 249.
- [88] V. C. Rubin *et al.*, *Rotation of the Andromeda Nebula from a Spectroscopic Survey of Emission Regions*, *apj* (1970) 379.
- [89] S. van den Bergh, *The Early history of dark matter*, *Publ. Astron. Soc. Pac.* (1999) 657, [astro-ph/9904251](#).
- [90] W. Tucker *et al.*, *1e0657-56: a contender for the hottest known cluster of galaxies*, *Astrophys. J.* (1998) L5, [astro-ph/9801120](#).
- [91] D. G. York *et al.* (SDSS Collaboration), *The Sloan Digital Sky Survey: Technical Summary*, *Astron. J.* (2000) 1579–1587, [astro-ph/0006396](#).
- [92] J. K. Adelman-McCarthy *et al.* (SDSS Collaboration), *The Fourth Data Release of the Sloan Digital Sky Survey*, *Astrophys. J. Suppl.* (2006) 38–48, [astro-ph/0507711](#).
- [93] U. G. Briel *et al.*, *An x-ray temperature map of coma* (1997), [astro-ph/9711237](#).
- [94] D. P. Bennett *et al.* (MACHO Collaboration), *The MACHO project dark matter search*, *ASP Conf. Ser.* (1996) 95, [astro-ph/9510104](#).
- [95] D. N. Spergel *et al.* (WMAP Collaboration), *First year Wilkinson Microwave Anisotropy Probe (WMAP) observations: Determination of cosmological parameters*, *Astrophys. J. Suppl.* (2003) 175–194, [astro-ph/0302209](#).
- [96] P. Ade *et al.* (Planck Collaboration), *Planck 2013 results. XVI. Cosmological parameters*, *Astron. Astrophys.* (2014) A16, [1303.5076](#).
- [97] M. Tegmark *et al.* (SDSS Collaboration), *Cosmological parameters from SDSS and WMAP*, *Phys. Rev.* (2004) 103 501, [astro-ph/0310723](#).

-
- [98] T. Aaltonen *et al.* (CDF, D0 Collaboration), *Combination of the top-quark mass measurements from the Tevatron collider*, **Phys. Rev.** (2012) 092 003, [1207.1069](https://arxiv.org/abs/1207.1069).
- [99] J. Wess *et al.*, *Supergauge Transformations in Four-Dimensions*, **Nucl. Phys.** (1974) 39–50.
- [100] W. Greiner, *The Weyl Equation — The Neutrino*, Springer Berlin Heidelberg, Berlin, Heidelberg, 1997, ISBN 978-3-662-03425-5, 333–345, http://dx.doi.org/10.1007/978-3-662-03425-5_14.
- [101] H. E. Haber, *Introductory low-energy supersymmetry*, in *Theoretical Advanced Study Institute (TASI 92): From Black Holes and Strings to Particles Boulder, Colorado, June 3-28, 1992*, 1993, 0589–688, [hep-ph/9306207](https://arxiv.org/abs/hep-ph/9306207).
- [102] H. Baer *et al.*, *Low-energy supersymmetry phenomenology* (1995), [hep-ph/9503479](https://arxiv.org/abs/hep-ph/9503479).
- [103] J. A. Bagger, *Weak scale supersymmetry: Theory and practice*, in *QCD and beyond. Proceedings, Theoretical Advanced Study Institute in Elementary Particle Physics, TASI-95, Boulder, USA, June 4-30, 1995*, 1996, 109–162, [hep-ph/9604232](https://arxiv.org/abs/hep-ph/9604232), <http://alice.cern.ch/format/showfull?sysnb=0222315>.
- [104] S. P. Martin, *A Supersymmetry primer* (1997), [hep-ph/9709356](https://arxiv.org/abs/hep-ph/9709356).
- [105] Y. Fukuda *et al.* (Super-Kamiokande Collaboration), *The Super-Kamiokande detector*, **Nucl. Instrum. Meth.** (2003) 418–462.
- [106] M. Miura, *Search for the proton decay in Super-Kamiokande*, in *Proceedings, 44th Rencontres de Moriond on Electroweak Interactions and Unified Theories: La Thuile, Italy, March 7-14, 2009*, 2009, 525–530, http://inspirehep.net/record/1385460/files/Pages_from_C09-03-07_525.pdf.
- [107] A. Djouadi *et al.* (MSSM Working Group Collaboration), *The Minimal supersymmetric standard model: Group summary report* (1998), [hep-ph/9901246](https://arxiv.org/abs/hep-ph/9901246).
- [108] A. J. Buras, *Minimal flavor violation*, **Acta Phys. Polon.** (2003) 5615–5668, [hep-ph/0310208](https://arxiv.org/abs/hep-ph/0310208).
- [109] V. Khachatryan *et al.* (CMS Collaboration, LHCb Collaboration Collaboration), *Observation of the rare $B_s^0 \rightarrow \mu^+ \mu^-$ decay from the combined analysis of CMS and LHCb data* (2014), [1411.4413](https://arxiv.org/abs/1411.4413).
- [110] G. W. Bennett *et al.* (Muon g-2 Collaboration), *Final Report of the Muon E821 Anomalous Magnetic Moment Measurement at BNL*, **Phys. Rev.** (2006) 072 003, [hep-ex/0602035](https://arxiv.org/abs/hep-ex/0602035).
- [111] D. Akerib *et al.* (LUX Collaboration Collaboration), *First results from the LUX dark matter experiment at the Sanford Underground Research Facility*, **Phys.Rev.Lett.** (2014) 091 303, [1310.8214](https://arxiv.org/abs/1310.8214).
- [112] A. Arbey *et al.*, *SUSY Constraints, Relic Density, and Very Early Universe*, **JHEP** (2010) 051, [0906.0368](https://arxiv.org/abs/0906.0368).

- [113] L. O, *Method and apparatus for the acceleration of ions* (1934), uS Patent 1,948,384, <http://www.google.co.uk/patents/US1948384>.
- [114] J. Jackson, *Classical Electrodynamics*, John Wiley and Sons, 3rd ed., 1998.
- [115] R. Mann, *An Introduction to Particle Physics and The Standard Model*, Taylor and Francis Group, 2010.
- [116] G. Corcella *et. al.*, *Bottom quark fragmentation in top quark decay*, **Nucl. Phys.** (2002) 247–270, [hep-ph/0110319](http://arxiv.org/abs/hep-ph/0110319).
- [117] Y. Kuno *et. al.*, *Muon decay and physics beyond the standard model*, **Rev. Mod. Phys.** (2001) 151–202, [hep-ph/9909265](http://arxiv.org/abs/hep-ph/9909265).
- [118] J. D. Wells *et. al.*, *Implications of Gamma ($Z \rightarrow b \text{ anti-}b$) for supersymmetry searches and model building*, **Phys. Lett.** (1994) 219–228, [hep-ph/9408228](http://arxiv.org/abs/hep-ph/9408228).
- [119] A. Heister *et. al.* (ALEPH Collaboration), *Search for scalar quarks in e^+e^- collisions at \sqrt{s} up to 209-GeV*, **Phys. Lett.** (2002) 5–20, [hep-ex/0204036](http://arxiv.org/abs/hep-ex/0204036).
- [120] J. Abdallah *et. al.* (DELPHI Collaboration), *Searches for supersymmetric particles in e^+e^- collisions up to 208 GeV and interpretation of the results within the MSSM*, **Eur. Phys. J.** (2003) 421–479, [hep-ex/0311019](http://arxiv.org/abs/hep-ex/0311019).
- [121] P. A. *et. al.*, *Search for scalar leptons and scalar quarks at {LEP}*, **Physics Letters B** (2004) (1–2) 37 – 49, ISSN 0370-2693, <http://www.sciencedirect.com/science/article/pii/S0370269303015545>.
- [122] G. Abbiendi *et. al.* (OPAL Collaboration), *Search for scalar top and scalar bottom quarks at LEP*, **Phys. Lett.** (2002) 272–284, [Erratum: Phys. Lett.B548,258(2002)], [hep-ex/0209026](http://arxiv.org/abs/hep-ex/0209026).
- [123] T. Adams (CDF, D0 Collaboration), *SUSY Searches at the Tevatron*, in *Hadron collider physics. Proceedings, 19th Symposium, HCP2008, Galena, USA, May 27-31, 2008*, 2008, 0808.0728, <https://inspirehep.net/record/792491/files/arXiv:0808.0728.pdf>.
- [124] T. Aaltonen *et. al.* (CDF Collaboration), *Search for Pair Production of Supersymmetric Top Quarks in Dilepton Events from $p \text{ anti-}p$ Collisions at $S^{*(1/2)} = 1.96 \text{ TeV}$* , **Phys. Rev. Lett.** (2010) 251 801, [0912.1308](https://arxiv.org/abs/0912.1308).
- [125] T. Aaltonen *et. al.* (CDF Collaboration Collaboration), *Searches for direct pair production of supersymmetric top and supersymmetric bottom quarks in $p\bar{p}$ collisions at $\sqrt{s} = 1.96 \text{ TeV}$* , **Phys. Rev. D** (2007) 072 010, <http://link.aps.org/doi/10.1103/PhysRevD.76.072010>.
- [126] V. M. Abazov *et. al.* (D0 Collaboration), *Search for scalar top quarks in the acoplanar charm jets and missing transverse energy final state in $p\bar{p}$ collisions at $\sqrt{s} = 1.96\text{-TeV}$* , **Phys. Lett.** (2008) 1–8, [0803.2263](https://arxiv.org/abs/0803.2263).
- [127] [online] https://twiki.cern.ch/twiki/bin/view/CMSPublic/PhysicsResultsSUS#Run_2_Summary_plots_13_TeV, https://twiki.cern.ch/twiki/bin/view/CMSPublic/PhysicsResultsSUS#Run_2_Summary_plots_13_TeV.

- [128] [online] <https://home.cern/topics/large-hadron-collider>, <https://home.cern/topics/large-hadron-collider>.
- [129] [online] <http://linac2.web.cern.ch/linac2/>, <http://linac2.web.cern.ch/linac2/>.
- [130] [online] <https://home.cern/about/accelerators/proton-synchrotron-booster>, <https://home.cern/about/accelerators/proton-synchrotron-booster>.
- [131] [online] <https://home.cern/about/accelerators/proton-synchrotron>, <https://home.cern/about/accelerators/proton-synchrotron>.
- [132] [online] <https://home.cern/about/accelerators/super-proton-synchrotron>, <https://home.cern/about/accelerators/super-proton-synchrotron>.
- [133] C. Rubbia, *The Discovery of the W and Z bosons*, **Phys. Rept.** (1994) 241–284.
- [134] M. Aaboud *et. al.* (ATLAS Collaboration), *Search for a new heavy gauge boson resonance decaying into a lepton and missing transverse momentum in 36 fb^{-1} of pp collisions at $\sqrt{s} = 13 \text{ TeV}$ with the ATLAS experiment* (2017), 1706.04786.
- [135] M. Kretz, *Performance Evaluation of the ATLAS IBL Calibration*, **Journal of Physics: Conference Series** (2015) (8) 082 022, <http://stacks.iop.org/1742-6596/664/i=8/a=082022>.
- [136] F. Hüggling *et. al.*, *The ATLAS Pixel Insertable B-layer (IBL)*, **Nuclear Instruments and Methods in Physics Research A** (2011) 45–49, 1012.2742.
- [137] G. Aad *et. al.*, *ATLAS pixel detector electronics and sensors*, **JINST** (2008) P07 007.
- [138] V. A. Mitsou (ATLAS TRT Collaboration), *The ATLAS transition radiation tracker*, in *Astroparticle, particle and space physics, detectors and medical physics applications. Proceedings, 8th Conference, ICATPP 2003, Como, Italy, October 6-10, 2003*, 2003, 497–501, hep-ex/0311058, <http://weplib.cern.ch/abstract?ATL-CONF-2003-012>.
- [139] D. Errede *et. al.*, *Use of a transition radiation detector in a beam of high-energy hadrons*, **Nucl. Instrum. Meth.** (1991) 386–400.
- [140] A. Airapetian *et. al.* (ATLAS Collaboration), *ATLAS calorimeter performance Technical Design Report* (1996).
- [141] R. Mann, *An Introduction to Particle Physics and The Standard Model*, Taylor and Francis Group, 2010.
- [142] A. Airapetian *et. al.* (ATLAS Collaboration), *ATLAS calorimeter performance Technical Design Report* (1996).
- [143] A. Hamilton (ATLAS Collaboration), *The ATLAS Trigger System Commissioning and Performance*, in *Hadron collider physics. Proceedings, 22nd Conference, HCP 2010, Toronto, Canada, August 23-27, 2010*, 2010, 1010.0017, <https://inspirehep.net/record/871608/files/arXiv:1010.0017.pdf>.
- [144] G. Aad *et. al.* (ATLAS Collaboration), *Expected Performance of the ATLAS Experiment - Detector, Trigger and Physics* (2009), 0901.0512.

-
- [145] *Trigger monitoring and rate predictions using Enhanced Bias data from the ATLAS Detector at the LHC*, Technical Report ATL-DAQ-PUB-2016-002, CERN, Geneva (2016), <https://cds.cern.ch/record/2223498>.
- [146] *2015 start-up trigger menu and initial performance assessment of the ATLAS trigger using Run-2 data*, Technical Report ATL-DAQ-PUB-2016-001, CERN, Geneva (2016), <https://cds.cern.ch/record/2136007>.
- [147] <https://twiki.cern.ch/twiki/bin/view/AtlasPublic/LuminosityPublicResults>.
- [148] <https://twiki.cern.ch/twiki/bin/view/AtlasPublic/LuminosityPublicResultsRun2>.
- [149] S. Agostinelli *et al.* (GEANT4 Collaboration), *GEANT4: A simulation toolkit*, **Nucl. Instrum. Meth.** (2003) 250–303.
- [150] T. Sjostrand *et al.*, *A Brief Introduction to PYTHIA 8.1*, **Comput. Phys. Commun.** (2008) 852–867, [0710.3820](https://arxiv.org/abs/0710.3820).
- [151] S. Frixione *et al.*, *Matching NLO QCD and parton showers in heavy flavor production*, **JHEP** (2003) 007, [hep-ph/0305252](https://arxiv.org/abs/hep-ph/0305252).
- [152] P. Nason, *A new method for combining NLO QCD with shower Monte Carlo algorithms* (2004) 040.
- [153] J. Alwall *et al.*, *MadGraph/MadEvent v4: the new web generation* (2007) 028, [0706.2334](https://arxiv.org/abs/0706.2334).
- [154] ATLAS Collaboration (ATLAS Collaboration), *ATLAS tunes of PYTHIA6 and Pythia8 for MC11*, ATL-PHYS-PUB-2011-009 (2011), <https://cds.cern.ch/record/1363300>.
- [155] T. Sjöstrand *et al.*, *Pythia 6.4 Physics and Manual*, **JHEP** (2006) 026, [0603175v2](https://arxiv.org/abs/0603175).
- [156] T. Sjöstrand *et al.*, *PYTHIA 6.4 Physics and Manual*, **JHEP** (2006) 026, [hep-ph/0603175](https://arxiv.org/abs/hep-ph/0603175).
- [157] S. Hoeche *et al.*, *Matching parton showers and matrix elements*, in *HERA and the LHC: A Workshop on the implications of HERA for LHC physics: Proceedings Part A*, 2006, [hep-ph/0602031](https://arxiv.org/abs/hep-ph/0602031), https://inspirehep.net/record/709818/files/arXiv:hep-ph_0602031.pdf.
- [158] F. Cascioli *et al.*, *NLO matching for $t\bar{t}b\bar{b}$ production with massive b -quarks*, **Phys. Lett.** (2014) 210–214, [1309.5912](https://arxiv.org/abs/1309.5912).
- [159] S. Hamilton *et al.*, *The ATLAS Fast Track Simulation Project*, CERN, CERN, Geneva, 2011, <http://cdsweb.cern.ch/record/1341541/files/ATL-SOFT-PROC-2011-038.pdf>.
- [160] D. Cavalli *et al.*, *Performance of the ATLAS fast simulation ATLFAST*, internal report ATL-PHYS-INT-2007-005; ATL-COM-PHYS-2007-012, CERN, Geneva. (2007).
- [161] K. Assamagan *et al.*, *The ATLAS Monte Carlo Project*, To be submitted to JINST (2009).

- [162] *Comparison of Monte Carlo generator predictions to ATLAS measurements of top pair production at 7 TeV*, Technical Report ATL-PHYS-PUB-2015-002, CERN, Geneva (2015), <https://cds.cern.ch/record/1981319>.
- [163] R. D. Ball *et al.*, *Parton distributions with LHC data*, *Nucl. Phys.* (2013) 244–289, 1207.1303.
- [164] G. Watt *et al.*, *Study of Monte Carlo approach to experimental uncertainty propagation with MSTW 2008 PDFs*, *JHEP* (2012) 052, 1205.4024.
- [165] **H1** and **ZEUS** Collaborations, *Combined Measurement and QCD Analysis of the Inclusive $e^\pm p$ Scattering Cross Sections at HERA*, *JHEP* (2010) 109, 0911.0884.
- [166] R. D. Ball *et al.* (NNPDF Collaboration), *Parton distributions for the LHC Run II*, *JHEP* (2015) 040, 1410.8849.
- [167] P. Z. Skands, *Tuning Monte Carlo generators: The Perugia tunes*, *Phys. Rev.* (2010) 074018, 1005.3457, <http://link.aps.org/doi/10.1103/PhysRevD.82.074018>.
- [168] G. Barrand *et al.*, *GAUDI - A software architecture and framework for building HEP data processing applications*, *Comput. Phys. Commun.* (2001) 45–55.
- [169] M. Baak *et al.*, *HistFitter software framework for statistical data analysis*, *Eur. Phys. J.* (2015) (4) 153, 1410.1280.
- [170] ATLAS, arXiv:1203.6193 [hep-ex] (2012). To be published in PR D.
- [171] G. Hanson *et al.*, *Evidence for Jet Structure in Hadron Production by $e^+ e^-$ Annihilation*, *Phys. Rev. Lett.* (1975) 1609–1612.
- [172] J. D. Bjorken *et al.*, *Statistical Model for Electron-Positron Annihilation into Hadrons*, *Phys. Rev. D* (1970) 1416–1420, <http://link.aps.org/doi/10.1103/PhysRevD.1.1416>.
- [173] R. Brandelik *et al.* (TASSO Collaboration), *Evidence for Planar Events in $e^+ e^-$ Annihilation at High-Energies*, *Phys. Lett.* (1979) 243–249.
- [174] H. Franz *et al.*, *Technical Report: PETRA III: DESY's New High Brilliance Third Generation Synchrotron Radiation Source*, *Synchrotron Radiation News* (2006) (6) 25–29, <http://dx.doi.org/10.1080/08940880601064984>, <http://dx.doi.org/10.1080/08940880601064984>.
- [175] G. Aad *et al.* (ATLAS Collaboration), *Topological cell clustering in the ATLAS calorimeters and its performance in LHC Run 1* (2016), 1603.02934.
- [176] J. R. Dandoy *et al.*, *Jet energy scale and resolution measurements and their systematic uncertainties in proton-proton collisions at $\sqrt{s} = 13$ TeV with the ATLAS detector*, Technical Report ATL-COM-PHYS-2016-213, CERN, Geneva (2016), <https://cds.cern.ch/record/2136864>.
- [177] M. Cacciari *et al.*, *The Anti- $k(t)$ jet clustering algorithm*, *JHEP* (2008) 063, 0802.1189.

- [178] M. Cacciari *et al.*, *The Anti-k(t) jet clustering algorithm*, **JHEP** (2008) 063, 0802.1189.
- [179] G. Aad *et al.* (ATLAS Collaboration), *Jet energy measurement and its systematic uncertainty in proton-proton collisions at $\sqrt{s} = 7$ TeV with the ATLAS detector*, **Eur. Phys. J.** (2015) 17, 1406.0076.
- [180] G. Aad *et al.* (ATLAS Collaboration), *Calibration of the performance of b-tagging for c and light-flavour jets in the 2012 ATLAS data* (2014).
- [181] *Optimisation of the ATLAS b-tagging performance for the 2016 LHC Run*, Technical Report ATL-PHYS-PUB-2016-012, CERN, Geneva (2016), <https://cds.cern.ch/record/2160731>.
- [182] M. Lehmacher, *b-Tagging Algorithms and their Performance at ATLAS*, in *Proceedings, 34th International Conference on High Energy Physics (ICHEP 2008): Philadelphia, Pennsylvania, July 30-August 5, 2008*, 2008, 2–3, 0809.4896, <http://weplib.cern.ch/abstract?ATL-PHYS-PROC-2008-052>.
- [183] M. Lehmacher, *b-Tagging Algorithms and their Performance at ATLAS*, in *Proceedings, 34th International Conference on High Energy Physics (ICHEP 2008): Philadelphia, Pennsylvania, July 30-August 5, 2008*, 2008, 4–6, 0809.4896, <http://weplib.cern.ch/abstract?ATL-PHYS-PROC-2008-052>.
- [184] M. Lehmacher, *b-Tagging Algorithms and their Performance at ATLAS*, in *Proceedings, 34th International Conference on High Energy Physics (ICHEP 2008): Philadelphia, Pennsylvania, July 30-August 5, 2008*, 2008, 3–4, 0809.4896, <http://weplib.cern.ch/abstract?ATL-PHYS-PROC-2008-052>.
- [185] B. P. Roe *et al.*, *Boosted decision trees, an alternative to artificial neural networks*, **Nucl. Instrum. Meth.** (2005) (2-3) 577–584, [physics/0408124](https://arxiv.org/abs/physics/0408124).
- [186] G. Aad *et al.* (ATLAS Collaboration), *Electron and photon energy calibration with the ATLAS detector using LHC Run 1 data*, **Eur. Phys. J.** (2014) (10) 3071, 1407.5063.
- [187] S. Hassani *et al.*, *A muon identification and combined reconstruction procedure for the {ATLAS} detector at the {LHC} using the (MUONBOY, STACO, MuTag) reconstruction packages*, **Nuclear Instruments and Methods in Physics Research Section A: Accelerators, Spectrometers, Detectors and Associated Equipment** (2007) (1) 77 – 79, ISSN 0168-9002, frontier Detectors for Frontier Physics Proceedings of the 10th Pisa Meeting on Advanced Detectors, <http://www.sciencedirect.com/science/article/pii/S0168900206019863>.
- [188] G. Aad *et al.* (ATLAS Collaboration), *Muon reconstruction performance of the ATLAS detector in proton–proton collision data at $\sqrt{s} = 13$ TeV*, **Eur. Phys. J.** (2016) (5) 292, 1603.05598.
- [189] G. Aad *et al.* (ATLAS Collaboration), *Electron reconstruction and identification efficiency measurements with the ATLAS detector using the 2011 LHC proton-proton collision data*, **Eur. Phys. J.** (2014) (7) 2941, 1404.2240.

-
- [190] M. Aaboud *et. al.* (ATLAS Collaboration), *Measurement of the photon identification efficiencies with the ATLAS detector using LHC Run-1 data* (2016), 1606.01813.
- [191] *Tagging and suppression of pileup jets with the ATLAS detector*, Technical Report ATLAS-CONF-2014-018, CERN, Geneva (2014), <https://cds.cern.ch/record/1700870>.
- [192] G. Aad *et. al.*, *Selection of jets produced in 13 TeV proton-proton collisions with the ATLAS detector* (2015).
- [193] *EfficiencyMeasurements*, available at: <http://twiki.cern.ch/twiki/bin/view/AtlasProtected/EfficiencyMeasurements>.
- [194] G. Aad *et. al.* (ATLAS Collaboration), *Muon reconstruction performance of the ATLAS detector in proton-proton collision data at $\sqrt{s} = 13$ TeV*, *Eur. Phys. J.* (2016) (5) 292, 1603.05598.
- [195] G. Aad *et. al.* (ATLAS Collaboration), *Studies of the performance of the ATLAS detector using cosmic-ray muons*, *Eur. Phys. J.* (2011) 1593, 1011.6665.
- [196] *Calibration of b-tagging using dileptonic top pair events in a combinatorial likelihood approach with the ATLAS experiment*, Technical Report ATLAS-CONF-2014-004, CERN, Geneva (2014), <https://cds.cern.ch/record/1664335>.
- [197] G. Aad *et. al.* (ATLAS Collaboration), *Calibration of the performance of b-tagging for c and light-flavour jets in the 2012 ATLAS data* (2014).
- [198] M. Goblirsch-Kolb (ATLAS Collaboration), *Muon Reconstruction Efficiency, Momentum Scale and Resolution in pp Collisions at 8 TeV with ATLAS*, in *Proceedings, 2nd Conference on Large Hadron Collider Physics Conference (LHCP 2014): New York, USA, June 2-7, 2014*, 2014, 1408.7086, <https://inspirehep.net/record/1312979/files/arXiv:1408.7086.pdf>.
- [199] G. Aad *et. al.* (ATLAS Collaboration), *Performance of the ATLAS muon trigger in pp collisions at $\sqrt{s} = 8$ TeV*, *Eur. Phys. J.* (2015) 120, 1408.3179.
- [200] F. U. Bernlochner *et. al.*, *The ATLAS Transverse Momentum Trigger Evolution at the LHC towards Run II* (2015), <https://cds.cern.ch/record/2047023>.
- [201] G. Aad *et. al.* (ATLAS Collaboration), *Jet energy measurement and its systematic uncertainty in proton-proton collisions at $\sqrt{s} = 7$ TeV with the ATLAS detector*, *Eur. Phys. J.* (2015) 17, 1406.0076.
- [202] G. Aad *et. al.* (ATLAS Collaboration), *Single hadron response measurement and calorimeter jet energy scale uncertainty with the ATLAS detector at the LHC*, *Eur. Phys. J.* (2013) (3) 2305, 1203.1302.
- [203] M. Aaboud *et. al.* (ATLAS Collaboration), *A measurement of the calorimeter response to single hadrons and determination of the jet energy scale uncertainty using LHC Run-1 pp-collision data with the ATLAS detector* (2016), 1607.08842.
- [204] *Jet Calibration and Systematic Uncertainties for Jets Reconstructed in the ATLAS Detector at $\sqrt{s} = 13$ TeV*, Technical Report ATL-PHYS-PUB-2015-015, CERN, Geneva (2015), <https://cds.cern.ch/record/2037613>.

- [205] S. Schramm *et al.*, *A method for the construction of strongly reduced representations of ATLAS experimental uncertainties and the application thereof to the jet energy scale*, Technical Report ATL-COM-PHYS-2015-374, CERN, Geneva (2015), <https://cds.cern.ch/record/2014656>.
- [206] G. Aad *et al.* (ATLAS Collaboration), *Jet energy resolution in proton-proton collisions at $\sqrt{s} = 7$ TeV recorded in 2010 with the ATLAS detector*, *Eur. Phys. J.* (2013) (3) 2306, [1210.6210](https://arxiv.org/abs/1210.6210).
- [207] *Performance of Missing Transverse Momentum Reconstruction in ATLAS with 2011 Proton-Proton Collisions at $\sqrt{s} = 7$ TeV*, Technical Report ATLAS-CONF-2012-101, CERN, Geneva (2012), <http://cds.cern.ch/record/1463915>.
- [208] *Performance of missing transverse momentum reconstruction for the ATLAS detector in the first proton-proton collisions at $\sqrt{s} = 13$ TeV*, Technical Report ATL-PHYS-PUB-2015-027, CERN, Geneva (2015), <http://cds.cern.ch/record/2037904>.
- [209] Daniel R. Tovey, *On measuring the masses of pair-produced semi-invisibly decaying particles at hadron colliders*, *JHEP* (2008) 034, [0802.2879v3](https://arxiv.org/abs/0802.2879v3).
- [210] A. Barr *et al.*, *$m(T2)$: The Truth behind the glamour*, *J.Phys.* (2003) 2343–2363, [hep-ph/0304226](https://arxiv.org/abs/hep-ph/0304226).
- [211] A. Barr *et al.*, *The race for supersymmetry: using $mT2$ for discovery*, *Phys. Rev.* (2009) 074 007, [0907.2713](https://arxiv.org/abs/0907.2713).
- [212] M. Baak *et al.*, *HistFitter software framework for statistical data analysis*, *Eur. Phys. J.* (2015) (4) 153, [1410.1280](https://arxiv.org/abs/1410.1280).
- [213] J. Linnemann, *Statistical Problems in Particle Physics, Astrophysics, and Cosmology*, in *et al.* (Editors) L. Lyons, 2003, 35, [physics/0312059](https://arxiv.org/abs/physics/0312059).
- [214] K. Cranmer, *Statistical Problems in Particle Physics, Astrophysics and Cosmology*, in *et al.* (Editors) L. Lyons, 2006, 112, [physics/0511028](https://arxiv.org/abs/physics/0511028).
- [215] A. R. DiDonato *et al.*, *The efficient calculation of the incomplete beta-function ratio for half-integer values of the parameters a, b* (1967) 652–662.
- [216] [online] https://root.cern.ch/doc/master/group__QuantFunc.html, https://root.cern.ch/doc/master/group__QuantFunc.html.
- [217] L. Moneta *et al.*, *The RooStats project*, in *Proceedings of the 13th International Workshop on Advanced Computing and Analysis Techniques in Physics Research.*, 2010, 57, [1009.1003](https://arxiv.org/abs/1009.1003).
- [218] R. Brun *et al.*, *ROOT: An object oriented data analysis framework*, *Nucl. Instrum. Meth.* (1997) 81–86.
- [219] G. Cowan *et al.*, *Asymptotic formulae for likelihood-based tests of new physics*, *Eur. Phys. J.* (2011) 1554, [1007.1727](https://arxiv.org/abs/1007.1727).

- [220] O. Behnke *et al.* (Editors) *Data analysis in high energy physics*, Wiley-VCH, Weinheim, Germany, 2013, ISBN 9783527410583, 9783527653447 (e-book), 9783527653430 (e-book), <http://www.wiley-vch.de/publish/dt/books/ISBN3-527-41058-9>.
- [221] G. T. Fletcher *et al.*, *Multijet Background Estimation For SUSY Searches And Particle Flow Offline Reconstruction Using The ATLAS Detector At The LHC*, Ph.D. thesis, Sheffield U. (2015), presented 01 Jun 2015, <http://cds.cern.ch/record/2054397>.
- [222] S. Owen, *Multijet Background Estimation for Supersymmetry Searches Using the ATLAS Detector at the Large Hadron Collider*, Ph.D. thesis, University of Sheffield (2012), <http://etheses.whiterose.ac.uk/2854/>.
- [223] T. Sjöstrand *et al.*, *A Brief Introduction to PYTHIA 8.1*, *Comput. Phys. Commun.* (2008) 852–867, [0710.3820](https://arxiv.org/abs/0710.3820).
- [224] G. Aad *et al.* (ATLAS Collaboration), *Performance of missing transverse momentum reconstruction in proton-proton collisions at 7 TeV with ATLAS*, *Eur. Phys. J.* (2012) 1844, [1108.5602](https://arxiv.org/abs/1108.5602).
- [225] ATLAS, *Jet energy resolution and reconstruction efficiencies from in-situ techniques with the ATLAS Detector Using Proton-Proton Collisions at a Center of Mass Energy $\sqrt{s} = 7$ TeV*, ATLAS-CONF-2010-054 (2010), <http://cdsweb.cern.ch/record/1281311>.
- [226] T. Aaltonen and others (CDF Collaboration), *Search for the Production of Scalar Bottom Quarks in $p\bar{p}$ collisions at $\sqrt{s} = 1.96$ TeV*, *Phys. Rev. Lett.* (2010) 081 802.
- [227] V. Abazov *et al.* (D0 Collaboration), *Search for scalar bottom quarks and third-generation leptoquarks in $p\bar{p}$ collisions at $\sqrt{s} = 1.96$ TeV*, *Phys. Lett.* (2010) 95–101.
- [228] *Search for direct sbottom or stop pair production in final states with Missing Transverse Energy and two b-jets*, Technical Report ATLAS-COM-PHYS-2013-072, CERN, Geneva (2014), <https://cds.cern.ch/record/1508045/files/ATL-COM-PHYS-2013-072.pdf>.
- [229] G. Aad *et al.* (ATLAS Collaboration), *Search for direct third-generation squark pair production in final states with missing transverse momentum and two b-jets in $\sqrt{s} = 8$ TeV pp collisions with the ATLAS detector*, *JHEP* (2013) 189, [1308.2631](https://arxiv.org/abs/1308.2631).
- [230] S. Chatrchyan *et al.* (CMS Collaboration), *Search for anomalous production of events with three or more leptons in pp collisions at $\sqrt{s} = 8$ TeV*, *Phys. Rev.* (2014) 032 006, [1404.5801](https://arxiv.org/abs/1404.5801).
- [231] S. Chatrchyan *et al.* (CMS Collaboration), *Search for supersymmetry in pp collisions at $\sqrt{s} = 8$ TeV in events with three leptons and at least one b-tagged jet* (2013).
- [232] S. Chatrchyan *et al.* (CMS Collaboration), *Search for new physics in events with same-sign dileptons and jets in pp collisions at $\sqrt{s} = 8$ TeV*, *JHEP* (2014) 163, [1311.6736](https://arxiv.org/abs/1311.6736).

- [233] S. Alioli *et al.*, *A general framework for implementing NLO calculations in shower Monte Carlo programs: the POWHEG BOX*, **JHEP** (2010) 043, [1002.2581](#).
- [234] D. J. Lange, *The EvtGen particle decay simulation package*, **Nucl. Instrum. Meth.** (2001) 152–155.
- [235] H.-L. Lai *et al.*, *New parton distributions for collider physics*, **Phys. Rev.** (2010) 074 024, [1007.2241](#).
- [236] S. Frixione *et al.*, *Matching NLO QCD computations with Parton Shower simulations: the POWHEG method*, **JHEP** (2007) 070, For $t\bar{t}$ (single top) production, POWHEG-BOX version 1.0 r2129 is interfaced with PYTHIA 6.427 (6.426)., [0709.2092](#).
- [237] K. Abe *et al.* (SLD Collaboration), *Improved measurement of the probability for gluon splitting into b anti- b in $Z0$ decays*, **Phys. Lett.** (2001) 61–69, [hep-ex/0102002](#).
- [238] *Z boson mass, width and decays*, available at: <http://pdg.lbl.gov/2011/listings/rpp2011-list-z-boson.pdf>.
- [239] J. Alwall *et al.*, *MadGraph 5 : Going Beyond*, **JHEP** (2011) 128, [1106.0522](#).
- [240] M. Bähr *et al.*, *Herwig++ Physics and Manual*, **Eur. Phys. J.** (2008) 639–707, [0803.0883](#).
- [241] *Monte Carlo Calibration and Combination of In-situ Measurements of Jet Energy Scale, Jet Energy Resolution and Jet Mass in ATLAS*, Technical Report ATLAS-CONF-2015-037, CERN, Geneva (2015), <https://cds.cern.ch/record/2044941>.
- [242] A. L. Read, *Presentation of search results: The $CL(s)$ technique*, **J.Phys.** (2002) 2693–2704.
- [243] *Performance assumptions based on full simulation for an upgraded ATLAS detector at a High-Luminosity LHC*, ATL-PHYS-PUB-2013-009 .
- [244] *Performance assumptions for an upgraded ATLAS detector at a High-Luminosity LHC*, ATL-PHYS-PUB-2013-004 .
- [245] F. Wang *et al.*, *A split SUSY model from SUSY GUT*, **JHEP** (2015) 050, [1501.02906](#).
- [246] G. Aad *et al.* (ATLAS Collaboration), *Summary of the searches for squarks and gluinos using $\sqrt{s} = 8$ TeV pp collisions with the ATLAS experiment at the LHC*, **JHEP** (2015) 054, [1507.05525](#).
- [247] M. Cahill-Rowley *et al.*, *Constraints on Higgs Properties and SUSY Partners in the p MSSM*, in *Proceedings, 2013 Community Summer Study on the Future of U.S. Particle Physics: Snowmass on the Mississippi (CSS2013): Minneapolis, MN, USA, July 29-August 6, 2013*, 2013, [1308.0297](#), <https://inspirehep.net/record/1246019/files/arXiv:1308.0297.pdf>.
- [248] ATLAS (ATLAS Collaboration), *The ATLAS Simulation Infrastructure*, **EPJ** (2010) 823–874, [1005.4568](#).

- [249] S. Frixione *et. al.*, *Matching NLO QCD computations and parton shower simulations*, **JHEP** (2002) 029, MC@NLO 4.03 interfaced to HERWIG+Jimmy using the AUET2-CT10 tune., [hep-ph/0204244](https://arxiv.org/abs/hep-ph/0204244).
- [250] J. Butterworth *et. al.*, *Multiparton interactions in photoproduction at HERA*, **ZfP** (1996) 637–646, [hep-ph/9601371](https://arxiv.org/abs/hep-ph/9601371).
- [251] B. P. Kersevan *et. al.*, *The Monte Carlo event generator AcerMC version 2.0 with interfaces to PYTHIA 6.2 and HERWIG 6.5* (2004), AcerMC version 3.8 is interfaced with PYTHIA 6.426., [hep-ph/0405247](https://arxiv.org/abs/hep-ph/0405247).
- [252] *Search for chargino and neutralino production in final states with one lepton, two b-jets consistent with a Higgs boson, and missing transverse momentum with the ATLAS detector in 20.3 fb⁻¹ of $\sqrt{s} = 8$ TeV pp collisions*, Technical Report ATLAS-CONF-2013-093, CERN, Geneva (2013), <https://cds.cern.ch/record/1595756>.
- [253] J. Alwall *et. al.*, *Computing decay rates for new physics theories with FeynRules and MadGraph5/aMC@NLO* (2014), [1402.1178](https://arxiv.org/abs/1402.1178).
- [254] M. W. Cahill-Rowley *et. al.*, *The New Look pMSSM with Neutralino and Gravitino LSPs*, **Eur.Phys.J.** (2012) 2156, [1206.4321](https://arxiv.org/abs/1206.4321).
- [255] G. Aad *et. al.* (ATLAS Collaboration), *Search for squarks and gluinos with the ATLAS detector in final states with jets and missing transverse momentum using $\sqrt{s} = 8$ TeV proton–proton collision data* (2014), [1405.7875](https://arxiv.org/abs/1405.7875).
- [256] G. Aad *et. al.* (ATLAS Collaboration), *Search for new phenomena in final states with large jet multiplicities and missing transverse momentum at $\sqrt{s} = 8$ TeV proton-proton collisions using the ATLAS experiment*, **JHEP** (2013) 130, [1308.1841](https://arxiv.org/abs/1308.1841).
- [257] G. Aad *et. al.* (ATLAS Collaboration), *Search for squarks and gluinos in events with isolated leptons, jets and missing transverse momentum at $\sqrt{s} = 8$ TeV with the ATLAS detector* (2014) (ATL-COM-PHYS-2014-727).
- [258] G. Aad *et. al.* (ATLAS Collaboration), *Search for supersymmetry in events with large missing transverse momentum, jets, and at least one tau lepton in 20 fb⁻¹ of $\sqrt{s} = 8$ TeV proton-proton collision data with the ATLAS detector*, **JHEP** (2014) 103, [1407.0603](https://arxiv.org/abs/1407.0603).
- [259] G. Aad *et. al.* (ATLAS Collaboration), *Search for supersymmetry at $\sqrt{s}=8$ TeV in final states with jets and two same-sign leptons or three leptons with the ATLAS detector*, **JHEP** (2014) 035, [1404.2500](https://arxiv.org/abs/1404.2500).
- [260] G. Aad *et. al.* (ATLAS Collaboration), *Search for strong production of supersymmetric particles in final states with missing transverse momentum and at least three b-jets at $\sqrt{s} = 8$ TeV proton-proton collisions with the ATLAS detector*, **JHEP** (2014) 24, [1407.0600](https://arxiv.org/abs/1407.0600).
- [261] G. Aad *et. al.* (ATLAS Collaboration), *Search for direct pair production of the top squark in all-hadronic final states in proton-proton collisions at $\sqrt{s} = 8$ TeV with the ATLAS detector*, **JHEP** (2014) 015, [1406.1122](https://arxiv.org/abs/1406.1122).

- [262] G. Aad *et. al.* (ATLAS Collaboration), *Search for top squark pair production in final states with one isolated lepton, jets, and missing transverse momentum in $\sqrt{s} = 8$ TeV pp collisions with the ATLAS detector*, **JHEP** (2014) 118, [1407.0583](#).
- [263] G. Aad *et. al.* (ATLAS Collaboration), *Search for direct top-squark pair production in final states with two leptons in pp collisions at $\sqrt{s} = 8$ TeV with the ATLAS detector*, **JHEP** (2014) 124, [1403.4853](#).
- [264] G. Aad *et. al.* (ATLAS Collaboration), *Search for pair-produced third-generation squarks decaying via charm quarks or in compressed supersymmetric scenarios in pp collisions at $\sqrt{s} = 8$ TeV with the ATLAS detector*, **Phys. Rev. D** (2014) 052 008, [1407.0608](#).
- [265] G. Aad *et. al.* (ATLAS Collaboration), *Search for direct top squark pair production in events with a Z boson, b-jets and missing transverse momentum in $\sqrt{s} = 8$ TeV pp collisions with the ATLAS detector*, **Eur.Phys.J.** (2014) (6) 2883, [1403.5222](#).
- [266] G. Aad *et. al.* (ATLAS Collaboration), *Search for direct production of charginos, neutralinos and sleptons in final states with two leptons and missing transverse momentum in pp collisions at $\sqrt{s} = 8$ TeV with the ATLAS detector*, **JHEP** (2014) 071, [1403.5294](#).
- [267] G. Aad *et. al.* (ATLAS Collaboration), *Search for the direct production of charginos, neutralinos and staus in final states with at least two hadronically decaying taus and missing transverse momentum in pp collisions at $\sqrt{s} = 8$ TeV with the ATLAS detector* (2014), [1407.0350](#).
- [268] G. Aad *et. al.* (ATLAS Collaboration), *Search for direct production of charginos and neutralinos in events with three leptons and missing transverse momentum in $\sqrt{s} = 8$ TeV pp collisions with the ATLAS detector*, **JHEP** (2014) 169, [1402.7029](#).
- [269] G. Aad *et. al.* (ATLAS Collaboration), *Search for supersymmetry in events with four or more leptons in $\sqrt{s} = 8$ TeV pp collisions with the ATLAS detector*, **Phys.Rev.** (2014) 052 001, [1405.5086](#).
- [270] G. Aad *et. al.* (ATLAS Collaboration), *Search for charginos nearly mass degenerate with the lightest neutralino based on a disappearing-track signature in pp collisions at $\sqrt{s} = 8$ TeV with the ATLAS detector*, **Phys.Rev.** (2013) (11) 112 006, [1310.3675](#).
- [271] G. Aad *et. al.* (ATLAS Collaboration), *Search for new phenomena in final states with an energetic jet and large missing transverse momentum in pp collisions at $\sqrt{s} = 8$ TeV with the ATLAS detector*, **Eur. Phys. J.** (2015) (7) 299, [Erratum: Eur. Phys. J.C75,no.9,408(2015)], [1502.01518](#).
- [272] G. Aad *et. al.* (ATLAS Collaboration), *Search for neutral Higgs bosons of the minimal supersymmetric standard model in pp collisions at $\sqrt{s} = 8$ TeV with the ATLAS detector*, **JHEP** (2014) 056, [1409.6064](#).

Appendix A

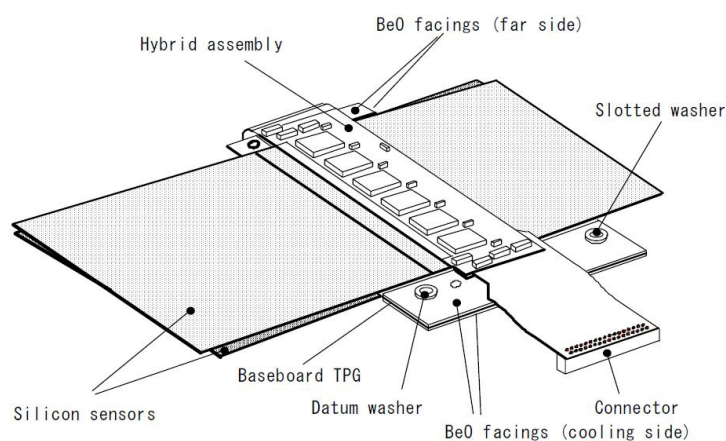
SCT Service Work

The author was involved in the operations of the SCT and developed an online tool to read live event dumps from the SCT Data-Acquisition (DAQ) in a human-readable format.

The SCT contains 4088 modules distributed in the barrel and endcaps. There are two types of SCT modules arranged into 4 regions named: BARREL_A, BARREL_C, ENDCAP_A, ENDCAP_C ; depending on the side on the detector and if they are part of one of the 4 barrel layers or one of the 9 endcaps. Each of these modules contain two back-to-back plates rotated by an angle of 40 mrad with respect to each other. The two plates contain 768 silicon strips. Figure A.1 shows a schematic diagram of one of these modules in one of the barrel layers.

Fig. A.1 Layout of one type of SCT module used in the 4 barrel layers.

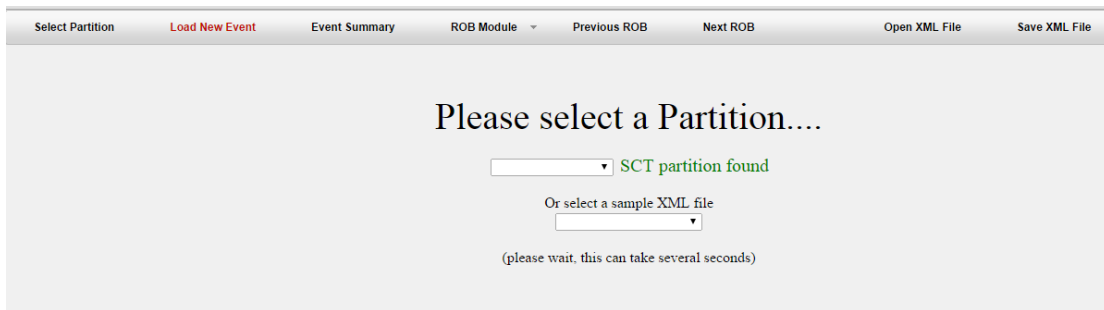
[_paper/figures/Chapter3/Figs/module.png](#) [_paper/figures/Chapter3/Figs/module.jpg](#)



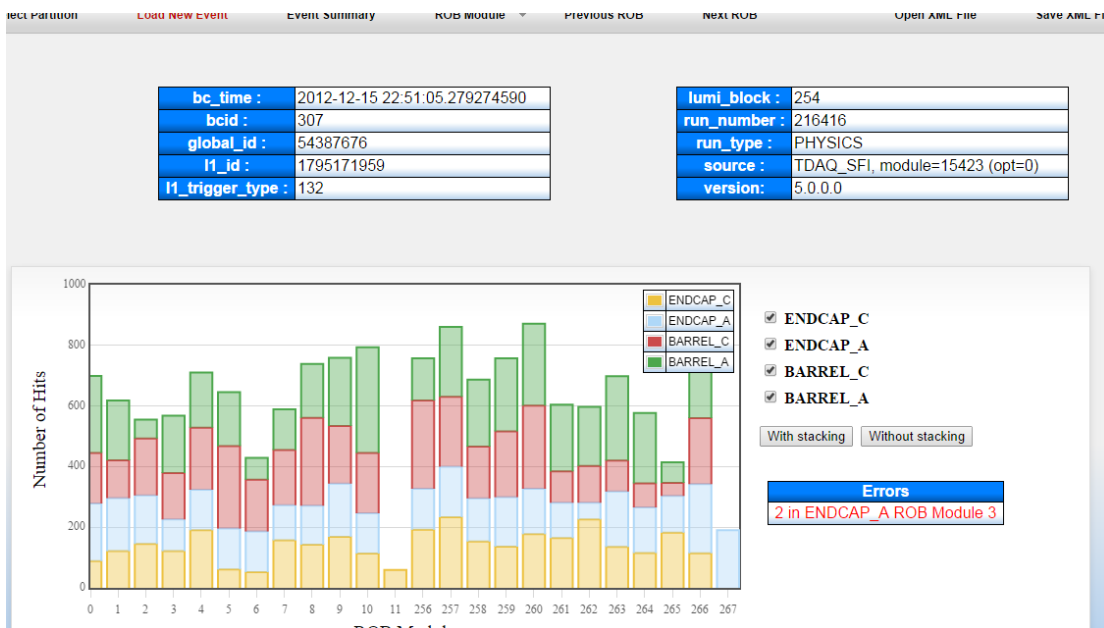
The modules are read out by optical connections and recorded by the Data Acquisition system (DAQ). The DAQ is composed of Readout Drivers (RODs) each containing up to 16 Readout Buffers (ROBs) which each read out 48 modules.

An online event dump viewer using Javascript, PHP, HTML and CSS languages is used to monitor and debug the ROD, ROB and module information. The event dump viewer reads random events in the form of .XML files that have been converted from binary to hexadecimal in real time detector. The details of the main SCT event dump viewer features are listed below:

- A main page displays a list of available SCT *partitions* at *point one*, if *emom services* are available and a list of example events.



- For each live or example event a main page displays information such as the bunch-crossing ID (bcid), the time of the bunch-crossing, the Luminosity block (lumi_block) and many more. It also displays a summary graph of the total number of hits per module. The total number of module errors is also displayed on the graph.



- For each ROB a break down of each module hit and error information can be viewed. The event dump viewer decodes the hexadecimal 32-bit numbers into human readable format, as displayed below:

Rob SCT_ENDCAP_C_SIDE, module=257 (opt=0) version : 5.0.0.0

Status Word	Word	Information
0	0x00200008	Data may be incorrect Condensed Mode Hit Pattern Error
1	0x00f00002	Count of Errors in Event Fragment: 2

bcid:	307
det_event_type:	2097152
l1_id:	1795171959
l1_trigger_type:	132
run_number:	216416

Data	Data split	Bitstream	Mode	Module	Side	Chip	Channel	Hits	Error
0x21029a20	2102	0010000100000010	Header, Link Number: 0x2	1	0	-	-	-	-
	9a20	1001101000100000	Super Condensed Mode	-	-	3	34	1	-
0x2103d4b1	2103	0010000100000011	Header, Link Number: 0x3	1	1	-	-	-	-
	d4b1	1101010010110001	Super Condensed Mode	-	-	10	75	2	-
0x210898e5	2108	0010000100001000	Header, Link Number: 0x8	4	0	-	-	-	-
	98e5	1001100011100101	Super Condensed Mode	-	-	3	14	6	-
0x2112ac91	2112	0010000100010010	Header, Link Number: 0x12	7	0	-	-	-	-
	ac91	1010110010010001	Super Condensed Mode	-	-	5	73	2	-
0x2113c382	2113	0010000100010011	Header, Link Number: 0x13	7	1	-	-	-	-
	c382	1100001110000010	Super Condensed Mode	-	-	8	56	3	-
0x211488a0	2114	0010000100010100	Header, Link Number: 0x14	8	0	-	-	-	-
	88a0	1000100010100000	Super Condensed Mode	-	-	1	10	1	-
0x9f52a8e0	9f52	1001111101010010	Super Condensed Mode	-	-	3	117	3	-
	a8e0	1010100011100000	Super Condensed Mode	-	-	5	14	1	-

- Additional features include the ability to save the event as an XML file, as well as upload local XML files to be viewed.

Appendix B

Auxillary material for the 2015 data direct $bb+E_T^{\text{miss}}$ analysis

In this appendix, auxillary material for Chapter 7 is presented for reference.

B.1 Systematic Uncertainties

The breakdown of the systematic uncertainties for the likelihood fits for each signal region are presented here. Table B.1 shows the results for SRA250, SRA350 is shown in Table B.2, SRA450 is shown in Table B.3 and SRB is shown in Table B.4.

B.1 Systematic Uncertainties

Table B.1 Breakdown of the dominant systematic uncertainties on background estimates in the SRA250 signal region. Note that the individual uncertainties can be correlated, and do not necessarily add up quadratically to the total background uncertainty. The percentages show the size of the uncertainty relative to the total expected background.

Uncertainty of channel	SRA250
Total background expectation	29.15
Total statistical ($\sqrt{N_{\text{exp}}}$)	± 5.40
Total background systematic	± 4.71 [16.16%]
μ_Z	± 2.86 [9.8%]
Data-Driven Z + jets	± 1.98 [6.8%]
Z + jets Theory	± 1.75 [6.0%]
JER	± 1.64 [5.6%]
b-tagging efficiency extrapolation	± 0.99 [3.4%]
μ_{ST}	± 0.80 [2.8%]
μ_W	± 0.66 [2.2%]
Single Top Theory	± 0.63 [2.2%]
E_T^{miss} Soft Track Resolution Para.	± 0.63 [2.1%]
W + jet bottom fraction	± 0.60 [2.1%]
b-jet Tagging	± 0.55 [1.9%]
Light jet mis-tagging	± 0.53 [1.8%]
JES (set 1)	± 0.49 [1.7%]
tbar Theory	± 0.37 [1.3%]
W + jets Theory	± 0.35 [1.2%]
W + jets charm fraction	± 0.34 [1.2%]
E_T^{miss} Soft Track Resolution Perp.	± 0.33 [1.1%]
Electron ID Efficiency	± 0.32 [1.1%]
JES (set 2)	± 0.18 [0.61%]
Muon Trigger SF (stat.)	± 0.16 [0.55%]
μ_{Top}	± 0.14 [0.50%]
Muon Efficiency	± 0.13 [0.45%]
Electron Reconstruction Efficiency	± 0.12 [0.40%]
Electron Isolation SF	± 0.11 [0.36%]
JVT	± 0.10 [0.33%]
Electron Efficiency Trigger SF	± 0.09 [0.30%]
c-jet mis-tagging	± 0.08 [0.26%]
Muon Trigger SF	± 0.07 [0.24%]
Muon MS Resolution	± 0.06 [0.21%]
E_T^{miss} Soft Track Scale	± 0.06 [0.20%]
JES (set 3)	± 0.06 [0.19%]
Muon ID Resolution	± 0.06 [0.19%]
Muon Isolation Systematic	± 0.05 [0.18%]
$E\gamma$ Energy Resolution	± 0.04 [0.15%]
Muon Reconstruction Energy Scale	± 0.04 [0.14%]
Muon Efficiency (stat.)	± 0.04 [0.13%]
$E\gamma$ Energy Scale	± 0.03 [0.11%]
Luminosity	± 0.02 [0.06%]
Muon Isolation Statistical	± 0.02 [0.05%]
Lumi	± 0.01 [0.05%]

B.1 Systematic Uncertainties

Table B.2 Breakdown of the dominant systematic uncertainties on background estimates in the SRA350 signal region. Note that the individual uncertainties can be correlated, and do not necessarily add up quadratically to the total background uncertainty. The percentages show the size of the uncertainty relative to the total expected background.

Uncertainty of channel	SRA350
Total background expectation	6.95
Total statistical ($\sqrt{N_{\text{exp}}}$)	± 2.64
Total background systematic	± 1.23 [17.75%]
μ_Z	± 0.66 [9.5%]
Data-Driven Systematic	± 0.63 [9.0%]
b-tagging efficiency extrapolation	± 0.42 [6.1%]
JER	± 0.39 [5.6%]
Z + jets Theory	± 0.35 [5.0%]
μ_{ST}	± 0.24 [3.4%]
W + jet bottom fraction	± 0.20 [2.9%]
b-jet Tagging	± 0.20 [2.8%]
Single Top Theory	± 0.19 [2.7%]
μ_W	± 0.18 [2.6%]
JES (set 1)	± 0.16 [2.4%]
Light jet mis-tagging	± 0.13 [1.9%]
W + jets charm fraction	± 0.13 [1.8%]
E_T^{miss} Soft Track Resolution Para.	± 0.10 [1.4%]
W + jets Theory	± 0.08 [1.2%]
Electron ID Efficiency	± 0.07 [1.1%]
tbar Theory	± 0.06 [0.85%]
JES (set 2)	± 0.05 [0.71%]
Muon Trigger SF (stat.)	± 0.04 [0.54%]
Muon Efficiency	± 0.03 [0.44%]
Electron Reconstruction Efficiency	± 0.03 [0.40%]
Electron Isolation SF	± 0.02 [0.36%]
μ_{Top}	± 0.02 [0.34%]
JVT	± 0.02 [0.30%]
Electron Efficiency Trigger SF	± 0.02 [0.30%]
E_T^{miss} Soft Track Resolution Perp.	± 0.02 [0.28%]
E_γ Energy Scale	± 0.02 [0.27%]
Muon Trigger SF	± 0.02 [0.24%]
Muon ID Resolution	± 0.01 [0.22%]
Muon MS Resolution	± 0.01 [0.20%]
c-jet mis-tagging	± 0.01 [0.17%]
Muon Isolation Systematic	± 0.01 [0.17%]
Muon Efficiency (stat.)	± 0.01 [0.13%]
Muon Reconstruction Energy Scale	± 0.01 [0.13%]
Luminosity	± 0.00 [0.07%]
Lumi	± 0.00 [0.06%]
Muon Isolation Statistical	± 0.00 [0.05%]
E_γ Energy Resolution	± 0.00 [0.04%]
JES (set 3)	± 0.00 [0.04%]
E_T^{miss} Soft Track Scale	± 0.00 [0.01%]

B.1 Systematic Uncertainties

Table B.3 Breakdown of the dominant systematic uncertainties on background estimates in the SRA450 signal region. Note that the individual uncertainties can be correlated, and do not necessarily add up quadratically to the total background uncertainty. The percentages show the size of the uncertainty relative to the total expected background.

Uncertainty of channel	SRA450
Total background expectation	1.84
Total statistical ($\sqrt{N_{\text{exp}}}$)	± 1.35
Total background systematic	± 0.39 [21.41%]
Data-Driven Systematic	± 0.25 [13.4%]
mu_Z	± 0.18 [9.7%]
b-tagging efficiency extrapolation	± 0.16 [8.8%]
Z + jets Theory	± 0.10 [5.4%]
JER	± 0.08 [4.5%]
b-jet Tagging	± 0.06 [3.2%]
mu_ST	± 0.06 [3.1%]
W + jet bottom fraction	± 0.05 [2.9%]
E_T^{miss} Soft Track Resolution Perp.	± 0.05 [2.9%]
mu_W	± 0.04 [2.4%]
Single Top Theory	± 0.04 [2.4%]
JES (set 2)	± 0.04 [2.1%]
W + jets charm fraction	± 0.03 [1.5%]
JES (set 1)	± 0.03 [1.4%]
E_T^{miss} Soft Track Resolution Para.	± 0.02 [1.3%]
Light jet mis-tagging	± 0.02 [1.2%]
W + jets Theory	± 0.02 [1.2%]
Electron ID Efficiency	± 0.02 [1.1%]
JES (set 3)	± 0.02 [1.0%]
tbar Theory	± 0.01 [0.80%]
Muon Trigger SF (stat.)	± 0.01 [0.54%]
Muon Efficiency	± 0.01 [0.44%]
Electron Reconstruction Efficiency	± 0.01 [0.40%]
c-jet mis-tagging	± 0.01 [0.40%]
Electron Isolation SF	± 0.01 [0.36%]
JVT	± 0.01 [0.36%]
mu_Top	± 0.01 [0.31%]
Electron Efficiency Trigger SF	± 0.01 [0.30%]
Muon Trigger SF	± 0.00 [0.24%]
Muon MS Resolution	± 0.00 [0.23%]
E_γ Energy Resolution	± 0.00 [0.21%]
Muon Isolation Systematic	± 0.00 [0.18%]
Muon ID Resolution	± 0.00 [0.16%]
Muon Efficiency (stat.)	± 0.00 [0.13%]
Muon Reconstruction Energy Scale	± 0.00 [0.12%]
E_T^{miss} Soft Track Scale	± 0.00 [0.08%]
Luminosity	± 0.00 [0.07%]
Lumi	± 0.00 [0.06%]
Muon Isolation Statistical	± 0.00 [0.05%]
E_γ Energy Scale	± 0.00 [0.04%]

B.1 Systematic Uncertainties

Table B.4 Breakdown of the dominant systematic uncertainties on background estimates in SRB, for an integrated luminosity of 3.2 fb^{-1} . Note that the individual uncertainties can be correlated, and do not necessarily add up quadratically to the total background uncertainty. The percentages show the size of the uncertainty relative to the total expected background.

Uncertainty of channel	SRB
Total background expectation	12.02
Total statistical ($\sqrt{N_{\text{exp}}}$)	± 3.47
Total background systematic	± 2.50 [20.77%]
tbar Theory	± 1.91 [15.9%]
Data-Driven Systematic	± 0.96 [8.0%]
mu_Z	± 0.77 [6.4%]
JES (set 1)	± 0.64 [5.3%]
mu_Top	± 0.53 [4.4%]
W + jets Theory	± 0.40 [3.4%]
W + jet bottom fraction	± 0.36 [3.0%]
Single Top Theory	± 0.35 [2.9%]
Z + jets Theory	± 0.28 [2.3%]
Light jet mis-tagging	± 0.19 [1.6%]
b-jet Tagging	± 0.14 [1.2%]
Luminosity	± 0.12 [0.98%]
Lumi	± 0.09 [0.76%]
c-jet mis-tagging	± 0.08 [0.69%]
Electron ID Efficiency	± 0.08 [0.65%]
W + jets charm fraction	± 0.07 [0.61%]
JER	± 0.07 [0.58%]
E_T^{miss} Soft Track Resolution Para.	± 0.07 [0.57%]
E_T^{miss} Soft Track Resolution Perp.	± 0.06 [0.54%]
Muon Trigger SF (stat.)	± 0.05 [0.45%]
JES (set 2)	± 0.05 [0.45%]
Muon Efficiency	± 0.03 [0.28%]
Electron Reconstruction Efficiency	± 0.03 [0.25%]
Electron Isolation SF	± 0.03 [0.22%]
JVT	± 0.02 [0.20%]
Electron Efficiency Trigger SF	± 0.02 [0.19%]
Muon Trigger SF	± 0.02 [0.19%]
Muon Reconstruction Energy Scale	± 0.02 [0.16%]
Muon ID Resolution	± 0.02 [0.15%]
Muon Isolation Systematic	± 0.01 [0.12%]
b-tagging efficiency extrapolation	± 0.01 [0.12%]
JES (set 3)	± 0.01 [0.11%]
E_γ Energy Scale	± 0.01 [0.11%]
Muon Efficiency (stat.)	± 0.01 [0.10%]
E_T^{miss} Soft Track Scale	± 0.01 [0.09%]
Muon MS Resolution	± 0.01 [0.05%]
E_γ Energy Resolution	± 0.01 [0.04%]
Muon Isolation Statistical	± 0.00 [0.03%]

B.2 Data-Driven Z + jets from an Extrapolation in b-jet Multiplicity

The data-driven method for estimating Z + b-jets using light-jets to model b-jets, developed by the author, relies on a series of corrections that are made in monte-carlo. These corrections, which account for correcting events with two selected signal leptons to events with zero baseline leptons, are shown in Table B.5 as a function of the variables m_{CT} . These corrections were derived using the MC generator Sherpa. Additionally corrections obtained using MadGraph+Pythia8 are shown in Table B.6.

Table B.5 Correction factors for the Z + jets derived in m_{CT} bins in SRA and ERzA-2b2l with Sherpa MC samples.

m_{CT} Low Bin	m_{CT} High Bin	SRA	ERzA-2b2l	Correction (2l→0l)
0	50	0.19 ± 0.06	0.02 ± 0.01	8.83 ± 4.64
50	100	2.81 ± 0.24	1.13 ± 0.46	2.50 ± 1.02
100	150	5.02 ± 0.29	0.78 ± 0.10	6.45 ± 0.80
150	200	7.31 ± 0.33	1.47 ± 0.12	4.98 ± 0.42
200	250	11.76 ± 0.70	2.45 ± 0.49	4.80 ± 0.96
250	300	8.43 ± 0.31	1.60 ± 0.10	5.27 ± 0.34
300	350	3.92 ± 0.16	0.94 ± 0.07	4.17 ± 0.33
350	450	2.70 ± 0.12	0.67 ± 0.05	4.02 ± 0.28
450	600	0.83 ± 0.04	0.18 ± 0.01	4.58 ± 0.35
600	∞	0.17 ± 0.01	0.04 ± 0.00	4.03 ± 0.47

B.2 Data-Driven Z + jets from an Extrapolation in b-jet Multiplicity

Table B.6 Correction factors for the Z + jets background derived in m_{CT} bins in SRA and CRzA-2b2l with MadGraph+Pythia8 MC samples.

m_{CT} Low Bin	m_{CT} High Bin	SRA	CRzA-2b2l	Correction (2l→0l)
0	50	0.29 ± 0.15	0.00 ± 0.00	0.00 ± 0.00
50	100	3.79 ± 0.82	0.10 ± 0.10	37.17 ± 37.17
100	150	7.00 ± 1.12	1.11 ± 0.41	6.30 ± 2.32
150	200	8.54 ± 1.14	1.71 ± 0.53	4.98 ± 1.53
200	250	14.83 ± 1.86	3.32 ± 0.76	4.47 ± 1.02
250	300	12.40 ± 1.64	3.18 ± 0.68	3.90 ± 0.84
300	350	6.97 ± 1.20	1.00 ± 0.34	6.95 ± 2.37
350	450	5.90 ± 1.18	1.14 ± 0.42	5.18 ± 1.92
450	600	1.53 ± 0.47	0.24 ± 0.24	6.36 ± 6.36
600	∞	0.00 ± 0.00	0.06 ± 0.06	0.00 ± 0.00

A summary of the single bin correction factor for 2l→0l is given in Table B.7. This was due to the lack of statistics as a function of m_{CT} .

Table B.7 Single bin correction factor for the Z + jets background derived in m_{CT} bins in SRA and CRzA-2b2l with Sherpa and MadGraph+Pythia8 MC samples.

m_{CT} MC Generator	Low Bin	m_{CT} High Bin	SRA	CRzA-2b2l	Correction (2l→0l)
Sherpa 2.1	200	∞	27.82 ± 0.79	5.89 ± 0.51	4.73 ± 0.43
MadGraph+Pythia8	200	∞	41.64 ± 3.03	8.94 ± 1.18	4.66 ± 0.70
Sherpa 2.1	250	∞	16.06 ± 0.37	3.44 ± 0.14	4.67 ± 0.21
Sherpa 2.1	350	∞	13.71 ± 0.12	0.90 ± 0.05	4.13 ± 0.27
Sherpa 2.1	450	∞	1.01 ± 0.04	0.22 ± 0.01	4.48 ± 0.34

For the method to be complete, the 0 b-jet distribution needs to be normalised to 2 b-jets with the use of two control regions. The yields observed in these regions are quoted in Table B.8.

B.3 Data-Driven Z + jets from γ + jets

Table B.8 Yields of the SM background processes predicted in (a) CRzA-0b2l and (b) CRzA-2b2l.

	CRzA-2b2l	CRzA-0b2l
Observed Data	9.00 ± 3.00	1011.00 ± 31.80
MC Total	8.23 ± 0.75	933.84 ± 10.91
$t\bar{t}$	0.07 ± 0.07	0.68 ± 0.23
SingleTop	0.07 ± 0.04	0.04 ± 0.03
Z+jets	7.84 ± 0.54	897.89 ± 9.27
W+jets	0.00 ± 0.00	0.00 ± 0.00
Other	0.24 ± 0.10	35.23 ± 1.38

B.3 Data-Driven Z + jets from γ + jets

The total observed yields for the emulation regions for γ + jets method of estimating Z + jets are reported in Table B.9. They show the high purity of events in each emulation of the signal regions.

Table B.9 Yields of the SM background processes and Data observed at 3.2 fb^{-1} in the template (emulation) regions ER γ A(s) and ER γ B. The Multi-jet background is estimated from MC and not the JetSmearing method. Only statistical uncertainties are shown.

	ER γ A-mbb	ER γ A-mct	ER γ A250	ER γ A350	ER γ A450	ER γ B
Observed Data	80.00 ± 8.94	16.00 ± 4.00	40.00 ± 6.32	8.00 ± 2.83	4.00 ± 2.00	6.00 ± 2.45
MC Total	68.76 ± 23.03	11.21 ± 1.36	26.50 ± 1.40	5.87 ± 0.55	1.66 ± 0.25	6.26 ± 0.59
W + jets	-0.01 ± 0.01	0.14 ± 0.05	0.10 ± 0.03	0.02 ± 0.01	0.01 ± 0.00	0.03 ± 0.01
Z + jets	-0.00 ± 0.01	0.02 ± 0.01	0.01 ± 0.01	0.00 ± 0.00	0.00 ± 0.00	0.00 ± 0.00
Other	0.00 ± 0.00	0.00 ± 0.00	0.00 ± 0.00	0.00 ± 0.00	0.00 ± 0.00	0.00 ± 0.00
SingleTop	0.02 ± 0.03	0.05 ± 0.03	0.03 ± 0.01	0.02 ± 0.01	0.01 ± 0.00	0.02 ± 0.01
Multi-jet	0.20 ± 0.20	0.00 ± 0.00	0.02 ± 0.02	0.02 ± 0.02	0.02 ± 0.02	0.00 ± 0.00
$t\bar{t}$	0.33 ± 0.15	0.28 ± 0.13	0.00 ± 0.00	0.00 ± 0.00	0.00 ± 0.00	0.14 ± 0.07
γ + jets	47.34 ± 1.88	10.67 ± 0.98	26.33 ± 1.33	5.81 ± 0.52	1.63 ± 0.22	6.08 ± 0.50

Table B.10 Yields of the SM background processes and Data observed at 3.2 fb^{-1} in CR γ L and CR z L.

	CR γ L	CR z L
Observed Data	381.00 ± 19.52	31.00 ± 5.57
MC Total	248.76 ± 5.06	26.14 ± 1.49
W + jets	0.62 ± 0.09	0.00 ± 0.00
SingleTop	0.49 ± 0.09	0.18 ± 0.06
$t\bar{t}$	2.28 ± 0.40	0.22 ± 0.13
Other	0.12 ± 0.07	2.58 ± 0.47
Z + jets	0.08 ± 0.02	23.15 ± 0.83

B.4 Limits

Finally, the breakdown of the exclusion limits for the 2015 $bb+E_T^{\text{miss}}$ analysis for each of the four signal regions are shown in Figure B.1.

Figure B.2 quotes the observed CLs values. Figure B.3 shows the best expected CLs values, best observed CLs values and best 95% CLs excluded model cross sections.

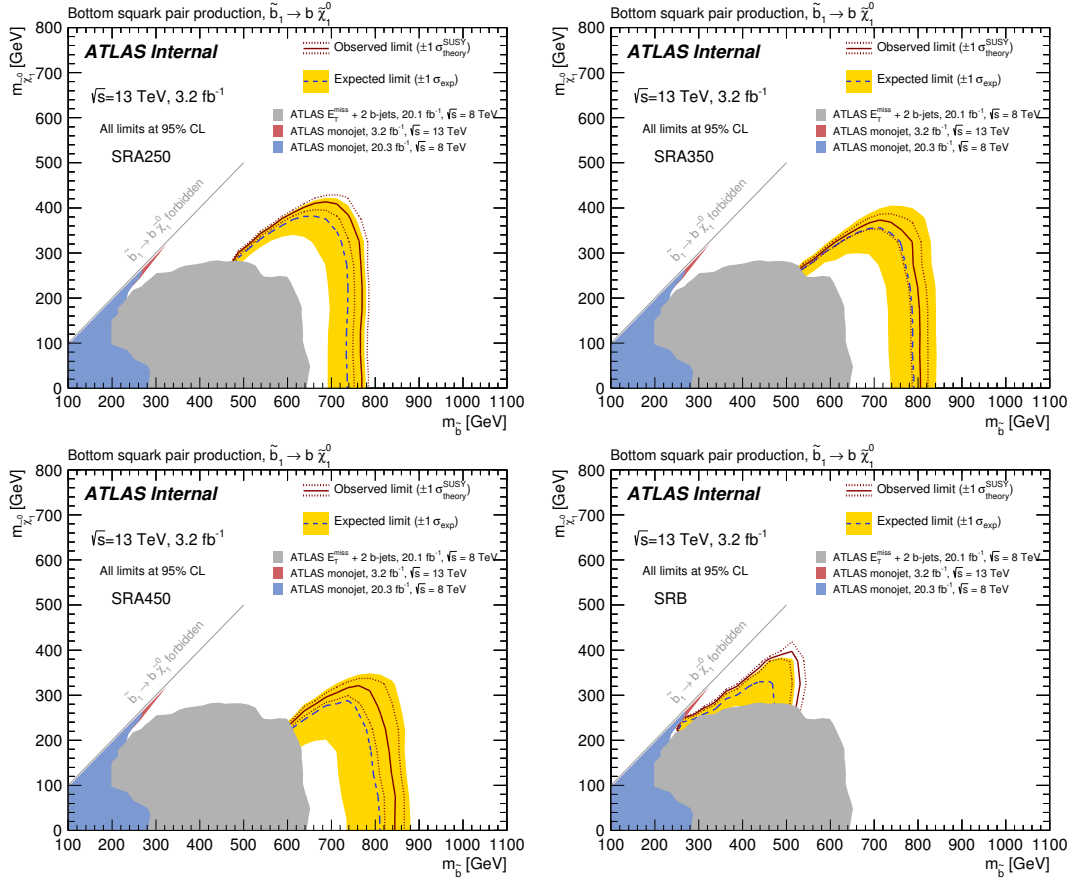


Fig. B.1 Expected and observed exclusion limits at 95% CL in the $(m_{\tilde{b}}, m_{\tilde{\chi}_1^0})$ plane for the four signal regions defined in this analysis. The dashed black and solid bold red lines show the 95% CL expected and observed limits respectively, including all uncertainties except the theoretical signal cross-section uncertainty. The shaded (yellow) bands around the expected limits show the impact of the experimental uncertainties while the dotted red lines show the impact on the observed limit of the variation of the nominal signal cross-section by 1σ theoretical uncertainty. Also shown for reference are the observed limits from the previous analysis [29].

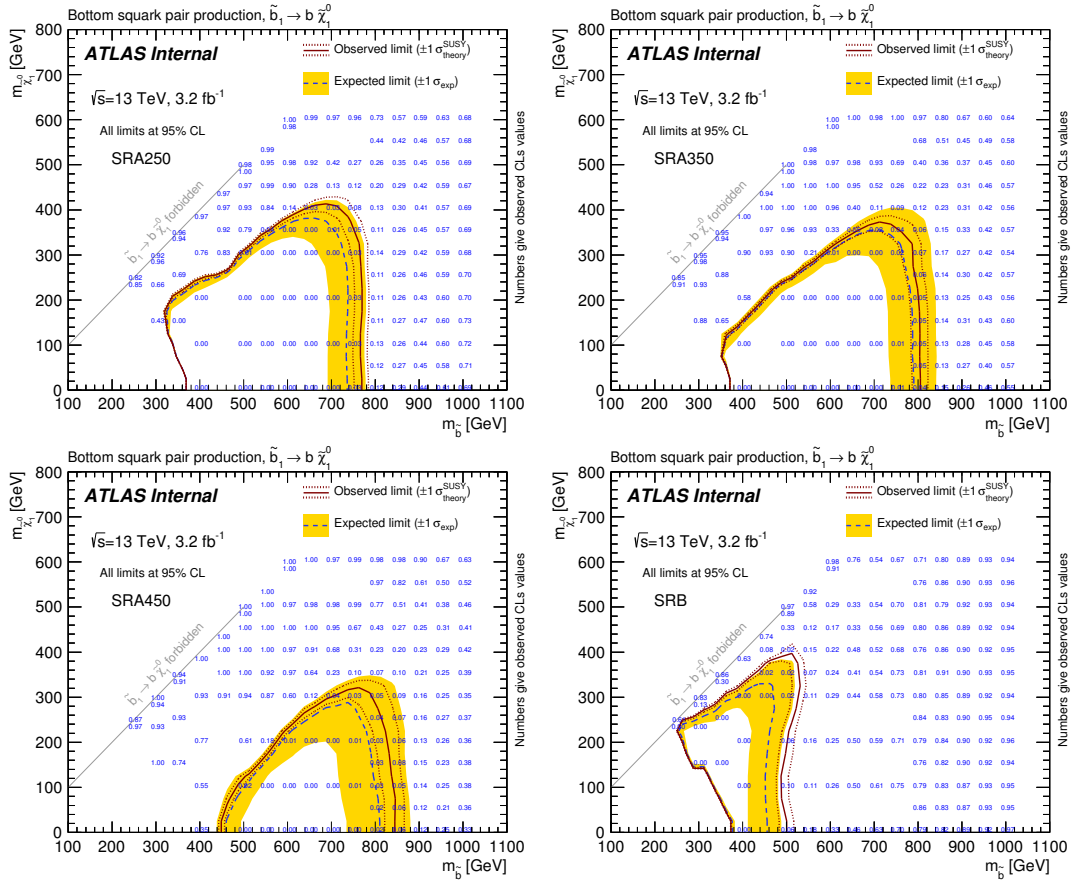


Fig. B.2 Expected and observed exclusion limits at 95% CL in the $(m_{\tilde{b}}, m_{\tilde{\chi}_1^0})$ plane for the four signal regions defined in this analysis. The dashed black and solid bold red lines show the 95% CL expected and observed limits respectively, including all uncertainties except the theoretical signal cross-section uncertainty. The shaded (yellow) bands around the expected limits show all the impact of the experimental uncertainties while the dotted red lines show the impact on the observed limit of the variation of the nominal signal cross-section by 1σ theoretical uncertainty. Numbers show the observed CLs values.

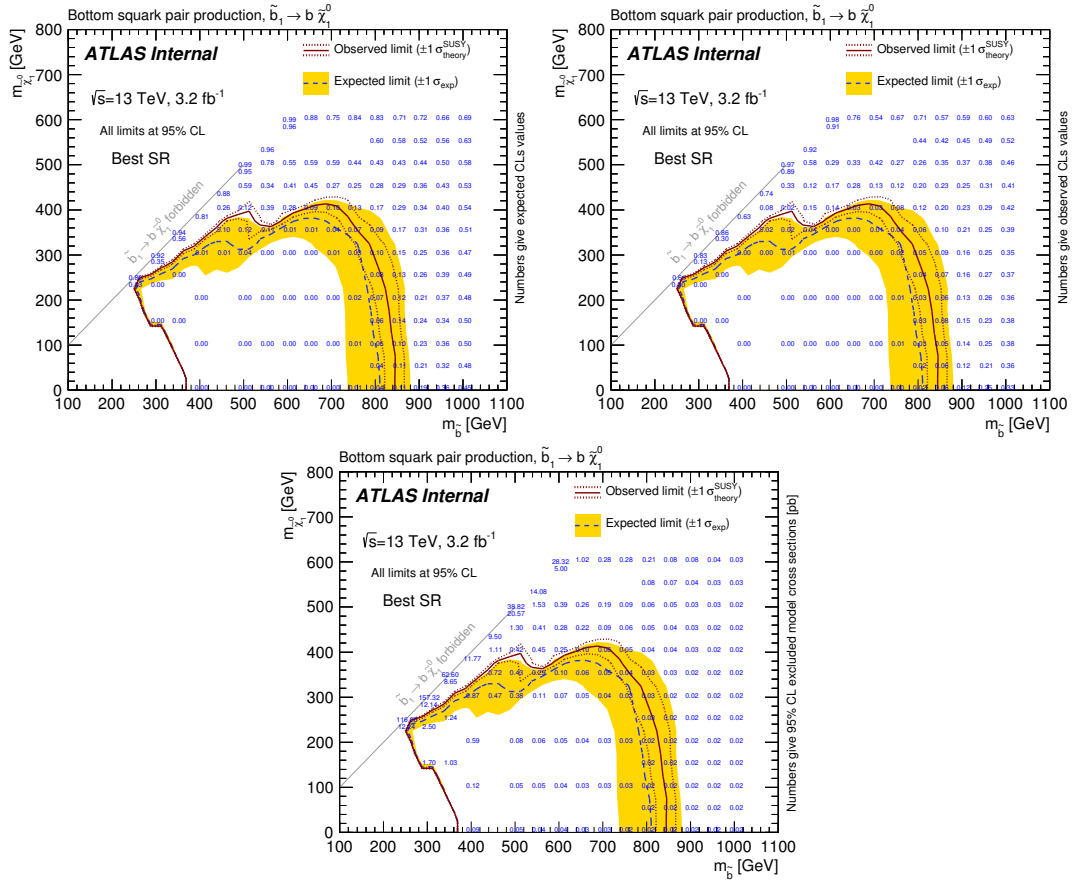


Fig. B.3 Combined expected and observed exclusion limits at 95% CL in the $(m_{\tilde{b}}, m_{\tilde{\chi}_1^0})$ plane (a). For each signal point, the signal region which leads to the best expected limit is chosen, indicated in (b). The dashed black and solid bold red lines show the 95% CL expected and observed limits respectively, including all uncertainties except the theoretical signal cross-section uncertainty. The shaded (yellow) bands around the expected limits show the impact of the experimental uncertainties while the dotted red lines show the impact on the observed limit of the variation of the nominal signal cross-section by 1σ theoretical uncertainty. Also shown for reference are the observed limits from the previous analysis [?]. The expected and observed CLs values are shown in (c) and (d), respectively. The 95% CL excluded model cross sections are shown in (e).

Appendix C

Auxillary material for the 2012 single top + E_T^{miss} analysis

Additional material for the Single Top + E_T^{miss} analysis performed in 2012 is presented in this Appendix.

C.1 Background Estimation

C.1.1 Control Region Definitions

The full selections for the various control regions are shown for the top control regions and W+jets control regions in Table C.1 and Table C.2 respectively.

Cut	Description	Top Control Regions (CRTs)			
		CRTinA	CRTinB	CRTinC	CRTexA
1	Event cleaning	Common to all SRs, VRs and CRs			
2	Trigger	1-electron or 1-muon			
3	1 Lepton	$pT > 25 \text{ GeV}$, $ \eta < 2.47(2.5)$ for e(mu)			
4	b-jets	$pT > 25 \text{ GeV}$, $ \eta < 2.5$			
5	Number of b-jets	2			
6	E_T^{miss}	$> 100, < 200 \text{ GeV}$	$> 120 \text{ GeV}$	$> 100, < 220 \text{ GeV}$	$> 100 \text{ GeV}$
7	MT	$> 140 \text{ GeV}$		$> 180 \text{ GeV}$	$> 120 \text{ GeV}$
8	am_{T2}	$< 160 \text{ GeV}$			$< 180 \text{ GeV}$
9	m_{eff}	$> 300 \text{ GeV}$	$> 450 \text{ GeV}$	$> 650 \text{ GeV}$	-
10	E_T^{miss} Sig.	$> 8 \text{ GeV}^{\frac{1}{2}}$	$> 6, < 12 \text{ GeV}^{\frac{1}{2}}$	$> 5 \text{ GeV}^{\frac{1}{2}}$	$> 5, < 10 \text{ GeV}^{\frac{1}{2}}$
11	m_{bc}^{min}	$< 170 \text{ GeV}$			
12	$\Delta\phi_{\text{min}}$	> 0.4			
13	$n_{\text{extrajets}}, (pT > 50 \text{ GeV})$	-	-	-	< 2

Table C.1 Summary of selections used in the Top Control Regions.

C.1 Background Estimation

Cut	Description	W+jets Control Regions (CRWs)			
		CRWinA	CRWinB	CRWinC	CRWexA
1	Event cleaning	Common to all SRs, VRs and CRs			
2	Trigger	1-electron or 1-muon			
3	1 Lepton	$pT > 25 \text{ GeV}$, $ \eta < 2.47(2.5)$ for e(mu)			
4	b-jets	$pT > 25 \text{ GeV}$, $ \eta < 2.5$			
5	Number of b-jets	1,2			2
6	E_T^{miss}	$> 100, < 200 \text{ GeV}$	$> 120 \text{ GeV}$	$> 100, < 220 \text{ GeV}$	$> 100 \text{ GeV}$
7	MT	$< 120 \text{ GeV}$			
8	am_{T2}	$> 180 \text{ GeV}$	$> 200 \text{ GeV}$	$> 180 \text{ GeV}$	
9	m_{eff}	$> 300 \text{ GeV}$	$> 450 \text{ GeV}$	$> 650 \text{ GeV}$	-
10	E_T^{miss} Sig.	$> 8 \text{ GeV}^{\frac{1}{2}}$	$> 6, < 12 \text{ GeV}^{\frac{1}{2}}$	$> 5 \text{ GeV}^{\frac{1}{2}}$	$> 5, < 10 \text{ GeV}^{\frac{1}{2}}$
11	$m_{b\ell}^{\text{min}}$	$< 170 \text{ GeV}$			
12	$\Delta\phi_{\text{min}}$	> 0.4			
13	$n_{\text{extrajets}}, (pT > 50 \text{ GeV})$	-			< 2

Table C.2 Summary of selections used in the inclusive W+jets Control Regions.

C.1 Background Estimation

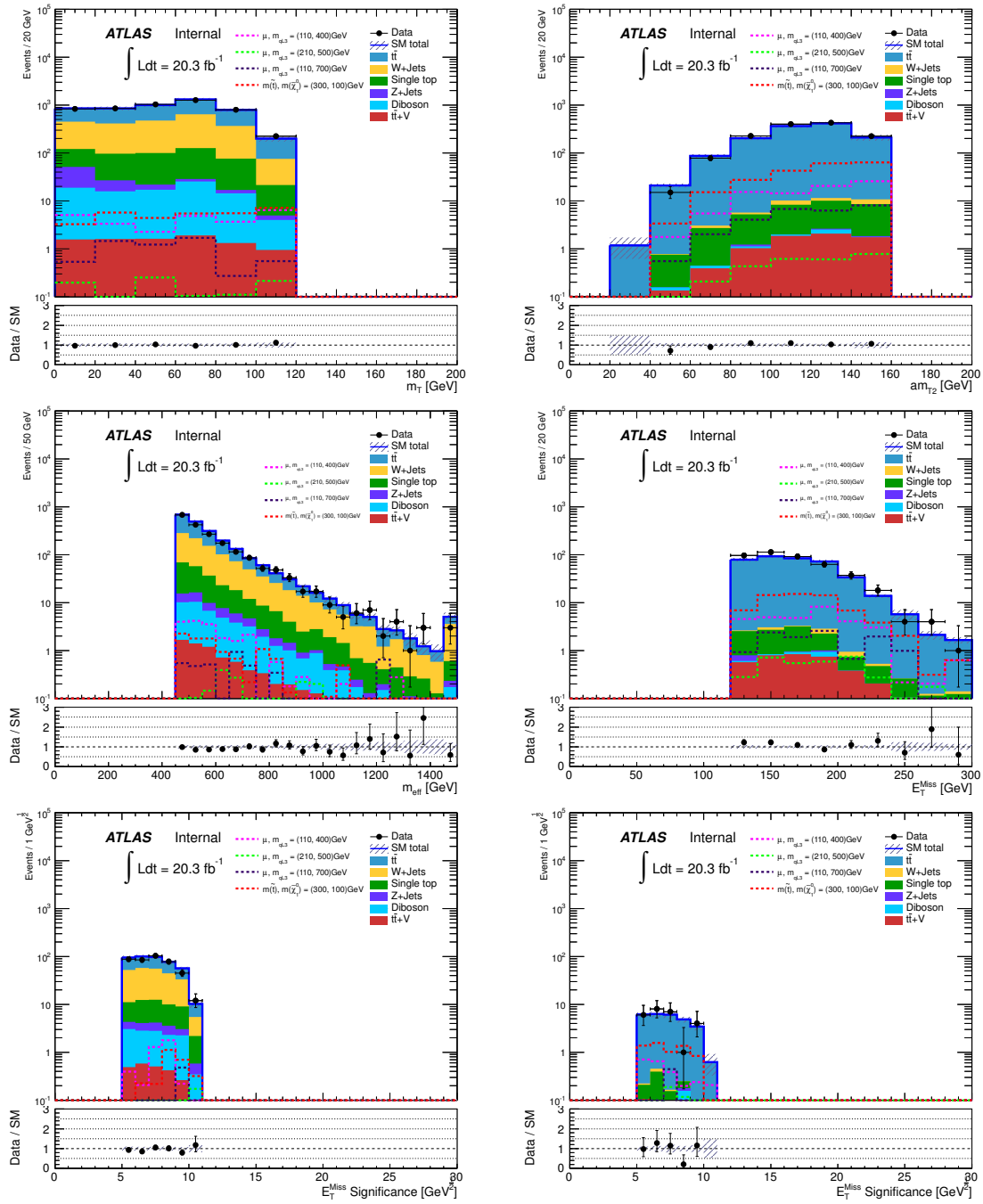


Fig. C.1 Pre-fit kinematic distribution plots for the inclusive CRs. The plots on the left show variables after cuts in the CRWs, the right shows variables after cuts in the CRTs. The rows correspond (in descending order) to the CRs associated with: SRinA, SRinB and SRinC.

C.1.2 Validation Region Definitions

Cut	Description	Top Validation Regions (VRTs)			W+jets Validation Regions (VRWs)		
		VRTinA	VRTinB	VRTinC	VRWinA	VRWinB	VRWinC
1	Event cleaning	Common to all SRs, VRs and CRs					
2	Trigger	1-electron or 1-muon					
3	1 Lepton	$pT > 25 \text{ GeV}$, $ \eta < 2.47(2.5)$ for e(mu)					
4	2 b-jets	$pT > 25 \text{ GeV}$, $ \eta < 2.5$					
5	E_T^{miss}	$> 200 \text{ GeV}$	$> 120 \text{ GeV}$	$> 220 \text{ GeV}$	$> 200 \text{ GeV}$	$> 120 \text{ GeV}$	$> 220 \text{ GeV}$
6	MT	$> 140 \text{ GeV}$		$> 180 \text{ GeV}$	$< 120 \text{ GeV}$		
7	am_{T2}	$< 160 \text{ GeV}$			$> 180 \text{ GeV}$	$> 200 \text{ GeV}$	$> 180 \text{ GeV}$
8	m_{eff}	$> 300 \text{ GeV}$	$> 450 \text{ GeV}$	$> 650 \text{ GeV}$	$> 300 \text{ GeV}$	$> 450 \text{ GeV}$	$> 650 \text{ GeV}$
9	$E_T^{\text{miss Sig.}}$	$> 8 \text{ GeV}^{\frac{1}{2}}$	$> 12 \text{ GeV}^{\frac{1}{2}}$	$> 5 \text{ GeV}^{\frac{1}{2}}$	$> 8 \text{ GeV}^{\frac{1}{2}}$	$> 12 \text{ GeV}^{\frac{1}{2}}$	$> 5 \text{ GeV}^{\frac{1}{2}}$
10	$m_{b\ell}^{\text{min}}$	$< 170 \text{ GeV}$					
11	$\Delta\phi_{\text{min}}$	> 0.4					

Table C.3 Summary of cuts used in all of the inclusive Validation Regions.

C.1 Background Estimation

Cut	Description	VRTexA	VRWexA
1	Trigger	1-electron or 1-muon	
2	Event cleaning	ATLAS Event Cleaning Selections	
3	2 b-jets	$p_T > 25 \text{ GeV}, \eta < 2.5$	
4	1 Lepton	$p_T > 25 \text{ GeV}, \eta < 2.5(2.47)$ for mu(e)	
5	E_T^{Miss}	$> 160 \text{ GeV}$	
6	m_T	$> 120 \text{ GeV}$	$< 120 \text{ GeV}$
7	am_{T2}	$< 180 \text{ GeV}$	$> 180 \text{ GeV}$
8	$m_{b,l}^{Min}$	$< 170 \text{ GeV}$	
9	E_T^{Miss} Significance	$> 10 \text{ GeV}^{\frac{1}{2}}$	
10	$\Delta\phi_{min}$	> 0.4	
11	m_{eff}	> 300	
12	$n_{extrajets}, (p_T > 50 \text{ GeV})$	< 2	

Table C.4 Summary of selections used in exclusive Top and W+jets Validation Regions

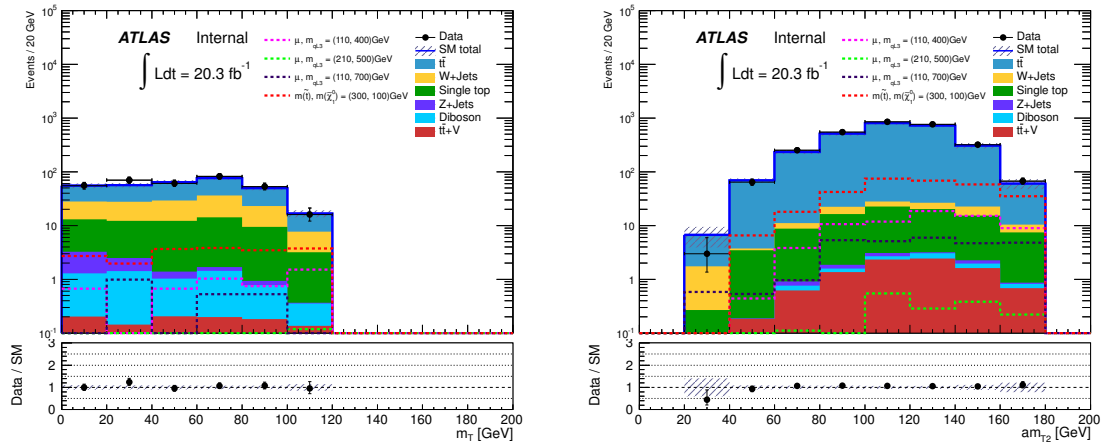


Fig. C.2 Pre-fit Kinematic distributions in the exclusive CRs. The plots in the left column show variables after cuts in the CRWs, the right column shows variables after cuts in the CRTs. In the CRs associated with SReXA are shown.

C.1.3 Results

INA region	CRT	CRW	VRT	VRW	SR1
Observed events	1371	4997	237	257	38
Fitted bkg events	1370 ± 37.0	5000 ± 70.8	251 ± 23.2	265 ± 30.6	27.0 ± 6.73
Fitted $t\bar{t}$ events	1330 ± 38.0	2710 ± 389	240 ± 22.9	125 ± 20.6	10.7 ± 5.64
Fitted Single Top events	27.4 ± 5.05	392 ± 50.9	4.63 ± 1.82	51.5 ± 20.5	9.08 ± 2.88
Fitted W+jets events	5.84 ± 2.24	1740 ± 381	2.32 ± 0.98	78.2 ± 26.0	3.21 ± 1.24
Fitted Z+jets events	0.31 ± 0.10	54.8 ± 7.62	$0.02^{+0.02}_{-0.02}$	2.01 ± 0.28	0.09 ± 0.02
Fitted DiBoson events	0.74 ± 0.20	86.8 ± 9.90	0.37 ± 0.12	6.28 ± 0.84	1.04 ± 0.18
Fitted $t\bar{t} + V$ events	7.26 ± 2.30	8.96 ± 2.72	2.83 ± 0.92	2.45 ± 0.81	2.92 ± 0.92
MC exp. SM events	1300	4990	238	265	26.7
MC exp. $t\bar{t}$ events	1260	2570	228	118	10.1
MC exp. Single Top events	27.4	392	4.63	51.5	9.07
MC exp. W+jets events	6.31	1880	2.50	84.6	3.47
MC exp. Z+jets events	0.31	54.8	0.02	2.01	0.09
MC exp. DiBoson events	0.74	86.8	0.37	6.28	1.04
MC exp. $t\bar{t} + V$ events	7.26	8.96	2.83	2.45	2.92

Table C.5 Background fit results for the inclusive A regions. Only systematic uncertainties are shown.

C.1 Background Estimation

INB region	CRT	CRW	VRT	VRW	SR1
Observed events	429	1946	122	138	20
Fitted bkg events	429 ± 20.7	1950 ± 44.1	134 ± 16.3	134 ± 17.4	14.1 ± 2.84
Fitted $t\bar{t}$ events	416 ± 21.0	1230 ± 179	129 ± 16.2	71.1 ± 11.1	4.98 ± 1.40
Fitted Single Top events	8.07 ± 1.63	178 ± 21.0	2.47 ± 1.20	27.4 ± 10.8	5.24 ± 2.07
Fitted W+jets events	0.86 ± 0.55	465 ± 179	0.20 ± 0.11	29.8 ± 14.0	1.24 ± 0.65
Fitted Z+jets events	0.28 ± 0.22	23.7 ± 4.07	$0.00^{+0.01}_{-0.00}$	0.94 ± 0.19	0.05 ± 0.01
Fitted DiBoson events	0.37 ± 0.07	39.4 ± 5.17	$0.15^{+0.20}_{-0.15}$	4.09 ± 0.49	0.72 ± 0.11
Fitted $t\bar{t} + V$ events	3.70 ± 1.19	7.37 ± 2.31	1.77 ± 0.59	1.19 ± 0.38	1.88 ± 0.61
MC exp. SM events	385	2120	120	146	14.4
MC exp. $t\bar{t}$ events	371	1100	115	63.5	4.44
MC exp. Single Top events	8.06	178	2.46	27.3	5.24
MC exp. W+jets events	1.43	768	0.33	49.2	2.04
MC exp. Z+jets events	0.27	23.6	0.00	0.94	0.05
MC exp. DiBoson events	0.37	39.3	0.15	4.08	0.72
MC exp. $t\bar{t} + V$ events	3.70	7.36	1.77	1.19	1.88

Table C.6 Background fit results for the inclusive B regions. Only systematic uncertainties are shown.

INC region	CRT	CRW	VRT	VRW	SR1
Observed events	26	411	36	83	10
Fitted bkg events	25.8 ± 5.05	411 ± 20.2	31.7 ± 6.61	97.3 ± 13.0	7.12 ± 2.93
Fitted $t\bar{t}$ events	24.5 ± 5.08	175 ± 48.3	30.3 ± 6.61	34.2 ± 8.93	2.04 ± 1.96
Fitted Single Top events	0.65 ± 0.17	37.5 ± 5.79	0.73 ± 0.32	23.8 ± 6.65	3.22 ± 2.14
Fitted W+jets events	$0.08^{+0.09}_{-0.08}$	179 ± 51.8	0.10 ± 0.05	33.9 ± 12.8	0.56 ± 0.26
Fitted Z+jets events	$0.04^{+0.04}_{-0.04}$	6.15 ± 0.82	0.00 ± 0.00	0.78 ± 0.12	0.03 ± 0.00
Fitted DiBoson events	0.12 ± 0.03	11.3 ± 1.23	$0.02^{+0.02}_{-0.02}$	3.52 ± 0.63	0.29 ± 0.06
Fitted $t\bar{t} + V$ events	0.41 ± 0.13	2.34 ± 0.73	0.58 ± 0.19	1.18 ± 0.38	0.98 ± 0.32
MC exp. SM events	27.4	436	33.6	102	7.28
MC exp. $t\bar{t}$ events	26.1	187	32.2	36.4	2.17
MC exp. Single Top events	0.65	37.5	0.73	23.8	3.21
MC exp. W+jets events	0.09	192	0.11	36.3	0.60
MC exp. Z+jets events	0.04	6.14	0.00	0.78	0.03
MC exp. DiBoson events	0.11	11.3	0.02	3.52	0.29
MC exp. $t\bar{t} + V$ events	0.41	2.34	0.58	1.18	0.98

Table C.7 Background fit results for the inclusive C regions. Only systematic uncertainties are shown.

C.1 Background Estimation

EXA region	CRT	CRW	VRT	VRW	SR1
Observed events	2870	337	665	280	46
Fitted bkg events	2870 ± 53.6	337 ± 18.3	640 ± 71.9	312 ± 41.6	31.3 ± 6.82
Fitted $t\bar{t}$ events	2740 ± 60.0	176 ± 26.4	613 ± 71.7	142 ± 20.3	13.2 ± 3.01
Fitted Single Top events	82.1 ± 15.2	54.4 ± 7.58	16.1 ± 6.58	50.3 ± 20.5	9.96 ± 5.34
Fitted W+jets events	35.8 ± 14.0	96.5 ± 29.3	6.14 ± 2.36	108 ± 35.3	4.35 ± 1.65
Fitted Z+jets events	1.30 ± 0.67	3.84 ± 0.70	0.15 ± 0.07	2.34 ± 0.40	0.07 ± 0.01
Fitted DiBoson events	1.88 ± 0.31	5.24 ± 0.84	0.84 ± 0.12	8.29 ± 1.01	1.48 ± 0.29
Fitted $t\bar{t} + V$ events	9.25 ± 2.91	1.06 ± 0.32	4.02 ± 1.29	1.26 ± 0.40	2.30 ± 0.72
MC exp. SM events	2720	318	606	294	30.2
MC exp. $t\bar{t}$ events	2590	166	579	134	12.4
MC exp. Single Top events	82.0	54.4	16.1	50.3	9.96
MC exp. W+jets events	32.4	87.4	5.56	97.4	3.94
MC exp. Z+jets events	1.30	3.84	0.15	2.34	0.07
MC exp. DiBoson events	1.88	5.24	0.84	8.28	1.48
MC exp. $t\bar{t} + V$ events	9.25	1.06	4.02	1.26	2.30

Table C.8 Background fit results for the exclusive A regions. Only systematic uncertainties are shown.

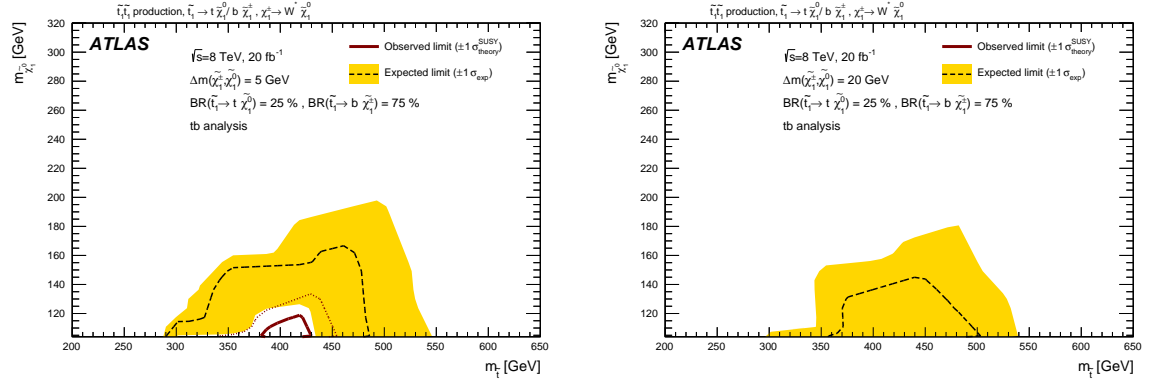
C.1.4 Limits

C.1.4.1 Breakdown of systematic uncertainties

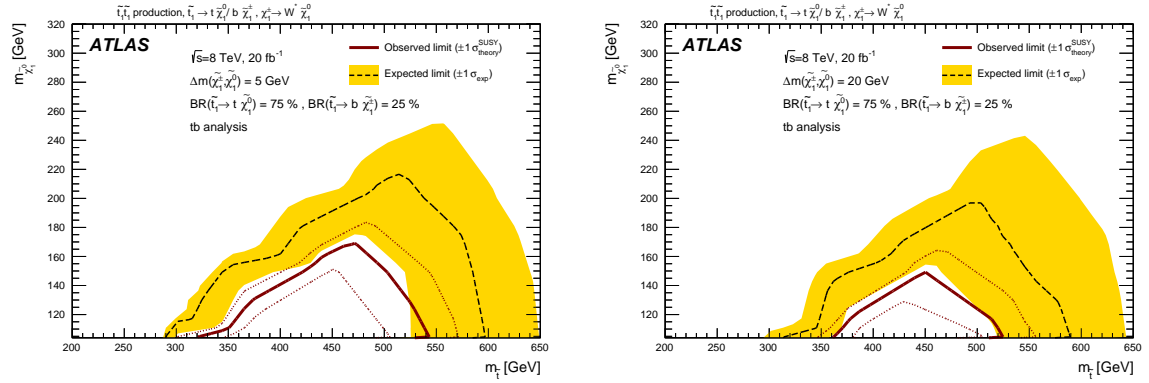
C.1 Background Estimation

Background prediction and uncertainties for	SRinA
Total background expectation	27.02
Total statistical ($\sqrt{N_{\text{exp}}}$)	± 5.20
Total background systematic	± 6.73 [24.92%]
$t\bar{t}$ Generator	± 5.46
Single Top Generator	± 2.43
JER	± 1.88
MC statistic in SR	± 1.13
$t\bar{t} + V$ cross section	± 0.87
b-tagging	± 0.75
$t\bar{t}$ scale factor	± 0.73
$t\bar{t}$ parton shower	± 0.71
W scale factor	± 0.71
Single Top parton shower	± 0.68
$t\bar{t}$ cross section	± 0.66
Single Top Wt channel cross section	± 0.65
JES	± 0.57
Luminosity	± 0.37
W b-filter cross section	± 0.32
$t\bar{t}$ ISR/FSR	± 0.27
W c-filter cross section	± 0.27
Single Top Interference	± 0.26
Soft term resolution	± 0.17
Single Top ISR/FSR	± 0.16
W scale	± 0.07
Pileup	± 0.07
W MLM	± 0.04
W extra radiation	± 0.03
W renscale	± 0.02
Soft term scale	± 0.01
MC statistics in VRT	± 0.00
MC statistics in CRW	± 0.00
MC statistics in CRT	± 0.00
MC statistics in VRW	± 0.00

Table C.9 List of fitted systematic uncertainties for the background prediction in SRinA. Since the different contributions are correlated, the total uncertainty is not obtained by simply adding them in quadrature.



(a) Limits obtained in the simplified model grid for $\Delta m(\tilde{\chi}_1^\pm, \tilde{\chi}_1^0) = 5 \text{ GeV}$ with $\text{BR}(\tilde{t} \rightarrow t\tilde{\chi}_1^0) = 0.25$, $\text{BR}(\tilde{t} \rightarrow b\tilde{\chi}_1^\pm) = 0.75$.
 (b) Limits obtained in the simplified model grid for $\Delta m(\tilde{\chi}_1^\pm, \tilde{\chi}_1^0) = 20 \text{ GeV}$ with $\text{BR}(\tilde{t} \rightarrow t\tilde{\chi}_1^0) = 0.25$, $\text{BR}(\tilde{t} \rightarrow b\tilde{\chi}_1^\pm) = 0.75$.



(c) Limits obtained in the simplified model grid for $\Delta m(\tilde{\chi}_1^\pm, \tilde{\chi}_1^0) = 5 \text{ GeV}$ with $\text{BR}(\tilde{t} \rightarrow t\tilde{\chi}_1^0) = 0.75$, $\text{BR}(\tilde{t} \rightarrow b\tilde{\chi}_1^\pm) = 0.25$.
 (d) Limits obtained in the simplified model grid for $\Delta m(\tilde{\chi}_1^\pm, \tilde{\chi}_1^0) = 20 \text{ GeV}$ with $\text{BR}(\tilde{t} \rightarrow t\tilde{\chi}_1^0) = 0.75$, $\text{BR}(\tilde{t} \rightarrow b\tilde{\chi}_1^\pm) = 0.25$.

Fig. C.3 Single Top + E_T^{miss} analysis limits on simplified model grids with alternative branching ratios of the scalar top decays.

C.1 Background Estimation

Background prediction and uncertainties for	SRinB
Total background expectation	14.11
Total statistical ($\sqrt{N_{\text{exp}}}$)	± 3.76
Total background systematic	± 2.84 [20.09%]
Single Top ISR/FSR	± 1.38
Single Top Generator	± 1.23
$t\bar{t}$ ISR/FSR	± 1.16
JER	± 0.92
MC statistic in SR	± 0.87
$t\bar{t} + V$ cross section	± 0.56
Single Top Interference	± 0.52
W scale factor	± 0.48
JES	± 0.44
b-tagging	± 0.43
$t\bar{t}$ scale factor	± 0.40
Single Top Wt channel cross section	± 0.38
$t\bar{t}$ cross section	± 0.31
Luminosity	± 0.22
Single Top parton shower	± 0.19
Soft term resolution	± 0.17
$t\bar{t}$ parton shower	± 0.16
W scale	± 0.16
W MLM	± 0.12
Soft term scale	± 0.11
W renscale	± 0.09
W c-filter cross section	± 0.09
W b-filter cross section	± 0.08
$t\bar{t}$ Generator	± 0.04
W extra raditation	± 0.03
Pileup	± 0.01
MC statistics in VRT	± 0.00
MC statistics in CRW	± 0.00
MC statistics in CRT	± 0.00

Table C.10 List of fitted systematic uncertainties for the background prediction in SRinB. Since the different contributions are correlated, the total uncertainty is not obtained by simply adding them in quadrature.

C.1 Background Estimation

Background prediction and uncertainties for	SRinC
Total background expectation	7.12
Total statistical ($\sqrt{N_{\text{exp}}}$)	± 2.67
Total background systematic	± 2.93 [41.20%]
$t\bar{t}$ Generator	± 1.43
Single Top Interference	± 1.31
$t\bar{t}$ parton shower	± 1.21
Single Top ISR/FSR	± 1.14
Single Top Generator	± 1.13
MC statistic in SR	± 0.45
$t\bar{t}$ scale factor	± 0.45
Single Top parton shower	± 0.36
$t\bar{t}$ ISR/FSR	± 0.33
$t\bar{t} + V$ cross section	± 0.29
b-tagging	± 0.29
Single Top Wt channel cross section	± 0.23
JER	± 0.20
JES	± 0.17
W scale factor	± 0.16
Luminosity	± 0.13
$t\bar{t}$ cross section	± 0.13
W b-filter cross section	± 0.06
Pileup	± 0.04
Soft term resolution	± 0.04
Soft term scale	± 0.04
W c-filter cross section	± 0.03
W scale	± 0.02
W MLM	± 0.01
W renscale	± 0.01
W extra raditation	± 0.01
MC statistics in VRT	± 0.00
MC statistics in CRW	± 0.00
MC statistics in CRT	± 0.00
MC statistics in VRW	± 0.00

Table C.11 List of fitted systematic uncertainties for the background prediction in SRinC. Since the different contributions are correlated, the total uncertainty is not obtained by simply adding them in quadrature.

C.1 Background Estimation

Uncertainty of channel	SRexA
Total background expectation	31.32
Total statistical ($\sqrt{N_{\text{exp}}}$)	± 5.60
Total background systematic	± 6.82 [21.76%]
Single Top Generator	± 4.40
Single Top Interference	± 3.30
JER	± 2.21
$t\bar{t}$ Generator	± 2.14
W scale factor	± 1.33
Single Top parton shower	± 1.25
MC statistic in SR	± 1.22
$t\bar{t}$ scale factor	± 0.86
$t\bar{t}$ cross section	± 0.81
Single Top Wt channel cross section	± 0.72
$t\bar{t} + V$ cross section	± 0.69
b-tagging	± 0.65
Soft term resolution	± 0.61
Single Top ISR/FSR	± 0.59
Soft term scale	± 0.49
Luminosity	± 0.39
JES	± 0.37
W scale	± 0.33
$t\bar{t}$ ISR/FSR	± 0.25
W MLM	± 0.23
W renscale	± 0.19
W c-filter cross section	± 0.13
W extra raditation	± 0.05
W b-filter cross section	± 0.04
Pileup	± 0.02
$t\bar{t}$ parton shower	± 0.01
MC statistics in VRT	± 0.00
MC statistics in CRW	± 0.00
MC statistics in CRT	± 0.00
MC statistics in VRW	± 0.00

Table C.12 List of fitted systematic uncertainties for the background prediction in SRexA. Since the different contributions are correlated, the total uncertainty is not obtained by simply adding them in quadrature.